Tampere University

MARGARITA GAPEYENKO

# System-Level Analysis of Blockage Dynamics in Millimeter-Wave Communications

Tampere University Dissertations 604

Tampere University Dissertations 604

MARGARITA GAPEYENKO

# System-Level Analysis of Blockage Dynamics in Millimeter-Wave Communications

ACADEMIC DISSERTATION
To be presented, with the permission of
the Faculty of Information Technology and Communication Sciences
of Tampere University,
for public discussion at Tampere University
on 31 May 2022, at 12 o'clock.

ACADEMIC DISSERTATION
Tampere University, Faculty of Information Technology and Communication Sciences
Finland

| | | |
|---|---|---|
| *Responsible supervisor and Custos* | Assoc. Prof. Sergey Andreev<br>Tampere University<br>Finland | |
| *Supervisor* | Dr. Dmitri Moltchanov<br>Tampere University<br>Finland | |
| *Pre-examiners* | Professor Riku Jäntti<br>Aalto University<br>Finland | Assoc. Prof. Harpreet S. Dhillon<br>Virginia Tech<br>USA |
| *Opponent* | Professor Petar Popovski<br>Aalborg University<br>Denmark | |



ISBN 978-952-03-2410-0 (print)
ISBN 978-952-03-2411-7 (pdf)
ISSN 2489-9860 (print)
ISSN 2490-0028 (pdf)
http://urn.fi/URN:ISBN:978-952-03-2411-7

PunaMusta Oy – Yliopistopaino
Joensuu 2022

*Dedicated to my family.*

# PREFACE

The research work summarized in this thesis has been carried out at the Unit of Electrical Engineering, Tampere University (former Department of Electronics and Communications Engineering, Tampere University of Technology) over the years 2016-2021.

First of all, I would like to thank my supervisor, Assoc. Prof. Sergey Andreev, who guided me throughout my doctoral studies and helped me to improve my research work. I really appreciate the numerous possibilities organized by Assoc. Prof. Sergey Andreev, to reach high-quality results during my research study. I am also very grateful to my co-supervisor, Dr. Dmitri Moltchanov, for being supportive along the road of my research career and helping me to strengthen my knowledge in various research areas. Furthermore, I would like to express my gratitude to Prof. Yevgeni Koucheryavy for giving me the opportunity to work with the wonderful research team and for all the support over these years. Special appreciation is dedicated to Dr. Nageen Himayat from Intel Labs, USA. The guidance and knowledge she shared helped me to grow professionally and personally. In addition to this, I would like to thank Dr. Shu-ping Yeh, Dr. Mustafa Riza Akdeniz, Dr. Sarabjot Singh, Assis. Prof. Ehsan Aryafar, for all your advice and deep involvement during our joint work between Intel Labs, USA and Tampere University.

I would like to sincerely thank the pre-examiners of this thesis, Prof. Riku Jäntti (Finland) and Assoc. Prof. Harpreet S. Dhillon (USA), for sharing their feedback on my work. The manuscript has significantly improved based on their valuable suggestions and constructive feedback. Special gratitude goes to Prof. Petar Popovski (Denmark) for agreeing to act as an opponent at my defense.

Financial sustainability is an essential part of any thorough research. This research has been primarily supported by the three-years Tampere University of Technology President's Scholarship (2017-2020). The work was also partially covered by Projects PRISMA, RADIANT, WiFiUS, and financial support from Intel Labs,

USA. I would also thank Nokia Foundation, HPY Research Foundation, and DELTA Network for their generous contribution to my research mobility.

The international academic collaboration was a valuable part of my doctoral studies. My first research visit was to Prof. Halim Yanikomeroglu's team at Carleton University, Ottawa, Canada, back in 2016. I am really grateful to Prof. Yanikomeroglu for all the lessons he taught me and his support during the visit and after. That experience gave me a lot of inspiration for my future work. I would like to take this opportunity to thank Dr. Sebastian S. Szyszkowicz and Dr. Irem Bor-Yaliniz for our enjoyable and fruitful collaboration during this visit. I also would like to thank Prof. Robert W. Heath Jr. for the chance to visit his research team at the University of Texas at Austin, USA, in 2018 and for his extreme hospitality and patience. It was a pleasure to do research under the guidance of Prof. Heath, thus learning best practices from one of the leading research groups in our field.

The research team I was fortunate to work with has become an important part of my research career and my life. First, I would like to express my gratitude to Prof. Mikko Valkama. Thank you for leading the research unit I worked in and the continued efforts that impact world research. In addition, my warmest thanks go to all my colleagues, co-authors, and friends who were working side-by-side with me, with whom I shared so many moments of our research life. This includes (in alphabetic order) Dr. Olga Galinina, Dr. Mikhail Gerasimenko, Roman Glazkov, Roman Kovalchukov, Ekaterina Olshannikova, Dr. Alexander Ometov, Dr. Rustam Pirmagamedov, Aleksei Ponomarenko-Timofeev, Dr. Alexander Pyattaev, Yekaterina Sadovaya, Andrey Samuylov, Dr. Dmitrii Solomitckii, Nikita Tafintsev, and Jani Urama.

With all my heart, I want to thank my dear family. You are the greatest source of inspiration to me. Thank you for believing in me and saying that everything is possible. There are not enough words to describe how much I love you and appreciate everything you did and continue doing for me. Last but definitely not least, I want to thank Dr. Vitaly Petrov. I had so much to say at the moment of writing that it would exceed all page limits. Vitaly, thank you for being in my life, giving me the strength to continue this exciting but challenging path.

MARGARITA GAPEYENKO

*March 15, 2022, Tampere, Finland*

# ABSTRACT

The new generation of wireless technology, termed as the fifth generation (5G), introduces a large amount of novel features. An operation in the millimeter-wave (mmWave) spectrum becomes one of those features unlocking a wide bandwidth. The latter allows for a notable increase in the peak data rate by up to tens of gigabits per second and decreases latency to as low as few milliseconds. These improvements provide an opportunity to support high-rate and low-latency applications, such as augmented and virtual reality, eHealth, and many others.

Though mmWave communications have great potential, they suffer from severe attenuation caused by signal blockage. In addition to large-scale blockers (i.e., buildings), small-scale blockers such as human bodies bring new challenges to the operation over mmWave bands. Large attenuation losses, as well as the unpredictable mobility of human body blockers, can significantly decrease a service quality when communicating over a mmWave link. Thereby, there is a need to properly model the blockage process, evaluate its impact on mmWave network performance, and estimate performance gains brought by different blockage mitigation techniques.

The thesis proposes a mathematical methodology to characterize and evaluate the effect of blockage dynamics in mmWave networks. With the help of stochastic geometry and probability theory, it delivers mathematical models of static and dynamic small-scale blockage, as well as static large-scale blockage. It then introduces system-level performance evaluation frameworks accounting for the main features of mmWave communications, such as blockage and multipath propagation. The mathematical frameworks can also evaluate the impact of several blockage mitigation techniques in realistic deployment scenarios.

# CONTENTS

## *List of Figures*

# ABBREVIATIONS

| | |
|---|---|
| 2D | two-dimensional |
| 3D | three-dimensional |
| 3G | third generation |
| 3GPP | 3rd Generation Partnership Project |
| 4G | fourth generation |
| 5G | fifth generation |
| AoA | angle of arrival |
| AoD | angle of departure |
| BS | base station |
| CDF | cumulative distribution function |
| COW-BS | cell-on-wheels BS |
| DS | delay spread |
| HAP | high altitude platform |
| IMT | International Mobile Telecommunications |
| ITU | International Telecommunication Union |
| LoS | line-of-sight |
| MC | multi-connectivity |
| MIMO | multiple-input multiple-output |
| mmWave | millimeter-wave |
| MPLP | Manhattan Poisson Line Process |
| NFV | network function virtualization |

| | |
|---|---|
| nLoS | non-line-of-sight |
| NR | New Radio |
| pdf | probability density function |
| pmf | probability mass function |
| PPP | Poisson Point Process |
| RAT | radio access technology |
| RSRP | reference signal received power |
| Rx | receiver |
| SCS | subcarrier spacing |
| SNR | signal-to-noise ratio |
| SpCon | spatially-consistent |
| SRS | sounding reference signal |
| TCP | Transmission Control Protocol |
| TR | technical report |
| Tx | transmitter |
| UAV | unmanned aerial vehicle |
| UAV-BS | unmanned aerial vehicle base station |
| UE | user equipment |
| ZoA | zenith angle of arrival |

# ORIGINAL PUBLICATIONS

Publication I M. Gapeyenko, A. Samuylov, M. Gerasimenko, D. Moltchanov, S. Singh, E. Aryafar, S. Yeh, N. Himayat, S. Andreev and Y. Koucheryavy. Analysis of human-body blockage in urban millimeter-wave cellular communications. *2016 IEEE International Conference on Communications (ICC)*. 2016, 1–7.

Publication II M. Gapeyenko, A. Samuylov, M. Gerasimenko, D. Moltchanov, S. Singh, M. R. Akdeniz, E. Aryafar, N. Himayat, S. Andreev and Y. Koucheryavy. On the Temporal Effects of Mobile Blockers in Urban Millimeter-Wave Cellular Scenarios. *IEEE Transactions on Vehicular Technology* 66.11 (2017), 10124–10138.

Publication III M. Gapeyenko, D. Moltchanov, S. Andreev and R. W. Heath Jr. Line-of-Sight Probability for mmWave-based UAV Communications in 3D Urban Grid Deployments. *IEEE Transactions on Wireless Communications* (2021).

Publication IV M. Gapeyenko, V. Petrov, D. Moltchanov, S. Andreev, Y. Koucheryavy, M. Valkama, M. R. Akdeniz and N. Himayat. An Analytical Representation of the 3GPP 3D Channel Model Parameters for MmWave Bands. *Proceedings of the 2nd ACM Workshop on Millimeter Wave Networks and Sensing Systems*. 2018, 33–38.

Publication V M. Gapeyenko, A. Samuylov, M. Gerasimenko, D. Moltchanov, S. Singh, M. Akdeniz, E. Aryafar, S. Andreev, N. Himayat and Y. Koucheryavy. Spatially-Consistent Human Body Blockage Modeling: A State Generation Procedure. *IEEE Transactions on Mobile Computing* 19.9 (2020), 2221–2233.

Publication VI M. Gapeyenko, V. Petrov, D. Moltchanov, M. R. Akdeniz, S. Andreev, N. Himayat and Y. Koucheryavy. On the Degree of Multi-Connectivity in 5G Millimeter-Wave Cellular Urban Deployments. *IEEE Transactions on Vehicular Technology* 68.2 (2019), 1973–1978.

Publication VII M. Gapeyenko, I. Bor-Yaliniz, S. Andreev, H. Yanikomeroglu and Y. Koucheryavy. Effects of Blockage in Deploying mmWave Drone Base Stations for 5G Networks and Beyond. *2018 IEEE International Conference on Communications Workshops (ICC Workshops)*. 2018, 1–6.

Publication VIII M. Gapeyenko, V. Petrov, D. Moltchanov, S. Andreev, N. Himayat and Y. Koucheryavy. Flexible and Reliable UAV-Assisted Backhaul Operation in 5G mmWave Cellular Networks. *IEEE Journal on Selected Areas in Communications* 36.11 (2018), 2486–2496.

### *Author's contribution*

All the articles presented in this thesis have been produced by the author when staying with the Faculty of Information Technology and Communication Sciences (ITC), Tampere University, former Faculty of Computing and Electrical Engineering, Tampere University of Technology, Tampere, Finland.

Publication I **"Analysis of human-body blockage in urban millimeter-wave cellular communications"**. The problem was identified together with the supervisors Assoc. Prof. Sergey Andreev, Dr. Dmitri Moltchanov, and Dr. Nageen Himayat from Intel Labs, CA, USA. The author developed the methodology and obtained the numerical results following the guidance of her supervisor Dr. Moltchanov. The author calculated the blockage probability for non-infinitesimal Rx and contributed to the development of blockage model for infinitesimal Rx together with Andrey Samuylov, Tampere University, and Dr. Sarabjot Singh, Intel Labs, CA, USA. Dr. Mikhail Gerasimenko contributed to the ray launch-

ing simulation results. The author wrote the paper. All authors contributed to developing the paper structure and editing the text.

Publication II — **"On the Temporal Effects of Mobile Blockers in Urban Millimeter-Wave Cellular Scenarios"**. The author contributed to the problem formulation together with her supervisors, as well as Dr. Nageen Himayat and Dr. Sarabjot Singh, both from Intel Labs, CA, USA. The author proposed the scenario of interest, then developed the methodology together with Andrey Samuylov under the guidance of supervisor Dr. Dmitri Moltchanov. The author obtained and analyzed the numerical results, as well as wrote the paper. All authors contributed to the paper writing and editing.

Publication III — **"Line-of-Sight Probability for mmWave-based UAV Communications in 3D Urban Grid Deployments"**. The author developed the problem formulation under the guidance of Prof. R.W. Heath during her research visit to Prof. Heath's research group, The University of Texas at Austin, TX, USA. The author proposed the representative scenario and developed the methodology to derive the LoS probability for grid type deployments for the UAV-to-BS link. The author conducted the numerical study and analyzed the results, as well as wrote the paper. All authors participated in the paper editing and revising.

Publication IV — **"An Analytical Representation of the 3GPP 3D Channel Model Parameters for mmWave Bands"**. The author identified the problem formulation. The author implemented the 3GPP 3D channel model. The author conducted the simulation study and proposed associated distributions for the particular channel model parameters together with supervisor Dr. Dmitri Moltchanov and Dr. Vitaly Petrov, Tampere University. The author delivered the multipath blockage model. The author wrote the paper. All authors participated in the paper editing and revising.

Publication V — **"Spatially-Consistent Human Body Blockage Modeling: A**

**State Generation Procedure"**. The author contributed to the problem formulation together with Dr. Nageen Himayat and Dr. Sarabjot Singh, Intel Labs, CA, USA. The author proposed the 3GPP-compatible algorithm to distribute spatially-consistent blocked and non-blocked states. Andrei Samuylov developed the analytical framework for the spatially-consistent blockage probability. The author conducted the numerical study and identified the effect of spatial correlation among the link states. The author wrote the paper. All authors contributed to the paper editing and revising.

Publication VI **"On the Degree of Multi-Connectivity in 5G Millimeter-Wave Cellular Urban Deployments"**. The author proposed the problem formulation together with Dr. Vitaly Petrov. The author identified the representative scenario together with supervisor Dr. Dmitri Moltchanov and Dr. Vitaly Petrov. The author developed the mathematical framework to account for multiple back-up connections in case of a blockage in mmWave communications. The author obtained the numerical results and identified the impact of the degree of multi-connectivity. All authors contributed to the paper editing and revising.

Publication VII **"Effects of Blockage in Deploying mmWave Drone Base Stations for 5G Networks and Beyond"**. This work is a result of the collaboration with Prof. Halim Yanikomeroglu and his research team at Carleton University, Ottawa, Canada. The author proposed the problem formulation together with the supervisor Assoc. Prof. Sergey Andreev, Prof. Yanikomeroglu, and Dr. Irem Bor, Carleton University. Dr. Bor proposed the drone placement algorithm. The author proposed the methodology for the analytical drone height optimization. The author and Dr. Bor conducted the numerical study. The author wrote the paper together with Dr. Bor. All authors contributed to the paper editing and revising.

Publication VIII **"Flexible and Reliable UAV-Assisted Backhaul Operation**

**in 5G mmWave Cellular Networks"**. The author proposed the problem formulation together with Dr. Vitaly Petrov and her supervisors Assoc. Prof. Sergey Andreev, Dr. Dmitri Moltchanov. The author proposed the methodology for the time-averaged analysis. Dr. Moltchanov proposed the methodology for the time continuous analysis. Dr. Petrov developed the simulation tool and conducted the simulation study. The author analyzed the numerical results. The author wrote the paper. All authors contributed to the paper editing and revising. The publication is also included in the PhD thesis by Dr. Petrov.

# 1 INTRODUCTION

## 1.1 General Background

International Telecommunication Union (ITU) continuously strives to provide various standards and requirements to harmonize mobile broadband systems throughout the world. In almost every decade since the year 2000, ITU has approved new International Mobile Telecommunications (IMT) standards such as IMT 2000 [48], IMT advanced [47], and most recently – IMT 2020 [49]. These standards are then employed by a different generation of mobile networks such as the third generation (3G), fourth generation (4G), and fifth generation (5G), respectively, where each generation is supposed to fulfill more stringent service requirements than its predecessor. Particularly, 5G networks, when compared to 4G, are required to deliver up to 10-100 higher data rate, support 10-100 more connected devices, and reach a millisecond-scale latency [46].

To satisfy these ambitious requirements, 5G incorporates various enabling technologies. For example, the main enablers such as massive multiple-input multiple-output (MIMO), advanced beamforming, and a new wide bandwidth [3, 5, 53, 62] can provide a tremendous increase in overall capacity, when comparing 5G to 4G [40, 44]. With the help of network function virtualization (NFV), 5G networks are expected to be more flexible and capable of supporting heterogeneous applications and services [12, 26]. Another promising technology is integrated access and backhaul, a wireless backhaul solution allowing densifying the network without a costly fiber installation [8, 81, 90].

A larger available bandwidth is one of the key drivers for the increased capacity at the air interface. Thus, millimeter-wave (mmWave) communications, operating in a range of 30-300 GHz, have become one of the important novelties introduced for 5G [38, 83]. With a wide bandwidth available at mmWave frequencies, these networks can reach up to tens of gigabits per second of data rates and significantly

reduce the latency when compared to lower frequency bands. The improved performance, in its turn, allows to accommodate high-rate applications such as augmented and virtual reality, autonomous driving, and many more [6, 63, 74].

Nowadays, the mmWave communications are included as a part of 5G New Radio (NR) – a radio access technology (RAT) developed within the 3rd Generation Partnership Project (3GPP) and first introduced in Release 15 [2, 44]. There are four mmWave bands in a frequency range of 24.2—52.6 GHz supported by NR Release 16 [7]. According to Release 16 TS 38.104, the maximum carrier bandwidth of 400 MHz is supported for a subcarrier spacing (SCS) of 120 kHz and available in each of the four mmWave bands [7]. Furthermore, there is an ongoing work item in 3GPP Release 17 to extend NR operation up to 71 GHz. Thereby, for Release 17, we can expect even wider bands to be supported of up to 2 GHz [9].

As soon as the first set of 5G specifications became available, commercial deployments of 5G networks started to launch throughout the world. Together with 5G networks operating in the sub-6 GHz frequency range, there are operators (including AT&T, T-Mobile, and Verizon in the USA) already providing mmWave connectivity for hot spot areas [25]. In response to the 5G networks roll-out, user devices began to appear on the global market. According to [105], by the end of April 2021, there were approximately 468 commercially available 5G devices. Some of these devices also support a mmWave connectivity, including the 5G-capable iPhone released by Apple in October 2020.

Despite their great benefits and potential, mmWave communications are facing several challenges. As compared to the lower frequencies, a theoretical communication range with mmWave isotropic antennas is significantly reduced [38]. The directional mmWave antennas on both transmitter (Tx) and receiver (Rx) sides become a solution for coverage extension but at the cost of increased system complexity [11, 79, 86, 89]. In addition to the above, mmWave links are severely attenuated by various objects in the environment [83]. Together with the directional transmissions and receptions needed for coverage, the former increases the link blockage problem, making it an essential factor to consider in the design and evaluation of mmWave communication systems.

## 1.2 Thesis Motivation

A blockage of mmWave signal by various objects is one of the crucial challenges in the design and analysis of mmWave networks. A line-of-sight (LoS) blockage by buildings and other large objects, referred to as large-scale blockage, was identified as an issue for the lower frequency bands in the previous generations of mobile networks including 4G and earlier [27]. For mmWave networks, this issue has become more profound due to an increased attenuation from large-scale blockers causing up to 40-80 dB of loss [83, 118]. Moreover, mmWave networks are also planned to support different applications and services that introduce new deployment scenarios to be modeled [14, 96]. For instance, unmanned aerial vehicles (UAVs) operating in urban areas require considering the variations of the heights of the buildings for more accurate system modeling. All these changes create a need to elaborate conventional LoS probability models to address a large-scale blockage in a broader range of scenarios.

In addition to a large-scale blockage, much smaller objects like cars, lampposts, and even human bodies in the environment act as obstacles for mmWave signals; these are referred to as small-scale blockers [83, 108]. The field experiments have demonstrated that a degradation of up to 40 dB can be caused by small-scale blockers, motivating to consider them as part of an overall mmWave system analysis [41, 58, 100]. On top of that, an unpredicted mobility of different small-scale objects (e.g., human bodies) provides additional challenges for mmWave connectivity. In that regard, understanding blockage process dynamics becomes of crucial importance.

A dense human crowd may lead to unpredictable and frequent link interruptions [59]. In order to support reliable connectivity, mmWave systems have to adopt appropriate blockage mitigation techniques [39, 88]. In its turn, these techniques increase overall system complexity, where conventional performance evaluation models are not well suited. Therefore, to provide a comprehensive and accurate analysis, more advanced models are needed. Moreover, to gain non-incremental gains by adopting sophisticated blockage mitigation techniques, one should adjust and optimize a solution to reach its best performance.

An increased number of different blockers, an unpredicted mobility of blockers, and new blockage mitigation techniques impose a new set of challenges that need to be addressed. These features call for creating new models and frameworks to evaluate

mmWave systems as well as potential enhancements to mitigate blockage, forming the motivation for this thesis.

## 1.3 Thesis Structure and Main Contributions

The main contribution of this thesis is a mathematical methodology that characterizes and evaluates the effect of blockage dynamics in mmWave communication systems. Particularly, the thesis develops mathematical models for small-scale and large-scale blockage. Furthermore, this work provides a set of mathematical frameworks to evaluate a performance of mmWave systems in different deployment scenarios with blockers and possible blockage mitigation techniques.

The introduction part of the thesis consists of five chapters and is followed by eight publications. Chapter 1 provides a general background of the studied area, the research motivation, the main contribution of the thesis, and the thesis structure. The following chapters feature dedicated brief reviews of the prior art in their respective areas, which are offered at the beginning of each.

Chapter 2 describes modeling of LoS blockage in mmWave systems. *The main research question of this chapter is to understand the effects of environmental conditions on the time-averaged and temporal characteristics of blockage process in mmWave communications.* For that purpose, it proposes a set of mathematical models with different Rx sizes for blockage caused by static human bodies. Then, blocked and non-blocked time distributions to characterize the dynamic process of mobile human body blockage are delivered. Next, a large-scale blockage associated with buildings is investigated, and the LoS probability for an urban grid scenario is derived. Finally, the numerical analysis demonstrates the blockage effect in various environmental conditions.

Chapter 3 extends the results from Chapter 2 and considers a multipath propagation of mmWave communications. *Particularly, this chapter explores the possible variations in the blockage process characteristics when considering multipath propagation and spatial consistency across the mmWave links states.* For that reason, the analytical approximations of the main channel model parameters such as a zenith angle of arrival (ZoA) and a power share are proposed. Extending the methodology from Chapter 2, the multipath blockage probability is derived. Further, the algorithm that distributes blocked/non-blocked states across various links and considers a spa-

tial consistency among links states is delivered. The numerical results demonstrate the difference between LoS-only and multipath blockage models, as well as the impact of a spatial consistency across links states.

Chapter 4 considers the main observations from previous chapters and concentrates on the overall performance evaluation of mmWave communication systems enhanced with different blockage mitigation techniques. *Notably, this chapter aims to study the performance gains enabled by various blockage mitigation techniques, including multi-connectivity and UAV-based communications, and identify the configurations where the introduced benefits are the most notable.* Thereby, it proposes a framework to account for multi-connectivity and support nodes in case of a sudden blockage. The framework provides a first-order analysis of a required number of back-up connections to maintain desired performance requirements. Further work in the direction of mmWave communication improvements considers an UAV as a potential carrier for a mmWave base station (BS). Particularly, a mathematical framework is proposed to account for mmWave connectivity with UAVs as well as their mobility. The numerical results demonstrate the ability of multi-connectivity and UAVs to efficiently mitigate blockage in mmWave networks, thus improving their performance. At the same time, the analysis also shows the limitations of these solutions when working in especially challenging configurations.

Finally, Chapter 5 concludes the summary and outlines the main future research directions.

# 2 LOS BLOCKAGE MODELING

## 2.1 Research Motivation

Due to its small wavelength and the use of directional antennas, mmWave communications is vulnerable to signal blockage caused by various objects [41, 85, 103]. These are not only large-scale objects such as buildings, but also small-scale blockers like cars, lampposts, and even human bodies that can lead to significant signal degradation [41, 111]. Therefore, to provide a comprehensive analysis of mmWave-based systems, it is crucial to consider a new type of blockers as well [13].

There has been already some experimental and simulation work done to assess the performance of the next generation network, namely 5G. In [59], the authors took field measurements in a street environment, employing horn antennas on both the Tx and Rx sides operating at 73 GHz carrier frequency. The experiment demonstrated a signal degradation of up to 20-25 dB due to human body blockage alone. By analyzing the statistical data gathered with the measurements, the authors proposed the Markov chain model to describe the blockage attenuation caused by human bodies. We note, that the transition probabilities from blocked to non-blocked state were calculated from the collected data. Further, in [64], end-to-end simulations, specifically tailored to capture the specifics of mmWave communications, have been conducted. Among different aspects, the simulator can also account for human body blockage employing the blockage model from [1].

The experimental and simulation frameworks mentioned above face certain limitations related to various deployments modeling due to their high operational and computational costs [76, 85]. Besides the said frameworks, there are analytical frameworks that allow to comprehensively study effects of different parameters on overall system performance. However, there are a lack of analytical models available that capture mmWave communications features, and especially those involving small-scale blockage, which limits in-depth analytical evaluations. In this chapter, we pro-

pose a set of analytical models that consider for small and large-scale blockages with sufficient details (e.g., various density of blockers, heights of nodes) yet under significantly decreased computational costs.

The rest of the chapter goes as follows. In Section 2.2, we describe the most common types of blockage affecting mmWave communications in an outdoor environment and the existing approaches to model them. Further, in Section 2.3 we propose a LoS blockage model, where a blockage is caused by static small-scale blockers, particularly human body blockers. In Section 2.4, we consider the mobility of human body blockers and provide the temporal characteristics (e.g., the time in blocked or non-blocked state) of a dynamic blockage process. Finally, in Section 2.5, a LoS blockage model, where the blockage is caused by large-scale blockers (buildings), is derived. The models developed in this chapter help explore the effects of the environmental conditions on the time-averaged and temporal characteristics of blockage process in mmWave communications.

## 2.2 Overview of Blockage Types and Models

There are different objects that may potentially block a mmWave signal and cause severe signal degradation in a typical outdoor scenario. We divide the most common sources of a mmWave signal blockage into three main categories: (i) self-body blockage, (ii) small-scale blockage, and (iii) large-scale blockage. Next, we describe these categories and associated modeling approaches in more detail.

### 2.2.1 Self-body blockage

The self-body blockage is a new type of blockage that becomes profound in mmWave communications [68]. This blockage mainly happens due to user equipment (UE) orientation, causing a signal blockage by the body itself [42]. As shown in [82], this scenario may cause 30-40 dB of loss for the carrier frequencies of 28 GHz and 40 GHz and thus should be considered in system modeling.

Different approaches allow to account for a self-body blockage available up to date. The first approach has been described by the 3GPP and is termed as Model A. The Model A [1] is a stochastic model with randomly distributed two-dimensional (2D) screens of random orientation and angles. One of the screens is assumed to be

a self-blocking region while other screens represent small-scale blockers. In the case of self-blockage, the attenuation of each multipath cluster is assumed to be 30 dB, otherwise it is 0 dB.

The second approach considers a random rotation of a user and, based on stochastic geometry, calculates a link blockage probability [16, 77]. It is assumed that the user is self-blocking any signal coming from a particular direction termed as a blocking cone. For every time slot, the user changes position by shifting a blocking cone. The model also applies a constant attenuation to a signal blocked by the user.

### 2.2.2 Small-scale blockage

Next, we consider a small-scale blockage, which has become an issue for mmWave band communications. There are a vast number of objects that can be termed as small-scale blockers present in urban conditions. Those could be static objects, e.g., lampposts, trees, or dynamic objects, e.g., human bodies or cars. The experiments on mmWave communications in outdoor and indoor scenarios conducted in [41, 58, 100] demonstrated that a signal degradation could be as high as 40 dB caused by small-scale blockers.

Similarly to self-body blockage, there are two main approaches to modeling small-scale blockage. The first one, introduced by 3GPP, consists of two models. Model B [1], assumes the physical mapping of small-scale blockers modeled as screens over an area of interest. The second model from 3GPP, termed as Model A [1], employs a stochastic approach to capture the characteristics of screens (e.g., an orientation and angles). Both models imply a particular algorithm to be executed and provide attenuation caused by small-scale blockers employing the knife edge diffraction model. Another approach to modeling a small-scale blockage is based on stochastic geometry and probability theory, as in [34, 75]. Following the second approach, the authors in [75] provided a vehicle blockage model.

As human body blockage is one of the most common blockage types in many different deployments, a suitable model to characterize it is essential. Besides the models provided by 3GPP, mostly suitable for simulation-related studies, an analytical model characterizing human body blockage is needed. An analytical human body blockage model can be further employed for comprehensive analytical studies as well as integrated into simulators to decrease computational complexity.

### 2.2.3 Large-scale blockage

Finally, we describe large-scale blockage, which is already widely considered in outdoor urban deployments. For the scope of this thesis, we refer to large-scale blockage, such as blockage primarily caused by surrounding buildings.

To date, there are several different large-scale modeling approaches available. Besides the physical modeling of buildings directly into a simulator, there is also a widely-used approach to account for blockage using stochastic methods. For instance, 3GPP proposed a LoS blockage probability for different deployment scenarios [1]. Due to the fixed parameters used in these models, it is not possible to change the deployment configurations (e.g., density of buildings). Further, in [17], the authors delivered a model for large-scale blockage by utilizing random shape theory. This method allowed model deployment with a random orientation of buildings, which is well suited for deployments similar to a university campus with no clear grid of buildings.

There is a broad range of applications that can be supported by the fifth generation of mobile networks. It is expected that these applications will be available in different environments. Therefore, appropriate LoS models [98] are required to account for various scenarios, e.g., urban grid scenario [109]. Moreover, heterogeneous types of devices beyond conventional users, e.g., UAVs, demand consideration of building height, which was not part of previous LoS blockage models [54, 66]. All these facilitate the work towards new LoS blockage models that cover a broader range of environments and applications.

Summarizing, the existing gaps in the analytical LoS blockage modeling (occlusion of mmWave links by various types of objects in different scenarios) call for further development of such models. Therefore, in this thesis, we deliver analytical models to account for the following blockage types:

- **Small-scale blockage.** We consider a human body blocker as a source of small-scale blockage. First, we deliver the blockage model for the scenario with static human body blockers. Next, we focus on the mobility of human body blockers and investigate temporal properties of the dynamic blockage process including mean values and distributions of blocked and non-blocked intervals. Finally, we provide the blockage model for the scenario with dynamic human body blockers.

- **Large-scale blockage.** We concentrate on an urban grid scenario with a fixed orientation of buildings. We propose the LoS probability model that accounts for different building heights and the associated distribution, density of buildings, heights of nodes, and other deployment-related parameters.

Next in Section 2.3, Section 2.4, and Section 2.5, we describe the proposed methodologies of these models and provide the main results.

## 2.3 Static Human Body Blockage Analysis

We proceed with our contribution towards the analytical formulation of the blockage model, developed in Publication I [34], where the small-scale blockage is caused by human bodies. First, to analytically model a human body blockage, we need to approximate a blocker with a certain geometrical shape. The experimental studies of a human body blockage in mmWave communications [50] demonstrate that a cylinder may be one of the possible shapes to approximate a human body. Thereby, we assume a cylinder with a height of $h_{\mathrm{B}}$ and a base diameter of $d_{\mathrm{B}}$ to represent a human body. The human body blockers are considered to be static with the center of each blocker distributed according to the Poisson Point Process (PPP) with density $\lambda_{\mathrm{B}}$ on the 2D plane, as depicted in Fig. 2.1.

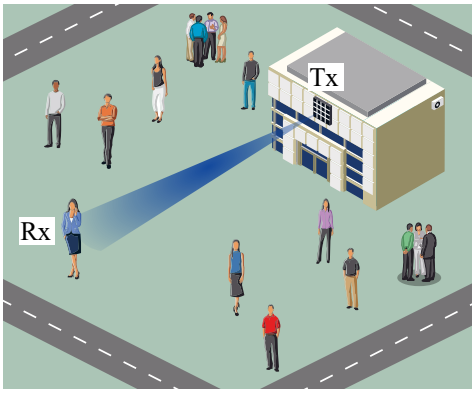


**(a)** Scenario of interest with human body blockers

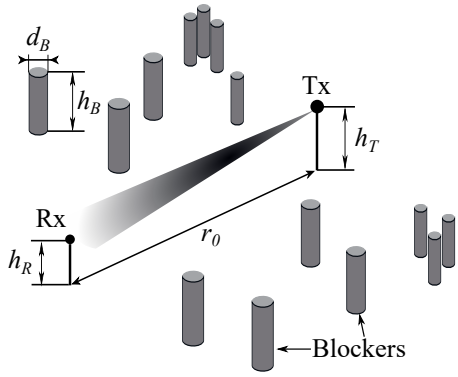


**(b)** Geometrical representation of scenario with human body blockers

**Figure 2.1** Considered scenario for analytical modeling of static human body blockers.

We consider the Tx (i.e., a mmWave BS) located at a distance $r_0$ from the Rx (i.e., a mmWave UE). The heights of Tx and Rx are equal to $h_{\mathrm{T}}$ and $h_{\mathrm{R}}$, respectively. The

primary metric of interest described in this section is termed as blockage probability, $p_{\mathrm{B}}$ – the probability that a link between Tx and Rx is occluded by a blocker. We specifically assume an optical link blockage, meaning that a link is considered to be blocked if the height of the blocker is higher than a visual LoS between the Tx and the Rx at their point of intersection. Other model parameters, beyond those used in this section, are summarized in Table I of Publication I [34].

Depending on the assumption regarding the size of the Rx, the blockage probability is calculated differently. Therefore, we consider two sizes of the Rx:

- **Non-infinitesimal Rx.** We assume the size of the Rx is non-negligible with respect to other geometrical objects in the scenario and has a certain length. In this case, the link blockage will happen if the height of a blocker is higher than the line connecting the Tx and the Rx at the intersection point and a blocker is shadowing the full Rx length.
- **Infinitesimal Rx.** We assume the size of the Rx is negligible with respect to other geometrical objects in the scenario and consider it as a point. This is a widely used assumption related to the Rx size [92]. Therefore, to block a link between the Rx and the Tx, a blocker has to be higher than the line connecting the Tx and the Rx at their point of intersection.

Next, we proceed with an explanation of the proposed methodologies and the final blockage probabilities for different Rx sizes described above.

### 2.3.1 Blockage probability with non-infinitesimal Rx

We consider an Rx of a certain length of $l$. Following [71], we characterize human body blockers with a random height following Normal distribution as $H_{\mathrm{B}} \sim \mathcal{N}(\mu_H, \sigma_H)$ and random diameter with Uniform distribution as $D_{\mathrm{B}} \sim \mathcal{U}(d_{\min}, d_{\max})$.

We further note that only blockers located between the Tx and the Rx with heights higher than the LoS path at the intersection point can block the LoS. Therefore, we thin out the PPP of blockers with initial density of $\lambda_{\mathrm{B}}$ to leave only those that can block the LoS. The resultant density of the thinned out PPP of blockers, $\lambda(x)$, is calculated as

$$\lambda(x) = \lambda_{\mathrm{B}} Pr\{H_{\mathrm{B}} > h_{\mathrm{m}}(x)\}, \tag{2.1}$$

where $h_{\mathrm{m}}(x)$ is the minimum height of a blocker that will start causing the blockage at a certain distance $x$ from the Tx given in Publication I [34].

Next, we assume the Rx is located on the circumference of a circle, and the Tx is located at the center of the same circle. We project the bases of the blockers from the thinned out PPP with the resultant density $\lambda(x)$ on the circumference with the Rx. From Fig. 2.2, we observe that one or more of the overlapped blockers projections create a blocked interval, $\eta$, on the circumference. The gaps between those blocked intervals are called non-blocked intervals, $\omega$. The sum of the consecutive blocked and non-blocked intervals, $\xi = \omega + \eta$, establishes an interval repeated at the end of every $\xi$. We notice that the blocked interval alternates with the non-blocked interval resulting in a process called an alternating renewal process [22].

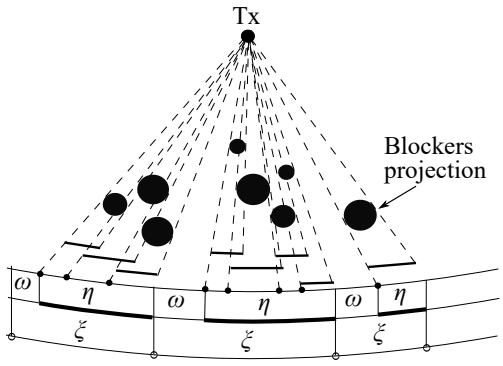


**Figure 2.2** Alternating renewal process of blocked/non-blocked intervals for scenario with non-infinitesimal Rx.

The blockage of the Tx-Rx link can occur when two events happen simultaneously: A – the left side point of the Rx with a length of $l$ is dropped on a blocked interval; and B – a distance from the left side point of the Rx to the end of a blocked interval will be greater than $l$. Therefore, we need to find the probabilities of events A and B to characterize the blockage probability for the non-infinitesimal Rx.

First, we need to obtain the characteristics of the blocked and non-blocked intervals of the alternating renewal process. The distance between the centers of every blocker's projection is distributed according to the exponential distribution with a parameter $\mu$, where $\mu$ is the density of blockers on the circumference given in Publication I [34]. The left points of the blockers' projections are statistically equally shifted from their centers. Thus, the distance between them is also exponentially

distributed with the parameter $\mu$. Following the memoryless property of the exponential distribution [55], the interval between the left point and the end of the previous projection is exponentially distributed. Therefore, the non-blocked interval, $\omega$, follows the exponential distribution, $F_\omega$, with the parameter $\mu$.

We proceed with the derivation of the cumulative distribution function (CDF) of blocked interval, $F_\eta(x)$, using the property of the Laplace–Stieltjes transformation, where $F^*_\xi(s)$, $F^*_\eta(s)$, $F^*_\omega(s)$ are the Laplace–Stieltjes transforms of $\xi$, $\eta$, $\omega$, respectively. With the help of this transformation we find the Laplace–Stieltjes transform of the interval $\xi$ as $F^*_\xi(s) = F^*_\eta(s)F^*_\omega(s) = \mu\frac{F^*_\eta(s)}{\mu+s}$. We can now find the CDF of the blocked interval, $\eta$, by transforming it back as

$$F_\eta(x) = F_\xi(x) + \frac{f_\xi(x)}{\mu}, \tag{2.2}$$

where $F_\xi(x)$ and $f_\xi(x)$ are a CDF and a probability density function (pdf) of the interval $\xi$, that can be found from the renewal equation [22, 34].

We further aim to calculate the probability of the event A, which is the probability that the left side point of the Rx is dropped on a blocked interval $\eta$. This probability corresponds to a ratio of a mean blocked interval, $E[\eta]$, to a mean of interval $\xi$, $E[\xi]$, as $E[\eta]/E[\xi]$, and is found as

$$Pr\{A\} = \frac{\exp(\mu E[W]) - 1}{\exp(\mu E[W])}, \tag{2.3}$$

where $E[W]$ is a mean of the individual blocker's shadow projection $W$ on the circumference given in Publication I [34].

Next, we find the probability of the event B, which is the probability that the distance from the left side point of the Rx to the end of the blocked interval will be greater than $l$ as

$$\begin{aligned} Pr\{B\} &= \frac{1}{E[\eta]}\int_l^\infty [1 - F_\eta(y)]dy = \\ &= \frac{\mu}{\exp(\mu E[W]) - 1}\int_l^\infty \left(1 - F_\xi(y) - \frac{1}{\mu}f_\xi(y)\right)dy. \end{aligned} \tag{2.4}$$

By multiplying two probabilities $Pr\{A\}$ and $Pr\{B\}$, we derive the blockage prob-

ability for the non-infinitesimal Rx with the length $l$ as

$$p_{\mathrm{B}} = \frac{\mu}{\exp(\mu E[W])} \int_{l}^{\infty} \left(1 - F_{\xi}(y) - \frac{1}{\mu} f_{\xi}(y)\right) dy. \tag{2.5}$$

### 2.3.2 Blockage probability with infinitesimal Rx

We continue with the proposed derivation of the blockage probability for the case of the infinitesimal Rx. The LoS link between the Tx and the Rx is called blocked if at least one blocker is higher than the LoS link at the point of their intersection. In this subsection, we assume a constant blocker's height $h_{\mathrm{B}}$ as well as a constant diameter of blocker $d_{\mathrm{B}}$. The derivations for the random height and diameter of a blocker are given in [34].

Recall that the blockers form the homogeneous PPP with the density $\lambda_{\mathrm{B}}$. Thus, to find the blockage probability for the infinitesimal Rx, we utilize the properties of PPP. According to the property of the process, a number of points (e.g., blockers centers) in a finite area follows the Poisson distribution [21, 23]. Therefore, we first find the probability of blockers in the finite area equal to zero (void probability), which refers to the non-blockage probability $p_{\mathrm{nB}}$. Further, we can derive the blockage probability as $p_{\mathrm{B}} = 1 - p_{\mathrm{nB}}$.

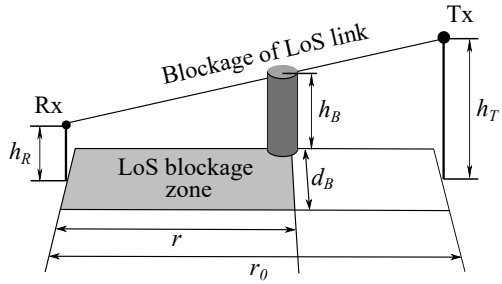


**Figure 2.3** LoS blockage zone.

We proceed with an introduction of a *LoS blockage zone* illustrated in Fig. 2.3. This zone refers to the area, where a presence of at least one blocker's center leads to an occlusion of Tx-Rx LoS link. The width of this zone is equal to the diameter

of blocker $d_B$ and the length of the zone is equal to $r$, where $r$ is found as

$$r = \frac{r_0(h_B - h_R)}{h_T - h_R} + d_B/2. \tag{2.6}$$

Now, we can calculate the LoS blockage zone area and find the density of blockers in this zone. We further derive the probability of zero blockers in the LoS blockage zone, which refers to the non-blockage probability $p_{nB}$. The final blockage probability is then found as

$$p_B = 1 - \exp\left(-d_B \lambda_B \left[\frac{r_0(h_B - h_R)}{h_T - h_R} + d_B/2\right]\right). \tag{2.7}$$

### 2.3.3 Effect of human body blockage

We proceed with analyzing the human body blockage probability in response to different deployment parameters. We consider the Rx height $h_R = 1.3$ m, the blockers height and diameter equal to 1.7 m and 0.5 m, respectively. The parameters for the blockers height and diameter distributions are $\mathcal{N}(1.7\,m, 0.1\,m)$ and $\mathcal{U}(0.2\,m, 0.8\,m)$. The remaining values for the parameters are given in Table II of Publication I [34]. First, from Fig. 2.4 we note that the blockage probability for the infinitesimal Rx is always higher than for the non-infinitesimal Rx. It is explained by greater chances to block the point than the line representing the Rx. For a constant mean diameter of a blocker and the Rx size of 8 cm, this difference may reach up to 5%. By decreasing the length of the Rx further, this difference decreases as well.

Further, from Fig. 2.4, one may notice that the distance between the Tx and the Rx plays a crucial role in the blockage probability. For the 2D distance of 100 m and the infinitesimal Rx, the blockage probability may reach up to 89% ($h_T = 4$ m, $h_R = 1.3$ m, and $\lambda_B = 0.3$). Next, we analyze the effect of density of blockers on the blockage probability in the case of the infinitesimal Rx as illustrated in Fig. 2.5. One may note that increasing the blockage density from 0.1 $bl/m^2$ up to 0.5 $bl/m^2$, the blockage probability increases from 0.52 to 0.98. The qualitative behavior in case of the non-infinitesimal Rx remains the same as for the infinitesimal Rx.

As shown in Fig. 2.5 for the case of the infinitesimal Rx, the blockage probability can be decreased by increasing the height of the Tx. For instance, by increasing the Tx height from 4 m to 10 m the blockage probability is decreased by 44% for

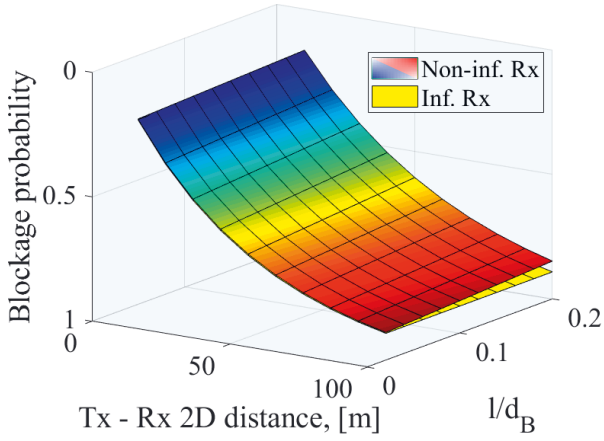


**Figure 2.4** Blockage probability for non-infinitesimal and infinitesimal Rx.

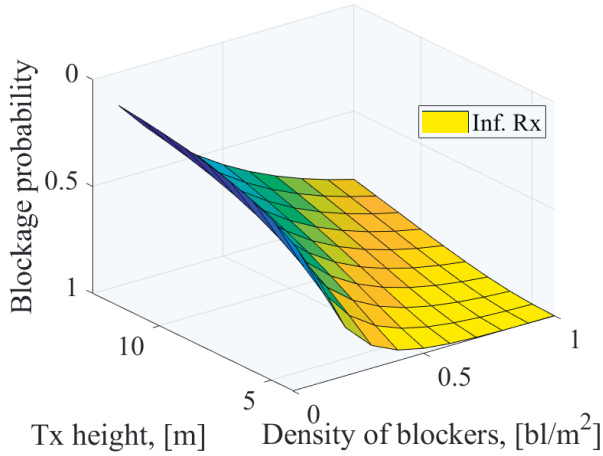


**Figure 2.5** Blockage probability as a function of Tx height and blockers density for infinitesimal Rx.

$\lambda_B = 0.3$. Therefore, by adjusting the Tx height, one may significantly decrease the blockage probability.

### 2.3.4 Key findings

The human body blockage can drastically attenuate the mmWave signal and, thus, should be considered when analyzing the performance of mmWave networks. To

characterize the blockage effect, we developed the analytical human body blockage model that accounts for the main deployment parameters such as density of blockers and height of nodes. This model can be further integrated into comprehensive system-level frameworks, as shown later in Chapter 4. Moreover, it can also replace complex physical blockage models in computer simulations to decrease computational time.

With the help of the developed model, we demonstrate that the blockage probability can be notably high in realistic deployments. The blockage probability can reach up to 0.89 for dense crowds (i.e., $\lambda_B = 0.3$ bl/m$^2$) and large Tx-Rx separation distance (i.e., $r_0 = 100$ m). At the same time, we have also shown that the blockage probability can be notably decreased by densifying the network with BSs and selecting an appropriate BS height. For instance, when increasing the BS height from 4 m to 10 m in the considered deployment, the blockage probability decreases from 0.89 to 0.5. Hence, we further analyze the BS height optimization and other blockage mitigation techniques in Chapter 4.

## 2.4 Dynamic Human Body Blockage Analysis

In the previous Section 2.3, we proposed the blockage probability that a user experiences on average in a static field of blockers. The human body blockers are also characterized by their mobility, introducing dynamics into the blockage process [41]. Besides time averaged metrics, it is also essential to determine temporal properties, such as a time of uninterrupted blocked and non-blocked states. These metrics may further clarify the behavior of a system under various environmental conditions, blockage intensity, and a total time duration in different states.

In this section, we deliver the blockage probability and the time in uninterrupted blocked and non-blocked states for a scenario with mobile human body blockers, developed in Publication II of [33]. Notably, we consider two typical outdoor deployments [63]: (i) sidewalk and (ii) square. The mobility of blockers in these scenarios are described below as

- **Sidewalk deployment.** The blockers' trajectories are parallel to each other and the side of a street as illustrated in Fig. 2.6a. The blockers crossing points of the street width are distributed uniformly.

- **Square deployment.** The blockers' trajectories are randomly oriented in a 2D area as shown in Fig. 2.6b. The blockers crossing points of the LoS blockage zone are distributed uniformly over the sides of this zone.

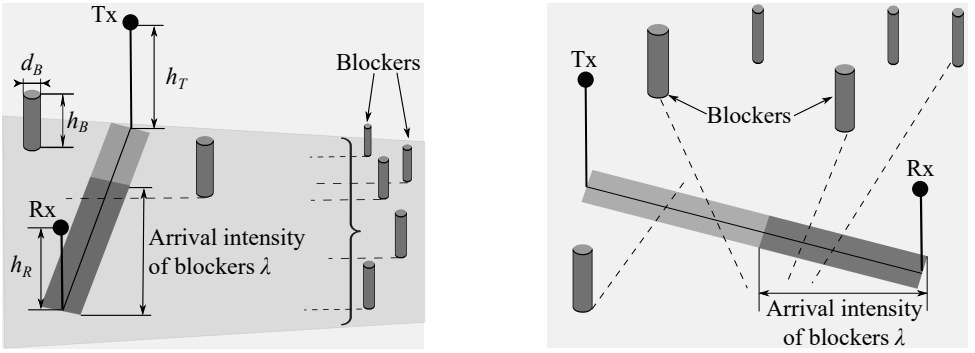


**(a)** Dynamic blockers in sidewalk deployment

**(b)** Dynamic blockers in square deployment

**Figure 2.6** Considered scenario for mathematical modeling of dynamic human body blockers.

For the sake of analytical tractability, we consider the infinitesimal Rx and blockers with a constant height $h_{\mathrm{B}}$ and a constant diameter $d_{\mathrm{B}}$, as described in Subsection 2.3.2. The Rx (a mmWave UE) of height $h_{\mathrm{R}}$ is located at 2D distance $r$ from the Tx (a mmWave BS) of height $h_{\mathrm{T}}$. All model parameters are readily given in Table I of Publication II [33].

### 2.4.1 Characteristics of dynamic human body blockage process

We start with the characterization of the process of blockers entering the LoS blockage zone (see Fig. 2.3), a zone where the existence of a human body leads to the occlusion of the LoS path as described in Subsection 2.3.2. We model the process of blockers entering the street in the sidewalk deployment according to the Poisson process in time, where time between each blocker crossing the width of the street follows the exponential distribution with a parameter $\lambda_I$. For the square deployment, we assume the process of blockers entering the LoS blockage zone according to the Poisson process in time with a parameter $\lambda_I$.

We note that the blockage process of a link by moving human bodies is well described by the alternating renewal process, as shown in Fig. 2.7. Similarly to the approach described in Subsection 2.3.1, we notice that an interval $\xi$ is equal to the

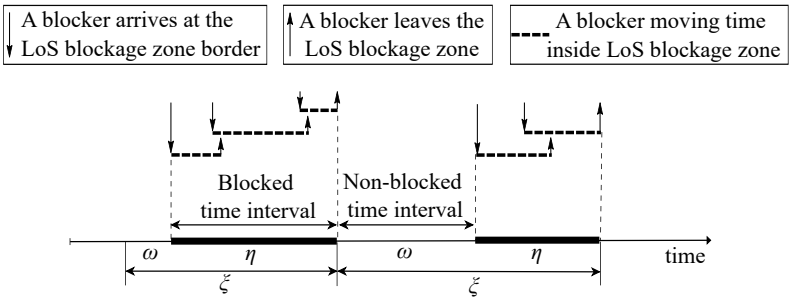


**Figure 2.7** Alternating renewal process of LoS blockage time.

sum of blocked and non-blocked time intervals, $\xi = \omega + \eta$. Moreover, the interval $\xi$ is always repeated at the end of its own time interval.

Let us continue with a derivation of the time in blocked, $\eta$, and non-blocked, $\omega$, states. To characterize the time in its non-blocked state, $\omega$, we apply the same logic as in Subsection 2.3.1. The time between the end of the blocked time interval and beginning of the next blocked time interval follows the exponential distribution with the parameter $\lambda$, where $\lambda$ is the intensity of blockers entering the LoS blockage zone. We also note that for the sidewalk deployment, $\lambda$ is derived from $\lambda_I$, while for the square deployment $\lambda$ is equal to $\lambda_I$. Therefore, a mean of the non-blocked time is given as $\mathbb{E}[\omega] = 1/\lambda$, while a CDF of the non-blocked time is $F_\omega(x) = 1 - \exp(-\lambda x)$.

Next, we derive the characteristics of the blocked time interval $\eta$. We follow the approach described in Subsection 2.3.1. Thereby, a mean of interval $\xi = \omega + \eta$ is found from the density of the alternating renewal process and is equal to $\mathbb{E}[\xi] = (1/\lambda)\exp(\lambda \mathbb{E}[T])$, where $\mathbb{E}[T]$ is a mean time of a single blocker moving inside the LoS blockage zone derived in Publication II [33]. The mean time in blocked interval is then found as

$$\begin{aligned}\mathbb{E}[\eta] &= \int_0^\infty [1 - F_\eta(x)]dx \\ &= \int_0^\infty \left(1 - F_\xi(x) - \frac{f_\xi(x)}{\lambda}\right)dx = \frac{1}{\lambda}[\exp(\lambda \mathbb{E}[T]) - 1],\end{aligned} \tag{2.8}$$

where $F_\eta(x)$ and $F_\xi(x)$ are CDFs of $\eta$ and $\xi$, respectively, while $f_\xi(x)$ is a pdf of $\xi$.

We further note that the blocked and non-blocked intervals can be seen as empty and busy periods in the M/GI/$\infty$ queuing system. Particularly, the inter-arrival time of blockers follows the exponential distribution referring to Kendall's notation

M. The blocked period of the Rx follows an arbitrary distribution, which is denoted as GI. Finally, an infinite number of blockers may theoretically arrive to the LoS blockage zone simultaneously, which refers to the infinite, $\infty$, capacity of the queuing system. Therefore, the blocked time interval can be interpreted as the busy period from the M/GI/$\infty$ queuing model, and its CDF is given as [24]

$$F_{\eta}(x) = 1 - \Bigg( \Big[1 - F_T(x)\Big] \Big[ 1 - \int_0^x \big(1 - F_{\eta}(x-z)\big) \exp\big(-\lambda F_T(z)\big) \lambda dz \Big] + \int_0^x \big(1 - F_{\eta}(x-z)\big) \big| d\, e^{-\lambda F_T(z)} \big| \Bigg), \tag{2.9}$$

where $F_T(x)$ is a CDF of time that a single blocker moves inside the LoS blockage zone.

Finally, we derive the blockage probability as a fraction of the mean blocked period to the sum of mean blocked and non-blocked periods, given below as

$$p_{\mathrm{B}} = \frac{\mathbb{E}[\eta]}{\mathbb{E}[\omega] + \mathbb{E}[\eta]}. \tag{2.10}$$

The described methodology can be then applied to account for different blockers' mobility models, e.g., the models described in Subsection 2.4. The chosen mobility model affects the time that a single blocker walks inside the LoS blockage zone. The exact derivations of the mean $\mathbb{E}[T]$ and the distribution $F_T(x)$ are given in Publication II [33].

### 2.4.2 Effect of dynamic human body blockage

The time in an uninterrupted blocked/non-blocked state can further describe a system behavior under various blockage conditions. We consider the Tx and Rx with heights equal to 3 m and 1.3 m, respectively. The height and diameter of blockers are equal to 1.7 m and 0.5 m, while their speed is 1 m/s. The remaining values of the system parameters are given in Table II of Publication II [33].

We first start by understanding the implications of the blockers' mobility models on the metrics of interest demonstrated in Fig. 2.8. Notably, the mean time in the blocked state is higher for the square deployment as compared to the sidewalk de-

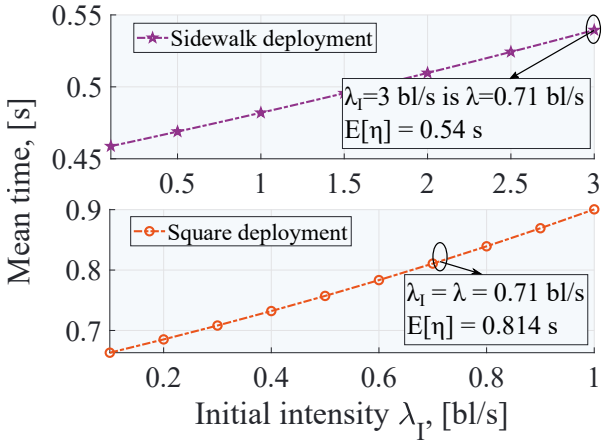


**Figure 2.8** Mean time in blocked state as a function of blockers intensity.

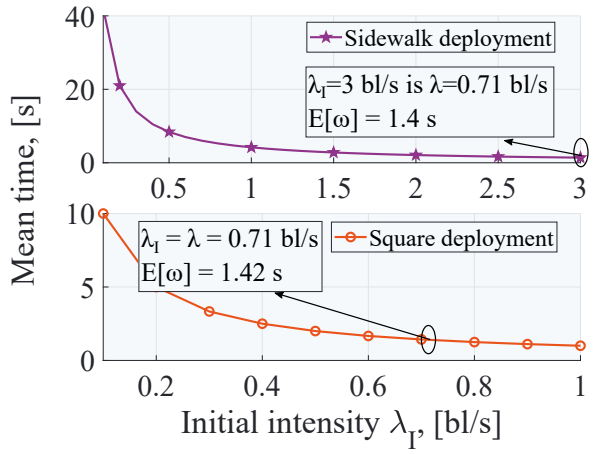


**Figure 2.9** Mean time in non-blocked state as a function of blockers intensity.

ployment. The reason for this difference is that the blockers are likely to spend more time in the LoS blockage zone with a random trajectory in the square deployment, as can be seen from the geometry (see Fig.2.6b). Given this observation, the choice of the human mobility model may greatly affect system performance.

Next, we demonstrate an impact of the blockers intensity on the mean time in blocked state. From Fig. 2.8, one may notice that for the blockers intensity of $\lambda_I =$ 0.5 bl/s the mean time in blocked state reaches 0.76 s for the square deployment. Compared to the frame length of 10 ms and 80 slots in one frame for SCS=120 kHz in NR [3], the overall time spent in a blockage might be quite significant for mmWave

NR systems in case of dense crowd scenarios. By increasing the blockage intensity further, the time in blocked state grows almost linearly. Note that this qualitative behavior is similar for the sidewalk deployment.

To further understand the dynamics of link blockage, we analyze the time spent in non-blocked state. From Fig. 2.9 we note that the said time reaches up to 10 s for $\lambda_I = 0.1$ bl/s (low blockers intensity) in the square deployment while the time in blocked state is equal to 0.66 s. By further increasing the intensity up to 0.5 bl/s, the mean time in the non-blocked state becomes around 2 s. While the time in the non-blocked state decreases exponentially with the increased blockers intensity, the time in the blocked state does not increase that much. This implies a significantly increased frequency of blockage events for high blockers density scenarios. In addition, the time in the blocked state is considerably long and reaches 0.76 s for the same set of parameters.

### 2.4.3 Key findings

In order to comprehensively characterize the effects of human body blockage, not just the blockage probability (as detailed in Section 2.3) but also uninterrupted time in the blocked and non-blocked states is needed. This section examines the dynamic blockage model, revealing the temporal metrics of the human body blockage process in real deployments to facilitate this goal. It may be especially important when modeling dynamic services over a network and higher layers, e.g., evaluation of Transmission Control Protocol (TCP) performance in 5G mmWave systems, as in [51], where our model was employed in a simulator.

Our numerical study concludes that time in the blocked state may reach up to several hundred milliseconds, e.g., 540 ms for the sidewalk deployment with the blockers intensity equal to 0.71 bl/s. Given the NR radio frame design for higher frequencies, it may lead to a loss of ten of frames, notably lowering system reliability. One potential solution is to provide at least one alternative link to minimize a service interruption time, e.g., by employing the multi-connectivity technique [30, 72]. We will further consider and analyze this technique in Chapter 4.

## 2.5 Large-scale Blockage Analysis

Despite several existing studies on the LoS probability, there is still a need in modeling a regular grid deployment of buildings, one of the typical scenarios in 5G [6]. Moreover, most of the models are specifically designed for terrestrial users and do not account for the height of buildings and their distribution. However, besides conventional users, future wireless networks are entitled to accommodate various types of users, e.g., a UAV [4]. The height of such users can be comparable to, or even much higher than, the height of surrounding buildings, thus making the latter an essential part of LoS probability models.

With all the above in mind, we propose an analytical model for the LoS probability in a city grid deployment illustrated in three-dimensional (3D) and 2D view in Fig. 2.10a and developed in Publication III [29]. We define the LoS probability as a probability that no building occludes the BS-UE link. We particularly consider a UAV as an exemplary UE, with a height that can be comparable to the height of surrounding buildings. Nevertheless, the analysis is valid for other types of users operating in grid type deployments, e.g., conventional UEs, high altitude platforms (HAPs), and others.

The BS with height $h_{\mathrm{T}}$ is located at 2D distance $\ell_{\mathrm{2D}}$ from the UAV of height $h_{\mathrm{R}}$. We also note that the BS is deployed along the street termed as a typical street. All model parameters are summarized in Table I of Publication III [29].

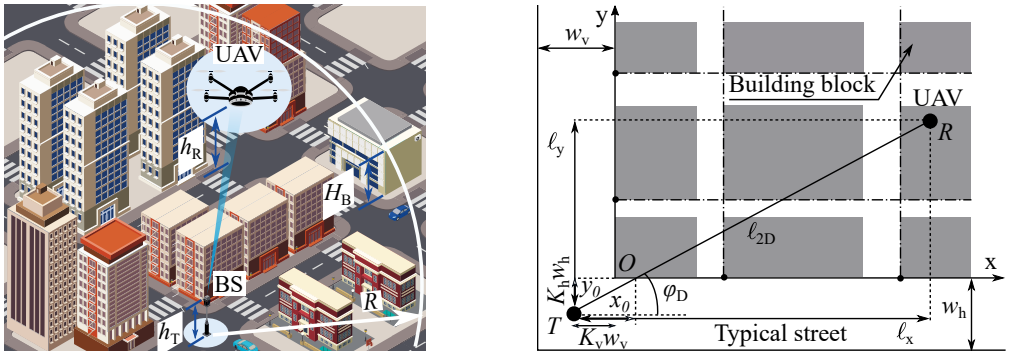


**(a)** 3D scenario of urban grid deployment

**(b)** 2D scenario of urban grid deployment

**Figure 2.10** Considered scenario for analytical modeling of large-scale blockers (reproduced from [29]).

### 2.5.1 LoS probability in urban grid deployment

We start by providing an analytically tractable model to approximate an urban grid deployment. It was shown in [15] that the Manhattan Poisson Line Process (MPLP) could well model a city grid, as pictured in Fig. 2.10b. The MPLP is described with the PPP on the X- and Y-axis, where the points represent the beginning of the streets with a density $\lambda$. The resultant rectangles are the blocks of buildings.

To derive the LoS probability, we need to find a probability that there are no buildings higher than the LoS at their intersection point. Due to the regular deployment of the buildings, the position of each block depends on the other. Therefore, the approach of directly thinning out all of building blocks (similar to the one in Subsection 2.3.1) will lead to recursive equations and extensive computations.

To solve the problem, we first note that there is just one side on a 2D plane (bottom or left for the geometry presented in Fig. 2.10) of every block that can occlude the link. The number of these sides coincides with the number of points generated on the X- and Y-axis, which also follows the Poisson distribution. Next, recall that not all sides on the X- or Y-axis will block the LoS, only those with height higher than the LoS at the intersection point. Thus, we employ the procedure described in Subsection 2.3.1 and thin out the given PPP on X-axis with a probability $Pr\{H_{\mathrm{B}} > h_{\mathrm{m}}^{x}(x, \ell_{2\mathrm{D}}, \phi_{\mathrm{D}})\}$. The resultant probability that no side on the X-axis is higher than LoS is given as

$$p_{\mathrm{nB}}^{(x)}(\ell_{2\mathrm{D}}, \phi_{\mathrm{D}}) = \exp\left[ -\lambda \int_{x_0}^{\ell_{\mathrm{x}}} \left(1 - F_{H_{\mathrm{B}}}\left(h_{\mathrm{m}}^{x}(x, \ell_{2\mathrm{D}}, \phi_{\mathrm{D}})\right)\right) \mathrm{d}x \right], \tag{2.11}$$

where $H_{\mathrm{B}}$ is the height of a building, $h_{\mathrm{m}}^{x}$ is the height of the LoS at the point of the intersection given in Publication III [29], and $\phi_{\mathrm{D}}$ is the LoS angle of departure (AoD).

The above procedure is also applied to thin out the PPP on Y-axis and given in Publication III [29].

Next, we need to find a probability that no points from the thinned PPP are generated on the X- and Y-axis between the BS and the UAV. Given the independence of the two processes on different axes, we multiply the probabilities of no points on the projection of LoS on the X- and Y-axis. We also need to account for a first

contact side, the side that the 2D projection of LoS intersects first, to be lower than the LoS height at the point of their intersection. The resulting LoS probability is then calculated as follows

$$\mathbb{P}_{\mathrm{LoS}}(\ell_{2\mathrm{D}},\phi_{\mathrm{D}}) = F_{H_{\mathrm{B}}}\left(h_{\mathrm{m}}^{0}(\ell_{2\mathrm{D}},\phi_{\mathrm{D}})\right)\exp\Bigg(-\lambda\int_{x_0}^{\ell_{\mathrm{x}}}\left[1-F_{H_{\mathrm{B}}}\left(h_{\mathrm{m}}^{x}(x,\ell_{2\mathrm{D}},\phi_{\mathrm{D}})\right)\right]\mathrm{d}x - \lambda\int_{y_0}^{\ell_{\mathrm{y}}}\left[1-F_{H_{\mathrm{B}}}\left(h_{\mathrm{m}}^{y}(y,\ell_{2\mathrm{D}},\phi_{\mathrm{D}})\right)\right]\mathrm{d}y\Bigg), \tag{2.12}$$

where $F_{H_{\mathrm{B}}}$ is a CDF of building height.

Note that the above (2.12) is the LoS probability for a general building height distribution. In Publication III [29], we provide closed-form solutions for three different distributions of building height: uniform, exponential, and Rayleigh.

### 2.5.2 Effect of large-scale blockage

We continue with the numerical assessment of the LoS probability for various deployment parameters. Particularly, we consider the BS with height equal to 10 m. The width of the typical horizontal and vertical streets is equal to 20 m. The values for the urban grid geometry are given in Table III of Publication III [29].

For the aerial users, large-scale blockers, e.g., buildings, would affect the existence of the LoS based on multiple factors. Notably, in Fig. 2.11, we notice that a spatial orientation of buildings significantly affects the LoS probability. As one may note, the user located closer to the street with the deployed BS, on average, has a larger LoS probability than the user located at the same distance from the BS but in the middle of two axes. This insight could further be used when planning a trajectory of aerial users in order to maximize the LoS probability.

It is also noted that the height of the aerial user plays a vital role in the LoS probability, as shown in Fig. 2.11. It is illustrated that increasing the height of the aerial user from 50 m up to 150 m increases the LoS probability by five times. Such significant improvement illustrates a benefit of optimizing the height of the aerial user together with its orientation when planning for a flight trajectory.

Further, in Fig. 2.12, we illustrate that the distribution of a building height no-

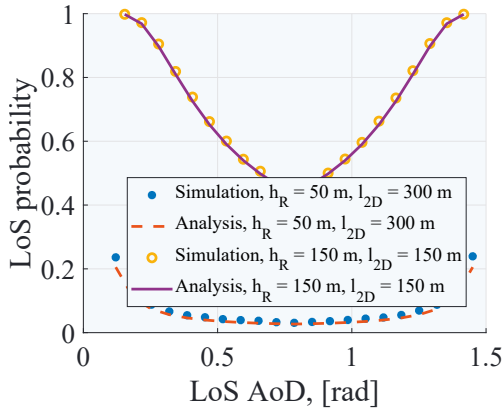


**Figure 2.11** LoS probability as a function of LoS AoD.

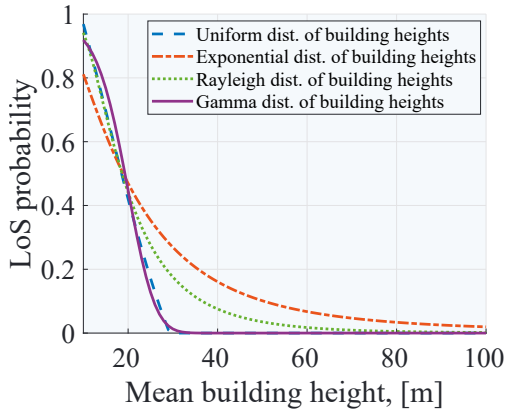


**Figure 2.12** LoS probability as a function of mean building height.

tably affects the metrics of interest. We provide the numerical results for the following building height distributions: (i) uniform [20], (ii) exponential [70, 95], (iii) Rayleigh [94], and (iv) gamma. In Fig. 2.12, we assume the UAV height of 150 m. It was noted that the difference between the models is relatively small (1%-20%) for the mean height of buildings in a range of (0 m, 20 m). When the mean height is increased from 20 m to 60 m, the values typical for urban deployments, the difference between the models becomes significant (up to 3.5 times). Furthermore, there is no essential difference for the mean height greater than 60 m as the LoS probability is small in that case.

### 2.5.3 Key findings

In this section, we contributed the LoS probability model for grid type deployments. We demonstrated that the choice of environment and the considered deployment parameters (e.g., the height of buildings and its distribution) would drastically impact the final metrics of interest. For instance, when changing the building height distribution alone, the difference between the LoS probabilities may reach up to 350% for the same set of parameters. Therefore, even for the first-order evaluation studies, one needs to select the appropriate deployments and the associated models carefully.

Our numerical evaluation demonstrated the LoS probability can be as low as 0.43 for the UAV height of 150 m and 2D distance of 150 m. Given the harmful effect of a blockage caused by a building for the mmWave signal (40-80 dB of loss as per [83]), it is of special importance to consider it in further evaluation studies. We also observe that not only the 3D BS-UAV distance but the relative locations of the UAV to the BS affect the LoS probability. For example, when the AoD is changed from 45° to 16°, the LoS probability increases by two times. This consideration can be further employed for a UAV trajectory optimization in future networks.

# 3 MULTIPATH BLOCKAGE MODELING

## 3.1 Research Motivation

As seen from numerous experiments, presence or absence of a LoS path notably affects an overall performance of directional mmWave communication systems [83, 84]. Therefore, it is essential to incorporate LoS state information into the evaluation of mmWave systems performance. In Chapter 2, we discussed the possible types of blockers that may occlude mmWave communication links. We then provided the analytical formulations for the blockage probability, when the LoS path can be occluded by human bodies and buildings.

In many real deployments, besides a LoS path, there are multiple other paths, e.g., reflected, diffracted, or scattered [91, 101, 107]. With highly directional and steerable antennas, mmWave devices can employ various paths to operate with [60, 102]. Therefore, if a LoS link is not available, e.g., the LoS link is blocked, a UE can choose an alternative link to continue the data exchange [84]. However, such alternative links are also susceptible to blockage from various objects, hence may be or not be available for a particular UE [13]. It thus implies the benefit of the blockage modeling of not only the LoS path, but also other possible paths [99].

3GPP provides a 3D channel model that generates multipath components via angles of arrivals/departures, delays, and powers [1]. The model can also account for blockage of a LoS and multipath components. However, due to the algorithmic nature of the model, the multipath generation becomes suitable for simulations and not for analytical studies. Moreover, 3GPP multipath generation procedure requires considering every blocker in a scenario individually. The latter leads to the increased simulation time when the density of blockers is high. Thus, it is desirable to deliver a faster method to account for blockage effects that can be used in analytical studies as well as to speed up computer simulations.

Below, in Section 3.2 we first describe the 3GPP 3D channel model in more de-

tail. Further, in Section 3.3 we propose an analytical approximation of the 3GPP channel model parameters. We then deliver multipath blockage and outage probabilities. Finally, in Section 3.4 we contribute with an algorithm assigning link states (blocked/non-blocked) by taking into account spatial consistency between these links states. All these allow investigating the potential alterations in the blockage process characteristics when considering multipath propagation and spatial consistency across the mmWave links states.

## 3.2 3GPP 3D channel model description

There were multiple requirements for the channel model for frequencies above 6 GHz settled by ITU [45]. Particularly, according to ITU, the channel model have to: (i) have 3D space and time characteristics for both LoS and non-line-of-sight (nLoS) conditions, (ii) support beamforming modeling, (iii) account for temporal characteristics of a channel to support a UE mobility and non-stationary environment modeling (e.g., moving crowd).

Following the recommendations, 3GPP delivered the geometry-based stochastic channel model for the frequencies up to 100 GHz [1]. The channel modeling consists of multiple steps:

1. **Scenario setting.** This step requires to choose an appropriate scenario. Different scenarios have different deployment parameters (e.g., height of BS) and propagation models.
2. **Antenna modeling.** A BS antenna is modeled with a uniform rectangular panel array described as $(M_g, N_g, M, N, P)$, where $M_g$ and $N_g$ are the numbers of panels in a column and a row, respectively, $M$ is the numbers of antenna elements per column and $N$ is the number of columns, while $P$ is the antenna polarization.
3. **Path loss and LoS probability modeling.** The scenario of interest determines appropriate models for a path loss in LoS/nLoS and a LoS probability model.
4. **Channel coefficient generation.** This step refers to a generation of multipath components described in more detail below.
5. **Additional components modeling.** This step is assumed for advanced simulations to model, e.g., blockage, spatial consistency, etc.

In this chapter, we are particularly interested in Step 4 from the channel modeling procedure above, which is responsible for generating multipath components. There are three main blocks needed to determine the parameters of interest: (i) an environment setting, a LoS/nLoS state assignment, and a path loss calculation; (ii) generation of large-scale parameters – delay spread (DS), angular spreads, Ricean K factor (K), and shadow fading (SF); (iii) generation of small-scale parameters – angles of arrival/departure, delays, clusters power share. By term cluster here, we assume a set of rays that traverse from Tx to Rx with a minor variation in their angles of arrival and departure [84].

After a scenario of interest is chosen, one may find a LoS/nLoS state by employing a LoS probability as provided in Table 7.4.2-1 of 3GPP technical report (TR) 38.901 [1] and then calculate a path loss from Table 7.4.1-1 [1]. The large-scale parameters are described by a mean and standard deviation as well as cross-correlation among the parameters taken from Table 7.5-6 of TR 38.901 [1].

Finally, the small-scale parameters can be calculated by following this step-by-step approach:

- Generate a delay $\tau_n$ for every cluster $n$. First, the delay for each cluster is randomly generated as $\tau_n^{'} = -r_\tau DS \ln(X_n)$, where $r_\tau$ is a delay distribution proportionality factor and $X_n = Uni(0,1)$. Next, the resultant delays $\tau_n$ are sorted in ascending order to account for the clusters with the shortest path up to one with the longest path.
- Generate power share $P_n$ of every cluster $n$. The power share of every cluster $n$ is given as $P_n = \exp(-\tau_n \frac{r_\tau - 1}{r_\tau DS}) 10^{-Z_n/10}$, where $Z_n \sim \mathcal{N}(0, \zeta^2)$ is per cluster shadowing term in dB. The cluster power shares are then normalized so that the sum of power shares to be equal to 1.
- Generate azimuth and elevation angles of arrival/departure for every cluster $n$. First, find the angle of arrival (AoA) as $\phi_{n,AOA}^{'} = \frac{2(ASA/1.4)\sqrt{-\ln(P_n/\max(P_n))}}{C_\phi}$, where ASA is the AoA spread, $C_\phi$ is a scaling factor. Then assign a negative or positive sign via uniformly distributed random variable $X_n = \{1, -1\}$ and introduce a random variation $Y_n \sim \mathcal{N}(0, (ASA/7)^2)$. The resultant AoA is then equal to $\phi_{n,AOA} = X_n \phi_{n,AOA}^{'} + Y_n + \phi_{LOS,AOA}$, where $\phi_{LOS,AOA}$ is the LoS AoA. A similar approach is applied to calculate other angles.

As a result of this procedure, every cluster from the multipath propagation model

is characterized by its delay, power share, and angles.

The cluster generation procedure shown above is based on the algorithmic approach and thus is not suitable for analytical studies. Meanwhile, to calculate the multipath blockage probability, it is important to have the analytical characteristics of the cluster parameters.

## 3.3 Multipath Blockage Analysis

The multipath propagation can be seen as one of the options to increase spatial diversity of available links [78, 84]. Thus, if a primary link is blocked, there are chances to continue operation over the strongest reflected path if it is available. To assess whether the path is available or not, we need to consider for possible occlusion of reflected paths. For that purpose, in this section, we introduce the multipath blockage model, developed in Publication IV [35].

In what follows, we focus on a small-scale blockage of multipath components considering no large-scale blockers occluding a LoS. Notably, we assume cylinders with height $h_B$ and base diameter $d_B$ (radius is $r_B$) representing human body blockers. The human bodies form the PPP with density $\lambda_B$. The Tx (a mmWave BS) is located at 2D distance $x$ from the Rx of infinitesimal size (a mmWave UE). The Tx and Rx heights are $h_A$ and $h_U$, respectively. All system parameters are given in Table I of Publication IV [35].

To provide the multipath blockage model, we need input parameters accounting for the multipath components, such as angles of arrival. As discussed earlier, 3GPP delivers the parameters needed to characterize the multipath propagation, e.g., angles of departure/arrival, power share from every path [1]. However, due to the algorithmic nature of the generation procedure, we first need to find an analytical approximation of the required parameters.

Therefore, in Subsection 3.3.1 we deliver the analytical approximation of a ZoA and power share of reflected signals. Then, in Subsection 3.3.2 we provide the multipath blockage probability of every path available at the Rx by taking the approximated parameters as an input. Next, we integrate the blockage probability into an outage probability. Finally, in Subsection 3.3.3 we provide the numerical results related to the multipath blockage modeling.

### 3.3.1 Analytical approximation of 3GPP channel model parameters

We start with approximating the 3GPP channel model parameters needed for our analysis of blockage and outage probabilities. For that purpose, we implement the 3GPP channel model in an in-house simulator. We collect statistical data of the following parameters as depicted in Fig.3.1: (i) ZoA of the $n$th cluster, $\theta_n$, and (ii) power share of the $n$th cluster, $P_{s,n}$.

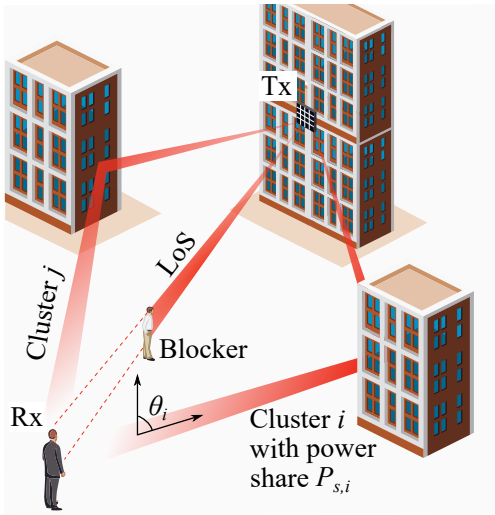


**Figure 3.1** Scenario with multipath propagation for mathematical modeling.

We continue with the approximation of ZoA, $\theta_n$, which is the parameter needed to define the blockage probability for each cluster described later in Subsection 3.3.2. By analyzing a pdf of the ZoA, we observe that it is well fitted into the Laplace distribution with parameters $(a_n, b_n)$, given below as

$$f_{\theta_n}(y) = \frac{1}{2b_n} \exp\left(-\frac{|y-a_n|}{b_n}\right), n = 2,3,\ldots,N, \tag{3.1}$$

where parameter $a_n$ is a mean and $b_n$ is a variance of the ZoA of $n$th cluster.

Next, we find the parameters $a_n$ and $b_n$ for the Laplace distribution. For that purpose, we collect the mean and variance of ZoA for a different set of geometric parameters (height of nodes, 2D distance, etc.). The obtained data demonstrates that the variance of each cluster, $b_n$, is a constant value and changes only if the cluster number changes (the exact values are provided in Publication IV [35]). Furthermore,

it is noted that the ZoA mean of each cluster, $a_n$, coincides with the LoS ZoA and thus can be written as

$$a_n = \frac{\pi}{2} - \arctan\left(\frac{h_A - h_U}{x}\right), n = 2,3,\ldots,N, \tag{3.2}$$

where $x$ is 2D distance between the Tx and the Rx.

We proceed with the analysis of data collected for the power share of every cluster, $P_{s,n}$. It is observed that a power share distribution of cluster $N = [2,\ldots,5]$ is well fitted to the log-normal distribution with parameters $(c_n, d_n)$ and is given below as

$$f_{P_{s,n}}(z) = \frac{1}{z d_n \sqrt{2\pi}} \exp\left(-\frac{(\ln z - c_n)^2}{2d_n^2}\right), n = 2,3,\ldots,N. \tag{3.3}$$

To find the parameters $c_n$ and $d_n$ we first define them via a mean and variance of power share of every cluster. We then collect the mean and variance in response to the different geometry of the scenario and observe that those can be approximated with a constant value different for every cluster. The parameters $(c_n, d_n)$ are then calculated from the relation to the mean and variance and are given in Publication IV [35].

We note that the power share distribution described above is found for the clusters $N = [2,\ldots,5]$. The power share distribution for the first cluster (LoS, N=1) appears to be different from the other clusters power. By collecting and analyzing the results, we reveal that the LoS power share distribution is approximated by the log-normal distribution with the argument (1-z) and the parameters $(c_1, d_1)$ as shown below

$$f_{P_{s,1}}(z) = \frac{1}{(1-z) d_1 \sqrt{2\pi}} \exp\left(-\frac{(\ln(1-z) - c_1)^2}{2d_1^2}\right), \tag{3.4}$$

where the values for $c_1$ and $d_1$ are given in Publication IV [35].

### 3.3.2 Multipath blockage and outage probabilities

Applying the above approximations, we proceed with the mathematical derivation of the multipath blockage and outage probabilities for the Tx-Rx link. We start by deriving the blockage probability for every cluster, employing the methodology shown in Chapter 2. Recall that the LoS blockage probability derived earlier for the

infinitesimal Rx is a function of various parameters, including distance between the Tx and the Rx. However, the distance between a reflected point and the Rx is not known from the 3GPP channel model.

To derive the blockage probability for a single cluster, we first need to obtain the required distance. In order to do that, we assume a single bounce reflection following the approach in [69] and then express the distance as a function of ZoA. The blockage probability of cluster $n$ as a function of ZoA, where ZoA $= (0, \pi/2)$, is given below in (3.5), while the expressions for other cases can be obtained following a similar approach.

$$q_n(y) = 1 - e^{-2\lambda_B r_B(\tan y(h_B - h_U) + r_B)}. \tag{3.5}$$

Due to a random ZoA for every cluster, we continue with an integration of $q_n(y)$ over possible angles multiplied by the ZoA distribution, $f_{\theta_n}(y)$, derived in Subsection 3.3.1. The resultant blockage probability of cluster $n$ is calculated as

$$p_n(x) = \int_{-\pi}^{\pi} \frac{q_n(y)}{2b_n e^{\frac{|y - a_n(x)|}{b_n}}} dy. \tag{3.6}$$

Next, we proceed with a derivation of the outage probability. First, we define an outage event as the summation of two mutually exclusive events: (A) all clusters are simultaneously blocked, or (B) the received power of the strongest non-blocked cluster is below a threshold. We assume that in the case of blockage, the blocked cluster experiences infinite attenuation.

The probability of event A is found as $p_{O,1}(x) = \prod_{n=1}^{N} p_n(x)$. To find the probability of event B, we first need to calculate a pdf of the received power of every cluster given a transmit power $P_T$ and the pdf of the power share of each cluster $f_{P_{s,n}}(z)$. By calculating the received power using path loss and employing the transformation of a random variable, we obtain the pdf of the received power of every cluster $P_n$ as

$$f_{P_n}(z; x) = \frac{1}{10^{(P_T - 30 - 32.4 - 20\log_{10} f_c - 21\log_{10}(D_3))/10}} f_{P_{s,n}}\left(\frac{P_n(x)}{10^{(P_T - 30 - 32.4 - 20\log_{10} f_c - 21\log_{10}(D_3))/10}}\right), \tag{3.7}$$

where $f_c$ is a carrier frequency in GHz and $D_3$ is the 3D distance between the Tx

and the Rx in meters. We also note that the path loss coefficients in (3.7) are taken directly from the 3GPP UMi - Street canyon model [1].

We continue with the pdf of the received power from the strongest non-blocked cluster as the sum of weighted pdfs. Recall that the clusters are enumerated in order of increased delay, and thus decreased power. Therefore, the pdf of the received power from the strongest cluster is found as

$$f_P(z;x) = \sum_{n=1}^{N} \left[ (1 - p_n(x)) \prod_{j=1}^{n-1} p_j(x) \right] f_{P_n}(z;x), \tag{3.8}$$

where the first term under the summation is the probability that cluster $n$ is not blocked while the product implies that all previous clusters $(1, \cdots, n-1)$ are blocked.

The probability of event B is then calculated as $p_{O,2}(x) = \int_0^{S_T} f_P(z;x)dz$, where $S_T$ is the received power threshold. Finally, the outage probability can be derived as follows

$$p_O(x) = \prod_{n=1}^{N} p_n(x) + \int_0^{S_T} f_P(z;x)dz. \tag{3.9}$$

### 3.3.3 Impact of multipath blockage modeling

We proceed with the numerical evaluation of the outage probability in the case of the multipath channel model. The BS height is equal to 10 m, while the UE height is 1.5 m. The height and diameter of blockers are equal to 1.7 m and 0.5 m, respectively. The remaining parameters are given in Table I of Publication IV [35].

First, in Fig. 3.2 we compare our mathematical results with simulator-based results where an implementation of the 3GPP channel model is used. We observe a good match between these results, demonstrating accuracy of the proposed approximations for the channel model parameters.

Next, we compare: (i) the outage probability in the scenario when the multipath channel model is in use; with (ii) the outage probability when only the LoS component is modeled. For the latter, in the case of the LoS blockage by human bodies, we subtract $X$ dB from the received power [30]. We assume $X = 20$ dB as per measurements in [108].

In Fig. 3.2 we present the outage probability models mentioned above as a func-

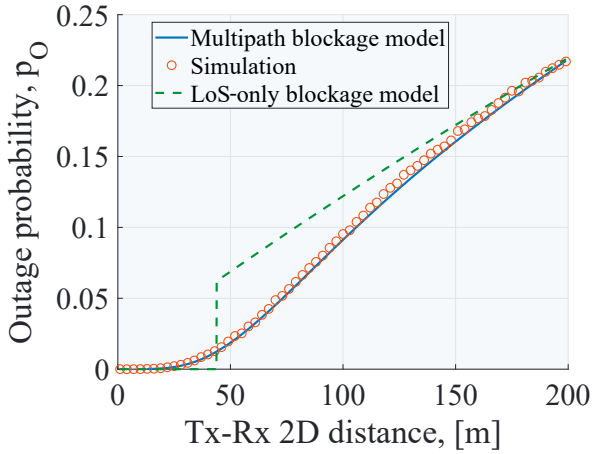


**Figure 3.2** Outage probability as a function of Tx-Rx distance.

tion of Tx-Rx distance. Our findings allow us to distinguish between the following intervals described below as

- **Less than 28 m.** The outage probability for both scenarios is close to 0. The reason for such behavior is that the user is located near its serving BS. Therefore, for the scenario with the multipath channel model, chances for all the clusters to be blocked simultaneously are low. Moreover, the power of the clusters is high enough for communication. For the scenario with the LoS only modeling, short distance between the UE and the BS also decreases the chances of the LoS to be blocked. In case the LoS is blocked and 20 dB is subtracted, the received power is still high enough to continue communication.
- **From 28 m to 44 m.** The outage probability for the scenario with the LoS-only modeling is still close to 0. The reason is that the received power, even in a blocked state, is still higher than the settled outage threshold. The outage probability for the scenario with the multipath channel model is slightly higher than 0. That is because the blockage probability is not negligible anymore, and the power of the reflected clusters becomes low. The difference between the models for the given interval is about 1%.
- **From 44 m to 170 m.** This interval demonstrates the largest difference between the models. We note that the outage probability in the scenario with the LoS only modeling is significantly higher than the one in the scenario with the multipath channel model. That is explained by the high blockage probability

of a single path as in the scenario with the LoS-only modeling. In contrast, extra multipath diversity in the multipath model brings more chances for at least one non-blocked path to be available, and having the received power higher than the outage threshold. The difference between the two models may reach up to six times in the given interval.

- **Over 170 m.** The difference between the models still exists, but it is less than 1%. The reason is that the blockage probability is high enough for all the paths, and the received power of the majority of clusters becomes smaller than the threshold. Hence, all the available paths are very likely blocked, and those that are not blocked still have the received power lower than needed for reliable data exchange.

### 3.3.4 Key findings

Not only characteristics of the LoS but also other paths, i.e., reflected/scattered from various objects in the environment, can impact the quality of a BS-UE link. Thereby, in this section, we developed a multipath blockage model that considers a mmWave-specific multipath propagation. Particularly, we provided the analytical approximation of the necessary 3GPP 3D channel model parameters (ZoA and power share of clusters) and delivered the blockage and outage probabilities.

The proposed model complements the LoS-only blockage model presented in Section 2.3. Compared to the latter model, the multipath blockage model enables a more accurate estimation of the outage probability, especially for the medium BS-UE separation distances (between 40 m and 100 m), which are typical for the upcoming deployments of mmWave systems [14]. On the other side, taking more parameters into account, the multipath blockage model is more complex than the LoS-only model. Hence, depending on the desired accuracy/complexity trade-offs, one can apply a more appropriate blockage model. We further utilize the multipath blockage model when evaluating the impact of UAV assistance in mmWave networks in Section 4.4.

## 3.4 Multipath and LoS Blockage States Generation

The LoS and multipath blockage models introduced in this thesis may be employed as a part of the mathematical frameworks for performance evaluation studies. The blockage probability can also be employed in the system level simulators instead of physical blockage modeling to decrease computational time.

There are two different approaches to identify the state of each link by using blockage probability. The first approach is to generate a state for every link independently from each other, applying the blockage probabilities derived earlier in Chapters 2 and 3. The second approach to generate links states is to consider spatial consistency between those. Although the second approach is more sophisticated than the first one, it can be favorable for scenarios where the spatial consistency among states is essential to obtain more accurate results (e.g., MIMO studies).

Following the ITU recommendations, 3GPP considered spatial and temporal consistency as a part of the channel model for the frequencies up to 100 GHz [45]. Particularly, 3GPP small-scale blockage model A [1] described in Chapter 2 is extended to account for the spatial and temporal consistency among blockers positions. The model introduces an auto-correlation function to account for the spatial and temporal consistency of blockers centers. It also considers a constant correlation distance and time for every 3GPP deployment scenario.

There are several limitations identified in this 3GPP blockage model. First, the blockers are generated at a constant distance from a user. In practice, it is more realistic to consider random distance from blockers to the UE. Second, the model aims to check every blocker in a scenario, whether it blocks every cluster or not. Such an approach helps to implicitly account for correlation between links states, but it also significantly increases simulation time, especially for high densities of blockers and users. Finally, due to constant correlation distance, nearby users on a border will face a lack of spatial consistency.

In order to overcome the limitations mentioned above, we aim to complement the 3GPP channel model by providing a spatially-consistent blockage state generation algorithm as described in Subsection 3.4.1 and developed in Publication V [32]. For that purpose, we extend the blockage modeling framework to account for correlation between link states. The proposed algorithm considers any density of blockers and provides a spatially-consistent zone dependent on deployment parameters. Fi-

nally, in Subsection 3.4.2, we conduct the numerical study to identify environments, where spatial consistency among the link states plays an important role.

### 3.4.1 Spatially-consistent blockage state generation algorithm

Here, we describe the contributed algorithm that distributes link states (blocked/non-blocked) among every Tx-Rx and Cluster-Rx pair. We first create a simple yet representative scenario with one Tx (a mmWave BS) and $K$ Rx (mmWave UEs) distributed uniformly in a cell. The human body blockers act as potential blockers and form the PPP with density $\lambda_B$. We assume a static environment (e.g., a snapshot), where all the nodes and blockers do not change their location during one simulation round. Once the nodes are distributed, we generate the 3GPP 3D channel model and multi-path parameters for every Tx-Rx pair. These include powers of every cluster arriving at the Rx side and their associated angles of arrival/departure. We note, that all parameters are summarized in Table I of Publication V [32].

The algorithm employs the mathematical spatially-consistent blockage model that considers correlation between links states. The overall framework is described in Publication V [32] and [93]. With all required parameters in hand, the algorithm proceeds with a state distribution for every Tx-Rx and Cluster-Rx pair taking into account spatial consistency between those links. We divide the algorithm into two parts: (i) blocked/non-blocked state generation for the Tx-Rx LoS links; (ii) blocked/non-blocked state generation for every cluster received by every Rx.

The first part of the algorithm starts with a blocked/non-blocked state assignment for the first reference Tx-Rx pair, using the LoS non-blockage probability (denoted as $\mathbb{P}_{\text{nB}}$ in Algorithm 1) derived following the approach in Section 2.3 of Chapter 2. Next, with the help of conditional probabilities [93] (denoted as $p_{10}$, $p_{00}$ in Algorithm 1), we derive a 2D spatially-consistent (SpCon) zone around the reference Rx, the state of which was identified earlier. The SpCon zone denotes the space, where any Rx falling within will have a spatially-consistent link state with the reference Rx.

Next, we find the states of all Rx inside the SpCon zone using the conditional probabilities from [32], where states 0 and 1 represent the non-blocked and blocked states, respectively. We continue to identify the SpCon zones and all Rx inside these zones around every Rx with a calculated state. The procedure repeats itself until all

**Algorithm 1:** Blocked/non-blocked LoS state generation

**Result:** Blocked/non-blocked LoS states for all Tx-Rx pairs

Generate uniformly distributed coordinates $(x_{R,1}, y_{R,1}), \ldots, (x_{R,K}, y_{R,K})$ of $K$ Rx
Define the sets $N_{\mathrm{U1}} = \varnothing$ and $N_{\mathrm{U2}} = \varnothing$ for the coordinates of Rx w/o and w/ blocked/non-blocked state, respectively
Define the set $N_{\mathrm{U,s}} = \varnothing$ for blocked/non-blocked states of every Rx
Save the coordinates of every Rx to the set $N_{\mathrm{U1}} = \{(x_{R,1}, y_{R,1}), \ldots, (x_{R,K}, y_{R,K})\}$
**while** $N_{U1} \neq \varnothing$ **do**
    Choose the coordinates of Rx $k$ from the set $N_{\mathrm{U1}}$
    Find the unconditional state $q^R_{u,k} = \{0 \text{ or } 1\}$ of Rx $k$ based on the non-blockage probability, $\mathbb{P}_{\mathrm{nB}}$ following [32]
    Save the state of Rx $k$ to the set $N_{\mathrm{U,s}} = N_{\mathrm{U,s}} \cup q^R_{u,k}$
    Remove the coordinates of Rx $k$ from the set $N_{\mathrm{U1}}$
    Add the coordinates of Rx $k$ to the set $N_{\mathrm{U2}} = N_{\mathrm{U2}} \cup (x_{R,k}, y_{R,k})$
    **while** $N_{U2} \neq \varnothing$ **do**
        Choose the coordinates of Rx $l$ from the set $N_{\mathrm{U2}}$
        Calculate the SpCon zone for Rx $l$ using the conditional probabilities, $p_{10}$, $p_{00}$, and the non-blockage probability, $\mathbb{P}_{\mathrm{nB}}$ following [32]
        Remove the coordinates of Rx $l$ from $N_{\mathrm{U2}}$
        Find any Rx from the set $N_{\mathrm{U1}}$ in the SpCon zone of Rx $l$
        **if** *Rx $m$ from the set $N_{U1}$ is in the SpCon zone* **then**
            Find the conditional state $q^R_{c,m} = \{0 \text{ or } 1\}$ of Rx $m$
            Add the coordinates of Rx $m$ to the set $N_{\mathrm{U2}} = N_{\mathrm{U2}} \cup (x_{R,m}, y_{R,m})$
            Save the state of Rx $m$ to the set $N_{\mathrm{U,s}} = N_{\mathrm{U,s}} \cup q^R_{c,m}$
            Remove the coordinates of Rx $m$ from the set $N_{\mathrm{U1}}$

the LoS links are assigned with a state. The exact step-by-step procedure is given in Algorithm 1 and further detailed in Publication V [32].

The second part of the algorithm refines the link states for all clusters of every Rx. Since the first part of the algorithm already provides the LoS link states, we use them as a reference state for cluster to Rx link states. Note that all the clusters have different heights for their reflection points. Thus, no common 2D SpCon zone can be derived, as in the previous part of the algorithm. Thereby, we take the reference link state and calculate a state for every cluster arriving at this Rx using the conditional probabilities from [32]. The developed algorithm distributes the states for other clusters of every Rx following the procedure described above, until all the links have their states. The exact step-by-step procedure is given in Publication V [32].

Concluding, the algorithm employs the blockage model that considers spatial

consistency among links states to generate link states. Compared with the 3GPP spatially-consistent blockage Model A, the proposed algorithm uniformly distributes blockers over the area, considering the SpCon zone dependent on deployment parameters. This approach avoids physical blockage modeling and allows to change density of blockers without increasing the time of a simulation.

### 3.4.2 Impact of spatial consistency among multipath and LoS blockage states

We compare two approaches to generate blockage states, as described earlier in this section. The first approach generates states without taking correlation among them into account, while the second approach considers correlation among states. The algorithm presented earlier in Subsection 3.4.1 covers the second approach and is more time-consuming than the independent blockage state generation algorithm. To motivate consideration of correlation among links states, we aim to identify deployment options, where the correlation plays a non-negligible role. For that purpose, we compare the numerical results in the case of the spatially-consistent state against independent state generation in terms of received power and its CDF.

We consider the Tx and Rx heights equal to 4 m and 1.5 m, respectively. The blockers density is equal to 1 blocker per square meter. All the remaining parameters are given in Table II of Publication V [32]. We consider a squared area, where a left bottom point of the area is located at coordinates $(x_{L,B}, y_{L,B}) = (15, 15)$, while the Tx is located at the origin (0,0). First, we start with analyzing the effect of correlation among the links states between the Tx and Rx distributed uniformly in a squared area of 10x10 $m^2$. Fig. 3.3a demonstrates a CDF of received power for four cases: (i) no blockers generated; (ii) independent link blockage state generation – every link is assigned with a state independently of each other; (iii) spatially-consistent link blockage state generation – every link state is assigned with a state via the algorithm described in Subsection 3.4.1; (iv) explicit blockage modeling via a physical blockers drop – the geometrical cylinders are dropped into the area, and the blockage is calculated based on the real occlusion by those.

One may note that the CDFs of received power depicted in Fig. 3.3a for the cases (ii)-(iv) are similar to each other. This is primarily explained by the fact that the SpCon zone is considerably small when compared to the overall deployment area (ap-

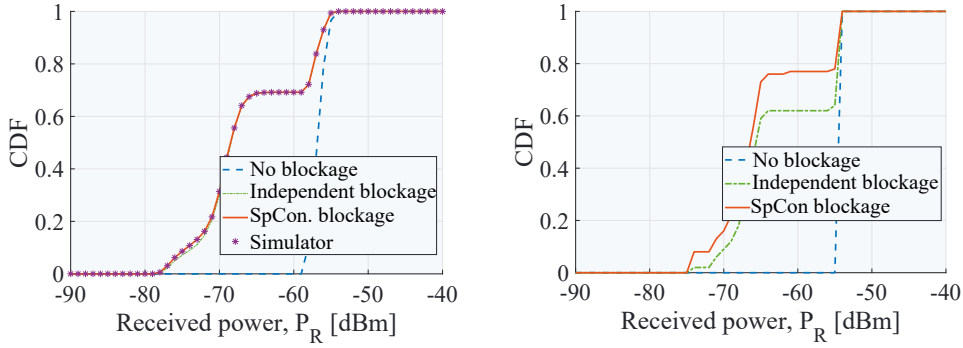


**(a)** Received power: 100 Rx deployed in 10x10 $m^2$ area **(b)** Received power: 100 Rx deployed in 1x1 $m^2$ area

**Figure 3.3** Comparison of spatially-consistent vs. independent state generation in terms of received power.

proximately 1 m wide and 10 m long). Hence, only a small fraction of Rx is located close enough to each other to experiences a strong correlation among link states.

In contrast, Fig. 3.3b illustrates an extreme case, where all the Rx are deployed within a small area of 1x1 $m^2$. Here, the overwhelming majority of deployed Rx will have link states correlated with each other. Hence, e.g., a blocked state for the first deployed Rx will lead to blocked states for the links to most other Rx and vice versa. Therefore, the overall CDF of the received power from spatially-consistent and independent blockage state generation procedures becomes different, as all the link states are randomized with independent state generation procedure.

### 3.4.3 Key findings

The multipath blockage model, developed in Section 3.3, does not take into account the possible correlation between the blockage states of individual paths. This section presents the algorithm that allows a generation of the blockage states for corresponding links, considering their correlation. The correlation among links states may be used for the development of practical communications algorithms. For instance, a link state of one user can be a reference for scheduling other neighboring users if the link quality is good or not scheduling if the link quality is low. This can help utilizing the resources more efficiently and improving the overall network performance.

From the conducted numerical study, we observe that for the averaged metrics and typical areas of interest, the correlation among the small-scale blockage states

does not drastically impact the final results. However, when focusing on a particular node and its neighbors, the difference between the spatially-consistent and independent state generation procedures, in terms of the received power, may reach up to 22%. Given the complexity/accuracy tradeoff and the scenario of interest, one may decide whether to account for the correlation among the small-scale blockage states aiming for improved accuracy or disregard it for simplicity.

# 4 SYSTEM-LEVEL ANALYSIS OF BLOCKAGE MITIGATION TECHNIQUES

## 4.1 Research Motivation

Small-scale blockers, particularly human body blockers, are characterized by their unpredicted mobility. The latter, together with the dimensions of these blockers - significantly larger than a millimeter wavelength - may lead to frequent and abrupt service interruptions, challenging the communication over mmWave links [41, 61]. That in turn calls for more advanced algorithms and techniques to support a reliable mmWave connection, even under severe blockage conditions.

There are various solutions to reduce the effect of signal blockage, which are actively discussed in the literature. In this chapter, we mainly focus on a multi-connectivity [72] and additional aerial connectivity from UAVs [66]. The multi-connectivity technique allows for switching to a back-up connection in a fast manner if a primary link is blocked [39]. UAVs capable to carry BSs (unmanned aerial vehicle base stations (UAV-BSs)), become attractive to the telecommunication sector due to their unconstrained 3D mobility and ability to be deployed on demand [66]. Particularly, the possibility to adjust UAV 3D location significantly helps to improve channel conditions between the UAV-BS and terrestrial users [19].

These enhancements do not come for granted, as they bring extra overheads as well as increase complexity and costs, both capital and operational. Thereby, it is essential to understand the best mode of operation to gain maximum benefits when integrating these functionalities into real systems. Despite several simulation studies on multi-connectivity [73, 87, 104] and UAV support [52, 65], there is still a lack of suitable mathematical frameworks that can explore these blockage mitigation techniques. In their turn, such mathematical frameworks allow for studying an extensive range of deployment parameters and their influence on overall performance metrics.

In this chapter, we propose a set of mathematical frameworks to evaluate the performance of mmWave systems enhanced with blockage mitigation techniques. For this purpose, the tools of stochastic geometry, probability theory, and queuing theory are applied. We take into account a detailed 3GPP-based mmWave channel model enhanced by the human body blockage model described in Chapter 2. The frameworks are capable of considering additional back-up connections and the mobility of UAV-BSs. This work helps to evaluate system performance, understand main trade-offs and dependencies, as well as reveal deployment parameters that reduce the harmful effect of blockage.

In Section 4.2, we describe the overall methodology to incorporate the multi-connectivity and associated performance improvements. Further, in Section 4.3, we quantify the benefits of a UAV-BS height optimization. Finally, in Section 4.4, we analyze the possible improvements brought by UAV-BSs serving users when flying over a service area. The system-level analysis of mmWave networks enhanced with the named blockage mitigation techniques allows to study the performance gains enabled by those and identify the configurations where the introduced benefits are the most profound.

## 4.2 Intra-RAT Multi-connectivity Support

One possible solution to deal with frequent and unpredicted mobility of human body blockers is to provide a spatial diversity between multiple serving nodes by employing the multi-connectivity technique. Among different multi-connectivity strategies discussed in the literature [10], in this thesis we focus on intra-RAT multi-connectivity [39]. Hence, in case of a sudden link blockage, a UE is switched to another BS in proximity within the same RAT.

A number of works on multi-connectivity actively explore various practical realizations and the performance evaluation of different schemes. The authors of [39] proposed a scheme where a UE sends sounding reference signals (SRSs) on every unit of time, in all directions, while potential serving nodes collects these SRSs and construct a table with a suitable path. In case a primary link is blocked, a central unit informs UE and a secondary cell in order to switch to a back-up link. Further, in [76], the authors proposed different approaches to choose a suitable alternative connection in case of a primary link blockage. It was demonstrated that even the

simplest reference signal received power (RSRP)-based connection can provide notable improvements.

Despite its benefits, various multi-connectivity schemes are associated with extra overheads in signaling with every additional link consuming extra energy at the UE and occupying additional radio resources [87]. Therefore, it is important to identify a sufficient number of BSs (degree of multi-connectivity) to support robust service provision. For that purpose, we present a mathematical framework, developed in Publication VI [30], that is able to evaluate a mean spectral efficiency and outage probability in a scenario with link blockages and multi-connectivity as a function of different deployment parameters. The resultant framework is then employed to numerically demonstrate the required degree of multi-connectivity needed to reach a given performance level.

### 4.2.1 Methodology and analysis

We continue with a description of our contributed framework specifically tailored to analyze a system that utilizes multi-connectivity. The scenario of interest is illustrated in Fig. 4.1. We particularly concentrate on a cell edge user as the one having, on average, challenging channel conditions. We thus imply there are no BSs closer than $R_{nL}$ to the target UE. The height of the UE is $h_U$, while the BSs of height $h_A$ form the PPP with density $\lambda_A$. We consider two types of blockers: (i) large-scale blockers (e.g., by buildings) and (ii) small-scale blockers (human bodies). The human body blockers form PPP with density $\lambda_B$. A human body is represented by a cylinder with the height $h_B$ and the base radius of $r_B$.

The UE selects $N$ BSs that have the highest received signal strength and is originally connected to the best BS among those $N$, where $N$ is termed as a degree of multi-connectivity. In case of blockage, the UE can switch to the next best BS among $N$ BSs. In order not to infinitely increase overheads associated with monitoring backup connections we need to find the minimal value of $N$ that provides sufficient performance. We thus proceed with characterizing an outage probability and a mean spectral efficiency as a function of the degree of multi-connectivity, $N$.

We distinguish between the following link states: (i) LoS non-blocked – neither large-scale nor small-scale blockage; (ii) LoS blocked – a small-scale blockage of the LoS; and (iii) nLoS – a large-scale blockage of the LoS. We model a LoS/nLoS state

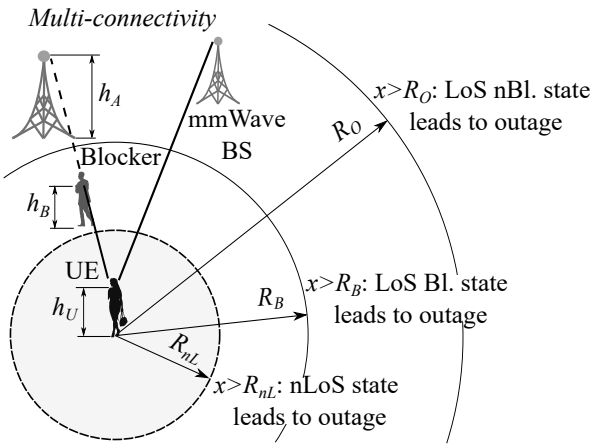


**Figure 4.1** Multi-connectivity scenario for mathematical modeling.

using a LoS probability given in 3GPP TR 38.901 [1]. The small-scale blockage is modeled employing our approach described in Chapter 2. In order to find an average received power, we employ a path loss in LoS/nLoS conditions as per [1]. In case of a small-scale blockage, we follow the field measurement results from [108] and assume 20 dB of signal degradation.

Next, we divide the area around the UE into multiple zones as illustrated in Fig. 4.1 and described below

- The distance between the UE and the BS is larger than $R_{nL}$ – the large-scale blockage between the user and the BS in this zone causes an outage.
- The distance between the UE and the BS is larger than $R_B$ – the small-scale blockage between the user and the BS in this zone causes an outage.
- The distance between the UE and the BS is larger than $R_O$ – the link between UE and BS in this zone is in outage even in LoS non-blocked state.

The distances $R_{nL}$, $R_B$, $R_O$ depend on the system parameters and are calculated as shown in Publication VI [30].

We start with the derivation of the outage probability $q_{O,N}$. We consider the outage on the BS to the UE link in case the signal strength is below a certain threshold level. The zones mentioned above help us identify scenarios leading to the outage between the UE and the BS: (i) no BSs in non-outage conditions in the ring ($R_{nL}$, $R_B$) and (ii) no BSs in non-outage conditions in the ring ($R_B$, $R_O$).

The outage in the scenario (i) appears when two mutually exclusive events happen: (a) the event $A_1$ – no BSs in the ring $(R_{nL}, R_B)$ and (b) the event $A_2^1$ – all BSs in the ring $(R_{nL}, R_B)$ are in nLoS in case of the event $A_2^2$ – there is at least one BS in that ring. Meanwhile, the outage in the scenario (ii) appears when the following mutually exclusive events happen: (a) the event $B_1$ – no BSs in the ring $(R_B, R_O)$; (b) the event $B_2^1$ – all BSs in the ring $(R_B, R_O)$ are in nLoS in case of the event $B_2^2$ – there is at least one BS in that ring; (c) the event $B_3^1$ – the nearest $\min(N, m)$ BSs in LoS blocked state in case of the event $B_3^2$ – only $m$ BSs in LoS in the ring $(R_B, R_O)$ and the event $B_3^3$ – at least one BS in the ring.

We continue with the derivation of the probabilities of the events $A_1$ and $B_1$, $Pr(A_1)$ and $Pr(B_1)$, which are derived via void probabilities and are equal to $Pr(A_1) = e^{-\lambda_A \pi [R_B^2 - R_{nL}^2]}$ and $Pr(B_1) = e^{-\lambda_A \pi [R_O^2 - R_B^2]}$. Next, we continue with the probability of the event $A_2^1$, $Pr(A_2^1)$. For that purpose we first thin the original PPP of BSs in the ring $(R_{nL}, R_B)$ to leave only those in LoS conditions

$$\Lambda_L^{R_{nL,B}} = \frac{1}{R_B^2 - R_{nL}^2} \int_{R_{nL}}^{R_B} 2x \lambda_A p_L(x) \mathrm{d}x. \tag{4.1}$$

We then employ the void probability to find no BSs in the ring $(R_{nL}, R_B)$ in LoS

$$Pr(A_2^1) = e^{-\Lambda_L^{R_{nL,B}} \pi [R_B^2 - R_{nL}^2]}. \tag{4.2}$$

The probability of the event $B_2^1$ is found similarly.

Next, we derive the probability, $Pr(B_3)$, of the event that there are $m$ LoS BSs in the ring $(R_B, R_O)$ and $\min(N, m)$ of BSs are blocked in case there is at least one BS in that ring. The general equation for $Pr(B_3)$ is given below as

$$Pr(B_3) = \left[1 - p_0^{R_{B,O}}\right] \sum_{m=1}^{\infty} p_m^{R_{B,O}} \prod_{i=1}^{\min(N,m)} p_{O,i}(m), \tag{4.3}$$

where $p_m^{R_{B,O}}$ is the probability of $m$ BSs in LoS derived from the Poisson distribution and $p_{O,i}(m)$ is the outage probability with the $i$-th nearest BS in $(R_B, R_O)$. The latter is derived as

$$p_{O,i}(m) = \int_{R_B}^{R_O} f_{Y_i^{R_{B,O}}}(x; m) \left[1 - p_{nB}(x)\right] \mathrm{d}x, \; i \leq m, \tag{4.4}$$

where $p_{nB}(x)$ is the non-blockage probability derived following the approach in Chapter 2 for the infinitesimal Rx and $f_{Y_i^{R_{B,O}}}$ is the pdf of distance to the $i$-th nearest BS from $m$ BSs given in Publication VI [30].

With the help of the derived intermediate probabilities for the events described earlier, we can proceed with the final equation for the outage probability as

$$\begin{aligned} q_{O,N} = &\left( e^{-\lambda_A \pi [R_B^2 - R_{nL}^2]} + \left(1 - e^{-\lambda_A \pi [R_B^2 - R_{nL}^2]}\right) e^{-\Lambda_L^{R_{nL,B}} \pi [R_B^2 - R_{nL}^2]} \right) \times \\ &\left( e^{-\lambda_A \pi [R_O^2 - R_B^2]} + \left(1 - e^{-\lambda_A \pi [R_O^2 - R_B^2]}\right) \times \right. \\ &\left. \left( e^{-\Lambda_L^{R_{B,O}} \pi [R_O^2 - R_B^2]} + \sum_{m=1}^{\infty} p_m^{R_{B,O}} \prod_{i=1}^{\min(N,m)} p_{O,i}(m) \right) \right). \end{aligned} \tag{4.5}$$

The derivation of the mean spectral efficiency follows a similar methodology as employed for the outage probability. Here, we give the final equation while all the intermediate calculations can be found in Publication VI [30]. The mean spectral efficiency is obtained as

$$\begin{aligned} E[C_N] = &\left(1 - p_0^{R_{nL,O}}\right) \sum_{k=1}^{\infty} p_k \sum_{j=1}^{\min(N,k)} v_{j,k} \int_{R_{nL}}^{R_O} f_{Z_j}(x;k) \log_2\left(1 + S_{nB,j}(x)\right) \mathrm{d}x + \\ &\left(1 - p_0^{R_{nL,O}}\right) \sum_{k=1}^{\infty} p_k w^{R_{nL,B}} p_{B,k} \times \\ &\prod_{j=2}^{\min(N,k)} p_{B,j,k} \int_{R_{nL}}^{R_B} f_{Z_1}(x;k) \log_2\left(1 + S_{B,1}(x)\right) \mathrm{d}x, \end{aligned} \tag{4.6}$$

where $S_{nB,j}(x)$ is the signal-to-noise ratio (SNR) when UE is connected to the $j$-th nearest BS in the LoS non-blocked state and $S_{B,1}(x)$ is the SNR when UE is connected to the first BS in the LoS blocked state in $(R_{nL}, R_B)$.

The first part of (4.6) corresponds to the event that the nearest LoS BSs with index $j$ out of $\min(N,k)$ is in a non-blocked state in case of having at least one BS in the ring $(R_{nL}, R_O)$ and $k$ BSs residing in LoS in that ring with probabilities $v_{j,k}$, $p_k$, $1 - p_0^{R_{nL,O}}$, respectively. The second part of (4.6) is associated with the event of having the closest BS in LoS residing in the ring $(R_{nL}, R_B)$ (with probability $w^{R_{nL,B}}$) in case of seeing $\min(N,k)$ LoS BSs in a blocked state having $k$ BSs in LoS and at

least one BS in the ring $(R_{nL}, R_O)$.

To summarize, we delivered a mathematical framework that calculates the outage probability and the mean spectral efficiency for the scenario with multi-connectivity of degree $N$, large-scale and small-scale blockers. In the following subsection, we apply this framework to numerically characterize the key metrics of interest as a function of $N$ and other deployment parameters.

### 4.2.2 Improvements introduced by multi-connectivity

The use of multi-connectivity enables more robust mmWave communications in scenarios with frequent and unpredictable blockage dynamics. However, every additional mmWave connection requires extra resources and signaling messages from the network. Therefore, one should carefully estimate an appropriate number of links to satisfy user requirements. In this subsection, with the help of analysis demonstrated above, we present the numerical results that show the mmWave system performance in response to the varying degree of multi-connectivity (MC).

We start with the evaluation of the outage probability and the mean spectral efficiency as a function of multiple deployment parameters and the degree of MC. The heights of BS, UE, and blockers are equal to 10 m, 1.5 m, and 1.7 m, respectively. The density of BSs is set to $\lambda_A = 10^{-4}$. We consider an operation over frequency equal to 28 GHz and 1 GHz of bandwidth. The remaining parameters are given in Table I of Publication VI [30].

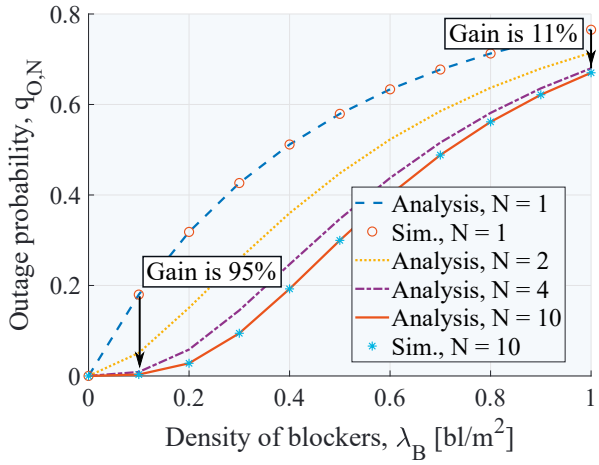


**Figure 4.2** Outage probability as a function of blockers density.

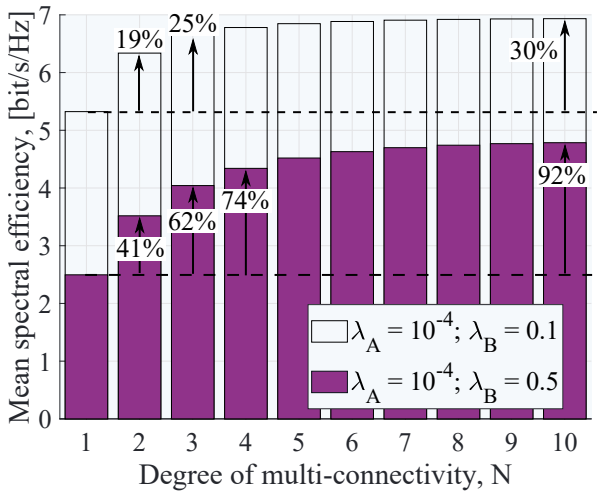


**Figure 4.3** Spectral efficiency as a function of degree of MC.

Fig. 4.2 demonstrates behavior of the outage probability in response to the blockers density with different degrees of MC. Let us first study the effect of $N$. We notice that the degree of MC larger than $N = 4$ does not bring any notable gains. The reason is that every additional BS is located farther away from the UE, and thus has a higher blockage probability and lower chances to be available for communication. Our second important observation is that the highest relative gain (up to 72% for considered set of parameters) is achieved with the degree of MC, $N$, equal to 2. Any additional link brings significantly less gain, calling for careful selection of the total links to maintain.

We now proceed exploring the impact of blockers density in Fig. 4.2. Here, we observe that the gain from an extra degree of MC increases when increasing the density of blockers up to 0.4 bl/s for modeled set of parameters. Meanwhile, by increasing the blockers density further, the gain from higher degree of MC decreases. The later is caused by the fact that when the blockers density is large the distant BS has a higher chance of being blocked and thus cannot bring sufficient gains. As an example, the difference between $N = 4$ and $N = 1$ decreases from 95% down to only 11%, when the blockers density grows from 0.1 bl/m$^2$ up to 1 bl/m$^2$.

Further, in Fig. 4.3 we demonstrate the mean spectral efficiency as a function of the degree of multi-connectivity. The behavior of the mean spectral efficiency as a function of the degree of MC is similar to what was observed with the outage probability. When the density of blockers increases from 0.1 to 0.5 bl per m$^2$ we notice

that the gain from degree of MC $N = 2$ increases from 19% to 41%. Therefore, the additional links bring more benefits for moderate rather than low blockers density.

### 4.2.3 Key findings

In this section, we evaluate the performance of the mmWave system enhanced with multi-connectivity to mitigate blockage in urban deployments. Given that the blockage probability is especially high at relatively large distances between a BS and a UE (e.g., 100 m as discussed in Section 2.3), we particularly focus on a cell edge user in this study. For such a setup, we deliver the mathematical framework that calculates the outage probability and the mean spectral efficiency for the scenario with multi-connectivity of degree $N$, large-scale and small-scale blockers. The framework is further employed in following studies focusing on the performance evaluation of mmWave systems with multi-connectivity, including [37].

Following our numerical study, we observe that multi-connectivity is indeed a powerful mechanism to mitigate the blockage effect and support the performance and reliability of mmWave communications. We observe that even one additional link (the degree of MC is $N = 2$) can decrease the outage probability by 1.6 times when the blockers density is equal to 0.3 bl/m$^2$. However, our study also indicates that the careful choice of the degree of MC is of paramount importance. We note that for the considered deployment parameters, the maximum degree of MC that brings non-incremental performance gains is $N = 4$. The further increase of the degree of MC does bring any substantial gain. These findings may be particularly useful when adjusting the multi-connectivity feature for the prospective mmWave communication systems.

## 4.3 Semi-Static UAV Support

With a rapid technology development, UAVs become in high demand in many different fields. Nowadays, UAVs with their unconstrained 3D mobility are actively employed for video monitoring, surveillance, package delivery, entertainment, and many other services [113]. Besides the named applications, a telecommunication sector also considers on-demand BSs carried by UAVs, termed as UAV-BSs [43].

The concept of a UAV-BS implies that a UAV carries a BS thus delivering wireless

communication to the desired location [80]. Such type of BS can provide several advantages to both operators and end users. One of the advantages is the ability of a UAV-BS to arrive at a location quickly in response to a spike in the service demand [65]. For instance, an operator can support massive temporal events (e.g., marathons, fairs) with on-demand UAV-BSs and avoid over-provisioning when the latter is not needed. Another scenario of interest, where a network can benefit from a UAV-BS, is a back-up communication in disaster areas, where some of the BSs are destroyed or temporary out of service. [112]. In such a case, a UAV-BS can establish a backhaul connection to a distant BS and provide communication to ground users in critical situations.

Despite numerous benefits, a UAV-BS has several limitations and challenges. One challenge is related to a UAV-BS operating in nLoS visual conditions, calling for appropriate route selection and/or a human operator involvement [18, 66]. Another challenge is service time limitation due to UAV battery constraint [97]. On top of those, there are also noise restrictions, weight limitations, and safety regulations that challenge UAV-BS operation [98]. All of these require careful investigation of the most efficient way to employ UAV-BSs to maximize possible gains.

A number of works actively studied UAV-BSs in various deployments and scenarios. In [19], authors propose an algorithm that provides an optimal 3D location for a UAV-BS to maximize performance metrics. Further, the paper [52] investigates backhaul constraints while optimizing a 3D UAV-BS location. The paper demonstrates the importance accounting for of backhaul connectivity as it significantly impacts the final UAV-BS location. The work in [106] describes an algorithm to plan a UAV-BS optimal paths from a charging place to a service area.

When referring to mmWave communications, a UAV-BS height optimization plays a significant role, especially, under severe link blockage conditions. The higher a UAV-BS is located, the lower blockage probability will be observed. However, increasing 3D distance from a UAV to a UE will also increase the path loss. In the next subsection we propose a UAV-BS height optimization to minimize the impact of the blockage effect, as developed in Publication VII [28].

### 4.3.1 Methodology and analysis

We consider the scenario illustrated in Fig. 4.4 for a contributed UAV-BS height optimization. We assume the area of interest with suddenly increased traffic demand. An operator sends a mmWave-based UAV-BS to support static infrastructure. The UAV-BS with height $h_D$ connects to a static infrastructure via a wireless backhaul link.

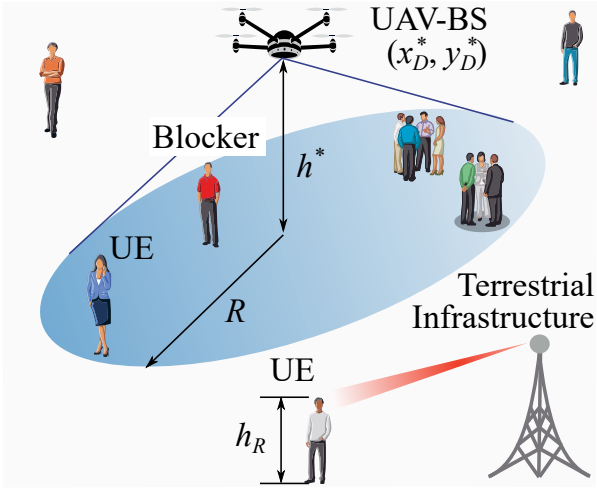


**Figure 4.4** Scenario with semi-static UAV-BS for mathematical modeling.

The users of height $h_R$ are randomly distributed in the scenario of interest following the PPP with density $\lambda$. Every user acts as a potential blocker to other users. We imply that in the open square scenario a human body is the only source of blockage. A human body is represented by a cylinder with height $h_B$ and base diameter $g_B$. Thus, we model two possible UE states: (i) LoS non-blocked and (ii) LoS blocked. The human body blockage is modeled as described in Chapter 2 and the path loss for the LoS is calculated following 3GPP TR 38.901 [1]. All the model parameters are summarized in Table I of Publication VII [28].

The optimization algorithm described in [28] finds the optimal $(x_D^*, y_D^*, h^*)$ – 2D and 3D locations of the UAV. The primary purpose of the 2D optimization is to maximize the number of served UEs with the appropriate SNR level. Further, the UAV-BS height optimization is performed aiming to improve channel conditions between the UAV-BS and the ground UEs. In the scope of this thesis, we provide the mathematical height optimization while the rest of the algorithm with 2D and 3D

placement is described in more detail in [28].

In order to deliver the optimal UAV height, we first need to provide the average path loss given below as

$$L_{a,i} = \mathbb{P}_L(R, h_D) L_{L,i} + [1 - \mathbb{P}_L(R, h_D)] L_{N,i}, \tag{4.7}$$

where $L_{L,i}$ and $L_{N,i}$ are the pass losses in non-blocked and blocked states, respectively.

The first term of (4.7) is referred to the path loss in non-blocked conditions with non-blockage probability $\mathbb{P}_L$ while the second term of (4.7) is referred to the blocked LoS conditions with blockage probability $1 - \mathbb{P}_L$. The blockage probability is found following the approach from Chapter 2. The optimization is provided for a cell edge user, assuming that the users located closer than the UAV-BS cell radius, $R$, will face better channel conditions on average.

We further note that the function $L_{a,i}$ has a unique minimum point under a certain height termed as optimal height of UAV, $h^*$. The prove of the above follows a similar approach as in Publication VII [28]. Thereby, to find an optimal height, we need to find the minimum of $L_{a,i}$ by taking the derivative of $L_{a,i}$ and equating it to 0 as

$$-C\big[\alpha_L - \alpha_N\big]\big[(h^* - h_R)^2 + R^2\big] e^{\frac{C}{h^* - h_R}} + 10C\big[\beta_N - \beta_L\big] \log_{10}\Big(\sqrt{(h^* - h_R)^2 + R^2}\Big)$$
$$+ \frac{10\big[\beta_L - \beta_N\big]\big[h^* - h_R\big]^3}{\ln(10)} e^{\frac{C}{h^* - h_R}} + 10\beta_N = 0, \tag{4.8}$$

where the auxiliary variable $C = -\lambda g_B R(h_B - h_R)$, $\alpha_L$, $\alpha_N$, $\beta_N$, $\beta_L$ are the parameters of path loss models.

Finally, we numerically solve (4.8) due to its complex structure. The equation (4.8) helps assessing the optimal UAV-BS height to minimize the blockage probability and keep the path loss at its minimum value. Besides UAV height optimization, the proposed approach can be applied to improve the performance of static mmWave infrastructure.

### 4.3.2 Improvements introduced by UAV-BS height optimization

We proceed with the numerical study to understand the effect of the UAV-BS optimal height by employing the analysis presented in the previous subsection. Specifically, we concentrate on the following metrics of interest: (i) the average path loss as a function of the UAV-BS height and (ii) the optimal UAV-BS height as a function of the blockers density. We assume a cell edge user that, on average, has the worst channel conditions.

We consider the UE with height equal to 1.3 m. The height and diameter of blockers are equal to 1.7 m and 0.5 m, respectively. The UAV-BS is operating over 28 GHz frequency band. The remaining parameters are given in Table II of Publication VII [28].

Fig. 4.5a illustrates the average path loss as a function of the UAV-BS height and the cell radius, $R$. As discussed in the previous subsection, there is a single point where the average path loss takes its minimum value. By increasing the UAV-BS height up to the optimal value, the average path loss decreases due to the decreased blockage probability. When increasing the UAV-BS height further, the average path loss starts increasing. The reason for the latter behavior is that increased path loss, caused by increased 3D distance, starts dominating the gains from decreased blockage probability.

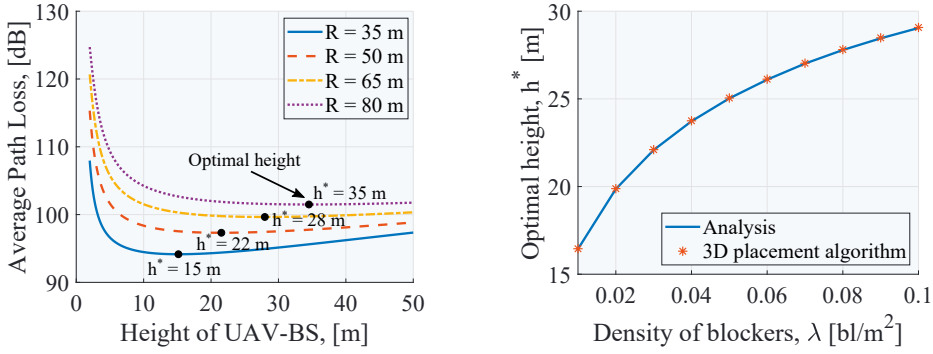


**(a)** Average path loss as a function of UAV-BS height

**(b)** Optimal height as a function of blockers density

**Figure 4.5** Effect of UAV-BS height optimization.

As one may also notice from Fig. 4.5a, the optimal height increases with the cell radius, $R$, growing. That is explained by increased blockage probability for larger 2D distance between the UAV-BS and the cell-edge UE, thus requiring higher UAV-BS

height to minimize the chances that the link is blocked. Similar behavior is observed in Fig. 4.5b, which demonstrates the optimal UAV-BS height as a function of the blockers density. By increasing the density of blockers, the blockage probability increases, calling for a higher altitude to mitigate the effect of blockage.

### 4.3.3 Key findings

In contrast to a static infrastructure, the UAV-BS, with its flexible mobility, can adjust the height and location to improve the performance of the corresponding cells. This section introduces the mathematical framework that allows achieving the minimum average path loss (thus a maximum average SNR) between a UAV-BS and a UE. The developed framework can also be reused to optimize the height of a static BS. We applied this approach in further studies evaluating the performance gains introduced by UAV-based mmWave infrastructure, including but not limited to [36, 77].

Our numerical findings reveal that there are two contradicting trends when increasing the height of a mmWave UAV-BS. On one side, the greater height results in lower blockage probability. On the other side, the increased height leads to a longer separation distance between the BS and the UE and thus increases the path loss. Using the developed framework, we observe that the average path loss (when both distance and blockage effects are taken into account) is a non-monotonic function of a BS height with a single minimum value. We also notice that the optimal height of the UAV-BS grows with the density of blockers in the area. Particularity, when increasing the radius of a UAV-BS mmWave cell from 35 m to 80 m, the UAV-BS height should be increased from 15 m to 35 m to keep the average path loss at its minimum value. The discovered findings, together with the developed framework, may help to improve the performance of prospective mmWave networks.

## 4.4 Mobile UAVs Support

In the previous Section 4.3, we focused on a single UAV-BS that serves users from an optimal location. Besides a semi-static UAV-BS operation, UAV-BSs could also provide service while flying over the area without hovering at any particular location [117]. On-the-fly connectivity can be employed in situations where e.g., UAV

wing configuration does not allow hovering (e.g., fixed-wing UAVs) or when there is a need to support mobile crowd (e.g., a marathon) [117]. Another possibility is to employ third-party UAVs that fly over the area on their mission [98], while providing a relay capability in case of mutual agreement with an operator [57]. The latter use of UAVs allows an operator to employ a fleet of UAVs without maintaining them directly.

In all the described scenarios, such UAVs provide both some benefits together with certain challenges. The benefits of UAV-BSs flying over the service area are, e.g., increased spatial diversity and decreased energy consumption when comparing to hovering UAVs [115]. Another benefit of mobile UAVs, particularly third-party UAVs on a mission (e.g., video monitoring during a concert), is that with an appropriate agreement, an operator can have extra relay opportunities without investing in a fleet of UAVs. At the same time, the dynamics of UAVs bring another level of mobility in addition to users and blockers mobility, thus increasing the system complexity. All these factors call for an appropriate system performance evaluation, where the main features of UAVs (e.g., mobility) and mmWave communications (e.g., blockage and multipath propagation) are considered. In-depth evaluation will further help to unleash the gains brought by mobile UAV-BSs to prospective wireless networks.

There are various papers that consider mobile UAVs available up to date. The paper [56] aims to optimize a trajectory of UAV-BSs to maximize a system throughput, taking into account the UAV speed, flight restriction areas, and the minimum required data rate. The work demonstrates an increase in the system throughput compared to the baseline scheme, where no trajectory optimization is made. In [114], the authors propose a convex optimization to maximize throughput for a mobile UAV-BS and a UAV-BS hovering at particular locations. The numerical results demonstrate that the scheme with mobile UAV provides a better performance compared to the hovering UAV scheme. Similarly, papers [110, 116] demonstrate an optimization of UAVs trajectory to maximize the performance taking the UAV energy constraint into account.

Despite several works on mobile UAV-BSs support of ground users, an integrated mathematical framework considering the main features of UAVs (e.g., mobility) and mmWave communications (e.g., blockage and multipath propagation) has not been delivered yet. Thereby, in the next Subsection 4.4.1, we propose a mathemati-

cal framework, developed in Publication VIII [31], that accounts for the mmWave-specific propagation, the small-scale link blockage, and the mobility of UAVs. Later, in Subsection 4.4.2, we quantify the gains brought by the mobile mmWave UAV-BSs under various deployment parameters.

### 4.4.1 Methodology and analysis

The scenario of interest, where mobile mmWave UAVs can assist ground UEs is illustrated in Fig. 4.6. We consider a circular area of radius $R$. A static BS with height $h_A$ is located at the circumference of the circle. The blockers in the scenario are human bodies modeled as cylinders with height $h_B$ and base radius $r_B$. The blockers form the PPP with density $\lambda_B$.

We assume a massive event, where on-demand infrastructure is needed to complement a single static BS. In our example scenario, these are cell-on-wheels BSs (COW-BSs), that are uniformly distributed in the open square scenario. The COW-BSs with height $h_C$ form the PPP with density $\lambda_C$. Several UAV-BSs fly across the area of interest with constant speed $v_D$ and at predefined height $h_D$. The process of UAV-BSs entering the area is assumed to be a Poisson in time with intensity $\lambda_D$. We assume that every UAV-BS enters the area at a random point of the circumference and flies through the center of this circle. Each of the UAV-BSs is capable of serving up to $K_D$ COW-BSs simultaneously. All the model parameters are given in Table I of Publication VIII [31].

The wireless backhaul link between the COW-BSs and the static mmWave BS located at the circumference of the area is provided via mmWave links. Due to the low height of COW-BS, there is a possibility that the nodes might be blocked by human bodies uniformly distributed in the area. In that case, we assume traffic is relayed to the static mmWave BS via one of the mmWave UAV-BSs flying over the area if at least one is available. For the mmWave channel model, we employ the 3GPP 3D channel model [1] with approximated parameters introduced in Chapter 3. With the proposed framework, we calculate the following main metrics of interest: (i) outage probability and (ii) mean spectral efficiency.

We start with a description of the outage probability derivation. We first note that the COW-BS is always connected directly to the static BS if there is no outage. The outage on the link between the COW-BS and the static BS may happen in case

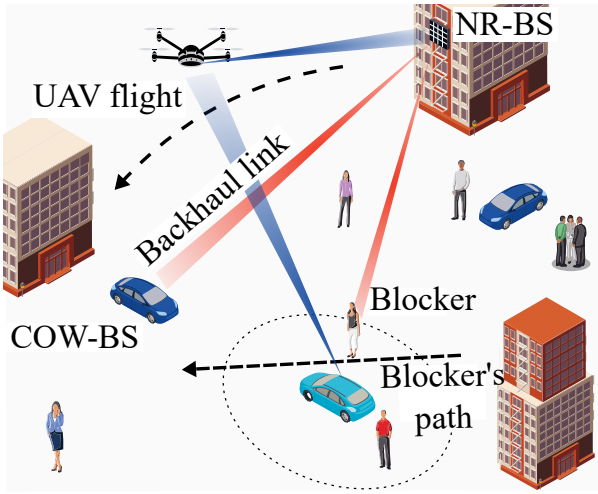


**Figure 4.6** Scenario with mobile UAV-BSs for mathematical modeling.

the signal strength on the COW-BS to BS link is below a threshold together with one of the following events: (i) the signal strength between COW-BS and UAV-BS is below a certain threshold or (ii) there is no UAV-BS available to relay traffic. Therefore, the outage probability is derived as

$$p_O = p_{A,O}\Big(u_0 + (1-u_0)\big(u_{0,n} + (1-u_{0,n})p_{D,nav}\big)\Big), \tag{4.9}$$

where $p_{A,O}$ and $u_{0,n}$ are the outage probability on the links between COW-BS and BS/UAV-BS, $u_0$ is the probability that no UAV-BS is currently traveling the area, and $p_{D,nav}$ is the probability that the UAV-BS is not available due to the limitation on the total users it could serve simultaneously ($K_D$).

The outage probability on the links between COW-BS and BS/UAV-BS is derived using the stochastic geometry tool and following the approach in Section 3.3. We proceed with the outage probability for the link between the COW-BS and the stationary BS $p_{A,O}$. Note that COW-BS operates not only with LoS link but also other nLoS clusters in case of LoS blockage.

We first find the pdf of the received power as follows

$$f_{P_A}(y) = \sum_{k=1}^{N}\left[(1-p_{A,k})\prod_{j=1}^{k-1}p_{A,j}\right] f_{P_{A,k}}(y), \tag{4.10}$$

where $N$ is the number of clusters generated per node, $p_{A,k}$ is the blockage probability for LoS (following Section 2.3) and other clusters (following Section 3.3), and $f_{P_{A,k}}$ is the pdf of received power of cluster $k$.

The outage probability, $p_{A,O}$, on the link between COW-BS to the BS is then derived as

$$p_{A,O} = Pr\{P_A(y) \leq N_0 T_S\} = \int_0^{N_0 T_S} f_{P_A}(y) dy, \tag{4.11}$$

where $N_0$ and $T_S$ are the Johnson-Nyquist noise and the SNR threshold, respectively.

We continue with the derivation of $p_{D,nav}$ – the probability that no UAV-BS is available at the moment the link between the COW-BS and the BS is in outage. To derive $p_{D,nav}$, we first obtain the probability that at least one UAV-BS is available $p_{D,av} = Pr\{K_D U - W > 0\}$, where $K_D$ is the number of simultaneously supported users by a single UAV-BS, while $U$ is the number of the UAV-BSs flying above the area at the moment and in non-outage conditions, and $W$ is the total number of COW-BSs that currently experience outage for their direct links towards the stationary BS.

Next, we find the number of UAV-BSs in the service area and in non-outage conditions $U$. Recall that the UAVs entering the zone are described via a Poisson process in time. We further note that the UAVs entering and leaving the service area can be described by the queuing model $M/G/\infty$. From [67], we learn that the UAVs in the service area at every instant of time form the PPP and the number of UAVs follows a Poisson distribution with a parameter $\lambda_D T_D$, where $T_D$ is the flight time of the UAV-BS over the area. To find $U$, we thin out the resultant PPP with the probability $(1 - p_{D,O})$ and get the following

$$u_n = \frac{[\lambda_D T_D (1 - p_{D,O})]^n}{n!} e^{-\lambda_D T_D (1 - p_{D,O})}, \; n = 0, 1, \ldots, \tag{4.12}$$

where $p_{D,O}$ is the probability that a randomly selected UAV-BS is in outage.

The number of COW-BSs in outage conditions follows the Poisson distribution with a parameter $\lambda_C p_{A,O} \pi R^2$. Therefore, the probability of the UAV-BS available

for a service is found as

$$p_{D,av} = Pr\{K_D U - W > 0\} = \sum_{i=1}^{\infty} Pr\{Z = i\}, \tag{4.13}$$

where $Z = K_D U - W$.

The probability mass function (pmf) of Z is then derived as

$$Pr\{Z = z\} = \sum_{x=0}^{\infty} \frac{|K_D x - 1|}{K_D} \frac{[\lambda_C p_{A,O} \pi R^2]^{(K_D x - z)}}{(K_D x - z)!} \times$$
$$e^{\left(-\lambda_C p_{A,O} \pi R^2 - \lambda_D T_D (1 - p_{D,O})\right)} \frac{[\lambda_D T_D (1 - p_{D,O})]^{x/K_D}}{(x/K_D)!}. \tag{4.14}$$

We now can calculate the outage probability given in (4.9) by employing all the intermediate probabilities for the events introduced earlier.

The framework for the mean spectral efficiency consists of similar elements as for the outage probability with the detailed derivations found in Publication VIII [31].

### 4.4.2 Improvements introduced by mobile UAV-BSs

To demonstrate the benefits from the UAV-BSs flying over the serving area, we proceed with the numerical evaluation of the modeled system. Particularly, we assume the height of BS is equal to 10 m, while the height of UAV-BSs is 20 m. The height and diameter of blockers are equal to 1.7 m and 0.4 m, respectively. The rest of parameters are given in Table II of Publication VIII [31].

In Fig.4.7a, we present the outage probability as a function of the UAV-BSs intensity, which is the number of the UAV-BSs entering the area per minute. This parameter directly affects the number of the UAV-BSs currently present in the area of interest. Therefore, by increasing the UAV-BSs intensity, the outage probability decreases as the chances increase that the COW-BS will find an alternative link in case of poor signal quality with its primary BS. We further note that for the crowded scenario ($\lambda_B = 0.3$) and UAV-BSs intensity equal to approximately 4 UAV-BSs per minute, the outage probability could reach a similar value as in less crowded ($\lambda_B = 0.1$) scenarios with no UAV-BS support. Hence, the use of UAV-BSs allows to mitigate the negative impacts of blockage.

Next, we study the impact of the UAV-BSs speed and the number of simultane-

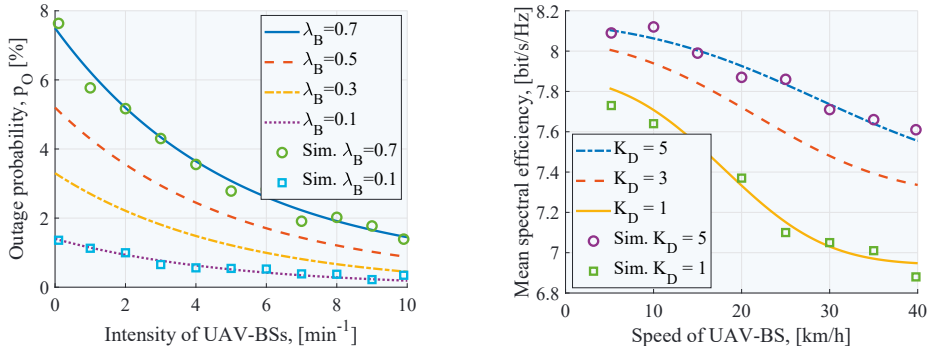


**(a)** Effect of UAV-BSs temporal intensity

**(b)** Effect of UAV-BSs speed

**Figure 4.7** Outage probability and spectral efficiency as a function of UAV-BSs temporal intensity, UAV-BSs speed, and number of supported users.

ously supported users $K_D$ on the mean spectral efficiency as shown in Fig. 4.7b. It is observed that decrease of the UAV-BSs speed increases the spectral efficiency. This is caused by the increased number of UAV-BSs present in the area of interest in case of a lower UAV-BSs speed. Our numerical study demonstrates that by decreasing the UAV-BSs speed from 30 km/h down to 15 km/h, one can increase the mean spectral efficiency by two times.

We continue by analyzing the effect of the number of simultaneously supported users by the UAV-BS, $K_D$. For low UAV-BSs speed equal to 5 km/h, increasing the number of $K_D$ from 1 to 5 increases the spectral efficiency by 22%. When increasing the speed to 20 km/h the difference in the mean spectral efficiency between $K_D = 1$ and $K_D = 5$ reaches 69%. Such behavior demonstrates that when the density of the UAV-BSs is high enough, there is no need to increase the radio part complexity by increasing the number of simultaneously supported users. However, for a low number of the UAV-BSs available, the advanced radios with more users supported simultaneously (high $K_D$) may notably increase performance.

### 4.4.3 Key findings

In this section, we study the performance gains brought by mobile mmWave UAV-BSs when assisting ground mmWave nodes. For this purpose, we develop the comprehensive mathematical framework that accounts for mmWave specific multipath propagation, the small-scale link blockage, and the mobility of UAVs. This com-

pound framework particularly reuses the LoS blockage model developed in Section 2.3 and multipath blockage model described in Section 3.3.

Our numerical study indicates that the mobile UAV-BSs can notably increase the performance of a static mmWave network. At the same time, we observe that the gains strongly depend on the number of UAVs entering the area. For example, the outage probability decreases from 5.5% down to 1% when the intensity of UAV-BSs entering the service area increases from 2 per min up to 10 per min for the density of blockers equal to 0.5 bl/m$^2$. Another possible approach to improve the performance (if applicable) is to send a dedicated request to UAVs entering the area to temporally decrease their flight speed. This allows increasing the amount of time that UAVs stay in the area to provide the additional connectivity. Hence, the study illustrates that not only the strategically allocated semi-static UAV-BSs but also the fully mobile UAV-BSs, can support mmWave users suffering from human body blockage.

# 5 CONCLUSIONS AND FUTURE WORK

## 5.1 Summary

A non-negligible impact of blockage on mmWave communications demands to include these effects in performance evaluation methodologies used for system-level analysis. Such analysis can further strengthen an understanding of mmWave communication system behavior in various deployments and conditions. For that purpose, in this thesis, we delivered the mathematical methodology to characterize the possible blockage of mmWave links by different objects and the impact of this effect on system performance. Moreover, we analyzed the mmWave system with various blockage mitigation techniques and demonstrated the possible gains of those in different deployment configurations.

First, in Chapter 2, we considered the LoS blockage by human bodies (small-scale blockers) and buildings (large-scale blockers). As a result, we calculated the blockage probabilities taking into account the size of Rx, the density of blockers (human bodies or buildings), the height of BS, UE, and blockers. To better understand the dynamics of the human body blockage process, we then presented the model to deliver the characteristics of uninterrupted time in blocked and non-blocked states in the scenario with mobile small-scale blockers.

In Chapter 3, we extended the LoS blockage model from Chapter 2 to the multipath blockage model, thus accounting for the multipath nature of mmWave propagation. For that purpose, we provided the approximation of the 3GPP mmWave channel model parameters and calculated the multipath blockage and outage probabilities. We also delivered the algorithm that distributes the blocked/non-blocked states across all Tx-Rx and Cluster-Rx links, taking into account the correlation between the links states.

Finally, in Chapter 4, we studied possible mechanisms to mitigate the blockage effect. We particularly developed mathematical frameworks capable of evaluating

the performance of mmWave networks enhanced with multi-connectivity and UAV relaying. First, we presented the framework capable of analyzing the benefits from intra-RAT multi-connectivity. Second, we considered possible assistance from the mmWave UAV-BSs and delivered the framework capable of accounting for the UAVs mobility, blockage, and mmWave multipath propagation.

The models and frameworks developed in this thesis enable an evaluation of mmWave system performance in various realistic deployment configurations. This study helps to quantify the impact of the blockage effect on the performance of mmWave systems. Moreover, it provides an assessment of the performance gains introduced by individual techniques to mitigate the blockage.

The main observations from our numerical study are summarized as follows:

- The blockage probability for mmWave link highly depends on the geometry of the scenario. Three main parameters play a key role here: the separation distance between a UE and a BS, difference in the nodes' heights, and the density of blockers. We identify that the blockage effect is especially profound for cell-edge users. Hence, network densification is identified as one possible solution to decrease the blockage probability in mmWave networks.
- Increasing the height of a BS can also decrease the blockage probability, but will simultaneously increase the separation distance between the BS and the target UE. Therefore, one needs to carefully choose the appropriate BS height to keep the average path loss to its minimal value. A UAV-BS with flexible mobility can be further exploited, as they can adapt its height dynamically, thus improving channel quality for connected users.
- The human body blockage is a highly dynamic process with two major states, blocked and non-blocked, with notably different channel conditions. The time spent in a blocked state can be as high as several hundreds of ms, leading to the potential loss of tens of NR frames. The multi-connectivity technique is a promising solution to maintain a reliable yet high data rate connection between a UE and network infrastructure in case of frequent blockage events.
- The choice of the degree of MC needs to be made carefully, as for higher degrees MC the overheads and the complexity of the underlying protocols also increase. Notably, it is shown that substantial performance gains can be achieved with the degree of MC equal to two, whilst the degree of MC higher

than four provides only incremental gains.

- Non-negligible benefits can be provided to a static mmWave infrastructure by mobile UAVs. With the intensity of UAV-BSs entering the service area equal to three per minute, the outage probability can be decreased two fold compared to the scenario with no UAV-BS support. Hence, the UAV-based infrastructure can be a promising addition to static mmWave networks.

## 5.2 Future Work

The work in this thesis highlights possible research directions for future study. The methodology developed here can be further employed to investigate other deployments and potential enhancements to mitigate the blockage effect in mmWave networks. Below, we discuss some areas of interest that could be explored.

First, in this thesis, we considered multi-connectivity as one of the options to maintain an uninterrupted connection in the case of a sudden blockage event. A rapid switch between available links can indeed provide better performance. However, in practical deployments, the trigger to switch the link activates when a blockage event has already occurred. In that case, the link will operate with diminished signal strength for a certain period of time. For particular applications, e.g., virtual and augmented reality, such a situation can significantly decrease session quality and the associated user experience. Therefore, one possible direction could be to create a method for detecting an upcoming blockage event, leading to a switch to the alternative link in a proactive manner. This will maintain the quality of the link to the desired level during any given session.

The second research direction is related to providing native support of flying UAVs with mmWave networks. It is expected that network operators will soon have to accommodate a new type of user known as a UAV. With an increased number of UAVs, the associated traffic will increase significantly, calling for more bandwidth to accommodate them. The mmWave networks can help provide the necessary bandwidth. However, the narrow beam mmWave communication can become a challenge for the UAV support due to its 3D mobility. New beam selection mechanisms, 3D beamforming, and many other enhancements are expected to reliably integrate the UAVs into the mmWave network.

Lastly, scheduling algorithms can further be improved to better account for the

inherent features of mmWave communications. Particularly, it could be essential to exploit additional information when distributing available resources within a highly dynamic environment and fragile mmWave links. For example, with the help of conditional blockage probabilities, one can take the spatial correlation between links states into account. Particularly, when a certain user is blocked, it is likely that the neighboring user is blocked as well. Considering the correlation between links states as extra information to adjust the scheduling decision may help in further improving the performance of mmWave networks.

# REFERENCES


[1] 3GPP. *Study on channel model for frequencies from 0.5 to 100 GHz (Release 14)*. 3GPP TR 38.901 V14.1.1. July 2017.

[2] 3GPP. *Summary of Rel-15 work items*. 3GPP TR 21.915 V15.0.0. Sept. 2019.

[3] 3GPP. *Physical channels and modulation (Release 16)*. 3GPP TS 38.211 V16.2.0. June 2020.

[4] 3GPP. *Service requirements for the 5G system (Release 17)*. 3GPP TR 22.261 V17.3.0. July 2020.

[5] 3GPP. *Study on New Radio (NR) access technology (Release 16)*. 3GPP TR 38.912 V16.0.0. July 2020.

[6] 3GPP. *Study on scenarios and requirements for next generation access technologies (Release 16)*. 3GPP TR 38.913 V16.0.0. July 2020.

[7] 3GPP. *Base Station (BS) radio transmission and reception (Release 16)*. 3GPP TS 38.104 V16.7.0. Apr. 2021.

[8] 3GPP. *Integrated Access and Backhaul (IAB) radio transmission and reception (Release 16)*. 3GPP TS 38.174 V16.3.0. July 2021.

[9] 3GPP. *Study on supporting NR from 52.6 GHz to 71 GHz (Release 17)*. 3GPP TR 38.808 V2.0.0. Mar. 2021.

[10] 3GPP. *System Architecture for the 5G System (Release 17)*. 3GPP TS 23.501 V17.0.0. Mar. 2021.

[11] M. R. Akdeniz, Y. Liu, M. K. Samimi, S. Sun, S. Rangan, T. S. Rappaport and E. Erkip. Millimeter wave channel modeling and cellular capacity evaluation. *IEEE Journal on Selected Areas in Communications* 32.6 (June 2014), 1164–1179.

[12] I. F. Akyildiz, S.-C. Lin and P. Wang. Wireless software-defined networks (W-SDNs) and network function virtualization (NFV) for 5G cellular systems: An overview and qualitative evaluation. *Computer Networks* 93 (2015), 66–79.

[13] J. G. Andrews, T. Bai, M. N. Kulkarni, A. Alkhateeb, A. K. Gupta and R. W. Heath. Modeling and analyzing millimeter wave cellular systems. *IEEE Transactions on Communications* 65.1 (Jan. 2017), 403–430.

[14] J. G. Andrews, S. Buzzi, W. Choi, S. V. Hanly, A. Lozano, A. C. K. Soong and J. C. Zhang. What will 5G be?: *IEEE Journal on Selected Areas in Communications* 32.6 (2014), 1065–1082.

[15] F. Baccelli and X. Zhang. A correlated shadowing model for urban wireless networks. *IEEE Conference on Computer Communications (INFOCOM)*. Apr. 2015, 801–809.

[16] T. Bai and R. W. Heath. Analysis of self-body blocking effects in millimeter wave cellular networks. *Proc. of ASILOMAR*. Nov. 2014, 1921–1925.

[17] T. Bai, R. Vaze and R. W. Heath. Analysis of blockage effects on urban cellular networks. *IEEE Transactions on Wireless Communications* 13.9 (2014), 5070–5083.

[18] L. Bertizzolo, S. D'Oro, L. Ferranti, L. Bonati, E. Demirors, Z. Guan, T. Melodia and S. Pudlewski. SwarmControl: An Automated Distributed Control Framework for Self-Optimizing Drone Networks. *IEEE INFOCOM 2020 - IEEE Conference on Computer Communications*. 2020, 1768–1777.

[19] R. I. Bor-Yaliniz, A. El-Keyi and H. Yanikomeroglu. Efficient 3-D placement of an aerial base station in next generation cellular networks. *IEEE International Conference on Communications (ICC)*. 2016, 1–5.

[20] L. Chen, J. Hang, M. Sandberg, L. Claesson, S. Di Sabatino and H. Wingo. The impacts of building height variations and building packing densities on flow adjustment and city breathability in idealized urban models. *Building and Environment* 118 (June 2017), 344–361.

[21] S. N. Chiu, D. Stoyan, W. S. Kendall and J. Mecke. *Stochastic Geometry and its applications*. Wiley, 2013.

[22] D. R. Cox. *Renewal theory*. Methuen and Co ltd., 1970.

[23] D. Cox and H. Miller. *The theory of stochastic processes*. Wiley, 1965.

[24] D. J. Daley. The Busy Period of the M/GI/$\infty$ Queue. *Queueing Systems: Theory and Applications* 38.2 (2001), 195–204.

[25] Digital trends. *5G network coverage map: Every U.S. city with 5G on Verizon, AT&T, and T-Mobile*. [Online]. Available: `https://www.digitaltrends.com/mobile/5g-availability-map/`. [Accessed on 08/2021]. Feb. 2021.

[26] ETSI NFV. *NFV Release 4 Definition*. ETSI ISG NFV v0.3.0. Feb. 2021.

[27] L. Ferreira, M. Kuipers, C. Rodrigues and L. M. Correia. Characterisation of signal penetration into buildings for GSM and UMTS. *3rd International Symposium on Wireless Communication Systems*. 2006, 63–67.

[28] M. Gapeyenko, I. Bor-Yaliniz, S. Andreev, H. Yanikomeroglu and Y. Koucheryavy. Effects of Blockage in Deploying mmWave Drone Base Stations for 5G Networks and Beyond. *2018 IEEE International Conference on Communications Workshops (ICC Workshops)*. 2018, 1–6.

[29] M. Gapeyenko, D. Moltchanov, S. Andreev and R. W. Heath Jr. Line-of-Sight Probability for mmWave-based UAV Communications in 3D Urban Grid Deployments. *IEEE Transactions on Wireless Communications* (2021).

[30] M. Gapeyenko, V. Petrov, D. Moltchanov, M. R. Akdeniz, S. Andreev, N. Himayat and Y. Koucheryavy. On the Degree of Multi-Connectivity in 5G Millimeter-Wave Cellular Urban Deployments. *IEEE Transactions on Vehicular Technology* 68.2 (2019), 1973–1978.

[31] M. Gapeyenko, V. Petrov, D. Moltchanov, S. Andreev, N. Himayat and Y. Koucheryavy. Flexible and Reliable UAV-Assisted Backhaul Operation in 5G mmWave Cellular Networks. *IEEE Journal on Selected Areas in Communications* 36.11 (2018), 2486–2496.

[32] M. Gapeyenko, A. Samuylov, M. Gerasimenko, D. Moltchanov, S. Singh, M. Akdeniz, E. Aryafar, S. Andreev, N. Himayat and Y. Koucheryavy. Spatially-Consistent Human Body Blockage Modeling: A State Generation Procedure. *IEEE Transactions on Mobile Computing* 19.9 (2020), 2221–2233.

[33] M. Gapeyenko, A. Samuylov, M. Gerasimenko, D. Moltchanov, S. Singh, M. R. Akdeniz, E. Aryafar, N. Himayat, S. Andreev and Y. Koucheryavy. On the Temporal Effects of Mobile Blockers in Urban Millimeter-Wave Cellu-

lar Scenarios. *IEEE Transactions on Vehicular Technology* 66.11 (2017), 10124–10138.

[34] M. Gapeyenko, A. Samuylov, M. Gerasimenko, D. Moltchanov, S. Singh, E. Aryafar, S. Yeh, N. Himayat, S. Andreev and Y. Koucheryavy. Analysis of human-body blockage in urban millimeter-wave cellular communications. *2016 IEEE International Conference on Communications (ICC)*. 2016, 1–7.

[35] M. Gapeyenko, V. Petrov, D. Moltchanov, S. Andreev, Y. Koucheryavy, M. Valkama, M. R. Akdeniz and N. Himayat. An Analytical Representation of the 3GPP 3D Channel Model Parameters for MmWave Bands. *Proceedings of the 2nd ACM Workshop on Millimeter Wave Networks and Sensing Systems*. 2018, 33–38.

[36] M. Gapeyenko, V. Petrov, D. Moltchanov, S.-P. Yeh, N. Himayat and S. Andreev. Comparing Capacity Gains of Static and UAV-Based Millimeter-Wave Relays in Clustered Deployments. *IEEE International Conference on Communications Workshops (ICC Workshops)*. 2020, 1–7.

[37] M. Gerasimenko, D. Moltchanov, M. Gapeyenko, S. Andreev and Y. Koucheryavy. Capacity of Multiconnectivity mmWave Systems With Dynamic Blockage and Directional Antennas. *IEEE Transactions on Vehicular Technology* 68.4 (2019), 3534–3549.

[38] A. Ghosh, T. A. Thomas, M. C. Cudak, R. Ratasuk, P. Moorut, F. W. Vook, T. S. Rappaport, G. R. MacCartney, S. Sun and S. Nie. Millimeter-wave enhanced local area systems: A high-data-rate approach for future wireless networks. *IEEE Journal on Selected Areas in Communications* 32.6 (June 2014), 1152–1163.

[39] M. Giordani, M. Mezzavilla, S. Rangan and M. Zorzi. An efficient uplink multi-connectivity scheme for 5G millimeter-wave control plane applications. *IEEE Transactions on Wireless Communications* 17.10 (2018), 6806–6821.

[40] GSMA. *The 5G guide: A reference for operators*. White paper [Online]. Available: `https://www.gsma.com/wp-content/uploads/2019/04/The-5G-Guide_GSMA_2019_04_29_compressed.pdf`. Apr. 2019.

[41] K. Haneda et al. 5G 3GPP-like channel models for outdoor urban microcellular and macrocellular environments. *IEEE 83rd Vehicular Technology Conference (VTC Spring)*. May 2016, 1–7.

[42] M. Heino, C. Icheln and K. Haneda. Self-user shadowing effects of millimeter-wave mobile phone antennas in a browsing mode. *13th European Conference on Antennas and Propagation (EuCAP)*. 2019, 1–5.

[43] H. Hellaoui, O. Bekkouche, M. Bagaa and T. Taleb. Aerial control system for spectrum efficiency in UAV-to-cellular communications. *IEEE Communications Magazine* 56.10 (2018), 108–113.

[44] H. Holma, A. Toskala and T. Nakamura. *5G Technology: 3GPP New Radio*. Wiley, 2020.

[45] ITU-R. *Technical feasibility of IMT in bands above 6 GHz*. Report ITU-R M.2376-0. July 2015.

[46] ITU-R. *Minimum requirements related to technical performance for IMT-2020 radio interface(s)*. Recommendation ITU-R M.2410-0. Nov. 2017.

[47] ITU-R. *Detailed specifications of the terrestrial radio interfaces of International Mobile Telecommunications-Advanced (IMT-Advanced)*. Recommendation ITU-R M.2012-4. Nov. 2019.

[48] ITU-R. *Detailed specifications of the terrestrial radio interfaces of International Mobile Telecommunications-2000 (IMT-2000)*. Recommendation ITU-R M.1457-15. Oct. 2020.

[49] ITU-R. *Detailed specifications of the terrestrial radio interfaces of International Mobile Telecommunications-2020 (IMT-2020)*. Recommendation ITU-R M.2150-0. Feb. 2021.

[50] M. Jacob, S. Priebe, T. Kurner, M. Peter, M. Wisotzki, R. Felbecker and W. Keusgen. Fundamental analyses of 60 GHz human blockage. *7th European Conference on Antennas and Propagation (EuCAP)* (Apr. 2013), 117–121.

[51] K. Kairbek. TCP Performance in 5G mmWave Systems with Dynamic Blockage. *Master's theses* (2018).

[52] E. Kalantari, M. Z. Shakir, H. Yanikomeroglu and A. Yongacoglu. Backhaul-aware robust 3D drone placement in 5G+ wireless networks. *IEEE International Conference on Communications Workshops (ICC Workshops)*. 2017, 109–114.

[53] P. Kela, M. Costa, J. Turkka, M. Koivisto, J. Werner, A. Hakkarainen, M. Valkama, R. Jantti and K. Leppanen. Location Based Beamforming in 5G Ultra-Dense Networks. *2016 IEEE 84th Vehicular Technology Conference (VTC-Fall)*. 2016, 1–7.

[54] A. A. Khuwaja, Y. Chen, N. Zhao, M. Alouini and P. Dobbins. A Survey of Channel Modeling for UAV Communications. *IEEE Communications Surveys & Tutorials* 20.4 (Fourthquarter 2018), 2804–2821.

[55] L. Kleinrock. *Theory, Volume 1, Queueing Systems*. USA: Wiley-Interscience, 1975.

[56] R. Li, Z. Wei, L. Yang, D. W. Kwan Ng, N. Yang, J. Yuan and J. An. Joint trajectory and resource allocation design for UAV communication systems. *IEEE Globecom Workshops (GC Wkshps)*. 2018, 1–6.

[57] T. Liu, H. Guo, C. Danilov and K. Nahrstedt. A privacy-preserving data collection and processing framework for third-party UAV services. *IEEE 19th International Conference on Trust, Security and Privacy in Computing and Communications (TrustCom)*. 2020, 683–690.

[58] G. R. MacCartney, S. Deng, S. Sun and T. S. Rappaport. Millimeter-wave human blockage at 73 GHz with a simple double knife-edge diffraction model and extension for directional antennas. *IEEE 84th Vehicular Technology Conference (VTC-Fall)*. 2016, 1–6.

[59] G. R. MacCartney, T. S. Rappaport and S. Rangan. Rapid fading due to human blockage in pedestrian crowds at 5G millimeter-wave frequencies. *IEEE Global Communications Conference (Globecom)*. 2017, 1–7.

[60] G. R. MacCartney and T. S. Rappaport. 73 GHz millimeter wave propagation measurements for outdoor urban mobile and backhaul communications in New York City. *2014 IEEE International Conference on Communications (ICC)*. 2014, 4862–4867.

[61] G. MacCartney. Millimeter-wave base station diversity and human blockage in dense urban environments for coordinated multipoint (CoMP) Applications. *Dissertation* (2018).

[62] À. O. Martínez, J. Ø. Nielsen, E. De Carvalho and P. Popovski. An Experimental Study of Massive MIMO Properties in 5G Scenarios. *IEEE Transactions on Antennas and Propagation* 66.12 (2018), 7206–7215.

[63] METIS. *Updated scenarios, requirements and KPIs for 5G mobile and wireless system with recommendations for future investigations*. Deliverable D1.5. Apr. 2015.

[64] M. Mezzavilla, M. Zhang, M. Polese, R. Ford, S. Dutta, S. Rangan and M. Zorzi. End-to-end simulation of 5G mmWave networks. *IEEE Communications Surveys Tutorials* 20.3 (2018), 2237–2263.

[65] M. Mozaffari, W. Saad, M. Bennis and M. Debbah. Efficient deployment of multiple unmanned aerial vehicles for optimal wireless coverage. *IEEE Communications Letters* 20.8 (2016), 1647–1650.

[66] M. Mozaffari, W. Saad, M. Bennis, Y. Nam and M. Debbah. A tutorial on UAVs for wireless networks: Applications, challenges, and open problems. *IEEE Communications Surveys Tutorials* 21.3 (2019), 2334–2360.

[67] G. Newell. The M/G/$\infty$ Queue. *SIAM Journal on Applied Mathematics* 14.1 (1966), 86–88.

[68] T. Q. K. Nguyen, M. S. Miah, L. Lizzi, K. Haneda and F. Ferrero. Experimental Evaluation of User's Finger Effects on a 5G Terminal Antenna Array at 26 GHz. *IEEE Antennas and Wireless Propagation Letters* 19.6 (2020), 892–896.

[69] Nokia et al. *5G channel model for bands up to 100 GHz*. 5GCM white paper available at: `http://www.5gworkshops.com`. Oct. 2016.

[70] E. Ogawa and A. Satoh. Propagation path visibility estimation for radio local distribution systems in built-Up areas. *IEEE Transactions on Communications* 34.7 (July 1986), 721–724.

[71] C. L. Ogden, C. D. Fryar, M. D. Carroll and K. M. Flegal. Mean body weight, height, and body mass index, United States 1960–2002. *Centers for Disease control and prevention* 347 (Oct. 2004).

[72] D. Öhmann, A. Awada, I. Viering, M. Simsek and G. P. Fettweis. Achieving high availability in wireless networks by inter-frequency multi-connectivity. *IEEE International Conference on Communications (ICC)*. 2016, 1–7.

[73] D. Öhmann, A. Awada, I. Viering, M. Simsek and G. P. Fettweis. Impact of mobility on the reliability performance of 5G multi-connectivity architectures. *IEEE Wireless Communications and Networking Conference (WCNC)*. Mar. 2017, 1–6.

[74] A. Osseiran, F. Boccardi, V. Braun, K. Kusume, P. Marsch, M. Maternia, O. Queseth, M. Schellmann, H. Schotten, H. Taoka, H. Tullberg, M. A. Uusitalo, B. Timus and M. Fallgren. Scenarios for 5G mobile and wireless communications: the vision of the METIS project. *IEEE Communications Magazine* 52.5 (2014), 26–35.

[75] V. Petrov, D. Moltchanov, S. Andreev and R. W. Heath. Analysis of intelligent vehicular relaying in urban 5G+ millimeter-wave cellular deployments. *IEEE Global Communications Conference (GLOBECOM)*. 2019, 1–6.

[76] V. Petrov, D. Solomitckii, A. Samuylov, M. A. Lema, M. Gapeyenko, D. Moltchanov, S. Andreev, V. Naumov, K. Samouylov, M. Dohler and Y. Koucheryavy. Dynamic multi-connectivity performance in ultra-dense urban mmWave deployments. *IEEE Journal on Selected Areas in Communications* 35.9 (2017), 2038–2055.

[77] V. Petrov, M. Gapeyenko, D. Moltchanov, S. Andreev and R. W. Heath. Hover or Perch: Comparing Capacity of Airborne and Landed Millimeter-Wave UAV Cells. *IEEE Wireless Communications Letters* 9.12 (2020), 2059–2063.

[78] V. Petrov, D. Moltchanov, J. M. Jornet and Y. Koucheryavy. Exploiting Multipath Terahertz Communications for Physical Layer Security in Beyond 5G Networks. *IEEE INFOCOM 2019 - IEEE Conference on Computer Communications Workshops (INFOCOM WKSHPS)*. 2019, 865–872.

[79] Z. Pi and F. Khan. An introduction to millimeter-wave mobile broadband systems. *IEEE Communications Magazine* 49.6 (2011), 101–107.

[80] M. Polese, L. Bertizzolo, L. Bonati, A. Gosain and T. Melodia. An Experimental MmWave Channel Model for UAV-to-UAV Communications. *Proceedings of the 4th ACM Workshop on Millimeter-Wave Networks and Sensing Systems*. 2020.

[81] M. Polese, M. Giordani, T. Zugno, A. Roy, S. Goyal, D. Castor and M. Zorzi. Integrated Access and Backhaul in 5G mmWave Networks: Potential and Challenges. *IEEE Communications Magazine* 58.3 (2020), 62–68.

[82] S. Rajagopal, S. Abu-Surra and M. Malmirchegini. Channel feasibility for outdoor non-line-of-sight mmWave mobile communication. *IEEE Vehicular Technology Conference (VTC Fall)*. 2012, 1–6.

[83] S. Rangan, T. S. Rappaport and E. Erkip. Millimeter-wave cellular wireless networks: Potentials and challenges. *Proceedings of the IEEE* 102.3 (2014), 366–385.

[84] T. S. Rappaport, G. R. MacCartney, M. K. Samimi and S. Sun. Wideband millimeter-wave propagation measurements and channel models for future wireless communication system design. *IEEE Transactions on Communications* 63.9 (2015), 3029–3056.

[85] T. S. Rappaport, Y. Xing, G. R. MacCartney, A. F. Molisch, E. Mellios and J. Zhang. Overview of millimeter wave communications for fifth-generation (5G) wireless networks - with a focus on propagation models. *IEEE Transactions on Antennas and Propagation* 65.12 (2017), 6213–6230.

[86] T. S. Rappaport, F. Gutierrez, E. Ben-Dor, J. N. Murdock, Y. Qiao and J. I. Tamir. Broadband millimeter-wave propagation measurements and models using adaptive-beam antennas for outdoor urban cellular communications. *IEEE Transactions on Antennas and Propagation* 61.4 (Dec. 2013), 1850–1859.

[87] A. Ravanshid et al. Multi-connectivity functional architectures in 5G. *Proc. of IEEE International Conference on Communications Workshops (ICC)*. May 2016, 187–192.

[88] A. Ravanshid, P. Rost, D. S. Michalopoulos, V. V. Phan, H. Bakker, D. Aziz, S. Tayade, H. D. Schotten, S. Wong and O. Holland. Multi-connectivity functional architectures in 5G. *2016 IEEE International Conference on Communications Workshops (ICC)*. 2016, 187–192.

[89] M. Rebato, L. Resteghini, C. Mazzucco and M. Zorzi. Study of Realistic Antenna Patterns in 5G mmWave Cellular Scenarios. *2018 IEEE International Conference on Communications (ICC)*. 2018, 1–6.

[90] C. Saha, M. Afshang and H. S. Dhillon. Integrated mmWave Access and Backhaul in 5G: Bandwidth Partitioning and Downlink Analysis. *IEEE International Conference on Communications (ICC)*. 2018, 1–6.

[91] A. Saleh and R. Valenzuela. A Statistical Model for Indoor Multipath Propagation. *IEEE Journal on Selected Areas in Communications* 5.2 (1987), 128–137.

[92] M. K. Samimi, T. S. Rappaport and G. R. MacCartney. Probabilistic Omnidirectional Path Loss Models for Millimeter-Wave Outdoor Communications. *IEEE Wireless Communications Letters* 4.4 (2015), 357–360.

[93] A. Samuylov, M. Gapeyenko, D. Moltchanov, M. Gerasimenko, S. Singh, N. Himayat, S. Andreev and Y. Koucheryavy. Characterizing spatial correlation of blockage statistics in urban mmWave systems. *IEEE Global Communications Workshops (GLOBECOM Wkshps)*. Dec. 2016, 1–7.

[94] S. Saunders, C. Tzaras and B. Evans. Physical–statistical methods for determining state transition probabilities in mobile–satellite channel models. *International Journal of Satellite Communications* 19.3 (May 2001), 207–222.

[95] S. Schubert, S. Grossman-Clarke and A. Martilli. A double-canyon radiation scheme for multi-layer urban canopy models. *Boundary-Layer Meteorology* 145.3 (Dec. 2012), 439–468.

[96] M. Shafi, A. F. Molisch, P. J. Smith, T. Haustein, P. Zhu, P. De Silva, F. Tufvesson, A. Benjebbour and G. Wunder. 5G: A Tutorial Overview of Standards, Trials, Challenges, Deployment, and Practice. *IEEE Journal on Selected Areas in Communications* 35.6 (2017), 1201–1221.

[97] H. Shakhatreh, A. Khreishah, J. Chakareski, H. B. Salameh and I. Khalil. On the continuous coverage problem for a swarm of UAVs. *IEEE 37th Sarnoff Symposium*. 2016, 130–135.

[98] H. Shakhatreh, A. H. Sawalmeh, A. Al-Fuqaha, Z. Dou, E. Almaita, I. Khalil, N. S. Othman, A. Khreishah and M. Guizani. Unmanned aerial vehicles (UAVs): A survey on civil applications and key research challenges. *IEEE Access* 7 (2019), 48572–48634.

[99] M. U. Sheikh, K. Ruttik, R. Jäntti and J. Hämäläinen. Blockage and Ray Tracing Propagation Model in 3GPP Specified Industrial Environment. *International Conference on Information Networking (ICOIN)*. 2021, 397–402.

[100] C. Slezak, V. Semkin, S. Andreev, Y. Koucheryavy and S. Rangan. Empirical effects of dynamic human-body blockage in 60 GHz communications. *IEEE Communications Magazine* 56.12 (2018), 60–66.

[101] Q. Spencer, M. Rice, B. Jeffs and M. Jensen. A statistical model for angle of arrival in indoor multipath propagation. *IEEE 47th Vehicular Technology Conference. Technology in Motion*. Vol. 3. 1997, 1415–1419 vol.3.

[102] S. Sur, X. Zhang, P. Ramanathan and R. Chandra. BeamSpy: Enabling Robust 60 GHz Links Under Blockage. *13th USENIX Symposium on Networked Systems Design and Implementation (NSDI 16)*. 2016, 193–206.

[103] H. Tataria, K. Haneda, A. F. Molisch, M. Shafi and F. Tufvesson. Standardization of Propagation Models for Terrestrial Cellular Systems: A Historical Perspective. *International Journal of Wireless Information Networks* 28 (2021), 20–44.

[104] F. B. Tesema, A. Awada, I. Viering, M. Simsek and G. Fettweis. Multiconnectivity for mobility robustness in standalone 5G ultra dense networks with intrafrequency cloud radio access. *Wireless Communications and Mobile Computing* (Jan. 2017), 1–17.

[105] Thales group. *Introducing 5G technology and networks (speed, use cases and rollout)*. [Online]. Available: `https://www.thalesgroup.com/en/markets/digital-identity-and-security/mobile/inspired/5G` [Accessed on 08/2021]. Mar. 2021.

[106] A. Trotta, M. D. Felice, F. Montori, K. R. Chowdhury and L. Bononi. Joint coverage, connectivity, and charging strategies for distributed UAV networks. *IEEE Transactions on Robotics* 34.4 (2018), 883–900.

[107] G. Turin, F. Clapp, T. Johnston, S. Fine and D. Lavry. A statistical model of urban multipath propagation. *IEEE Transactions on Vehicular Technology* 21.1 (1972), 1–9.

[108] U. T. Virk and K. Haneda. Modeling Human Blockage at 5G Millimeter-Wave Frequencies. *IEEE Transactions on Antennas and Propagation* 68.3 (2020), 2256–2266.

[109] D. Wisely, N. Wang and R. Tafazolli. Capacity and costs for 5G networks in dense urban areas. *IET Communications* 12 (19 Dec. 2018), 2502–2510.

[110] Q. Wu, Y. Zeng and R. Zhang. Joint trajectory and communication design for multi-UAV enabled wireless networks. *IEEE Transactions on Wireless Communications* 17.3 (2018), 2109–2121.

[111] T. Wu, T. S. Rappaport and C. M. Collins. The human body and millimeter-wave wireless communication systems: Interactions and implications. *IEEE International Conference on Communications (ICC)*. 2015, 2423–2429.

[112] W. Xia, M. Polese, M. Mezzavilla, G. Loianno, S. Rangan and M. Zorzi. Millimeter wave remote UAV control and communications for public safety scenarios. *2019 16th Annual IEEE International Conference on Sensing, Communication, and Networking (SECON)*. 2019, 1–7.

[113] Y. Zeng, J. Lyu and R. Zhang. Cellular-connected UAV: Potential, challenges, and promising technologies. *IEEE Wireless Communications* 26.1 (2019), 120–127.

[114] Y. Zeng, J. Xu and R. Zhang. Rotary-wing UAV enabled wireless network: Trajectory design and resource allocation. *IEEE Global Communications Conference (GLOBECOM)*. 2018, 1–6.

[115] Y. Zeng, J. Xu and R. Zhang. Energy minimization for wireless communication with rotary-wing UAV. *IEEE Transactions on Wireless Communications* 18.4 (2019), 2329–2345.

[116] Y. Zeng and R. Zhang. Energy-efficient UAV communication with trajectory optimization. *IEEE Transactions on Wireless Communications* 16.6 (2017), 3747–3760.

[117] L. Zhang, H. Zhao, S. Hou, Z. Zhao, H. Xu, X. Wu, Q. Wu and R. Zhang. A survey on 5G millimeter wave communications for UAV-assisted wireless networks. *IEEE Access* 7 (2019), 117460–117504.

[118] H. Zhao, R. Mayzus, S. Sun, M. Samimi, J. K. Schulz, Y. Azar, K. Wang, G. N. Wong, F. Gutierrez and T. S. Rappaport. 28 GHz millimeter wave cellular communication measurements for reflection and penetration loss in and around buildings in New York city. *IEEE International Conference on Communications (ICC)*. 2013, 5163–5167.

# PUBLICATIONS

# PUBLICATION I

**Analysis of human-body blockage in urban millimeter-wave cellular communications**

M. Gapeyenko, A. Samuylov, M. Gerasimenko, D. Moltchanov, S. Singh, E. Aryafar, S. Yeh, N. Himayat, S. Andreev and Y. Koucheryavy

*2016 IEEE International Conference on Communications (ICC)*2016, 1–7

# Analysis of Human-Body Blockage in Urban Millimeter-Wave Cellular Communications

Margarita Gapeyenko†, Andrey Samuylov†, Mikhail Gerasimenko†, Dmitri Moltchanov†, Sarabjot Singh⋆, Ehsan Aryafar⋆, Shu-ping Yeh⋆, Nageen Himayat⋆, Sergey Andreev†, and Yevgeni Koucheryavy†
†W.I.N.T.E.R. Group, Tampere University of Technology, Tampere, Finland
⋆Intel Corporation, Santa Clara, CA, USA.

***Abstract*—The presence of a line-of-sight (LoS) component is of particular importance for extremely high frequency (EHF) systems, including millimeter-wave (mmWave) communications technology, as it helps differentiate between acceptable and poor wireless links. While these emerging systems are expected to be deployed outdoors as a part of the fifth-generation (5G) mobile technology, thus delivering high-rate connectivity in crowded urban environments, the presence of obstacles such as humans will become a crucial factor that affects the existence of a LoS link. In this paper, we propose a novel model for analyzing human-body blockage in cellular mmWave systems. We model the human body locations as three-dimensional cylinders with random positions, height, and radius as well as apply the renewal process theory to characterize metrics related to receiver blockage. Finally, we demonstrate how our model can be employed to optimize the transmitter location across various deployment parameters and confirm our findings with detailed mmWave ray-launching simulations.**

***Index Terms*—Fifth-generation networks; cellular mmWave communications; urban environment; human-body blockage.**

## I. Introduction and motivation

The use of extremely high frequency (EHF) band, also known as millimeter-wave (mmWave), as a part of fifth-generation (5G) ecosystem brings along its unique specifics to the wireless system designers. Given that electromagnetic waves cannot travel around obstacles with the dimensions exceeding their wavelength, numerous objects in the wireless channel act as natural blockers. According to the recent empirical and theoretical studies, even at the frequencies that are much lower than the EHF band, around 60%-85% of useful power comes from the line-of-sight (LoS) propagation path [1]. Further, employing directional antennas for future mmWave cellular systems has been demonstrated to provide reliable coverage on the order of up to tens of meters, thus making them suitable for extremely high-rate mobile user access in outdoor scenarios including streets, intersections, and squares [2]. In these crowded urban environments, human bodies around the receiver could become the major factor to impact the blockage of the LoS component.

In this paper, we propose a new analytical model for characterizing LoS mmWave communications in the presence of human-body blockage. The proposed model represents humans as cylinders with arbitrarily distributed heights and bases of arbitrary radii, whose centers follow the Matern hard-core process in two dimensions. Coupling the tools from stochastic geometry and renewal processes, we estimate the total blockage probability of the receiver having a certain length and located at a particular distance from the transmitter. We also consider infinitesimal (that is, extremely small) receiver – approximating it by a point – and show that the corresponding modeling complexity can be reduced significantly. We also calibrate our proposed mathematical model with detailed mmWave ray-launching simulations and confirm that the former allows to accurately predict the presence of a LoS path. Finally, we demonstrate how the model at hand can be utilized by the system designers to decide upon the best possible placement of the mmWave transmitter in crowded outdoor environments.

The major claims of our paper are: (i) we use the ray-launching simulator to show a considerable gap in LoS and non-LoS path loss; (ii) our proposed model captures all the key characteristics of the considered environment, including the random height and width of blockers, different heights of transmitter (Tx) and receiver (Rx), as well as variable distance between them. The rest of this text is organized as follows. The overview of the related work is provided in Section II. We introduce our system model and the corresponding analytical framework in Section III. This proposed model is calibrated with the ray-launching simulations in Section IV. We also discuss how to optimize the mmWave Tx placements in the same section. Conclusions and future work are highlighted in the last section.

## II. Background and related work

The aspect of the LoS blockage has been addressed in a number of previous papers. These studies, however, vary in the range of environmental characteristics taken into account and the applicability of the respective scenarios. In particular, the early models were developed for microwave systems. In [3], the authors addressed the problem of LoS blockage in conventional cellular networks, where the buildings block the direct propagation path. This model included dimensions of buildings and the distance between the Tx and Rx. The authors continued their efforts in [4], where their proposed model was extended to take into account the height of the Tx and Rx. The receiver size was assumed to be infinitesimally-small and the blockers (those high enough to block LoS) were distributed uniformly, without considering alternative deployment patterns. The results of [4] were then used by [5] to derive the probability of blockage for mmWave wearable networks.

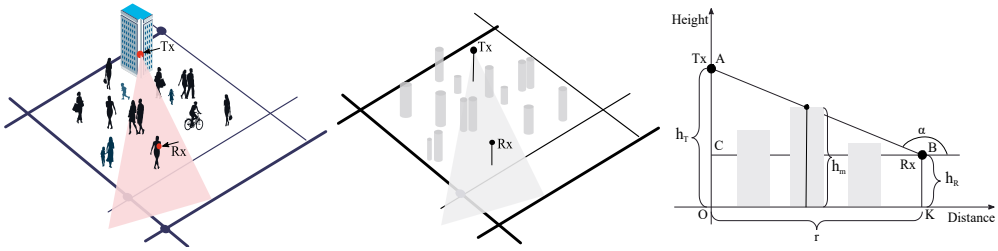


(a) (b) (c)

Fig. 1. The considered scenario for analytical modeling.

This model included the distance between the Tx and Rx, as well as the dimensions of a human body, where wearable devices have been deployed. Further, the statistical 3GPP urban outdoor micro-cellular model [6] has been developed to evaluate the probability of LoS as a function of distance only, thus providing a first-order approximation for the LoS analysis. The comparison between different LoS models for cellular systems, all having different levels of detail, has been completed in [7].

Compared to microwave wireless systems, cellular mmWave communications are expected to operate over much shorter distances in crowded urban environments [2]. Since the height of the Tx would then need to be much lower, humans of various heights are becoming to act as blockers. Hence, in addition to the heights of the Rx and Tx, the distance between them, and the spatial dimensions of blocking objects, we also have to take into account the random heights of humans. Further, due to much smaller distances between the Tx and Rx, and accounting for the possible antenna arrays at the Rx [2], the linear dimensions of the receiver may be non-negligible in practice. In a number of studies [8], an empirically-estimated mmWave LoS probability has been assumed [2]. This empirical LoS probability is a function of the Tx-Rx distance only and does not take into account the aforementioned important system parameters.

In contrast to past studies, this paper takes into account the key parameters of interest that affect the resulting throughput of the mmWave cellular system. Particularly, the heights of the Tx and Rx, the distance between them, the random width and the height of blockers as well as human user density across the landscape are taken into account. Further, our proposed model allows for a number of useful extensions as well as simplifications, including those that lead to closed-form expressions for the LoS probability.

## III. Proposed Analytical Framework

### A. Spatial model

Consider the scenario illustrated in Fig. 1(a, b). There is a Tx located at a certain height $h_T$ above the ground and a Rx located at the height $h_R$. The base of the Rx is at the distance $r$ from the base of the Tx. The potential blockers, humans, are distributed over the landscape. We model the blockers as cylinders [9] with a certain height, $H$, and the base diameter of $D$. Both $D$ and $H$ are random variables (RVs). It is known that the distribution of the height for men and women is Normal with the mean and the standard deviation provided in [10]. Following [10], the mixture of users is closely approximated by the Normal distribution $H \sim N(\mu_H, \sigma_H)$. Generally, any distribution could be used to provide a result based on the current methodology. The RV $D$ is assumed to be uniformly-distributed between $d_{min}$ and $d_{max}$. The centers of cylinder bases follow a Matern hard-core point process on the plane with the intensity $\lambda_I$. The length of the Rx is assumed to be $l$m. In summary, the main parameters and the description of employed notation are given in Table I. In what follows, our main metric of interest is the probability of blockage for both the non-infinitesimal and infinitesimal receiver.

### B. Blockage probability

To represent the centers of blockers on the landscape, we have employed the Matern hard-core process ensuring that the locations of blockers do not overlap. Using the results of [11], the Matern process can be replaced by the equivalent Poisson process for a wide range of intensities $\lambda_I$. Further, observe that for different values of $h_T$, $h_R$, and the distribution of the blocker heights $H$, not all the blockers affect the LoS between the Tx and Rx. The number of blockers should increase as the $x$-coordinate grows from $O$ to $r$, as in Fig. 1(c). The spatially-varying intensity of centers of blockers along the radial lines that may potentially affect the LoS between the Tx and Rx is given by

$$\lambda(x) = \lambda_I g(x), \;\; g(x) = Pr\{H > h_m(x)\}\, x \in (0, r), \quad (1)$$

where $h_m(x)$ is a function describing the distance between the line $AB$ and $OX$ at $x$.

Note that $h_m(x)$ is linear, $h_m(x) = ax + b$, where $a$ is the tangent of $h_m(x)$ with respect to the positive direction of $OX$, while $b$ is the height of a function at $x = 0$. We thus have

$$h_m(x) = -\frac{h_T - h_R}{r} x + h_T, \;\; x \in (0, r). \quad (2)$$

The probability $g(x) = Pr\{H > h_m(x)\}$ for each $x$ is a complementary cumulative distribution function (CCDF) of $H$. Since $H \sim N(\mu_H, \sigma_H)$, we have

$$g(x) = 1 - \frac{1}{2}\left[1 + \text{erf}\left(\frac{h_m(x) - \mu_H}{\sigma_H \sqrt{2}}\right)\right], \quad (3)$$

where erf$(\cdot)$ is the error function.

To determine the effective density of blockers at any separation distance $x$, the original homogeneous Poisson process is thinned with the probability $g(x)$. The resulting process is non-homogeneous, but still Poisson, with spatially-varying intensity along the radial lines, $\lambda(x)$ [12]. The intensity $\lambda(x)$ is minimal at $x = 0$ and increases non-linearly as $x$ grows. Consider now the projection of the blocker centers along the radial lines, represented by points on the circumference of the circle with radius $r$ and center at Tx, see Fig. 3. It is easy to prove that the process of projections on the circumference is homogeneous Poisson, as it has a Poisson distribution of projections in any bounded arc that depends only on the length of an arc and satisfies the independence property of the Poisson process.

To establish the intensity of blocker centers at the circumference, consider the arc with length $l_{arc}$ as illustrated in Fig. 3. The mean number of points, $E[N_B]$, in the sector $ATxB$ is

$$E[N_B] = \int_0^r \lambda(x) x \frac{l_{arc}}{r} dx, \tag{4}$$

leading to the intensity of blockers at the circumference as

$$\mu = \frac{1}{l_{arc}} \int_0^r \lambda(x) x \frac{l_{arc}}{r} dx = \frac{\lambda_I}{r} \int_0^r x g(x) dx, \tag{5}$$

where $g(x)$ is given in (3). Although this integral cannot be expressed in elementary functions due to the error function in $g(x)$, it can be easily computed numerically with any required accuracy.

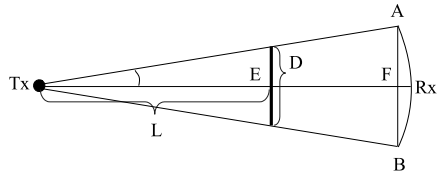


Fig. 2. The top view of the scenario of interest.

To this end, we have characterized the point process of the centers of blockers. Further, the distribution of a "shadow" created by an individual blocker at circumference is given. Consider Fig. 2, which shows the top view of our scenario. Observe that for $r >> D$, where $r$ is the distance from the base of Tx to Rx, we could replace the arc $ARxB$ by a chord $AFB$. From the geometric properties, we arrive at $W$, that is, a RV denoting the length of a shadow as

$$W = \frac{rD}{L}, \tag{6}$$

where $L$ and $D$ are the RVs denoting the distance from the Tx to a blocker and the width of a blocker, respectively. Recalling the principles of linear transformation of RVs [13], the numerator of (6) reads as

$$f_{rD}(x) = \frac{1}{r(d_{\max} - d_{\min})}, \;\; x \in (r d_{\min}, r d_{\max}). \tag{7}$$

Consider now the denominator of (6). Recall that the intensity of blockers increases along the radial lines according to (1). Therefore, the probability to have a blocker increases as we move from $x = 0$ to $x = r$. The density to have a blocker at $x$ conditioned on the event that there is a blocker shall increase proportionally to $g(x)$, as obtained in (3), and the only aspect we have to determine calculating the probability density function (pdf) of $L$ is the normalization constant, such that the area under $f_L(x)$ over $x \in (0, r)$ is exactly 1. It can be found as

$$N = \int_0^r \left(1 - \frac{1}{2}\left[1 + \text{erf}\left(\frac{h_m(x) - \mu_H}{\sigma_H \sqrt{2}}\right)\right]\right) dx, \tag{8}$$

and normalized to obtain

$$f_L(x) = \frac{g(x)}{N}, \;\; x \in (0, r). \tag{9}$$

Now, to determine the pdf of the shadow, we have to find the ratio between the RV $rD$ and $L$, whose densities are given by (7) and (9). Since these RVs are independent, the ratio is formally offered by [13]

$$f_W(y) = \begin{cases} \int_{\frac{r d_{min}}{y}}^{r} x f_{rD}(yx) f_L(x) dx, & \text{for } d_{min} < y < d_{max} \\ \int_{\frac{r d_{min}}{y}}^{\frac{r d_{max}}{y}} x f_{rD}(yx) f_L(x) dx, & \text{for } y > d_{max}. \end{cases} \tag{10}$$

The integral (10) cannot be solved in elementary functions due to the density of $L$ in (9). However, one can compute the distribution of $W$ numerically.

### C. Non-infinitesimal receiver

Consider now the Rx of length $l$. In practice, it corresponds to when more than a single antenna is used at the user equipment and/or the distance between the bases of the Tx and Rx, $r$, is relatively small. In this case, we have to take into account the length of the Rx explicitly and the task at hand reduces to expressing the probability that an arc of a constant non-zero width $l$ is fully covered by arcs of random length, whose center points follow a Poisson process with the intensity $\mu$ as found in (4) and with the length pdf $f_W(x)$ provided by (10).

Consider the projections of blockers on the circumference as illustrated in Fig. 3. The widths of those projections are independent and identically distributed (i.i.d) RVs with the CDF $F_W(x) = \int_{-\infty}^{x} f_W(x) dx$ and the expected value $E[W] = \int_{-\infty}^{\infty} x f_W(x) dx$, where $f_W(x)$ is obtained from (10). It is easy to show that not only the projections of the centers of blockers, but also their left- and right-hand side projections, form a stationary Poisson process on the line with the intensity $\mu$. The superposed process of all projections forms a renewal process with the alternating blocked and unblocked parts. An arbitrary point on the line is considered blocked, if it belongs to one of the blocked intervals. The question of blocking is then formulated as the probability of blocking this interval by

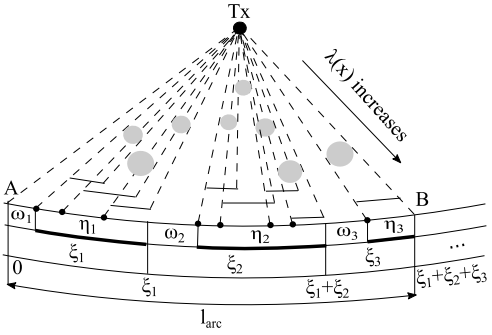


Fig. 3. Projections of blocker widths on the circumference.

the renewal process. An arc of length $l$ is said to be blocked, if all the points of this arc are blocked.

Let $\omega_j$ $\eta_j$, $j = 1, 2, \dots$ , denote the length of the unblocked and blocked intervals respectively, and define $\xi_j = \omega_j + \eta_j$. Points 0, $\xi_1$, $\xi_1+\xi_2$, and $\xi_1+\xi_2+\xi_3$ are the renewal moments that form the renewal process. The density of this process is [14], [15]

$$f(x) = \mu F_W(x) \exp\left(-\mu \int_0^l [1 - F_W(y)]dy\right). \quad (11)$$

Let $f_\xi(t)$ be the density function of $\xi_j$, $j = 1, 2, \dots$ Functions $f_\xi(x)$ and $f(x)$ are related to each other via the renewal equation as [14], [15]

$$f(x) = f_\xi(x) + \int_0^l f_\xi(x-y) f(y) dy. \quad (12)$$

The length of the unblocked part $\omega_j$ follows the exponential distribution with the parameter $\mu$, $F_\omega(x) = 1 - e^{-\mu x}$, with the mean $E[\omega] = 1/\mu$ [15]. This can be verified by observing that the left-hand sides of the individual shadows follow a Poisson process with the intensity $\mu$. Hence, the distance from the end of the blocked part, considered as an arbitrary point, to the starting point of the next blocked interval is distributed exponentially. Let $F_\eta(x)$ and $F_\xi(x)$ be the CDFs of the length of the blocked intervals $\eta_j$, $j = 1, 2, \dots$, and the joint blocked/unblocked intervals, $\xi_j$, respectively, with the means $E[\eta]$ and $E[\xi]$. Further, let $F^*_\eta(s)$ and $F^*_\xi(s)$ be the corresponding Laplace-Stieltjes transforms (LSTs). For the joint interval $\xi_j$, we have

$$F^*_\xi(s) = F^*_\eta(s) F^*_\omega(s) = \mu \frac{F^*_\eta(s)}{\mu + s}, \quad (13)$$

which can be solved for $F_\eta(x)$ in the RV domain as

$$F_\eta(x) = F_\xi(x) + \frac{f_\xi(x)}{\mu}. \quad (14)$$

Observe that the renewal density $f(x)$ is $f(x) = 1/E[\xi]$, when $l \to \infty$. From (11), we see that it is also equal to $f(x) = \mu \exp(-\mu E[W])$, where $E[W]$ is the mean length of the blocked intervals. Consequently,

$$E[\xi] = \frac{1}{\mu} \exp(\mu E[W]). \quad (15)$$

Then, $E[\eta]$ can be established as

$$E[\eta] = \int_0^\infty [1 - F_\eta(x)]dx = \\ = \int_0^\infty \left(1 - F_\xi(x) - \frac{f_\xi(x)}{\mu}\right) dx = E[\xi] - \frac{1}{\mu}. \quad (16)$$

Substituting (15) into (16), we arrive at

$$E[\eta] = \frac{1}{\mu}[\exp(\mu E[W]) - 1]. \quad (17)$$

The probabilities that a random point on the line will be on the unblocked and blocked intervals, respectively, are the ratios of the corresponding parts, $E[\omega]/E[\xi]$ and $E[\eta]/E[\xi]$.

If a point is on the blocked part, then the distribution function of the length of the interval from this point to the right end of the blocked interval is

$$\tilde{F}_\eta(x) = \frac{1}{E[\eta]} \int_0^l [1 - F_\eta(y)]dy. \quad (18)$$

Knowing the probability of blockage for a point, we can now obtain the probability of total blockage of the Rx of length $l$. Let $P(l)$ be the conditional probability that the interval $(0, l)$ is not blocked completely, meaning that the blocked interval containing the left-hand side of the Rx will end before $l$. The probability of the total blockage of the interval of length $l$, given that the left-hand side of this interval is blocked, can be found by using (14), (17), and (18) as

$$1 - \tilde{F}_\eta(x) = \frac{1}{E[\eta]} \int_l^\infty [1 - F_\eta(y)]dy = \\ = \frac{\mu}{\exp(\mu E[W]) - 1} \int_l^\infty \left(1 - F_\xi(y) - \frac{1}{\mu} f_\xi(y)\right) dy, \quad (19)$$

and the probability that the left-hand side is blocked is $E[\eta]/E[\xi]$.

Finally, the probability of the total blockage follows from (19) as

$$P_B = 1 - P(l) = \mu \exp(-\mu E[W]) \times \\ \times \int_l^\infty \left(1 - F_\xi(y) - \frac{1}{\mu} f_\xi(y)\right) dy. \quad (20)$$

In the special case when the length of the receiver is less than the minimum diameter of the blocker the probability of the total blockage is given by

$$P_B = \mu \exp(-\mu E[W])[1 + \mu l]. \quad (21)$$

TABLE I
DESCRIPTION OF NOTATION AND PARAMETERS

| Notation | Description |
|---|---|
| $h_T$ | Height of Tx |
| $h_R$ | Height of Rx |
| $r$ | Distance between the bases of Tx and Rx |
| $l$ | Length of Rx |
| $H \sim\ N(\mu_H, \sigma_H)$ | Normally-distributed height of blockers |
| $D \sim\ U(d_{min}, d_{max})$ | Uniformly-distributed width of blockers |
| $\lambda_I$ | Initial intensity of blockers |
| $\lambda(x)$ | Spatially-varying intensity of centers of blockers along the radial line |
| $g(x)$, $F_H(y)$ | CCDF, CDF of height of blockers |
| $\mu$ | Intensity of blockers at the circumference |
| $W$ | Length of a blocker's shadow |
| $f_L(x)$ | pdf of a distance between Tx and a blocker |
| $f_W(y)$, $F_W(y)$, $E[W]$ | pdf, CDF, and mean of a blocker's shadow |
| $\omega_j$, $F_\omega(x)$, $E[\omega]$ | Length, CDF, and mean of unblocked intervals |
| $\eta_j$, $F_\eta(x)$, $E[\eta]$ | Length, CDF, and mean of blocked intervals |
| $\xi_j$, $F_\xi(x)$, $E[\xi]$ | Length, CDF, and mean of $\omega_j + \eta_j$ |
| $f(x)$ | pdf of renewal process |
| $f_\xi(x)$ | pdf of $\xi_j, j = 1, 2 \ldots$ |
| $f_R(y)$, $F_R(y)$ | pdf, CDF of blocker's radius |

### D. Infinitesimal receiver

In many important cases, the size of the Rx can be assumed to be infinitesimally-small compared to other linear dimensions of objects. Equipped with this assumption, we provide a simpler method for calculating the LoS and blockage probabilities for a point receiver, when the width of the Rx is not considered. To this end, consider a rectangularly-shaped area as illustrated in Fig. 4. Since this area is supposed to fit all the potential LoS blockers, its width is bounded by $d_{\max}$, that is, the maximum width of blockers. The length of the area is $r$. Note that the coordinates of each particular center are uniformly-distributed over $(0, d_{\max})$ and $(0, r)$. To determine the probability of LoS blockage, we have to estimate the probability that at least one blocker, which is falling into the area of interest, blocks the LoS path.

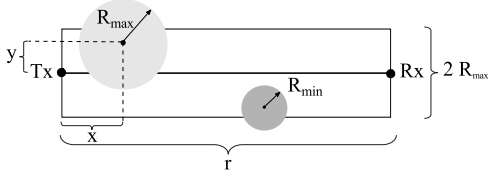


Fig. 4. Top view of the blocking area.

Let the events $A_i$ define the probability of having $i$ blockers in the area of interest. Since each blocker has its own dimensions, for each of those we define the following events: (i) event $B_0$ that the radius of a blocker's base is not large enough to cross the LoS between the Tx and Rx and (ii) event $B_1$, which is complementary to event $B_0$. To calculate the probabilities of these events, we integrate over the blocker's $y$ coordinate as

$$Pr\{B_0\} = \int_{-r_{max}}^{r_{max}} f_R(y) F_R\left(|y|\right) dy, \tag{22}$$

and $Pr\{B_1\} = 1 - Pr\{B_0\}$, where $f_R(y)$ and $F_R(y)$ are the pdf and CDF of the blocker's radius, respectively. The radius of a blocker is uniformly-distributed in $(d_{\min}/2, d_{\max}/2)$.

Recall that the radius and height of a blocker are independent. Define the following events: (i) event $C_0$ that the blocker is not high enough to block the LoS and (ii) event $C_1$, which is complementary to event $C_0$. The probabilities of these events are

$$Pr\{C_0\} = \int_0^r f_R(x) F_H\left(\frac{h_T r - (h_T - h_R)x}{r}\right) dx, \tag{23}$$

and $Pr\{C_1\} = 1 - Pr\{C_0\}$, where $f_R(x)$ is the pdf of a uniform distribution from 0 to $r$, and $F_H(y)$ is the CDF of the blocker's height.

Having defined all the events of interest, we can proceed with obtaining the probability of LoS. It includes the probability of the event $A_0$, when there are no blockers in the area. Using the law of total probability, we establish

$$P_{LoS} = Pr\{A_0\} + \\ + \sum_{i=1}^{\infty} Pr\{A_i\} \prod_{j=1}^{\infty} \left(Pr\{B_0\} + Pr\{B_1|C_0\}\right). \tag{24}$$

Since the height of a blocker is assumed to be independent from its width, we have $Pr\{B_1|C_0\} = Pr\{B_1\}Pr\{C_0\}$. Substituting these parameters into (24), we arrive at

$$P_{LoS} = p_0 + \sum_{i=1}^{\infty} p_i \prod_{j=1}^{\infty} \left( \int_{-r_{max}}^{r_{max}} f_R(y) F_R(|y|) dy + \right. \\ + \int_{-r_{max}}^{r_{max}} \int_0^r f_R(y)(1 - F_R(|y|)) f_R(x) \times \\ \left. \times F_H\left(\frac{h_T - (h_T - h_R)x}{r}\right) \right) dy dx. \tag{25}$$

where $p_i$, $i = 0, 1, \ldots$ are the Poisson probabilities.

## IV. NUMERICAL RESULTS AND DISCUSSION

### A. Calibration with simulations

For the verification of our analytical model, we employed our own mmWave ray-launching simulator, which approximates the propagation of electromagnetic waves with geometric lines. In addition, the tool accounts for detailed reflection effects, which accurately mimic mmWave diffraction, refraction, and scattering. Based on the information about the ray delays, phase, and received power, any relevant statistical data could be obtained. As a result, our industry-grade ray-launching tool makes it possible to recreate the needed urban environment and obtain results, which are reasonably close to real measurements. A simplified example of a ray-launching based simulation run without scattering and diffraction effects (for simplicity of exposition) is shown in Fig. 5(a).

We continue by calibrating the model with the ray-launching tool based on the path loss comparison. In Fig. 5(b), the results of the simulated LoS and non-LoS path loss are given by red and blue dots, respectively, while the average ray-launching path loss is plotted in green. Finally, the results

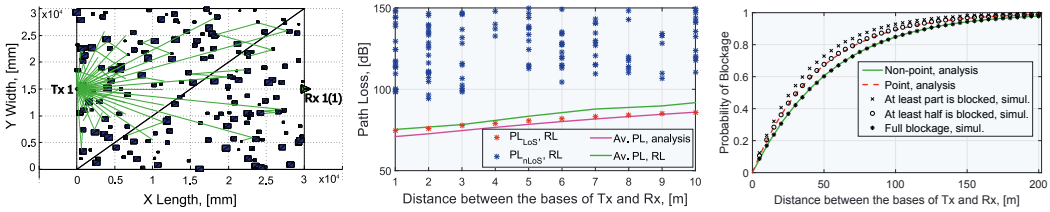


(a) Scenario modeled with ray-launching (b) Path loss calibration with ray-launching (c) Blockage probability calibration

Fig. 5. Summary of calibration results.

of our analytical modeling are presented in a form of average path loss calculated as

$$L_e = P_{LoS} L_{LoS} + (1 - P_{LoS}) L_{nLoS}, \tag{26}$$

where $P_{LoS}$ is the LoS probability computed according to (25), $L_{LoS}$ and $L_{nLoS}$ are the path loss for LoS and non-LoS components, which have been parameterized according to the real measurements in [2]. The comparison between the average ray-launching and the average analytical path loss indicates a marginal difference. However, it should be noted that the results have only been simulated at shorter distances due to excessive computational complexity. In the plot, it is also visible that the LoS path loss values differ from the corresponding non-LoS figures by at least 20 dB. Based on this observation, we conclude that if the LoS component is not present, there is a high probability of poor mmWave link, similar to complete receiver blockage due to very low SNR.

To facilitate a more detailed comparison, and in addition to ray-launching, we developed a simplified system-level simulator providing the blockage probability as a function of the model parameters, which are given in Table II. First, in a square area of interest with the dimensions of ten times greater than the distance between the Tx and Rx, we generated the blockers according to the modified Matern hard-core process with the parameters $\lambda_I$ and $U(0, d_{\max}/2)$ following the algorithm described in [12]. Here, the Tx is assumed to be a point and is placed in the center, while the Rx is a segment with the length of $l$ positioned at the distance $r$ from Tx, such that the line connecting the center of Rx and Tx is a normal. Both Tx and Rx are associated with heights $h_T$ and $h_R$, respectively. We further divide the segment $l$ into $N$ parts. In these settings, (i) the event when the Rx is fully blocked occurs when all of the lines are blocked; (ii) the event that at least half of the Rx is blocked corresponds to having at least half of the lines blocked; and (iii) the event of at least part of the Rx blocked occurs when at least one line is blocked.

TABLE II
MAIN SIMULATION PARAMETERS

| Parameter | Value |
|---|---|
| Height of Tx | $4m$ |
| Height of Rx | $1.3m$ |
| Distance between the bases of Tx and Rx | $30m$ |
| Height of a blocker, $N(\mu_H, \sigma_H)$ | $N(1.7m, 0.1m)$ |
| Diameter of a blocker, $U(d_{min}, d_{max})$ | $U(0.2m, 0.8m)$ |
| Length of Rx | $0.1m$ |
| Initial intensity of blockers | $0.3\ blockers/m^2$ |
| Frequency | $28GHz$ |

The comparison of the results obtained with simulations and the proposed mathematical model for point and interval Rx of size 10cm is shown in Fig. 5(c). First, notice that the maximum absolute difference is attained at the average distances of around $40 - 100$ meters. For short and long distances, the deviation is marginal. Nevertheless, the maximum difference is always less than $0.1$ for a reasonably large Rx of 10cm. The slight deviations of the analytical results from simulations are explained by the fact that we replaced the actual Matern hard-core process by a Poisson process with the same intensity.

### B. Understanding analytical results

First, Fig. 6 shows the results for the average path loss ($L_e$) as a function of the Tx height calculated according to (26). As one may observe, for each separation distance between the bases of Tx and Rx, there always exists an optimal height of the Tx, where the average path loss takes the minimum value.

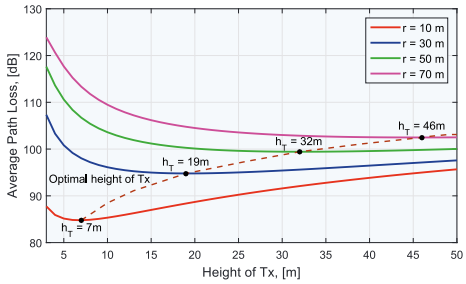


Fig. 6. Average path loss and optimal $h_T$ for different $r$.

To characterize the effect of non-infinitesimal Rx, Fig. 7 demonstrates the blockage probability for the interval Rx across different ratios of the Rx size and the mean blocker diameter $l/d_{\max}$, as well as the distance between the bases of Tx and Rx $r$. We notice that for any value of $r$ and $l/d_{\max}$, the blockage probability for the point Rx is slightly higher than that for the interval Rx. The increase in $l/d_{\max}$, however, decreases the blockage probability.

The height of the Tx, $h_T$, is one of the most important parameters available for system designers. Intuitively, the higher the height is, the smaller the probability of the LoS

blockage should be. However, the final effect is expected to heavily depend on the Tx-Rx separation distance.

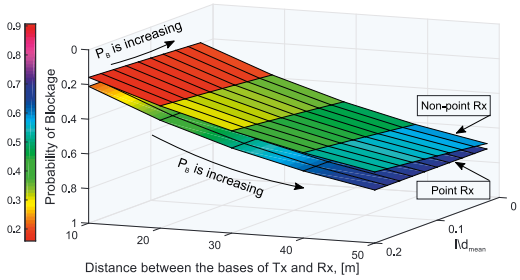


Fig. 7. Blockage probability as a function of $r$ and $l/d_{mean}$.

The impact of the Tx height and distance between the Tx and Rx for a point Rx is demonstrated in Fig. 8. As we expected, the probability of blockage reduces exponentially as $h_T$ increases. The effect of the Tx-Rx distance is however inverse – longer separation distances lead to higher blockage probability. Fandrewsor large $h_T$, the increase is linear, whereas for smaller $h_T$ it is exponential. Also, notice that starting from a certain Tx-Rx separation distance, the blockage probability remains nearly the same. It is explained by the fact that at such distances, and for a given human user density $\lambda_I = 0.3$, the probability to "meet" a blocker along the LoS path is extremely high.

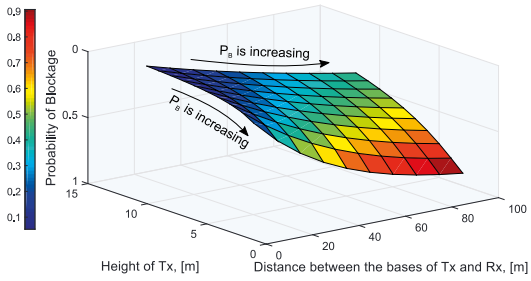


Fig. 8. Blockage probability for different $h_T$ and $r$.

## V. Conclusions

The presence of the LoS signal path is crucial in determining the ultimate performance of the 5G-grade mmWave cellular communications, especially in highly-crowded outdoor environments. Using the ray-launching simulator, we first demonstrated that the difference between the LoS and non-LoS path loss values is at least 20 dB. Moreover, due to shorter ranges of mmWave cellular technology, smaller obstacles will affect the corresponding quality of signal propagation. All of the above leads to the need of having a comprehensive analytical methodology for determining the presence of the LoS link. However, existing models, such as 3GPP urban outdoor micro-cellular model, do not deliver the desired detalization. This substantiates the importance of our conducted LoS-centric analysis.

To this end, we developed a novel framework for capturing the effects of the most important mmWave system parameters on the probability of blockage for both the infinitesimal receiver and the receiver of a fixed non-zero length. As a result, it was shown that an increase in the ratio between the length of the Rx and blocker sizes leads to a closer match between the two. Moreover, we demonstrated the existence of the optimal Tx height, which is an important learning for system designers. The studied parameters of interest included the distance between the bases of the Tx and Rx and their heights, as well as the density of blockers on the landscape and their random dimensions.

Finally, also with the help of an advanced ray-launching tool, it was confirmed that our analysis offers accurate results to model human-body blockage in urban mmWave deployments.

## VI. Acknowledgements

This work is supported by Intel Corporation. The authors would like to thank Dmitrii Solomitckii, Tampere University of Technology, for helping with ray-launching simulations.

## References

[1] J. Nuckelt, T. Abbas, F. Tufvesson, C. Mecklenbrauker, L. Bernado, and T. Kurner, "Comparison of ray tracing and channel-sounder measurements for vehicular communications," *IEEE 77th Vehicular Technology Conference (VTC Spring)*, June 2013.

[2] M. R. Akdeniz, Y. Liu, M. K. Samimi, S. Sun, S. Rangan, T. S. Rappaport, and E. Erkip, "Millimeter wave channel modelingand cellular capacity evaluation," *IEEE Journal on Selected Areas in Communications*, vol. 32, pp. 1164–1179, June 2014.

[3] T. Bai, R. Vaze, and R. W. Heath Jr., "Using random shape theory to model blockage in random cellular networks," *Signal Processing and Communications (SPCOM)*, July 2012.

[4] T. Bai, R. Vaze, and R. W. Heath Jr., "Analysis of blockage effects on urban cellular networks," *IEEE Transactions on Wireless Communications*, pp. 5070–5083, September 2014.

[5] G. George and A. Lozano, "Performance of enclosed mmWave wearable networks," *IEEE Int'l Workshop on Computational Advances in Multi-Sensor Adaptive Processing (CAMSAP15)*, December 2015.

[6] "Evolved universal terrestrial radio access (E-UTRA); further advancements for E-UTRA physical layer aspects (Release 9)," *3GPP TR 36.814 V9.0.0*, March 2010.

[7] M. N. Kulkarni, S. Singh, and J. G. Andrews, "Coverage and rate trends in dense urban mmWave cellular networks," *IEEE Global Communications Conference (GLOBECOM)*, pp. 3809–3814, December 2014.

[8] M. Di Renzo, "Stochastic geometry modeling and performanceevaluation of mmWave cellular communications," *IEEE International Conference on Communications (ICC)*, pp. 5992–5997, June 2015.

[9] M. Jacob, S. Priebe, T. Kurner, M. Peter, M. Wisotzki, R. Felbecker, and W. Keusgen, "Fundamental analyses of 60 GHz human blockage," *7th European Conference on Antennas and Propagation (EuCAP)*, pp. 117–121, April 2013.

[10] C. L. Ogden, C. D. Fryar, M. D. Carroll, and K. M. Flegal, "Mean body weight, height, and body mass index, United States 1960–2002," *Centers for Disease control and prevention*, October 2004.

[11] J. Andrews, K. Ganti, M. Haenggi, N. Jindal, and S. Weber, "A primer on spatial modeling and analysis in wireless networks," *IEEE Communications Magazine*, vol. 48, pp. 156–163, November 2010.

[12] S. N. Chiu, D. Stoyan, W. S. Kendall, and J. Mecke, *Stochastic Geometry and its applications*. Wiley, 2013.

[13] S. Ross, *Introduction to probability models*. Academic Press, 10th ed., 2009.

[14] D. Cox and H. Miller, *The theory of stochastic processes*. Wiley, 1965.

[15] D. R. Cox, *Renewal theory*. Methuen and Co ltd., 1970.

# PUBLICATION
# II

**On the Temporal Effects of Mobile Blockers in Urban Millimeter-Wave Cellular Scenarios**

M. Gapeyenko, A. Samuylov, M. Gerasimenko, D. Moltchanov, S. Singh, M. R. Akdeniz, E. Aryafar, N. Himayat, S. Andreev and Y. Koucheryavy

*IEEE Transactions on Vehicular Technology* 66.11 (2017), 10124–10138

# On the Temporal Effects of Mobile Blockers in Urban Millimeter-Wave Cellular Scenarios

Margarita Gapeyenko, Andrey Samuylov, Mikhail Gerasimenko, Dmitri Moltchanov, Sarabjot Singh, Mustafa Riza Akdeniz, Ehsan Aryafar, Nageen Himayat, Sergey Andreev, and Yevgeni Koucheryavy

***Abstract*—Millimeter-wave (mmWave) propagation is known to be severely affected by the blockage of the line-of-sight (LoS) path. In contrast to microwave systems, at shorter mmWave wavelengths such blockage can be caused by human bodies, where their mobility within environment makes wireless channel alternate between the blocked and non-blocked LoS states. Following the recent 3GPP requirements on modeling the *dynamic blockage* as well as the *temporal consistency* of the channel at mmWave frequencies, in this paper a new model for predicting the state of a user in the presence of mobile blockers for representative 3GPP scenarios is developed: urban micro cell (UMi) street canyon and park/stadium/square. It is demonstrated that the blockage effects produce an *alternating renewal process* with exponentially distributed non-blocked intervals, and blocked durations that follow the general distribution. The following metrics are derived (i) the mean and the fraction of time spent in blocked/non-blocked state, (ii) the residual blocked/non-blocked time, and (iii) the time-dependent conditional probability of having blockage/no blockage at time $t_1$ given that there was blockage/no blockage at time $t_0$. The latter is a function of the arrival rate (intensity), width, and height of moving blockers, distance to the mmWave access point (AP), as well as the heights of the AP and the user device. The proposed model can be used for system-level characterization of mmWave cellular communication systems. For example, the optimal height and the maximum coverage radius of the mmWave APs are derived, while satisfying the required mean data rate constraint. The system-level simulations corroborate that the use of the proposed method considerably reduces the *modeling complexity*.**

***Index Terms*—Cellular networks, mmWave, human body blockage, temporal consistency, mobility of blockers.**

## I. Introduction

The rapidly growing number of mobile devices as well as the associated growth of mobile traffic call for an unprecedented increase in access capacity. To meet more stringent performance requirements, the use of the so-called cellular millimeter-wave (mmWave) technology operating at frequencies such as 28 GHz and 73 GHz has been proposed in fifth-generation (5G) mobile systems [1]–[3].

Together with the phenomenal increase in access capacity, the use of the extremely high frequency (EHF) bands creates unique challenges for wireless communication systems. One of them is a need for development of appropriate mmWave channel models. Indeed, various groups and organizations have recently developed a number of such channel models [4]–[10]. In contrast to microwave systems, the propagation characteristics of mmWave systems (with wavelengths of under a centimeter) are impacted not only by larger objects such as buildings, but also by much smaller obstacles such as cars, lampposts, and even humans. Given that mmWave systems are envisioned to be deployed in urban squares and streets, 3GPP has identified humans as one of the major factors affecting the mmWave propagation and has incorporated a blockage model into TR 38.901 of Release 14 [5].

The performance of mobile communications systems is typically characterized by developing system-level simulation (SLS) frameworks [11], [12]. Modeling the path loss with simple power-law abstractions, these SLS tools may take into account the necessary details of the target technologies and deliver their output results within a reasonable time. However, when conducting system-level evaluation of a mmWave system, in addition to the path loss model that captures the propagation environment, one needs to explicitly represent and track all of the relevant static and mobile objects with dimensions larger than a few centimeters. This significantly increases the required computational resources and expands simulation time.

Motivated by the new effects in mmWave communications systems as well as by the recent 3GPP requirements for 5G channel modeling, this paper studies the *dynamic blockage* caused by humans in outdoor urban mmWave cellular deployments, while specifically concentrating on the *temporal consistency* of the link states for a static user.

### A. Background and Related Work

The importance of dynamic blockage of the LoS path in mmWave deployments has recently been shown to be one of the critical design factors that affect system performance [4]–[6], [13]. An example illustration of the measured path gain experienced by a node in a realistic crowded environment is shown in Fig. 1. As one may observe, dynamic blockage by small mobile objects within the environment, such as moving people, cars, trucks, etc., introduces additional uncertainty in the channel, which may eventually result in sharp drops (up to $30 \sim 40$ dB) in the received signal strength [14], [15]. The blockage frequency, duration, and the resultant degradation of signal strength affect the performance of a mmWave system.

Recent work has studied the impact of LoS blockage in urban microwave systems [16], [17]. However, the results do



M. Gapeyenko, A. Samuylov, M. Gerasimenko, D. Moltchanov, S. Andreev, and Y. Koucheryavy are with Tampere University of Technology, Tampere, Finland (e-mail: {firstname.lastname, evgeni.kucheryavy}@tut.fi).

S. Singh, M. R. Akdeniz, N. Himayat are with Intel Corporation, Santa Clara, CA, USA (e-mail: sarabjotsingh.in@gmail.com, {mustafa.akdeniz, nageen.himayat}@intel.com)

E. Aryafar is with Portland State University, Portland, OR, USA (e-mail: earyafar@gmail.com)

This work was supported by Intel Corporation and the Academy of Finland. The work of S. Andreev was supported in part by a Postdoctoral Researcher grant from the Academy of Finland and in part by a Jorma Ollila grant from Nokia Foundation.

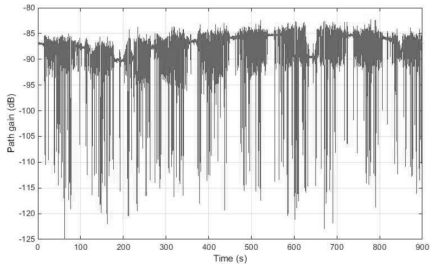


Fig. 1. Path gain in presence of dynamic blockage, reproduced from [14].

not directly apply to mmWave systems as the objects of interest in mmWave and microwave systems are of fundamentally different nature and hence would require different models for their accurate representation. Indeed, in addition to mobility of smaller obstacles, such as humans, one also needs to take into account their inherently random dimensions.

The LoS blockage by humans in mmWave systems has been evaluated through simulation studies in [18]. In [19], a LoS blockage model where humans are represented as cylinders of random width and height was proposed. However, there the authors assumed that both the users and the blockers are stationary. In addition to academic work, the 3GPP community is currently exploring various options for modeling the impact of human blockage appropriately [14], [20].

In [5], the human body blockage is taken into account by creating rectangular screens dropped onto the simulation map. A similar approach is adopted by [21], [22], where the authors also evaluated the accuracy of their methods. Due to the properties of the propagation model, which generates a random sample of the propagation path at each run, a particular attention of the 3GPP work groups is being paid to spatial and temporal consistency of the mmWave links [5], [20].

In [23], the authors contributed a model for temporal correlation of interference in a mobile network with a certain density of users. It was demonstrated that the correlated propagation states across the users significantly impact the temporal interference statistics. Analytically tractable models for correlated outdoor and indoor shadowing have been proposed in [24] and [25], thus accentuating the high correlation between the locations of the nodes and the shadowing effects. The analytical expression to characterize the correlation between the signals of two antennas was given in [26].

Even though there has been a considerable literature coverage on user mobility in general [27]–[30], to the best of our knowledge there are only a few studies that incorporate the user mobility into analytically tractable models [31], [32]. These latest results confirm the presence of memory in the LoS blockage process and highlight its dependence on the mobility characteristics of the users.

### *B. State-of-the-Art and Contributions*

The goal of this paper is to contribute a novel mathematical methodology that aims to characterize the dynamics and the temporal correlation of LoS human body blockage statistics. In this work, a model of the LoS blockage for a stationary user in a moving field of blockers is proposed. This scenario is more typical for outdoor mmWave systems as compared to stationary blockage models assumed in prior work. The blockers are modeled as cylinders of a certain height and width that enter the LoS zone of a mmWave receiver according to a Poisson process in time.

The analysis is based on the combined application of stochastic geometry, renewal process theory, and queuing models. Three different scenarios are addressed, including two street canyon use cases and a park layout (see Fig. 2). The metrics of interest are those reflecting temporal behavior of the LoS blockage process, such as the mean and the fraction of blocked/non-blocked LoS, the residual time in blocked/non-blocked states, and the time-dependent effects of conditional blocked/non-blocked state probabilities.

In summary, the following contributions are delivered by this work:

- To analyze the *temporal correlation* and the *dynamic blockage process* by human bodies at mmWave frequencies, a novel mathematical model is proposed. It is shown that the analytical expression could be utilized to replace explicit simulation of the mobile blockers in the SLS studies. The associated improvement in the simulation times depends on the crowd intensity and may reach several orders of magnitude.
- To capture the general structure of the dynamic LoS blockage process, including the impact of mobile obstacles, the corresponding mathematical methodology is developed. It is observed that non-blocked/blocked periods form an *alternating renewal process* where the non-blocked intervals follow an exponential distribution and the blocked intervals have a general distribution. The latter is captured by employing methods for the busy period analysis in the $M/GI/\infty$ queuing model.
- To characterize the *temporally consistent* human body blockage process, a simplified approach is developed to calculate the *conditional probabilities*. It is demonstrated that for realistic input parameter values, in all the considered scenarios there always is a significant dependence between the states of the user at $t_0$ and $t_1$ over small timescales.
- To demonstrate the applicability of the proposed methodology, the optimal height of the mmWave AP that maximizes the average time in non-blocked LoS conditions as well as the maximum coverage radius that satisfies the required mean data rate are estimated.

The rest of this paper is organized as follows. In Section II, the system model and a description of the outdoor scenarios proposed by 3GPP, which reflect real-life mmWave system usage situations, are introduced. The analysis for the performance metrics of interest is summarized in Section III. The numerical results, particularly those related to the temporal dependencies in the LoS blockage process, are discussed in Section IV. Section V elaborates on the applications of the proposed methodology. Conclusions are presented in the last section of the paper.

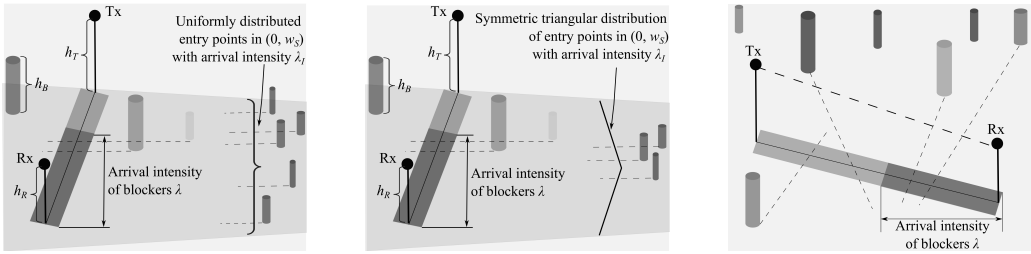


(a) Sidewalk 1, S1 (b) Sidewalk 2, S2 (c) Park/stadium/square, S3

Fig. 2. Three considered scenarios for further analytical modeling.

## II. System Model

### A. General Considerations

The proposed system model is illustrated in Fig. 2. The transmitter (Tx) and the receiver (Rx) are deployed at the heights of $h_T$ and $h_R$ from the ground, respectively. The two-dimensional distance between the Tx and Rx is $r_0$. Following [33], the potential blockers (i.e., humans) are modeled as cylinders with the height of $h_B$ and the base diameter of $d_m$.

Note that there always is an area between Tx and Rx, where the emergence of a blocker will cause occlusion of the mmWave LoS link. With the above parameters, this area may be approximated by a rectangular shape, named here the *LoS blockage zone* and denoted as $ABCD$ in Fig. 3. The particular dimensions of this area, its geometrical shape, and the position with respect to Tx and Rx can be estimated given the aforementioned parameters as discussed in what follows.

The speed of blockers $V$ is assumed to be constant. However, the actual mobility model of blockers depends on the scenario as introduced below. The main parameters and the description of employed notation are collected in Table I.

### B. Blocker Mobility and Arrival Modeling

To characterize the human mobility, the following three scenarios are considered:

- *Sidewalk 1 (First scenario, S1).* In this scenario, the mmWave Tx (the AP) is assumed to be mounted on the wall of a building while the Rx may reside at any location on the sidewalk of width $w_S$ within the coverage area of the mmWave AP. The blockers move along the straight line parallel to each other and the side of the sidewalk at a constant speed of $V$ while their y-coordinates of crossing the width of the sidewalk are distributed uniformly within $(0, w_S)$, see Fig. 2(a). The arrival process of blockers crossing a vertical line – the width of the sidewalk $w_S$ – is Poisson in time with the arrival intensity $\lambda_I$.
- *Sidewalk 2 (Second scenario, S2).* This scenario is similar to the previous case, except for how the blocker positions are distributed in the sidewalk. In practice, the users tend to move closer to the center of the walkway. Therefore, y-coordinates of crossing the width of the sidewalk are modeled by employing a symmetric triangular distribution over $(0, w_S)$, see Fig. 2(b). The arrival process of blockers crossing the width of the sidewalk is again Poisson in time with the arrival intensity $\lambda_I$ of blockers per time unit.
- *Park/Stadium/Square (Third scenario, S3).* In this scenario, the users are allowed to enter and leave the mmWave LoS blockage zone at any point along the three sides of the rectangle, see Fig. 2(c). It is assumed that both the entry and the exit points are distributed uniformly over the side lengths for each individual user. The arrival process of users into the *LoS blockage zone* is Poisson with the arrival intensity of $\lambda_I$ per time unit.

The proposed methodology generally allows to capture more specific types of blocker mobility. For example, one may decide to relax the assumption of the straight movement

TABLE I
Summary of Notation and Parameters

| Notation | Description |
|---|---|
| $h_T$, $h_R$, $h_B$ | Height of Tx, Rx, blockers |
| $r_0$ | Two-dimensional distance between Tx and Rx |
| $d_m$, $V$ | Diameter and speed of blockers |
| $w_S$ | Width of the sidewalk |
| $w_E$, $r$ | Effective width and length of LoS blockage zone |
| $\lambda_I$ | Initial arrival intensity of blockers per time unit |
| $\lambda$ | Arrival intensity of blockers entering the LoS blockage zone per time unit |
| $\lambda_S$ | Arrival intensity of blockers entering the unit area of LoS blockage zone |
| $\lambda_N$ | Density of users per unit area |
| $y_A$, $y_B$, $y_C$, $y_D$ | y-coordinates of the edges of the LoS blockage zone |
| $\alpha$ | Angle between Y-axis and the segment Tx-Rx |
| $L$ | Distance walked by a blocker in LoS blockage zone |
| $T$ | Residence time of a blocker in LoS blockage zone |
| $\omega_j$, $\eta_j$ | The non-blocked and blocked time interval |
| $F_\omega(x)$, $E[\omega]$ | CDF, the mean of non-blocked time interval |
| $F_\eta(x)$, $E[\eta]$ | CDF, the mean of blocked time interval |
| $F_T(x), f_T(x), \mathbb{E}[T]$ | CDF, pdf, the mean of LoS zone residence time |
| $F_Y(x)$ | CDF of the y-coordinate of blocker entry point |
| $F_{\bar{Y}}(x)$ | Truncated distribution of the entry point defined on $y_A \leq x \leq y_C$ |
| $F_L$, $f_L$ | CDF and pdf of the residence distance $L$ |
| $\mathbb{E}[T_l]$, $\mathbb{E}[T_n]$ | Fraction of time in non-blocked/blocked states |
| $F_{t_\omega}(x)$, $F_{t_\eta}(x)$ | Residual time in non-blocked/blocked states |
| $\xi_j$ | $j^{th}$ time interval equal to $\omega_j + \eta_j$ |
| $F_\xi(x), f_\xi(x), E[\xi]$ | CDF, pdf, the mean of $\omega_j + \eta_j$ |
| $f(x)$ | pdf of renewal process |
| $p_{00}$, $p_{01}$ | Conditional probabilities to be in non-blocked/blocked states at time $t_1$ (0 and 1) given that there was non-blocked state at $t_0$ |
| $p_{10}$, $p_{11}$ | Conditional probabilities to be in non-blocked/blocked states at time $t_1$ (0 and 1) given that there was blocked state at $t_0$ |

and thus model the *walking street* environment, where the user trajectories are not required to remain parallel to the sides of the street. Also note that the straight trajectories of blocker mobility inside the LoS blockage zone are the direct consequence of small dimensions of the said zone, hence resulting in negligible changes of behavior with respect to the angle of motion.

The considered metrics of interest are those pertaining to the temporal behavior of the LoS blockage process and include (i) the mean and the fraction of time in the blocked/non-blocked state as experienced by the Rx, (ii) the residual time in the blocked/non-blocked state, and (iii) the conditional probability that there is blocked/non-blocked state at $t_1$ given that there was blocked/non-blocked state at $t_0$, $t_1 > t_0$.

## III. Proposed System Analysis

All of the three scenarios introduced in the previous Section II can be characterized by following the proposed methodology. The key difference between them is in the distribution of the residence time in the LoS blockage zone (that is, the time that a blocker spends in the LoS blockage zone while crossing it). In this section, the general method to obtain the distribution of the zone residence time in the LoS blockage for the first scenario (i.e., Sidewalk 1, S1) is described. For the second and the third scenarios, the corresponding derivations are reported in Appendix A. Finally, the target metrics of interest are produced.

The step-by-step analytical approach may be summarized as follows:

- Specify the zone where blockers may occlude the LoS path and thus determine the LoS blockage zone geometry;
- Describe the process of blockage by introducing the alternating renewal process that captures the non-blocked/blocked intervals;
- Obtain the probability density function (pdf) of the non-blocked time interval by analyzing the alternating renewal process in question;
- Produce the pdf of the blocked interval by representing it as a busy period in the M/GI/$\infty$ queuing system[1], where the service time distribution corresponds to the time spent by a blocker in the LoS blockage zone;
- Calculate all of the metrics of interest, including the moments, the residual time distributions, as well as the conditional non-blocked/blocked state probabilities by applying conventional techniques.

### A. LoS Blockage Zone Geometry

Consider the geometrical scenario represented in Fig. 3. It should be noted that rectangle ABCD, named the LoS blockage zone, is the only area where the presence of a blocker causes blockage of the LoS link. Any blocker which appears outside of this zone (closer to Tx, outside of ABCD) will not affect the LoS link.

Since any blocker entering the LoS blockage zone in question (particularly, the center of a cylinder) occludes the LoS, the width of the zone equals the base diameter of the blocker, $d_m$. The length of this zone reflects the maximum possible distance, where the height of the blocker still affects the LoS. As illustrated in Fig. 3, from the geometrical considerations the latter follows as

$$r = \frac{r_0(h_B - h_R)}{h_T - h_R} + d_m/2, \tag{1}$$

where $r_0$ is two-dimensional distance between the Tx and the Rx, while $h_B$, $h_R$, and $h_T$ are the heights of the blocker, Rx, and Tx, respectively.

The coordinates of Tx and Rx located at the points P and O (see Fig. 3), respectively, are then given by

$$\begin{aligned} x_P &= 0, & y_P &= w_S, \\ x_O &= r_0 \sin(\alpha), & y_O &= w_S - r_0 \cos(\alpha). \end{aligned} \tag{2}$$

The coordinates of the blockage zone vertices are thus

$$\begin{aligned} x_A &= x_O - \frac{d_m}{2}\cos(\alpha), \quad y_A = y_O - \frac{d_m}{2}\sin(\alpha), \\ x_B &= x_O + \frac{d_m}{2}\cos(\alpha), \quad y_B = y_O + \frac{d_m}{2}\sin(\alpha), \\ x_C &= x_B - r\cos(\frac{\pi}{2} - \alpha), y_C = y_B + r\sin(\frac{\pi}{2} - \alpha), \\ x_D &= x_A - r\cos(\frac{\pi}{2} - \alpha), y_D = y_A + r\sin(\frac{\pi}{2} - \alpha), \end{aligned} \tag{3}$$

where $\alpha$ is the angle characterizing the position of the Rx in relation to the Tx location, as shown in Fig. 3.

### B. Renewal process analysis

Let $\omega_j$ and $\eta_j$, $j = 1, 2, \ldots$, denote the time spent in the non-blocked and blocked intervals, respectively, as shown in Fig. 4. As one may observe, these intervals alternate, that is, non-blocked period always precedes the blocked one and vice versa. Since the entry of blockers into the LoS blockage zone is modeled as a Poisson process, durations of non-blocked and

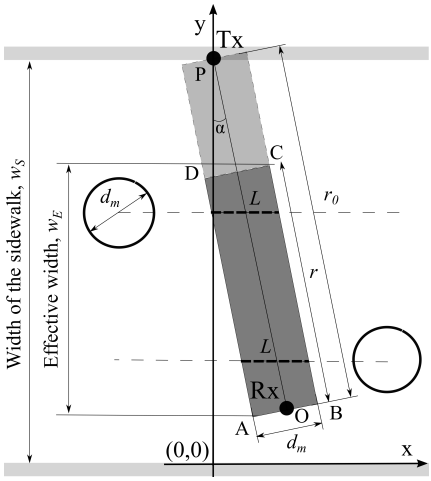


Fig. 3. Geometry of the LoS blockage zone.

[1]According to the Kendall notation: $M$ is Poisson arrival process, $GI$ is general distribution of service time, and $\infty$ is infinite number of servers.

$$F_\eta(x) = 1 - \left( [1 - F_T(x)] \left[ 1 - \int_0^x (1 - F_\eta(x-z)) \exp(-\lambda F_T(z)) \lambda dz \right] + \int_0^x (1 - F_\eta(x-z)) |de^{-\lambda F_T(z)}| \right). \quad (4)$$

blocked intervals are mutually independent. Hence, the process of the LoS blockage can be modeled as an alternating renewal process, as displayed in Fig. 4. The proposed methodology is valid for all three scenarios of interest.

Define $\xi_j = \omega_j + \eta_j$. The points $0, \xi_1, \xi_1+\xi_2$, and $\xi_1+\xi_2+\xi_3$ are the renewal moments that form the process at hand. The density of this process follows from [34] as

$$f(x) = \lambda F_T(x) \exp\left( -\lambda \int_0^x [1 - F_T(y)] dy \right), \quad (5)$$

where $\lambda$ is the intensity of the blocker arrivals into the zone, $F_T(y)$ is the cumulative distribution function (CDF) of the zone residence time $T = L/V$ for a single blocker, where $L$ is the distance over which a blocker travels inside the blockage zone.

The time spent in the non-blocked part, $\omega_j$, follows an exponential distribution with the parameter $\lambda$, $F_\omega(x) = 1 - e^{-\lambda x}$, with the mean $\mathbb{E}[\omega] = 1/\lambda$ [35]. This result follows directly from the fact that the left-hand sides of the time intervals spent in the LoS blockage zone by a single blocker follow a Poisson process in time with the arrival intensity of $\lambda$ per time unit. Therefore, the time period between the end of an interval $\eta_j$ (see Fig. 4), which is considered as an arbitrary point, and the starting point of the next interval $\eta_{j+1}$ is distributed exponentially.

Consider now the blocked interval.

**Proposition 1.** *Let $F_\eta(x)$ be the CDFs of the time in the blocked intervals, $\eta_j$, $j = 1, 2, \ldots$, with the mean of $\mathbb{E}[\eta]$. The distribution of the blocked interval, $F_\eta(x)$, is the same as the distribution of a busy period in the $M/GI/\infty$ queuing system given by (4), see e.g., [36].*

*Proof.* The proposition is proved by exploiting the analogy with the busy time distribution in $M/GI/\infty$ queuing system. Consider now an evolution of a busy period in $M/GI/\infty$ system. It starts at some $t = t_1$ with a customer arriving into the system. Each arrival during the service time of this customer prolongs the busy period if and only if its service time is greater than the service time of the customers that are currently in service. The busy period ends when a customer upon its departure leaves an empty system. Analyzing the illustration of the renewal process associated with the LoS blockage interval, the analogy with the busy period in $M/GI/\infty$ system is established. Indeed, each blocker extends the LoS blockage period if and only if its blockage time is greater than the blockage time of those blockers currently occluding the LoS. The CDF of the busy period in $M/GI/\infty$ system has been obtained in [36] and is provided in (4). □

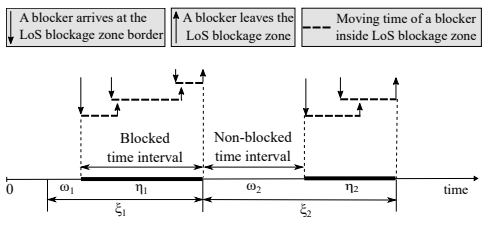


Fig. 4. Renewal process associated with the LoS blockage, where every blocker might spend different time when occluding the LoS.

Note that (4) can be evaluated numerically for any $F_T(x)$.

### C. Residence Time in the LoS Blockage Zone

To proceed further with deriving the metrics of interest, the CDF of the residence time $T = L/V$ in the LoS blockage zone for a single user is required. Recalling the principles of linear transformation of random variables [37], the pdf of the time $T = L/V$ (for all the scenarios of interest) reads as

$$f_T(x) = V f_L(xV). \quad (6)$$

Hence, it is sufficient to find the pdf of distance $L$ that one blocker travels inside the LoS blockage zone, $f_L$, in order to derive $f_T$. The notation employed in what follows is clarified in Fig. 3. Note that the arrival intensity of the blockers $\lambda$ that enter the LoS blockage zone is different for all the considered scenarios and is derived in what follows by using $\lambda_I$. The latter is the initial arrival intensity of blockers that cross the width of the sidewalk for the first and second scenarios, S1 and S2 (see Fig. 2). For the sake of the analysis, the park/square scenario, S3, has the arrival intensity of $\lambda_I = \lambda$.

Note that the derivation of distance $L$ is a scenario-specific part of the analysis as it requires a certain distribution of the entry points of blockers to the LoS blockage zone.

*First scenario, S1.* Let $F_Y(x), 0 \le x \le w_S$, be the CDF of the $y$-coordinate of the entry point for a blocker. Since only the blockers crossing the blockage area are of interest, this distribution is truncated. The resulting distribution $F_{\widetilde{Y}}(x)$ is defined on $y_A \le x \le y_C$.

The CDF of the distance $L$ traversed by a blocker in the LoS blockage zone is therefore

$$F_L(x) = \begin{cases} 0, x < 0, \\ F_{\widetilde{Y}}(y_C) - F_{\widetilde{Y}}\left(y_C - x\cos(\alpha)\sin(\alpha)\right) \\ - \left(F_{\widetilde{Y}}(y_A) - F_{\widetilde{Y}}\left(y_A + x\cos(\alpha)\sin(\alpha)\right)\right), \\ 0 \le x < x_{min}, \\ 1, x \ge x_{min}, \end{cases} \quad (7)$$

where $x_{min} = \min(d_m/\cos(\alpha), r/\sin(\alpha))$.

For the sidewalk 1 scenario (S1) (see Fig. 2(a)), (7) takes the form of

$$F_L^1(x) = \begin{cases} 0, & x \le 0, \\ \dfrac{x\sin(2\alpha)}{y_C - y_A}, & 0 < x \le x_{min}, \\ 1, & x > x_{min}. \end{cases} \quad (8)$$

The arrival intensity of blockers entering the zone that affects the LoS for the first scenario, S1, is delivered as

$$\lambda = \lambda_I \frac{w_E}{w_S}, \tag{9}$$

where $w_S$ is the width of the sidewalk, $\lambda_I$ is the arrival intensity of blockers on the width $w_S$, and $w_E = \max(y_A, y_B, y_C, y_D) - \min(y_A, y_B, y_C, y_D)$ is the projection of rectangle $ABCD$ on Y-axis, named the effective width, as shown in Fig. 3.

The residence time in the LoS blockage zone for the second and the third scenario is derived in Appendix A.

### D. Metrics of Interest

*1) Mean and Fraction of Time in Non-Blocked/Blocked State:* The fraction of time in the non-blocked/blocked state can be produced by utilizing the mean time spent in each state, i.e., [35]

$$\mathbb{E}[T_l] = \frac{\mathbb{E}[\omega]}{\mathbb{E}[\omega] + \mathbb{E}[\eta]}, \mathbb{E}[T_n] = \frac{\mathbb{E}[\eta]}{\mathbb{E}[\omega] + \mathbb{E}[\eta]}, \tag{10}$$

where $\mathbb{E}[\omega]$ and $\mathbb{E}[\eta]$ are the means of the non-blocked/blocked intervals.

Recall that due to the exponential nature of $\omega$, $\mathbb{E}[\omega] = 1/\lambda$. The mean $\mathbb{E}[\eta]$ can be obtained numerically by using (4). However, there is a simpler approach that is outlined below. Observe that the renewal density $f(x)$ is $f(x) = 1/\mathbb{E}[\xi]$, when $t \to \infty$. From (5), after employing the Laplace transform (LT), we establish that it is also equal to $f(x) = \lambda \exp(-\lambda \mathbb{E}[T])$, where $\mathbb{E}[T]$ is the mean zone residence time for a single blocker, see [19] for details. Hence, the following holds

$$\mathbb{E}[\xi] = \frac{1}{\lambda} \exp(\lambda \mathbb{E}[T]). \tag{11}$$

Then, $\mathbb{E}[\eta]$ can be established as

$$\begin{aligned} \mathbb{E}[\eta] &= \int_0^\infty [1 - F_\eta(x)] dx \\ &= \int_0^\infty \left(1 - F_\xi(x) - \frac{f_\xi(x)}{\lambda}\right) dx = \mathbb{E}[\xi] - \frac{1}{\lambda}. \end{aligned} \tag{12}$$

Substituting (11) into (12), we arrive at

$$\mathbb{E}[\eta] = \frac{1}{\lambda}[\exp(\lambda \mathbb{E}[T]) - 1]. \tag{13}$$

*2) Residual Time in Non-Blocked/Blocked State:* Here, the distribution of the residual time spent in the non-blocked/blocked state given that the user is currently in the non-blocked/blocked state is characterized. Recall that the distribution of the non-blocked interval is exponential, while the CDF for the blocked interval is provided in (4). Hence, the residual time distribution in the non-blocked state is also exponential with the same parameter. Therefore, the residual blocked time CDF is

$$F_{t_\eta}(t) = \frac{1}{\mathbb{E}[\eta]} \int_0^t [1 - F_\eta(y)] dy, \tag{14}$$

and the residual non-blocked time CDF is

$$F_{t_\omega}(t) = 1 - e^{-\lambda t},\ t \geq 0. \tag{15}$$

*3) Conditional Non-Blocked/Blocked State Probabilities:* Consider now two instants of time, $t_0 = 0$ and $t_1$, $t_1 - t_0 = t > 0$. Denoting the non-blocked and the blocked states by 0 and 1, respectively, the conditional probabilities, $p_{00}(t)$, $p_{01}(t)$ as well as $p_{10}(t)$, $p_{11}(t)$ that there is non-blocked/blocked state at $t_1$ given that there was non-blocked/blocked state at $t_0$ are calculated further. The general solution for this problem follows from [35] and particularly $p_{00}(t)$ can be established as

$$p_{00}(t) = \frac{\mathbb{E}[\omega]}{\mathbb{E}[\omega] + \mathbb{E}[\eta]} + \frac{g(t)}{\mathbb{E}[\omega]}, \tag{16}$$

where $g(t)$ has the LT of

$$g^*(s) = \frac{\mathbb{E}[\omega]\mathbb{E}[\eta]}{(\mathbb{E}[\omega] + \mathbb{E}[\eta])s} - \frac{(1 - f_\omega^*(s))(1 - f_\eta^*(s))}{s^2(1 - f_\omega^*(s) f_\eta^*(s))}, \tag{17}$$

where $f_\omega^*(s)$ and $f_\eta^*(s)$ are the LTs of $f_\omega(x)$ and $f_\eta(x)$, respectively.

In the target case, the density of the blocked period is not available in a closed form, thus preventing from transitioning to the LT domain. For practical calculations, a simpler approach is proposed below based on utilizing the time domain convolutions. Observe that the probabilities $p_{00}(\Delta t)$ and $p_{01}(\Delta t)$ can be represented as

$$\begin{aligned} p_{00}(\Delta t) &= \sum_{i=0}^{\infty} \mathbb{P}\{A_i(\Delta t)\}, \\ p_{01}(\Delta t) &= \sum_{i=1}^{\infty} \mathbb{P}\{B_i(\Delta t)\}, \end{aligned} \tag{18}$$

where $A_i(t)$ are the events corresponding to starting in the non-blocked interval at $t_0$ and ending in the non-blocked interval after some $\Delta t = t_1 - t_0$, while having exactly $i$, $i = 0, 1, \ldots$, blocked periods during $\Delta t$. Similarly, $B_i(t)$ are the events corresponding to starting in the non-blocked interval at $t_0$ and ending in the blocked interval at $t_1$, while having exactly $i$, $i = 1, 2, \ldots$, non-blocked periods during $\Delta t$.

The probability of the event $A_0$, which is defined as residing in the non-blocked interval $\omega$ at time $t_1 = t_0 + \Delta t$ given that the system was in the same non-blocked state $\omega$ at time $t_0$, is produced by

$$\mathbb{P}\{A_0(\Delta t)\} = 1 - F_{t_\omega}(\Delta t), \tag{19}$$

where $F_{t_\omega}(\Delta t)$ is the residual time in the non-blocked period as obtained in (15).

The probability of the event $B_1$, which is defined as residing in the blocked interval $\eta$ at time $t_1$ given that the system was in the preceding non-blocked state $\omega$ at time $t_0$, is

$$\begin{aligned} \mathbb{P}\{B_1(\Delta t)\} &= 1 - F_{\eta + t_\omega}(\Delta t) - (1 - F_{t_\omega}(\Delta t)) \\ &= F_{t_\omega}(\Delta t) - F_{\eta + t_\omega}(\Delta t), \end{aligned} \tag{20}$$

where $F_\eta$ is the CDF of the blocked interval from (4) and $F_{\eta+\omega}$ denotes the CDF of the sum of random variables $x$ and $y$. As it was stated previously, note that the random variables $\eta$, $\omega$, and $t_\omega$ are independent. Hence, the CDF of the sum $F_{\eta+\omega}$ is obtained by convolving the densities of $x$ and $y$ and then integrating from 0 to $x$.

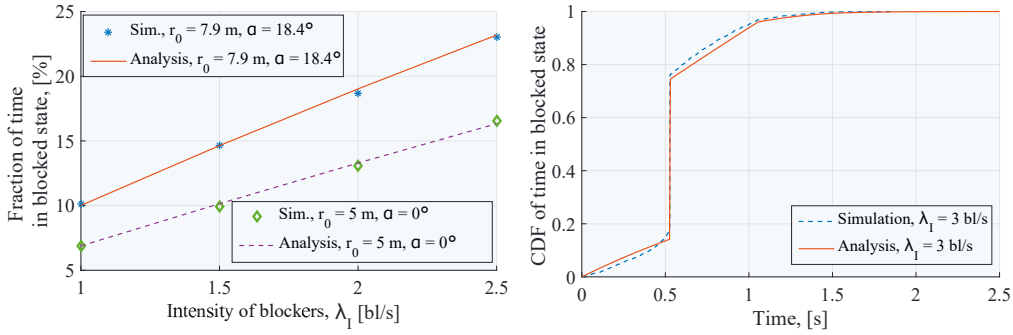


(a) Fraction of time spent in the blocked interval for one user

(b) CDF of time in the blocked interval, $\lambda_I$ = 3 bl/s

Fig. 5. Benchmarking the analytical model against the simulation results for the first usage scenario, S1.

Consider the event $A_1$ corresponding to when the Rx is in the non-blocked interval at time $t_1$ given that it was in the preceding non-blocked interval at time $t_0$ (there is a blocked interval embedded in between $t_0$ and $t_1$). The probability of this event is

$$\mathbb{P}\{A_1(\Delta t)\} = F_{\eta+t_\omega}(\Delta t) - F_{\omega+\eta+t_\omega}(\Delta t), \tag{21}$$

where $F_\omega$ is the CDF of the non-blocked interval.

Further, the probability of the event $B_2$ that the Rx is in the blocked interval at $t_1$ given that it was in the preceding blocked interval at $t_0$ (there is an additional non-blocked interval embedded in between $t_0$ and $t_1$), is established as

$$\mathbb{P}\{B_2(\Delta t)\} = F_{\omega+\eta+t_\omega}(\Delta t) - F_{\eta+\omega+\eta+t_\omega}(\Delta t). \tag{22}$$

Finally, the following is obtained

$$\begin{aligned}\mathbb{P}\{A_i(\Delta t)\} &= F_{\sum_{j=1}^{i-1}(\eta+\omega)+\eta+t_\omega}(\Delta t) \\ &\quad - F_{\sum_{j=1}^{i}(\eta+\omega)+t_\omega}(\Delta t), \qquad i \geq 1, \\ \mathbb{P}\{B_i(\Delta t)\} &= F_{\sum_{j=1}^{i-1}(\eta+\omega)+t_\omega}(\Delta t) \\ &\quad - F_{\sum_{j=1}^{i-1}(\eta+\omega)+\eta+t_\omega}(\Delta t), \quad i \geq 1. \end{aligned} \tag{23}$$

Note that the sum in (18) is infinite, and the probabilities $p_{00}$ and $p_{01}$ are numerically approximated by summing the terms up to the next summand that is sufficiently close to zero, until when the desired accuracy is achieved. The probabilities $p_{10}(\Delta t)$ and $p_{11}(\Delta t)$ are obtained similarly.

## IV. Accuracy Assessment and Numerical Analysis

In this section, the accuracy of the proposed model is assessed by benchmarking against system-level simulations. Then, the extent of temporal dependence under study is characterized as a function of the input parameters.

### A. Accuracy Assessment

In Fig. 5, the benchmarking of the proposed analytical model is conducted by utilizing our in-house simulation framework developed specifically for the purposes of this study. For the sake of exposition, it is assumed that the location of the user device of interest is fixed. The initial number of deployed blockers is calculated based on the arrival intensity of blockers entering the width of the sidewalk, $\lambda_I$. Particularly, considering the first usage scenario, S1, whenever the simulation is started, new blockers appear at the sidewalk edge of length $w_S$ according to a Poisson process with the arrival intensity of $\lambda_I$. Blockers then move around across the deployment with the constant speed up to the edge of the deployment area.

Fig. 5(a) reports on the average user blockage time for the first scenario (S1) obtained by using simulations as well as produced with the proposed analytical model for the width of the sidewalk, $w_S = 10$ m where the remaining parameters are given in the plot and Table II. The target accuracy was set to $10^{-4}$ which required from 6 to 9 summands in (18) to achieve it. As one may observe, the analytical results agree well with the simulation data, while both increase linearly with the growing arrival intensity of blockers. To assess the time correlation in the non-blocked/blocked state, the CDF of blocked duration is displayed in Fig. 5(b), where the width of the sidewalk is taken as $w_S = 10$ m, $r_0 = 7.9$ m, and $\alpha = 18.4^{\text{o}}$ with the rest of the parameters given in the Table II.

Here, close match between the analytical and the simulation results is also clearly visible. Small discrepancy between simulation and analysis is caused by the specifics of the analytical model. Particularly, in simulations the LoS blockage zone is explicitly modeled by taking into account the circular nature of the blocker. In the developed mathematical model, the LoS blockage zone is assumed to be of rectangular shape thus neglecting the curvature caused by the blocker, see Section III

TABLE II
Baseline System Parameters

| Parameter | Value |
|---|---|
| Height of Tx, $h_T$ | 3 m |
| Height of Rx, $h_R$ | 1.3 m |
| Tx-Rx distance, $r_0$ | 4.6 m |
| Height of a blocker, $h_B$ | 1.7 m |
| Diameter of a blocker, $d_m$ | 0.5 m |
| Speed of a blocker, $V$ | 1 m/s |
| Width of the sidewalk, $w_S$ | 5 m |
| Angle, $\alpha$ | $\pi/6$ |
| Frequency | 28 GHz |
| Bandwidth, $B$ | 1 GHz |
| Noise level | $-84$ dBm |
| Transmit power | 30 dBm |

for details. Even though one could extend the model to the case of more complex geometry of the LoS blockage zone thus leading to more complex expressions, the resulting error of approximation by a rectangle is negligible. Also, note that the steep behavior of the CDF around $0.5$ s is explained by the fact that for these particular environmental parameters and intensity of blockers most of the busy periods on the associated M/GI/$\infty$ queue are caused by a single blocker.

### *B. Numerical Analysis*

Further, the response of the blockage-related metrics to the selected ranges of input mmWave system parameters is analyzed. It should be mentioned that the choice of values for the parameters, and especially the Tx-Rx distance, is according to the need to compare all three mobility models. However, all parameters are adjustable during the computation if needed. Therefore, the key performance indicator in the deployment of interest is considered, namely, the fraction of time spent in the non-blocked state as illustrated in Fig. 6. It is a function of the arrival intensity of blockers, $\lambda_I$, for all the three scenarios under study. It should be noted that the fraction of time in blocked state is the complement of the fraction of time in the non-blocked state. The parameters for scenarios that are collected in the plot are shown in Table II.

For the purposes of a numerical comparison, consider the initial intensities for the first (S1) and the second scenario (S2) to be equal to 1 and 3 blockers per second, respectively. This corresponds to the following intensities of entering the LoS zone: $0.24$ and $0.71$ blockers per second. The initial arrival intensity is equal to the intensity of entering the LoS zone for the third scenario (S3). Clearly, as the arrival intensity of blockers grows, the fraction of time spent in the non-blocked/blocked state decreases/increases correspondingly. The main observation here is that the resulting trend is close to linear. One may notice further that for the arrival intensity of $0.24$ blockers per second the fraction of time spent in the non-blocked state is almost the same for all the three scenarios. As the arrival intensity increases and approaches the value of $0.71$, the difference between the first two scenarios and the third scenario becomes more considerable.

Fig. 7(a) and 7(b) report on the absolute values of the mean time spent in the non-blocked/blocked state for the same input parameters. As one may observe, the mean time spent in the non-blocked state decreases significantly as $\lambda_I$ increases from $0$ to $3$. However, the difference between the three scenarios for the two selected intensities is not significant. The mean time spent in the blocked state is the longest for the third scenario. It may be explained by the fact that the possible walking distance of a blocker is higher in this third scenario, since the blocker can move closer to the diagonal of the rectangle. Note that the blocked state behavior does not change drastically over a wide range of the considered blocker intensities. This is because even for higher intensities of blockers the blocked intervals are likely to feature only a single blocker occluding the LoS.

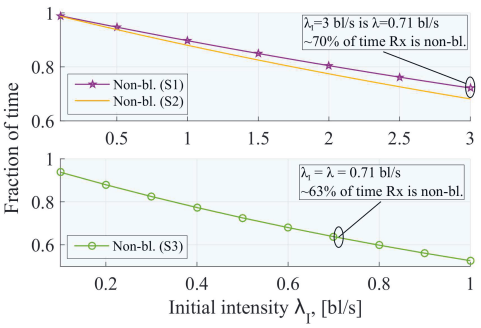


Fig. 6. Fraction of time in non-blocked/blocked state as a function of $\lambda_I$.

The mean time spent in the non-blocked/blocked state together with the associated fractions produce a direct implication on the dimensioning of mmWave systems. More specifically, using an appropriate propagation model, such as the one presented in [38], as well as accounting for the set of the modulation and coding schemes, one can evaluate the average throughput of a user located at a certain distance from the mmWave AP over a particular time slot. Given a certain value of the target mean data rate at the input, this information can be used further for determining the optimal coverage of a single mmWave AP. A close match with the result in [29] in terms of the mean time of LoS link blockage under the corresponding values of parameters is noted.

In Fig. 7(c) and 7(d), the CDFs of the residual time in the blocked/non-blocked state are shown. As one may observe, the probability for the time spent in the blocked interval to exceed the blocker's mean residence time is rather small. For example, the mean time in the blocked interval for the first scenario with $\lambda_I = 1$ bl/s is about $0.5$ s and the CDF $F_{t_\eta}(t < 0.5) = 0.9$ approximately. This fact implies that for a wide range of the considered intensities, in most cases, the blocked interval coincides with the residence time of a single blocker. Therefore, a user enters the non-blocked state after a certain time interval, which mainly depends on the size and the speed of the blocker, and less so on the arrival intensity of the blockers (note that the mean time in the blocked interval, Fig. 7(a), and the CDF of the residual time in the blocked state, Fig. 7(c), do not change drastically with increasing arrival intensity of blockers). Generally, knowing that the Rx is in the blocked interval, one can estimate the remaining time in this period. This may reduce the amounts of signaling information required for tracking the state of mmWave receivers. Also, the shape of the CDF curves for the residual time in the blocked interval is explained by the particular behavior of the CDF of time for a single blocker movement inside the LoS blockage zone, which has a distinct plateau.

Fig. 7(e) and 7(f) illustrate the behavior of the conditional probability to be in the non-blocked/blocked state at time $t_1$ given that the Rx was in the non-blocked/blocked state at time $t_0 = 0$, $t_1 > t_0$. Due to the long average time in the non-blocked state as compared to the average time in the blocked state, the probability to change the state from non-blocked to blocked is rather small for the considered values of $t_1$. In contrast, the probability to become non-blocked given that the Rx was blocked at time $t_0$ increases significantly. After that, the conditional probability converges to the unconditional one and the process in question "loses" its memory.

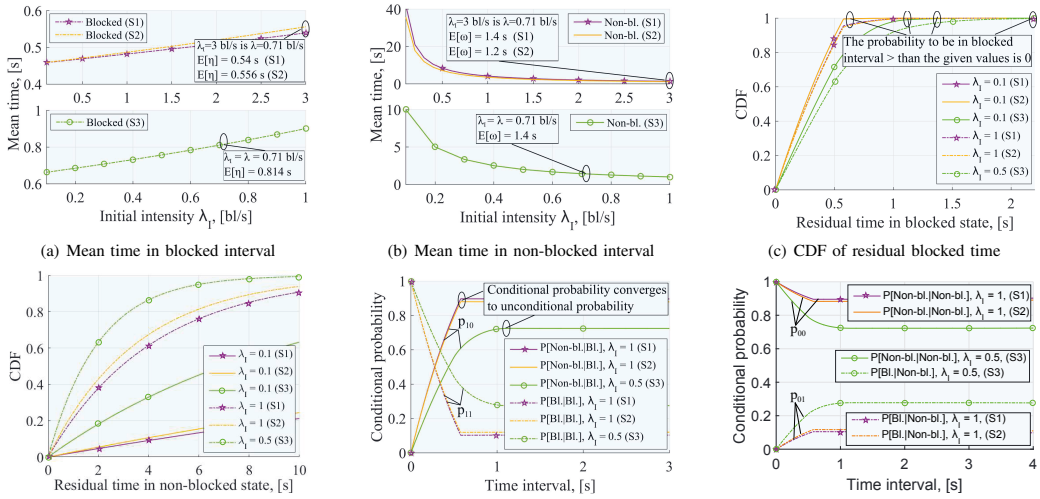


(a) Mean time in blocked interval

(b) Mean time in non-blocked interval

(c) CDF of residual blocked time

(d) CDF of residual non-blocked time

(e) Non-blocked/blocked state conditioned on blocked state at $t_0$

(f) Non-blocked/blocked state conditioned on non-blocked state at $t_0$

Fig. 7. Mean and residual time in non-blocked/blocked state and conditional probability of non-blocked/blocked state given that Rx is non-blocked/blocked.

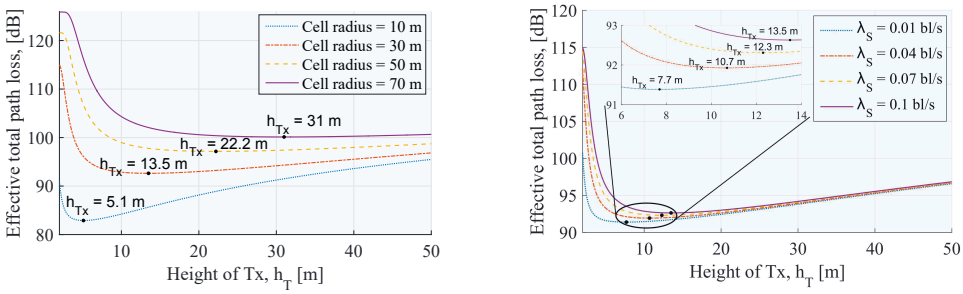


(a) Varying the cell radius

(b) Varying the arrival intensity of blockers

Fig. 8. Optimal height of the mmWave AP vs. cell radius and arrival intensity of blockers for the third scenario, S3.

## V. Example Applications of The Methodology

This section first summarizes two important analytical results stemming from the direct application of the proposed methodology. Then, the achievable performance gains in terms of the computation complexity are demonstrated after applying the model for system-level evaluation of mmWave systems.

### A. Optimal Height of the mmWave AP

Let us first determine the height of the mmWave AP, such that the average path loss to the user is minimal. To this end, the blocker mobility model to estimate the fraction of time in the non-blocked state as a function of $h_T$ is utilized, and then the mmWave propagation model from [38] to characterize the mean path loss as a function of $h_T$ is applied.

The average path loss can thus be established as in [19]

$$L_e = \mathbb{E}[T_l]L_{LoS} + (1 - \mathbb{E}[T_l])L_{nLoS}, \qquad (24)$$

where $\mathbb{E}[T_l]$ is the fraction of time that the Rx spends in the non-blocked state, which has been derived in (14), while $L_{LoS} = 61.4 + 20\log_{10}(d)$ and $L_{nLoS} = 72 + 29.2\log_{10}(d)$ are the path loss values for the LoS and the nLoS components for 28 GHz as obtained in [38] and $d = \sqrt{(h_T - h_R)^2 + r_0^2}$ is the three-dimensional distance between Tx and Rx.

For any value of the arrival intensity of blockers, the optimal height of the mmWave AP within the range of reasonable values can now be established by utilizing the graphical approach and plotting (24) to identify the value minimizing the average path loss at the cell edge (two-dimensional distance between Tx and Rx, $r_0$, is equal to the cell radius in that particular problem). The same could be derived numerically by taking a derivative of the average path loss from (24). To vary the arrival intensity of blockers that enter the LoS blockage zone proportionally to its dimensions, it is assumed that $\lambda_S = 0.1$ bl/s is the arrival intensity of blockers crossing the unit square area. The intensity of blockers entering the LoS blockage zone can then be written as $\lambda = \lambda_S r d_m$.

Fig. 8(a) demonstrates the optimal Tx height for different cell radius values in the third scenario. Here, the constant

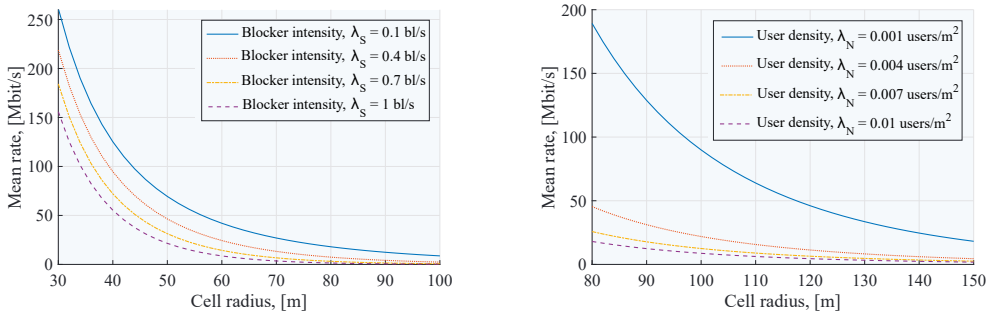


(a) Varying the cell radius and blocker arrival intensity

(b) Varying the cell radius and user density

Fig. 9. Mean data rate of the user at the cell edge vs. cell radius, user densities, and blocker arrival intensities for the third scenario, S3.

arrival intensity of blockers is set to $\lambda_S = 0.1$ bl/s, while the remaining parameters are given in Table II. As one may learn, an increase in the cell radius requires the mmWave Tx to be deployed higher in order to achieve the optimized propagation conditions at the cell edge. Further, Fig. 8(b) shows the optimal height of the Tx for a fixed cell radius of 30 m and different intensities of blockers that enter the unit square area of the LoS blockage zone, $\lambda_S$. It could be noticed that with the growing blocker arrival intensity the optimal height of the mmWave Tx increases as well. This effect is explained by the fact that the probability of residing in the non-blocked state decreases; hence, one needs to increase the height of the Tx to maximize the fraction of time spent in the non-blocked state.

The impact of the cell radius and intensity of blockers on the optimal height of the AP is summarized as follows:

- The optimal height of the AP from the range of realistic values highly depends on the cell radius, e.g., after increasing the cell radius by 7 times the optimal height grows by approximately 6 times.
- The impact of the intensity of blockers on the optimal height is less pronounced. For example, after increasing the intensity of blockers by 10 times the optimal height grows by only 1.7 times.

### B. Cell Range Analysis

Another direct application of the proposed model is to determine the maximum coverage range of the mmWave AP, such that a certain average data rate is delivered to all of the users. The latter can be achieved by ensuring that the user data rate at the cell edge is higher than the required minimum.

Assume a Poisson field of users in $\Re^2$ with the density of $\lambda_N$ users per square unit. Let $x$ be the intended radius of the mmWave coverage zone. The number of users in this covered area follows a Poisson distribution with the parameter $\lambda_N \pi x^2$. The traffic model is considered here to be "full buffer", that is, the mmWave system is observed in the highly-loaded conditions. Further, the maximum radius $x$ is determined, such that the capacity of at least $k$ Mbps is provided to each user. The bandwidth of the mmWave system, $B$, is allowed to be infinitesimally divisible. For simplicity, an equal division of bandwidth between all of the users is considered, even though any reasonable resource allocation mechanism can in principle be assumed, e.g., max-min or proportional fair [39].

The capacity delivered to the mmWave Rx located at $x$ can be derived as

$$R(x) = cB_i \log[1 + S(x)], \tag{25}$$

where $B_i$ is the bandwidth made available to the user of interest, $S(x)$ is the average signal-to-noise ratio (SNR) at this user, and $c$ is a constant accounting for imperfections of the modulation and coding schemes. In what follows, $c = 1$ is taken for simplicity.

Since the radio resource in the system is assumed to be distributed equally between all of the users, the bandwidth share actually available[2] to the Rx located at $x$ is $B_i = B/N$, where $N$ is a discrete random variable (RV) having a Poisson distribution with the density of $\lambda_N \pi x^2$ per considered area of interest. To obtain the SNR $S(x)$, the mmWave propagation model in [38] is employed by defining as $s_0(x)$ the SNR associated with the LoS state and as $s_1(x)$ the SNR associated with the nLoS state. The aggregate SNR is a two-valued discrete RV taking the values of $s_i(x)$, $i = 0, 1$, with the probabilities corresponding to the fraction of time spent in the non-blocked ($\mathbb{E}[T_l]$) and blocked ($1 - \mathbb{E}[T_l]$) state, respectively. The RVs $B_i$ and $S(x)$ are independent and their joint probability mass function (pmf) is derived as the product of the individual pmfs.

Once this joint pmf is obtained, one may proceed with determining the mean capacity $R(x_c)$ that is provided to a user located at the cell edge $x_c$ as

$$\begin{aligned}\mathbb{E}[R] = \sum_{N=1}^{\infty} \frac{(\lambda_N \pi x_c^2)^N (e^{-\lambda_N \pi x_c^2})}{N!} \\ \times \Big( \mathbb{E}[T_l] c \frac{B}{N} \log[1 + s_0(x_c)] \\ + (1 - \mathbb{E}[T_l]) c \frac{B}{N} \log[1 + s_1(x_c)] \Big),\end{aligned} \tag{26}$$

which can be evaluated numerically.

The mean capacity made available to a user located at the cell edge $x_c$ is reported in Fig. 9 for different user and blocker

[2]Note that instead of equal division of the bandwidth, more sophisticated resource allocation strategies can be enforced providing a certain degree of trade-off between fairness of per-user rates and aggregate system capacity, e.g., max-min, proportional fairness, weighted $\alpha$-fairness, see [40].

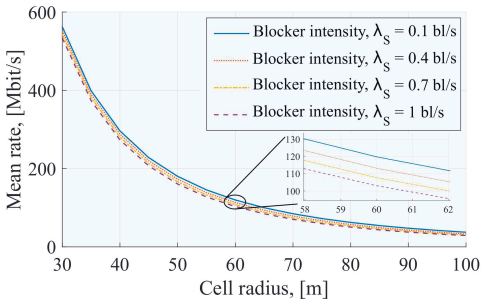


Fig. 10. Mean data rate across the cell vs. cell radius, user, and blocker arrival intensities for the third scenario, S3.

intensities. It is a function of the cell radius as well as the user and blocker intensities. The rest of the parameters are collected in Table II. In Fig. 9(a), the density of the users is set as $\lambda_N = 0.01$ users/m$^2$, and the height of the mmWave Tx is assumed to be $h_T = 10$ m. As an example, these plots correspond to the third scenario of interest. As one may observe, the mean data rate decreases as the cell range and/or the arrival intensity of blockers grows. It should be noted that for equal density of users and cell radius, increase in the density of human blockers leads to the drop in the mean data rate. Provided with a particular target data rate, one may use Fig. 9 to estimate the maximum cell radius for given blocker and user intensities, such that the chosen data rate is made available to all of the mmWave users.

In addition to the above, the analytical formulation for the mean data rate $R(x)$ of each user in the cell is given as

$$\mathbb{E}[R] = \sum_{N=1}^{\infty} \frac{(\lambda_N \pi x^2)^N (e^{-\lambda_N \pi x^2})}{N!} c\frac{B}{N} \times \int_0^{x_c} \Big( \mathbb{E}[T_l(x)] \log[1 + s_0(x)] + (1 - \mathbb{E}[T_l(x)]) \log[1 + s_1(x)] \Big) f_{X_U}(x) dx, \quad (27)$$

where $f_{X_U}(x) = 2x/x_c^2$ is the pdf of the distance $X_U$ between Tx and Rxs uniformly distributed in the cell of the radius $x_c$, while the fraction of time in non-blocked state is obtained by using (10) and (13) as

$$\mathbb{E}[T_l(x)] = \frac{1}{\exp(\lambda \mathbb{E}[T])}, \quad (28)$$

where $\mathbb{E}[T]$ is the mean residence time.

The mean rate of a randomly selected user in the cell is illustrated in Fig. 10. As one may observe, increasing the arrival intensity of blockers entering the unit area of the LoS blockage zone, $\lambda_S$, does not drastically affect the mean rate of a randomly selected user, as opposed to the mean rate at the cell edge.

The main points of the cell range analysis are summarized below:

- It is demonstrated that higher intensity of blockers decreases the mean rate of the user at the cell edge. By increasing the cell radius, the impact of the intensity of blockers becomes stronger, e.g., at the cell edge of 30 m the mean rate of a user is decreased by 1.7 times when the intensity grows by 10 times. However, when the cell radius is 100 m, the mean rate is 30 times lower.
- The mean rate of an arbitrarily chosen user decreases with the increased intensity of blockers. However, the effect of cell coverage on the mean rate is rather limited for all the considered intensities, e.g., 10 times higher intensity of blockers in the cell of radius 30 m decreases the mean rate by a factor of 1.05, whereas the same increase for 100 m radius cell decreases the mean rate by 1.3.

### C. System-Level Simulation Complexity

Today, the performance of complex wireless systems is primarily assessed within large-scale system-level simulation (SLS, see e.g., [41]) environments. The proposed mathematical model can be efficiently utilized as part of an SLS tool to substitute for the need to explicitly model the blockage process. This may drastically improve the simulation run times, especially in highly crowded urban scenarios.

In Table III, the computation complexity measurements is reported in terms of the SLS run time as a function of the blocker arrival intensity and the *environment update interval*, $T_U$ for the two cases: (i) direct simulation of the blockage process and (ii) application of the proposed model. From the SLS perspective, the environment update interval corresponds to how frequently the state of the users is monitored. In the latter case, each user has been associated with the pdf of the non-blocked and blocked intervals, thus implying that there is a need to update its state whenever the said interval expires. In the former direct modeling approach, at each environment update interval, one has to re-estimate the state of the users by employing the straightforward geometry considerations. Doing so significantly increases the computation complexity of the SLS evaluation, especially in dense environments. The experiments were conducted for the following parameters: the distance between the mmWave AP and the user is $r_0 = 10$ m and the blocker speed is $V = 1$ m/s. The simulation time was set to 50 s, while the hardware parameters were Intel Core i7-6700HQ CPU, 2.60 GHz (1 core run), and 32 GB RAM.

As it can be established by analyzing Table III, the complexity of both simulation and analysis grows as the environment update interval decreases. Even though the simulation run time does not depend on the blocker density (nor on the distance between the mmWave AP and the Rx), the SLS modeling complexity increases with a higher number of blockers. This

TABLE III
ABSOLUTE RUN TIME MEASUREMENTS IN SLS EVALUATION, S.

| $T_u$, ms \ $\lambda_I$, bl./s. | | 0.1 | 0.3 | 0.5 | 0.7 | 1.0 |
|---|---|---|---|---|---|---|
| 100 | simulation | 0.101 | 0.215 | 0.532 | 0.860 | 0.928 |
| | analysis | 0.250 | 0.272 | 0.243 | 0.256 | 0.292 |
| 70 | simulation | 0.208 | 0.290 | 0.820 | 1.356 | 2.801 |
| | analysis | 0.342 | 0.398 | 0.287 | 0.316 | 0.351 |
| 50 | simulation | 0.581 | 1.012 | 1.91 | 3.282 | 5.982 |
| | analysis | 0.681 | 0.538 | 0.369 | 0.694 | 0.499 |
| 10 | simulation | 1.211 | 3.921 | 5.867 | 7.119 | 10.92 |
| | analysis | 2.968 | 3.690 | 1.762 | 2.774 | 2.104 |
| 1 | simulation | 10.28 | 21.40 | 54.91 | 78.92 | 1.24e2 |
| | analysis | 22.64 | 18.18 | 23.98 | 19.09 | 22.11 |

is because the computation complexity is associated with the need to characterize an intersection with every blocker to determine the current state of each user. For the SLS results reported in this work, the blockers are deployed at the edge of the modeled scenario and move across the street. From the simulation perspective, computation complexity grows linearly as blocker arrival intensity increases, i.e., the overall modeling complexity is $O(n)$. Although the use of sophisticated techniques, such as spatial hashing, may reduce the complexity down to $O(log(n))$ at the expense of more cumbersome implementation, the resulting complexity would still grow rapidly for higher user densities. In stark contrast, with the proposed analytical modeling, the complexity remains constant at $O(1)$. Finally, with the decreasing update interval $T_U$, both analytical and simulation complexity grow linearly ($O(n)$). However, it may not be as important, because the value of $T_U$ <1 ms is seldom used in practical systems.

## VI. Conclusions

This work is aimed at a systematic characterization of the effects caused by the LoS blockage in cellular mmWave systems in presence of mobile blockers. To this end, three representative urban scenarios – as discussed in the current 3GPP specifications – were considered. The underlying process in the proposed mathematical approach was shown to be of alternating renewal nature, where non-blocked periods interchange with blocked intervals. The distribution of the non-blocked intervals was characterized by a simple memoryless exponential formulation, while the blocked periods were established to follow a general distribution. As example applications of the model, the height optimization of the mmWave AP, the mmWave cell range analysis, and the system-level modeling complexity reduction were considered.

Relying on the developed mathematical methodology, the impact of the LoS blockage is analyzed by establishing that the mean time in the blocked state is around 400-1000 ms for the typical input parameters, which amounts to a significant number of mmWave cellular superframes (around 20-50 according to [2]). Moreover, a strong temporal correlation for the timescales of interest in mmWave systems (i.e., less than about a second) was demonstrated. The contributed temporal analysis could be useful for modeling human body blockage in the mmWave-specific system-level evaluation tools as well as when designing the mmWave-centric communication protocols.

## Appendix A
## Residence Time in the LoS Blockage Zone

Here, the CDFs of the residence time in the LoS blockage zone is derived for the sidewalk 2 and the park/square/stadium scenarios (see Fig. 2).

*Second scenario, S2.* Consider the sidewalk 2 scenario. Here, the main difference as compared to the sidewalk 1 scenario is in that the users tend to move closer to the central lane of the street. We model this effect by using the triangular distribution with the following CDF

$$F_Y(x) = \begin{cases} 0, & x \le 0, \\ \dfrac{x^2}{w_S c}, & 0 < x \le c, \\ 1 - \dfrac{(w_S - x)^2}{w_S(w_S - c)}, & c < x \le w_S, \\ 1, & x > w_S, \end{cases} \tag{29}$$

where $c$ is the mode of the triangular distribution, which denotes the point with the highest probability density.

The distribution of distance, which is traveled by a blocker in the blockage zone, depends on the position of the LoS blockage zone with respect to the mode of the triangular distribution. The following five different cases are observed:

1) If $y_C \le c$:

$$F_L^{2,1}(x) = \begin{cases} 0, & x \le 0, \\ \dfrac{x\sin(2\alpha)}{y_C - y_A}, & 0 < x \le x_{min}, \\ 1, & x > x_{min}. \end{cases} \tag{30}$$

2) If $y_C - y_{min} \le c < y_C$, $y_{min} = x_{min}\cos(\alpha)\sin(\alpha)$:

$$F_L^{2,2}(x) = \begin{cases} 0, x \le 0, \\ \frac{\sin(2\alpha)(4c(y_A+y_C) - w_S(x\sin(2\alpha)+4(c+y_A)))}{4w_S(y_A^2+c(c-2y_C))+c(y_C^2-y_A^2)}, \\ 0 \le x < \frac{y_C - c}{\sin(\alpha)\cos(\alpha)}, \\ \frac{w_S(c-y_C)^2 + x\sin(2\alpha)(c-w_S)(y_A+y_C)}{w_S(y_A^2+c(c-2y_C))+c(y_C^2-y_A^2)}, \\ \frac{y_C - c}{\sin(\alpha)\cos(\alpha)} < x \le x_{min}, \\ 1, x > x_{min}. \end{cases} \tag{31}$$

3) If $y_A + y_{min} \le c < y_C - y_{min}$:

$$F_L^{2,3}(x) = \begin{cases} 0, x \le 0, \\ \frac{x\sin(2\alpha)(4c(y_A+y_C) - w_S(x\sin(2\alpha)+4(c+y_A)))}{4(w_S(y_A^2+c(c-2y_C))+c(y_C^2-y_A^2))}, \\ 0 < x \le x_{min}, \\ 1, x > x_{min}. \end{cases} \tag{32}$$

4) If $y_A \le c < y_A + y_{min}$:

$$F_L^{2,4}(x) = \begin{cases} 0, x \le 0, \\ \frac{x\sin(2\alpha)(4c(y_A+y_C) - w_S(x\sin(2\alpha)+4(c+y_A)))}{4(w_S(y_A^2+c(c-2y_C))+c(y_C^2-y_A^2))}, \\ 0 < x \le \frac{c - y_A}{\sin(\alpha)\cos(\alpha)}, \\ \frac{w_S(c-y_A)^2 + xc\sin(2\alpha)(y_A+y_C-2w_S)}{w_S(y_A^2+c(c-2y_C))+c(y_C^2-y_A^2)}, \\ \frac{c - y_A}{\sin(\alpha)\cos(\alpha)} < x \le x_{min}, \\ 1, x > x_{min}. \end{cases} \tag{33}$$

5) If $c \le y_A$:

$$F_L^{2,5}(x) = \begin{cases} 0, x \le 0, \\ \frac{x\sin(2\alpha)}{y_C - y_A}, 0 < x \le x_{min}, \\ 1, x > x_{min}. \end{cases} \tag{34}$$

For the second scenario, the arrival intensity of the blockers that enter the LoS blockage zone is given by

$$\lambda = \lambda_I \Big( F_Y(y_C) - F_Y(y_A) \Big). \tag{35}$$

The above may be explained by the fact that the majority of blockers cross the width of the sidewalk in the middle by following the triangular distribution for the entry point. Therefore, the Poisson process in time has the arrival intensity of blockers emerging at the effective width per time unit, $w_E$, equal to $\lambda$ as derived in (35).

*Third scenario, S3.* Finally, for the park/stadium/square scenario, the CDF of distance walked by a blocker in the blockage zone is given by

$$F_L^3(x) = \begin{cases} 0, \, x \leq 0, \\ w_1 F_L^{3,1}(x) + w_2 F_L^{3,2}(x), \\ 0 < x \leq \sqrt{d_m^2 + r^2}, \\ 1, \, x > \sqrt{d_m^2 + r^2}, \end{cases} \tag{36}$$

where the weights $w_1$ and $w_2$ are the probability for a blocker to enter from the long side (AD or CB, see Fig. 3) and to leave from another long side (AD or CB), and the probability for a blocker to enter from the short side (DC) and to leave from the long side (AD or CB), respectively, which are given by

$$\begin{aligned} w_1 &= \frac{d_m^2 + 3 d_m r}{d_m^2 + 3 d_m r + 2 r^2}, \\ w_2 &= \frac{2 r^2}{d_m^2 + 3 d_m r + 2 r^2}, \end{aligned} \tag{37}$$

and the corresponding CDFs are

$$F_L^{3,2}(x) = \begin{cases} 0, \, x \leq d_m, \\ \frac{d_m^2 - x^2 + 2r\sqrt{x^2 - d_m^2}}{r^2}, \\ d_m < x \leq \sqrt{d_m^2 + r^2}, \\ 1, \, x > \sqrt{d_m^2 + r^2}, \end{cases} \tag{38}$$

and

$$F_L^{3,1}(x) = \begin{cases} 0, x \leq 0, \\ \frac{\pi x^2}{4 r d_m}, 0 < x \leq \min(r, d_m), \\ \frac{1}{2 r d_m} (\min(r, d_m) \sqrt{x^2 - \min(r, d_m)^2} \\ + x^2 \arcsin(\frac{\min(r, d_m)}{x})), \\ \min(r, d_m) < x \leq \max(r, d_m), \\ \frac{1}{2 r d_m} (\min(r, d_m) \sqrt{\max(r, d_m)^2 - \min(r, d_m)^2} \\ + d_m (\sqrt{x^2 - d_m^2} - \sqrt{\max(r, d_m)^2 - d_m^2}) \\ + r (\sqrt{x^2 - r^2} - \sqrt{\max(r, d_m)^2 - r^2}) \\ + \max(r, d_m)^2 (\arccos(\frac{r}{\max(r, d_m)}) \\ + \arcsin(\frac{\min(r, d_m)}{\max(r, d_m)}) - \arcsin(\frac{d_m}{\max(r, d_m)})) \\ + x^2 (\arcsin(\frac{d_m}{x}) - \arccos(\frac{r}{x}))), \\ \max(r, d_m) < x \leq \sqrt{d_m^2 + r^2}, \\ 1, x > \sqrt{d_m^2 + r^2}. \end{cases} \tag{39}$$

The arrival intensity of the blockers that enter the zone, which affects the LoS for the third scenario, is then $\lambda = \lambda_I$.

## REFERENCES


[1] J. G. Andrews, S. Buzzi, C. Wan, S. V. Hanly, A. Lozano, A. C. K. Soong, and J. C. Zhang, "What will 5G be?," *IEEE Journal on Selected Areas in Communications*, vol. 32, pp. 1065–1082, June 2014.

[2] A. Ghosh, T. A. Thomas, M. C. Cudak, R. Ratasuk, P. Moorut, F. W. Vook, T. S. Rappaport, G. R. MacCartney, S. Sun, and S. Nie, "Millimeter-wave enhanced local area systems: a high-data-rate approach for future wireless networks," *IEEE Journal on Selected Areas in Communications*, vol. 32, pp. 1152–1163, June 2014.

[3] T. S. Rappaport, S. Sun, R. Mayzus, H. Zhao, Y. Azar, K. Wang, G. N. Wong, J. K. Schulz, M. K. Samimi, and F. Gutierrez Jr., "Millimeter wave mobile communications for 5G cellular: It will work!," *IEEE Access*, vol. 1, pp. 335–349, May 2013.

[4] METIS, "Initial channel models based on measurements," METIS deliverable D1.2, April 2014.

[5] 3GPP, "Study on channel model for frequencies from 0.5 to 100 GHz (Release 14)," 3GPP TR 38.901 V14.1.1, July 2017.

[6] COST IC1004 , "Channel measurements and modeling for 5G networks in the frequency bands above 6 GHz," white paper, April 2016.

[7] S. Hur, S. Baek, B. Kim, Y. Chang, A. F. Molisch, T. S. Rappaport, K. Haneda, and J. Park, "Proposal on millimeter-wave channel modeling for 5G cellular system," *IEEE Journal on Selected Areas in Communications*, vol. 10, pp. 454 – 469, April 2016.

[8] S. Sun, T. Rappaport, T. A. Thomas, H. C. A. Ghosh, Nguyen, I. Z. Kovacs, I. Rodriguez, O. Koymen, and A. Partyka, "Investigation of prediction accuracy, sensitivity, and parameter stability of large-scale propagation path loss models for 5G wireless communications," *IEEE Transactions on Vehicular Technology*, vol. 65, pp. 2843–2860, May 2016.

[9] M. K. Samimi and T. S. Rappaport, "3-D millimeter-wave statistical channel model for 5G wireless system design," *IEEE Transactions on Microwave Theory and Techniques*, vol. 64, pp. 2207–2225, July 2016.

[10] S. Sun, G. R. MacCartney Jr., and T. S. Rappaport, "A novel millimeter-wave channel simulator and applications for 5G wireless communications," in *IEEE International Conference on Communications (ICC)*, pp. 1–7, May 2017.

[11] M. Zhang, M. Mezzavilla, R. Ford, S. Rangan, S. S. Panwar, E. Mellios, D. Kong, A. R. Nix, and M. Zorzi, "Transport layer performance in 5G mmWave cellular," in *IEEE Conference on Computer Communications Workshops (INFOCOM WKSHPS)*, pp. 730–735, April 2016.

[12] M. Mezzavilla, S. Dutta, M. Zhang, M. R. Akdeniz, and S. Rangan, "5G mmWave module for the ns-3 network simulator," in *ACM International Conference on Modeling, Analysis and Simulation of Wireless and Mobile Systems*, pp. 283–290, November 2015.

[13] V. Petrov, D. Solomitckii, A. Samuylov, M. A. Lema, M. Gapeyenko, D. Moltchanov, S. Andreev, V. Naumov, K. Samouylov, M. Dohler, and Y. Koucheryavy, "Dynamic multi-connectivity performance in ultra-dense urban mmWave deployments," *IEEE Journal on Selected Areas in Communications*, vol. 35, pp. 2038–2055, September 2017.

[14] K. Haneda *et al.*, "5G 3GPP-like channel models for outdoor urban microcellular and macrocellular environments," in *IEEE 83rd Vehicular Technology Conference (VTC Spring)*, pp. 1–7, May 2016.

[15] R. J. Weiler, M. Peter, W. Keusgen, K. Sakaguchi, and F. Undi, "Environment induced shadowing of urban millimeter-wave access links," *IEEE Wireless Communications Letters*, vol. 5, pp. 440–443, August 2016.

[16] T. Bai, R. Vaze, and R. W. Heath Jr., "Using random shape theory to model blockage in random cellular networks," in *International Conference on Signal Processing and Communications (SPCOM)*, pp. 1–5, July 2012.

[17] T. Bai, R. Vaze, and R. W. Heath Jr., "Analysis of blockage effects on urban cellular networks," *IEEE Transactions on Wireless Communications*, vol. 13, pp. 5070–5083, September 2014.

[18] M. Abouelseoud and G. Charlton, "The effect of human blockage on the performance of millimeter-wave access link for outdoor coverage," in *IEEE Vehicular Technology Conference (VTC Spring)*, pp. 1–5, June 2013.

[19] M. Gapeyenko, A. Samuylov, M. Gerasimenko, D. Moltchanov, S. Singh, E. Aryafar, S. Yeh, N. Himayat, S. Andreev, and Y. Koucheryavy, "Analysis of human-body blockage in urban millimeter-wave cellular communications," in *IEEE International Conference on Communications (ICC)*, pp. 1–7, May 2016.

[20] Aalto University *et al.*, "5G channel model for bands up to 100 GHz," in *Workshop on Mobile Communications in Higher Frequency Bands, IEEE Globecom*, October 2016. [Online]. Available: http://www.5gworkshops.com/5GCM.html.

[21] M. Jacob, S. Priebe, A. Maltsev, A. Lomayev, V. Erceg, and T. Kürner, "A ray tracing based stochastic human blockage model for the IEEE 802.11ad 60 GHz channel model," in *Proc. of European Conference on Antennas and Propagation (EUCAP)*, pp. 3084–3088, April 2011.

[22] G. MacCartney, S. Deng, S. Sun, and T. S. Rappaport, "Millimeter-Wave human blockage at 73 GHz with a simple double knife-edge diffraction model and extension for directional antennas," in *IEEE Vehicular Technology Conference (VTC Fall)*, pp. 1–6, September 2016.

[23] K. Koufos and C. P. Dettmann, "Temporal correlation of interference in bounded mobile ad hoc networks with blockage," *IEEE Communications Letters*, vol. 20, pp. 2494–2497, December 2016.

[24] X. Zhang, F. Baccelli, and R. W. Heath Jr., "An indoor correlated shadowing model," in *IEEE Global Communications Conference (GLOBECOM)*, pp. 1–7, December 2015.

[25] F. Baccelli and X. Zhang, "A correlated shadowing model for urban wireless networks," in *IEEE Conference on Computer Communications (INFOCOM)*, pp. 801–809, August 2015.

[26] M. A. M. Miranda, J. C. S. Santos Filho, G. Fraidenraich, M. D. Yacoub, J. R. Moreira Neto, and Y. C. Zúñiga, "Correlation between signals from spaced antennas of stationary meteorological radars," *IEEE Transactions on Geoscience and Remote Sensing*, vol. 52, pp. 3116–3124, June 2014.

[27] K. Mahler, W. Keusgen, F. Tufvesson, T. Zemen, and G. Caire, "Tracking of wideband multipath components in a vehicular communication scenario," *IEEE Transactions on Vehicular Technology*, vol. 66, pp. 15–25, January 2017.

[28] S. Hahn, D. M. Rose, J. Sulak, and T. Kürner, "Impact of realistic pedestrian mobility modelling in the context of mobile network simulation scenarios," in *IEEE Vehicular Technology Conference (VTC Spring)*, pp. 1–5, May 2015.

[29] M. Jacob, C. Mbianke, and T. Kürner, "A dynamic 60 GHz radio channel model for system level simulations with MAC protocols for IEEE 802.11ad," in *IEEE International Symposium on Consumer Electronics (ISCE)*, pp. 1–5, June 2010.

[30] I. Kashiwagi, T. Taga, and T. Imai, "Time-varying path-shadowing model for indoor populated environments," *IEEE Transactions on Vehicular Technology*, vol. 59, pp. 16–28, January 2010.

[31] A. Samuylov, M. Gapeyenko, D. Moltchanov, M. Gerasimenko, S. Singh, N. Himayat, S. Andreev, and Y. Koucheryavy, "Characterizing spatial correlation of blockage statistics in urban mmWave systems," in *IEEE Global Communications Workshops (GLOBECOM Wkshps)*, pp. 1–7, December 2016.

[32] P. Madadi, F. Baccelli, and G. Veciana, "On temporal variations in mobile user SNR with applications to perceived QoS," in *International Symposium on Modeling and Optimization in Mobile, Ad Hoc, and Wireless Networks (WiOpt)*, pp. 1–8, May 2016.

[33] M. Jacob, S. Priebe, T. Kürner, M. Peter, M. Wisotzki, R. Felbecker, and W. Keusgen, "Fundamental analyses of 60 GHz human blockage," in *European Conference on Antennas and Propagation (EuCAP)*, pp. 117–121, April 2013.

[34] D. R. Cox and H. D. Miller, *The theory of stochastic processes*. Wiley, 1965.

[35] D. R. Cox, *Renewal theory*. Methuen and Co ltd., 1970.

[36] D. J. Daley, "The busy period of the M/GI/$\infty$ queue," *Queueing Systems: Theory and Applications*, vol. 38, no. 2, pp. 195–204, 2001.

[37] S. Ross, *Introduction to probability models*. Academic Press, 10th ed., 2009.

[38] M. R. Akdeniz, Y. Liu, M. K. Samimi, S. Sun, S. Rangan, T. S. Rappaport, and E. Erkip, "Millimeter wave channel modeling and cellular capacity evaluation," *IEEE Journal on Selected Areas in Communications*, vol. 32, pp. 1164–1179, June 2014.

[39] J. Walrand and A. K. Parekh, "Congestion control, routing and scheduling in communication networks: A tutorial," *IEICE Transactions on Communications*, vol. 96, no. 11, pp. 2714–2723, 2013.

[40] E. Yaacoub and Z. Dawy, "A survey on uplink resource allocation in OFDMA wireless networks," *IEEE Communications Surveys & Tutorials*, vol. 14, no. 2, pp. 322–337, 2012.

[41] "WINTERsim system-level simulator, 2015," *http://winter-group.net/downloads/*.


**Margarita Gapeyenko** is a Ph.D. candidate at the Laboratory of Electronics and Communications Engineering at Tampere University of Technology, Finland. She earned her M.Sc. degree in Telecommunication Engineering from University of Vaasa, Finland, in 2014, and B.Sc. degree in Radio-Engineering, Electronics, and Telecommunications from Karaganda State Technical University, Kazakhstan, in 2012. Her research interests include mathematical analysis, performance evaluation, and optimization methods of future wireless networks, device-to-device communication, and 5G-grade heterogeneous networks.

**Andrey Samuylov** received the Ms.C. in Applied Mathematics and Cand.Sc. in Physics and Mathematics from the RUDN University, Russia, in 2012 and 2015, respectively. Since 2015 he is working at Tampere University of Technology as a researcher, focusing on mathematical performance analysis of various 5G wireless networks technologies. His research interests include P2P networks performance analysis, performance evaluation of wireless networks with enabled D2D communications, and mmWave band communications.

**Mikhail Gerasimenko** is a Researcher at Tampere University of Technology in the Laboratory of Electronics and Communications Engineering. Mikhail received Specialist degree from Saint-Petersburg University of Telecommunications in 2011. In 2013, he obtained Master of Science degree from Tampere University of Technology. Mikhail started his academic career in 2011 and since then he appeared as (co-)author of multiple scientific journal and conference publications, as well as several patents. He also acted as reviewer and participated in educational activities. His main subjects of interest are wireless communications, machine-type communications, and heterogeneous networks.

**Dmitri Moltchanov** is a Senior Research Scientist in the Laboratory of Electronics and Communications Engineering, Tampere University of Technology, Finland. He received his M.Sc. and Cand.Sc. degrees from Saint-Petersburg State University of Telecommunications, Russia, in 2000 and 2002, respectively, and Ph.D. degree from Tampere University of Technology in 2006. His research interests include performance evaluation and optimization issues of wired and wireless IP networks, Internet traffic dynamics, quality of user experience of real-time applications, and traffic localization P2P networks. Dmitri Moltchanov serves as TPC member in a number of international conferences. He authored more than 80 publications.

**Sarabjot Singh** ('SM 09, M' 15) is a Principal Engineer at Uhana Inc. CA. He received the B. Tech. from IIT, India, and the M.S.E and Ph.D. in EE from UT Austin. His past affiliations include Intel, Nokia Technologies, Bell Labs, and Qualcomm Inc, where he worked on protocol and algorithm design for next generation of cellular and WiFi networks. Dr. Singh is interested in the system and architecture design of wireless networks leveraging theoretical and applied tools. He is a co-author of more than 40 patent applications, and multiple conference and journal papers. He was the recipient of the President of India Gold Medal in 2010, the ICC Best Paper Award in 2013, and recognized for being a prolific inventor at Intel Corp.

**Mustafa Riza Akdeniz** (S'09) received the B.S. degree in electrical and electronics engineering from Bogazici University, Istanbul, Turkey, in 2010 and the Ph.D. degree in electrical and computer engineering at New York University Tandon School of Engineering, Brooklyn, NY in 2016. He is working as a research scientist for Intel Labs in Santa Clara, CA. His research interests include wireless communications, wireless channel modeling, and information theory.

**Ehsan Aryafar** is an Assistant Professor of Computer Science at Portland State University. Prior to that and from 2013 to 2017, he was a Research Scientist at Intel Labs in Santa Clara, CA. He received the B.S. degree in Electrical Engineering from Sharif University of Technology, Iran, in 2005, and the M.S. and Ph.D. degrees in Electrical and Computer Engineering from Rice University, Houston, Texas, in 2007 and 2011, respectively. From 2011 to 2013, he was a Post-Doctoral Research Associate in the Department of Electrical Engineering at Princeton University. His research interests are in the areas of wireless networks and networked systems, and span both algorithm design as well as system prototyping. He has more than 30 issued and pending patents in the areas of mobile and wireless systems.

**Nageen Himayat** is a Principal Engineer with Intel Labs, where she leads a team conducting research on several aspects of next generation (5G/5G+) of mobile broadband systems. Her research contributions span areas such as multi-radio heterogeneous networks, mm-wave communication, energy-efficient designs, cross layer radio resource management, multi-antenna, and non-linear signal processing techniques. She has authored over 250 technical publications, contributing to several IEEE peer-reviewed publications, 3GPP/IEEE standards, as well as holds numerous patents. Prior to Intel, Dr. Himayat was with Lucent Technologies and General Instrument Corp, where she developed standards and systems for both wireless and wire-line broadband access networks. Dr. Himayat obtained her B.S.E.E degree from Rice University, and her Ph.D. degree from the University of Pennsylvania. She also holds an MBA degree from the Haas School of Business at University of California, Berkeley.

**Sergey Andreev** is a Senior Research Scientist in the Laboratory of Electronics and Communications Engineering at Tampere University of Technology, Finland. He received the Specialist degree (2006) and the Cand.Sc. degree (2009) both from St. Petersburg State University of Aerospace Instrumentation, St. Petersburg, Russia, as well as the Ph.D. degree (2012) from Tampere University of Technology. Sergey (co-)authored more than 100 published research works on wireless communications, energy efficiency, heterogeneous networking, cooperative communications, and machine-to-machine applications.

**Yevgeni Koucheryavy** is a Full Professor in the Laboratory of Electronics and Communications Engineering of Tampere University of Technology (TUT), Finland. He received his Ph.D. degree (2004) from TUT. He is the author of numerous publications in the field of advanced wired and wireless networking and communications. His current research interests include various aspects in heterogeneous wireless communication networks and systems, the Internet of Things and its standardization, as well as nanocommunications. He is Associate Technical Editor of IEEE Communications Magazine and Editor of IEEE Communications Surveys and Tutorials.

# PUBLICATION III

**Line-of-Sight Probability for mmWave-based UAV Communications in 3D Urban Grid Deployments**

M. Gapeyenko, D. Moltchanov, S. Andreev and R. W. Heath Jr.

*IEEE Transactions on Wireless Communications* (2021)

# Line-of-Sight Probability for mmWave-based UAV Communications in 3D Urban Grid Deployments

Margarita Gapeyenko, Dmitri Moltchanov, Sergey Andreev, and Robert W. Heath Jr.

***Abstract*—The network operators will soon be accommodating a new type of users: unmanned aerial vehicles (UAVs). 5G New Radio (NR) technology operating in the millimeter-wave (mmWave) frequency bands can support the emerging bandwidth-hungry applications facilitated by such aerial devices. To reliably integrate UAVs into the NR-based network infrastructure, new system models that capture the features of UAVs in urban environments are required. As city building blocks constitute one of the primary sources of blockage on the links from the UAV to its serving base station (BS), the corresponding line-of-sight (LoS) probability models are essential for accurate performance evaluation in realistic scenarios. We propose a LoS probability model in UAV communication setups over regular urban grid deployments, which is based on a Manhattan Poisson line process. Our approach captures different building height distributions as well as their dimensions and densities. Under certain characteristic distributions, closed-form expressions for the LoS probability are offered. Our numerical results demonstrate the importance of accounting for the building height distribution type as well as the orientation of the UAV with respect to its BS. By comparing our model with the standard ITU and 3GPP formulations, we establish that the latter provide an overly optimistic approximation for various deployments.**

***Index Terms*—3D LoS probability, urban grid deployment, mmWave radio, UAV communication, 5G NR technology**

## I. Introduction

According to recent studies, millimeter-wave (mmWave) communication promises to support connectivity between unmanned aerial vehicles (UAVs) and their serving radio infrastructure [1], [2]. With larger available bandwidths, mmWave transmission enables UAV-based applications and services that require high data rates, such as real-time video transfer, area surveillance, and many more. As mmWave bands are embraced by 5G New Radio (NR) access technology, the latter is expected to accommodate a new type of UAV users [3]–[5]. However, the incorporation of specific UAV features, such as their three-dimensional (3D) mobility, introduces further challenges and requires modifications to the existing channel models [6], [7].

One of the essential roadblocks for arranging seamless UAV support in mmWave-based 5G NR systems is the blockage of line-of-sight (LoS) radio propagation paths. As UAVs are envisioned to be utilized in city deployments [8], buildings constitute a major source of LoS blockage for the UAV to base station (BS) links [9]. The penetration losses on mmWave links occluded by a building may reach up to 40 dB [10], which can cause frequent and harmful service interruptions. As a result, characterizing the LoS blockage probability is a timely and important problem in the field.

The challenge of LoS blockage by buildings in urban deployments has been addressed in the literature, where several models were ratified by 3GPP and ITU-R [11], [12]. However, as we review in Section II, most of these earlier efforts consider fixed building heights and/or widths as well as randomized building layouts. These deployment parameters may significantly affect the resultant LoS probability, especially in urban grid scenarios. Moreover, some of the past models do not allow for simple closed-form solutions for the LoS probability that are suitable for further performance assessment of the prospective UAV deployments with system-level evaluations.

In this work, we develop an analytical model to derive the LoS probability for both fixed UAV locations and the cases where the UAVs are distributed uniformly over the BS coverage area. We consider a regular urban grid deployment of building blocks captured by a Manhattan Poisson line process (MPLP) having generally distributed building heights. For the fixed UAV location case, we produce a closed-form expression for the LoS probability under certain characteristic distributions of building heights. Our proposed model is capable of assessing the impact of urban grid deployment type on the LoS probability for the UAV to BS connections. Further, we systematically study the effects of the building heights and densities on the links between the UAV and its serving BS.

The main contributions of this work are the following.

- We propose a novel mathematical model that captures the essential details of 3D urban grid deployments to assess the existence of the LoS BS-to-UAV path. The developed model provides the LoS probability as a closed-form solution for a set of well-known building height distributions.
- Our performance evaluation campaign demonstrates that the LoS probability is highly sensitive to the (i) type of the urban grid deployment, (ii) form of the building height distribution, and (iii) UAV location with respect to the BS.
- Our comparison of the proposed model with the existing standardized formulations (e.g., those by 3GPP and ITU-R) indicates that the latter offer an overly optimistic approximation for the UAV LoS probability for a range of various deployments.

The rest of this text is organized as follows. In Section II, we provide a brief account of the related studies. Further,

M. Gapeyenko, D. Moltchanov, and S. Andreev are with Tampere University, Tampere, Finland (e-mail: firstname.lastname@tuni.fi)

R. W. Heath Jr. is with North Carolina State University, Raleigh NC (e-mail: rwheathjr@ncsu.edu)

This work was supported in part by the Academy of Finland (projects RADIANT and IDEA-MILL), JAES Foundation (project STREAM) and in part by the National Science Foundation under Grant No. ECCS-1711702 and CNS-1731658.

in Section III, our system model is outlined together with its main components. In Section IV, the respective analysis method is developed. We study the effects of the key system parameters on the UAV LoS blockage probability in Section V. The conclusions are offered in the last section.

## II. Related Work

In this section, we provide a literature review related to the blockage in general. We then give a comprehensive description of the LoS blockage models available to the academia and standardization bodies.

### A. Blockage Modeling

According to the IMT-2020 requirements [13], the channel models for the bands of above 6 GHz should have accurate 3D space-time characteristics in LoS and non-LoS (nLoS) conditions. Different types of blockage may transition the channel state from LoS to nLoS, namely: (i) self-body blockage, e.g., head of a user; (ii) small-scale blockage, e.g., vehicle or human body; and (iii) large-scale blockage, e.g., buildings.

In [14], the study delivered a model characterizing self-body blockage via a cone blockage approach. In [15], the authors proposed a method to calculate the probability of blockage caused by human bodies, where humans are distributed uniformly over the area. Application of stochastic geometry tools allowed to capture more comprehensive human-body blockage scenarios. For example, in [16], the proposed model simultaneously accounted for link blockage, transmission directivity, and vertical or horizontal directionality of transmit and receive antennas in mmWave UAV-to-ground communication scenarios. In [17], a coverage analysis was offered, while in [18], an overview of mathematical models for mmWave system modeling was provided.

There are two inherent properties of the reviewed models that allow for in-depth analysis: (i) distance between the BS and the user equipment (UE) is assumed to be much larger as compared to the dimensions of blockers and (ii) humans are distributed irregularly over the landscape. The latter property permits to utilize purely random models of UE locations, such as Poisson Point Process (PPP), while the former one does not force to count the exact number of blockers that may or may not occlude the LoS propagation path. However, these two properties do not hold for large-scale blockage. Below, we conduct a review of the existing LoS probability models that consider large-scale blockage and complete this section by indicating the gap that the proposed model can fill in.

### B. Large-Scale Blockage

There has been extensive work to estimate, analytically evaluate, or otherwise compute the LoS probability due to blockage by buildings. The research back from 1984 [19] proposed a mathematical formulation to derive the LoS probability in built-up areas for a receiver (Rx) to transmitter (Tx) pair. The proposed framework [19] relied on an analysis of the mean free path of moving particles in randomly distributed targets. The resultant LoS probability was calculated for the scenario where buildings are located along the $X$-axis between the Tx and the Rx, and under exponentially distributed building heights.

Further, in [20], the scenario considered a link between a ground user and a satellite. That study addressed the blockage arising from the buildings directly adjacent to the Rx because of the high altitudes of satellites. Hence, the derivation of the LoS probability was reduced to an integration of the building heights. The work in [21] considered the Fresnel zone to derive the LoS probability. For this purpose, a single knife-edge diffraction model was employed to identify the radius of the Fresnel zone and thus characterize the LoS probability.

The recent studies of terrestrial mmWave users actively considered the LoS probability due to its significant role in mmWave communication scenarios [18]. Particularly, the research in [22] contributed an analytical framework to establish the LoS probability for Tx to Rx links in an irregular deployment of buildings. The latter was represented as random-sized rectangles with the centers forming a PPP on a plane. The proposed approach argued for a reasonable approximation of the LoS probability in the scenarios where deployment is irregular, e.g., a university campus.

Later, the research in [23] contributed the LoS probability for air-to-everything links in a scenario with randomly distributed screens by following a similar approach as in [22]. The screens were representative of buildings with their height disregarded in the derivations. To further simplify the LoS modeling and provide a closed-form expression for the LoS probability, the work in [24] demonstrated the so-called LoS ball model. Accordingly, there is a circular area of a certain radius around the BS, where there is LoS with probability 1. Otherwise, there is link blockage for the Rx located outside of this radius.

The study in [25] proposed a frequency-dependent LoS probability model for a scenario with randomly-dropped cuboid buildings and uniformly-distributed building heights. That work also considered the first Fresnel zone and delivered the LoS probability in its integral form. Closed-form solutions were obtained for a number of special cases of interest including the situation where there is no height difference between the Tx and the Rx.

Not limited to irregular urban deployments, a number of studies addressed regular urban grids. In [26], the derived framework captured an urban grid with the MPLP wherein its lines represented the streets. Due to the features of the considered setup, where the user height was assumed to be shorter than the building height, the model imposed LoS conditions whenever a user was located on the street where the BS was deployed. However, this approach is not directly applicable to the UAV users as their altitudes of flight are comparable to the heights of buildings and cannot be ignored.

In [27], the authors contributed system-level simulation results for LTE and mmWave-based systems that support UAVs. That study was based upon real-world data from the city of Gent. Particularly, it reported the LoS probability between the terrestrial BSs and the UAV as a function of the UAV height derived from simulation data. The research in [28] proposed a method for deriving the LoS probability based on a

point cloud collected with a scan laser, where it was checked whether any point fell into the Fresnel zone of a BS-to-UE link. The methodology in question was applied to both open-square and shopping-mall scenarios for gathering the data and fitting them into an exponential LoS probability model.

A large-scale measurement campaign for the LoS probability was performed in [29] by using a ray-tracing approach. Similarly to [28], the obtained statistical data were fitted to the model. A limitation of these past studies is in the amounts of time required to conduct measurement campaigns, ray-tracing studies, or system-level simulations on the city-wide scales and with varying parameters, such as BS and building heights, etc.

### C. UAV LoS Modeling by 3GPP and ITU-R

ITU-R and 3GPP also considered an urban grid deployment as part of their efforts. Particularly, ITU-R P.1410 [12] addressed the frequency range of 20 to 50 GHz. The LoS probability was defined as $\mathbb{P}_{\text{LoS}}^{\text{ITU}}(r, h_{\text{T}}, h_{\text{R}}, \alpha, \beta, \gamma)$, which is the probability that the Tx-to-Rx link is not occluded by a building. The input parameter $r$ is the two-dimensional (2D) distance in kilometers between the Tx and the Rx, $h_{\text{T}}$ and $h_{\text{R}}$ are the Tx and Rx heights, respectively. The value of $\alpha$ is the fraction of the area covered by buildings to the total area, $\beta$ is the average number of buildings per unit area, and $\gamma$ is a height distribution parameter.

To simplify the notation, we further employ $\mathbb{P}_{\text{LoS}}^{\text{ITU}}$ as the ITU LoS probability, which is given as

$$\mathbb{P}_{\text{LoS}}^{\text{ITU}} = \prod_{n=0}^{m} \left( 1 - \exp\left( \frac{(h_{\text{T}} - \frac{(n+\frac{1}{2})(h_{\text{T}}-h_{\text{R}})}{m+1})^2}{2\gamma^2} \right) \right), \quad (1)$$

where $m = \lfloor r\sqrt{(\alpha\beta)} \rfloor - 1$ is the number of buildings in-between Tx and Rx. The work in [30] considered this model for the air-to-ground LoS probability modeling. One of the limitations of this formulation is that it assumes the building bases to be perpendicular to the LoS projection between the Rx and the Tx onto $\Re^2$. Even though the model accounts for different mean heights of Tx and Rx, it captures neither alternative building height distributions nor the LoS angle of departure (AoD). Finally, the output of this modeling is only available in the product-form, which limits its applicability.

To broadly characterize the UAV-based scenarios, 3GPP in TR 36.777 [11] proposed a LoS probability model for the link between the UAV and the BS. It distinguishes various deployment types by delivering separate dedicated solutions. The structure of this model is different for various heights of the BS and the UAV. Below, we provide an example for the UMi street canyon LoS model $\mathbb{P}_{\text{LoS}}^{\text{3GPP}}(\ell_{\text{2D}}, h_{\text{R}})$, which is applicable for $h_{\text{T}} = 10\,\text{m}$ and the UAV heights in the range of $22.5\,\text{m} < h_{\text{R}} < 300\,\text{m}$. The input parameter $\ell_{\text{2D}}$ is the 2D distance in meters between the UAV and the BS.

We further employ $\mathbb{P}_{\text{LoS}}^{\text{3GPP}}$ as the 3GPP LoS probability that is defined as follows[1]

$$\mathbb{P}_{\text{LoS}}^{\text{3GPP}} = \begin{cases} 1, & \ell_{\text{2D}} \leq d, \\ \frac{d}{\ell_{\text{2D}}} + \left[1 - \frac{d}{\ell_{\text{2D}}}\right] \exp\left[\frac{-\ell_{\text{2D}}}{p_1}\right], & \ell_{\text{2D}} > d, \end{cases} \quad (2)$$

where the variables $p_1$ and $d$ are given as

$$p_1 = 233.98 \log_{10}(h_{\text{R}}) - 0.95,$$
$$d = \max(294.05 \log_{10}(h_{\text{R}}) - 432.94,\ 18). \quad (3)$$

The precomputed parameters of the 3GPP LoS model do not permit to alter the deployment dimensions, such as building heights or densities. Furthermore, 3GPP provided the LoS model for a fixed BS height.

To summarize, when considering the UAV-to-BS operation in typical urban deployments, one cannot assume purely stochastic deployments of blockers as cities typically follow semi-regular street layouts. Moreover, the sizes of blockers are then comparable to the lengths of the propagation paths. Hence, one needs to explicitly consider each potential blocker and its position with respect to the LoS path. Finally, as the UAV height is comparable to the heights of buildings (in contrast to the terrestrial users), the latter cannot be disregarded in the LoS blockage modeling.

Despite several studies completed to date, there are no LoS probability models that simultaneously capture the features of a regular urban grid deployment, the planar urban geometry, and the building height distribution. As many of the civil UAV-based applications, such as video monitoring and package delivery, are more relevant in urban deployments, the intended LoS link blockage analysis in the corresponding environment becomes essential.

Having an accurate LoS probability model as part of system-level analysis allows to calculate the metrics of interest more carefully and thus assess the operation of a UAV-ready network. The system-level simulation times in UAV-centric scenarios may be reduced dramatically by avoiding exact modeling of the city deployment and instead employing analytical LoS probability values. In what follows, we propose a new LoS model that captures the said parameters, assess their effects, and compare the results against those for the formulations ratified by 3GPP and ITU-R.

## III. System Model

In this section, we introduce the considered urban grid deployment. We then specify additional assumptions on the locations of the communicating entities and define the metrics of interest. The main parameters are collected in Table I.

### A. Urban Grid Layout

We consider an urban grid setup illustrated in Fig. 1. It assumes that the mean side of a building block is equal to $\mu_{\text{b}}$ and the mean street width is $\mu_{\text{s}}$. To capture a Manhattan-type urban grid deployment, we utilize a commonly-employed MPLP [26] as shown in Fig. 1(b). This process is specified by

[1]For different BS heights, $h_{\text{T}}$, 35 m for RMa-AV, 25 m for UMa-AV, refer to Table B-1, TR 36.777. For $h_{\text{R}}$ below 22.5 m, the UMi model in Table 7.4.2-1 of TR 38.901 becomes applicable.

two one-dimensional (1D) homogeneous PPPs along the $X$- and $Y$-axis with the intensity $\lambda = 1/(\mu_\mathrm{b} + \mu_\mathrm{s})$ and the origin at point $O$. The points generated by the PPPs are the origins of the streets displayed as parallel straight lines in Fig. 1(b).

We assume that the line segment between two neighboring points along the $X$- and $Y$-axis contains the side of a building block (hereinafter referred to as "block") in the proportion of $\mu_\mathrm{b}/(\mu_\mathrm{b} + \mu_\mathrm{s})$, while the remainder is the street. As demonstrated in Fig. 1(b), the resultant rectangles represent buildings. They act as potential blockers for the LoS path between the BS and the UAV. The height of each block is a random variable (RV) $H_\mathrm{B}$ with the probability density function (pdf) $f_{H_\mathrm{B}}(h)$ and the cumulative distribution function (CDF) $F_{H_\mathrm{B}}(h)$.

### B. Network Deployment

Further, we consider the locations of the BS and the UAV in our urban grid layout as illustrated in Fig. 1(a). We assume that the BS is deployed along the street named a *typical street*. The location ground point of the BS is point $T$ and the height is $h_\mathrm{T}$. The UAV is placed at point $R$ and at height $h_\mathrm{R}$. We assume that the UAVs cannot be located inside buildings. The building always remains below the UAV in the case where their 2D positions coincide. There are two commonly considered BS locations in urban grid deployments, which are studied in our work [31]:

- The BS is placed at the intersection of two perpendicular typical streets with a constant width of $w_\mathrm{h}$ and $w_\mathrm{v}$. In this scenario, the origin of the urban grid is located $K_\mathrm{h}w_\mathrm{h}$ and $K_\mathrm{v}w_\mathrm{v}$ away from the BS position as depicted in Fig. 2(a). The coefficients $K_\mathrm{h}$ and $K_\mathrm{v}$ in the range of $(0, 1)$ represent the relative position of the BS along the typical street, e.g., $K_\mathrm{h} = K_\mathrm{v} = 0.5$ refers to the BS located at the center of the intersection.
- The BS is placed on the typical street with a constant width of $w_\mathrm{v}$. In this scenario, the origin of the urban grid is $K_\mathrm{v}w_\mathrm{v}$ away from the BS position as shown in Fig. 2(b).

TABLE I
SUMMARY OF NOTATION AND PARAMETERS

| Notation | Description |
|---|---|
| $h_\mathrm{T}$ | BS height |
| $h_\mathrm{R}$ | UAV height |
| $H_\mathrm{B}$ | Building block height |
| $f_{H_\mathrm{B}}(h)$ | pdf of building block heights |
| $F_{H_\mathrm{B}}(h)$ | CDF of building block heights |
| $\ell_\mathrm{2D}$ | 2D distance between BS and UAV |
| $\phi_\mathrm{D}$ | LoS AoD |
| $\lambda$ | Intensity of points along $X$- and $Y$-axis |
| $w_\mathrm{h}$, $w_\mathrm{v}$ | Width of horizontal and vertical typical streets |
| $K_\mathrm{h}$, $K_\mathrm{v}$ | BS position coefficients on horizontal/vertical streets |
| $h_\mathrm{m}^0$ | LoS height at the intersection point with the first contact side |
| $h_\mathrm{m}^x(x)$ | LoS height at the intersection point with the vertical sides |
| $h_\mathrm{m}^y(y)$ | LoS height at the intersection point with the horizontal sides |
| $x_0$, $l_\mathrm{x}$ | $x$-coordinates of the first two LoS projections on $X$-axis |
| $y_0$, $l_\mathrm{y}$ | $y$-coordinates of the first two LoS projections on $Y$-axis |
| $p_\mathrm{s}$ | Probability of UAV being located on a typical street |
| $R$ | Cell radius |
| $f_\Phi(\phi_\mathrm{D})$ | pdf of LoS AoD |
| $f_L(l_\mathrm{2D})$ | pdf of BS to UAV 2D distance |
| $\mathbb{P}_\mathrm{LoS}$ | LoS probability |
| $\mathbb{P}^*_\mathrm{LoS}$ | Area LoS probability |

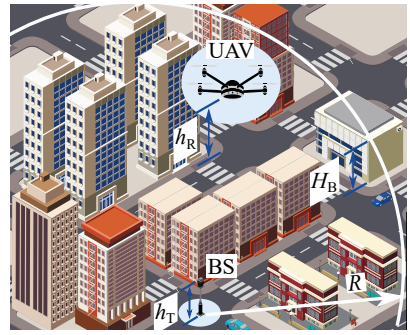


(a) 3D view of our scenario

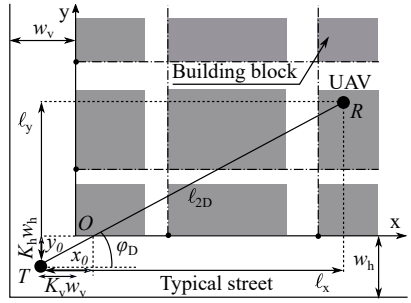


(b) 2D view of our scenario

Fig. 1. 3D and 2D urban grid snapshots for analytical modeling. BS base is located at point $T$. UAV having base projection $R$ onto 2D plane is separated by $\ell_\mathrm{2D}$ 2D distance from BS. Points along $X$- and $Y$-axis represent starting points of streets generated according to PPP with intensity $\lambda$.

We note that if $K_h = K_v = 0.5$, our scenario becomes fully symmetric. In this work, we also consider the BS coverage as a circle of radius $R$ on the plane, see Fig. 1.

### C. LoS Blockage

We proceed with the conditions leading to blockage of the BS-to-UAV link by buildings. Here, a LoS blockage decision is made based on an occlusion of the optical LoS. Therefore, a blockage occurs if at least one building that intersects the LoS is higher than the optical BS-to-UAV LoS path.

Note that the LoS projection on the 2D plane $TR$ can only cross the 2D projection of the left (perpendicular to the $X$-axis) and bottom (parallel to the $Y$-axis) sides of the blocks. We thus consider only the sides that actually affect the LoS blockage. We further refer to the side that is the first one to intersect with $TR$ as the *contact side*. The LoS 2D projection $TR$ can in fact intersect only one contact side of the block that it interacts with.

We continue with UAV placement in the considered deployment. For certainty, we consider the UAV located at any point of the first quadrant. Observe that such analysis is similar to that for other quadrants. Further, UAV location parameters $K_h = K_v = 0.5$ make our setup fully symmetric. We also require the height of the UAV to always remain above the

height of the block if its position coincides with this block. The latter forces the UAV to reside in the LoS or nLoS state depending on the blockage from buildings along the LoS path between the BS and the UAV. The 2D distance from the BS to the UAV is denoted as $\ell_{\text{2D}}$, while the LoS AoD is $\phi_{\text{D}}$ as displayed in Fig. 1(b).

### D. Metrics of Interest

We conclude with a description of two metrics of interest, which are considered in our mathematical modeling. To characterize communication between the UAV and the BS in different urban deployments, we first address the *LoS probability* parameter. To capture the UAV inside the BS coverage, we then calculate the *area LoS probability*.

**Definition 1.** *The LoS probability is the probability that the height of every building with its base intersecting the LoS link projection is lower than the height of the LoS link between the BS and the UAV at the point of their intersection.*

Therefore, for a fixed UAV location, we derive the LoS probability conditioned on the urban grid deployment, the UAV height, the UAV-to-BS separation distance, and the AoD value. This parameter of interest can be incorporated into further system-level analysis of UAV networks. Comprehensive performance evaluation of such setups aims at demonstrating the capability of wireless networks to accommodate UAV users.

**Definition 2.** *The area LoS probability is the probability that the LoS link between the UAV (distributed randomly and uniformly within the BS coverage of radius $R$) and the BS is not occluded by any building with its base intersecting the LoS link projection on a 2D plane.*

We evaluate the area LoS probability within the region of radius $R$, where $R$ can be selected, e.g., based on the BS density. The latter parameter of interest provides insights into whether the current BS deployment is sufficiently provisioned to support the UAVs. If the area LoS probability is low, one may adjust the inter-site distance between the BSs by reducing their coverage radius. Another option is to consider different BS heights for supporting aerial users.

## IV. Proposed Analysis

In this section, we derive the two metrics of interest based on the system model and the assumptions introduced above. Below, we briefly outline our approach and then proceed by calculating the UAV LoS probability and the area LoS probability.

### A. Methodology at Glance

To determine the LoS probability, $\mathbb{P}_{\text{LoS}}$, it is sufficient to establish the probability that the 2D projection of the LoS path, $TR$, does not intersect a block, whose height is higher than the LoS height at the point of intersection. We then need to determine all the contact sides of $TR$ by specifying the probability that the height of the building side at 2D distance of $x$ is lower than the height of LoS at $x$, $Pr\{H_{\text{B}} < h_{\text{m}}^{x}(x)\}$.

We continue with determining the number of intersections of $TR$ with the contact sides. Even though there is a number of sides for every line perpendicular to the $X$-axis, the $TR$ can in fact intersect only one of them. Therefore, the number of intersections of $TR$ with the contact sides perpendicular to the $X$-axis equals the number of points on the $X$-axis generated between the points $T$ and $R$. The same holds for the sides perpendicular to the $Y$-axis.

Hence, to determine the LoS probability, there is no need to iterate over all of the possible combinations of blocks. To preserve analytical tractability, we recall that the width of the street is significantly smaller than the width of the block side. Consequently, we assume that the LoS path always intersects the side of the block. In Section V, we numerically confirm that this simplification does not impact the results significantly.

After identifying the number of intersections of $TR$ with the contact sides, we consider the actual LoS probability. For an UAV to experience the LoS conditions, all the contact sides intersecting the LoS path need to be lower than the LoS height at the point of their intersection. Hence, to determine the effective density of points occluding the LoS path, one has to thin the PPP with the probability of side height being above

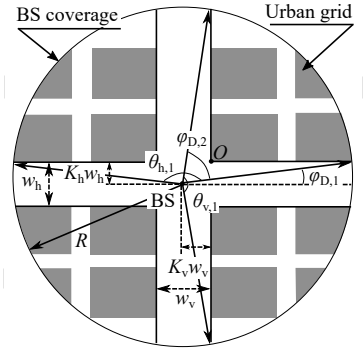


(a) BS located at intersection

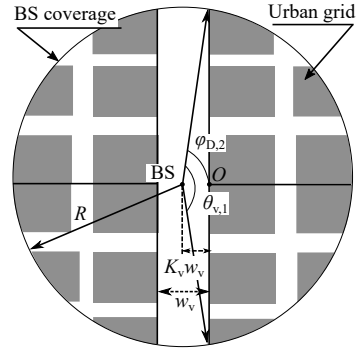


(b) BS located on street

Fig. 2. UAV is located randomly within BS coverage of radius $R$. Coefficients $K_h$ and $K_v$ in (0,1) determine BS location on typical streets. UAV located outside of typical streets has LoS AoD ($\phi_{\text{D},1}$, $\phi_{\text{D},2}$).

the LoS path, which leads to a non-homogeneous PPP.

Further, using the void probability of the resulting non-homogeneous PPP, one may determine the probability that there are no sides occluding the LoS path. The only exception to this procedure is that one also needs to account for the *first contact side*. The latter is the first side to be intersected by $TR$, which is located at a fixed distance from the BS position.

### *B. Main Formulations*

In this subsection, we derive our main results including the LoS probability and the area LoS probability.

**Proposition 1.** *The LoS probability, $\mathbb{P}_{LoS}(\ell_{2D},\phi_D)$, for the general distribution of building heights is given below. The expression employs $F_{H_B}(h)$ as the CDF of the block heights. $F_{H_B}\big(h_m^0(\ell_{2D},\phi_D)\big)$ is the probability that the first contact side height is lower than the LoS height, $h_m^0(\ell_{2D},\phi_D)$, at the point of their intersection.*

*$F_{H_B}\big(h_m^x(x,\ell_{2D},\phi_D)\big)$ and $F_{H_B}\big(h_m^y(y,\ell_{2D},\phi_D)\big)$ are the probabilities that the sides perpendicular to the $X$- and $Y$-axis are lower than the LoS heights, $h_m^x(x,\ell_{2D},\phi_D)$ and $h_m^y(y,\ell_{2D},\phi_D)$, at the point of their intersection, respectively.*

$$\mathbb{P}_{LoS}(\ell_{2D},\phi_D)=F_{H_B}\big(h_m^0(\ell_{2D},\phi_D)\big)\times \exp\left(-\lambda\int_{x_0}^{\ell_x}\Big[1-F_{H_B}\big(h_m^x(x,\ell_{2D},\phi_D)\big)\Big]dx- \lambda\int_{y_0}^{\ell_y}\Big[1-F_{H_B}\big(h_m^y(y,\ell_{2D},\phi_D)\big)\Big]dy\right). \tag{7}$$

*Proof.* First, we determine the distances from the point $T$ to the first and the second endpoints of the $TR$ projection on the $X$- and $Y$-axis, $x_0$, $\ell_{\rm x}$ and $y_0$, $\ell_{\rm y}$ as illustrated in Fig. 1(b) and is given below. These expressions contain the parameters $K_{\rm v}$ and $K_{\rm h}$, which are the coefficients related to the position of the BS on the typical vertical and horizontal streets, $w_{\rm v}$ and $w_{\rm h}$ that are the widths of such streets, and $\phi_{\rm D}$ as the LoS AoD.

$$\begin{aligned} x_0&=\max\big(K_{\rm v}w_{\rm v},K_{\rm h}w_{\rm h}\cot(\phi_{\rm D})\big),\\ \ell_{\rm x}&=\ell_{\rm 2D}\cos(\phi_{\rm D}),\\ y_0&=\max\big(K_{\rm h}w_{\rm h},K_{\rm v}w_{\rm v}\tan(\phi_{\rm D})\big),\\ \ell_{\rm y}&=\ell_{\rm 2D}\sin(\phi_{\rm D}). \end{aligned} \tag{8}$$

To derive the CDF $F_{H_{\rm B}}\big(h_{\rm m}^x(x,\ell_{\rm 2D},\phi_{\rm D})\big)$, one has to obtain the LoS height at the points of intersection with the sides perpendicular to the $X$-axis as a function of the 2D $TR$ projection on the $X$-axis, $x$. From the model geometry, the latter is calculated as

$$h_{\rm m}^x(x,\ell_{\rm 2D},\phi_{\rm D})=\frac{x(h_{\rm R}-h_{\rm T})+h_{\rm T}\ell_{\rm 2D}\cos(\phi_{\rm D})}{\ell_{\rm 2D}\cos(\phi_{\rm D})}. \tag{9}$$

Similarly, to find the CDF $F_{H_{\rm B}}\big(h_{\rm m}^y(y,\ell_{\rm 2D},\phi_{\rm D})\big)$, we establish the LoS height at the points of intersection with the sides that are perpendicular to the $Y$-axis as a function of the 2D $TR$ projection on the $Y$-axis, $y$ as

$$h_{\rm m}^y(y,\ell_{\rm 2D},\phi_{\rm D})=\frac{y(h_{\rm R}-h_{\rm T})+h_{\rm T}\ell_{\rm 2D}\sin(\phi_{\rm D})}{\ell_{\rm 2D}\sin(\phi_{\rm D})}. \tag{10}$$

The LoS height at the point of intersection with the first contact side for the CDF $F_{H_{\rm B}}\big(h_{\rm m}^0(\ell_{\rm 2D},\phi_{\rm D})\big)$ is provided below as

$$h_{\rm m}^0(\ell_{\rm 2D},\phi_{\rm D})=\frac{x_0(h_{\rm R}-h_{\rm T})}{\ell_{\rm 2D}\cos(\phi_{\rm D})}+h_{\rm T}. \tag{11}$$

Recalling the PPP properties [32], the probability that there are no sides perpendicular to the $X$-axis, which are higher than the LoS at the point of their intersection is derived by using the void probability of the thinned PPP, i.e.,

$$p_{\rm nB}^{(x)}(\ell_{\rm 2D},\phi_{\rm D})= \exp\left[-\lambda\int_{x_0}^{\ell_{\rm x}}\Big(1-F_{H_{\rm B}}\big(h_{\rm m}^x(x,\ell_{\rm 2D},\phi_{\rm D})\big)\Big){\rm d}x\right]. \tag{12}$$

Similarly, the probability that there are no sides perpendicular to the $Y$-axis, which are higher than the LoS, is given by

$$p_{\rm nB}^{(y)}(\ell_{\rm 2D},\phi_{\rm D})= \exp\left[-\lambda\int_{y_0}^{\ell_{\rm y}}\Big(1-F_{H_{\rm B}}\big(h_{\rm m}^y(y,\ell_{\rm 2D},\phi_{\rm D})\big)\Big){\rm d}y\right]. \tag{13}$$

The probability that the first contact side does not occlude the LoS is readily available by using the block height distribution in the form

$$p_{\rm nB}^{(0)}(\ell_{\rm 2D},\phi_{\rm D})=F_{H_{\rm B}}\big(h_{\rm m}^0(\ell_{\rm 2D},\phi_{\rm D})\big). \tag{14}$$

Since vertical and horizontal block and street deployments are independent from each other, the LoS probability is provided by a direct product of (12)-(14) as in (7). □

We now formulate three important corollaries that offer closed-form solutions for the LoS probability under three block height distributions that are widely used in the literature: uniform [33], exponential [19], and Rayleigh [12], [20]. These results are available via direct integration of (7).

**Corollary 1.** *For the uniformly distributed block heights $H_B\sim\mathcal{U}(h_1,h_2)$, the LoS probability is provided by*

$$\mathbb{P}_{LoS}(\ell_{2D},\phi_D)=\frac{h_m^0(\ell_{2D},\phi_D)-h_1}{h_2-h_1}\times \exp\left(-\lambda\int_{x_0}^{\ell_x}\Big[1-\frac{h_m^x(x,\ell_{2D},\phi_D)-h_1}{h_2-h_1}\Big]dx- \lambda\int_{y_0}^{\ell_y}\Big[1-\frac{h_m^y(y,\ell_{2D},\phi_D)-h_1}{h_2-h_1}\Big]dy\right), \tag{15}$$

*which leads to a closed-form solution in (4).*

**Corollary 2.** *For the exponentially distributed block heights $H_B\sim\exp(\lambda_B)$, the LoS probability is provided by*

$$\mathbb{P}_{LoS}(\ell_{2D},\phi_D)=\Big(1-\exp\big(-h_m^0(\ell_{2D},\phi_D)\lambda_B\big)\Big)\times \exp\left(-\lambda\int_{x_0}^{\ell_x}\exp\big(-h_m^x(x,\ell_{2D},\phi_D)\lambda_B\big)dx- \lambda\int_{y_0}^{\ell_y}\exp\big(-h_m^y(y,\ell_{2D},\phi_D)\lambda_B\big)dy\right), \tag{16}$$

$$\mathbb{P}_{\text{LoS}}(\ell_{\text{2D}},\phi_{\text{D}}) = \frac{h_{\text{m}}^0 - h_1}{h_2 - h_1} \times \exp\left(\frac{(h_2-h_{\text{T}})\big(-\lambda(\ell_{\text{x}}-x_0)-\lambda(\ell_{\text{y}}-y_0)\big)}{h_2-h_1} + \frac{\lambda(\ell_{\text{x}}^2-x_0^2)(h_{\text{R}}-h_{\text{T}})}{2\ell_{\text{2D}}(h_2-h_1)\cos(\phi_{\text{D}})} + \frac{\lambda(\ell_{\text{y}}^2-y_0^2)(h_{\text{R}}-h_{\text{T}})}{2\ell_{\text{2D}}(h_2-h_1)\sin(\phi_{\text{D}})}\right). \quad (4)$$

$$\mathbb{P}_{\text{LoS}}(\ell_{\text{2D}},\phi_{\text{D}}) = \big[1-\exp(-h_{\text{m}}^0\lambda_{\text{B}})\big]\exp\left(\frac{\lambda\ell_{\text{2D}}\exp(-\lambda_{\text{B}}h_{\text{T}})\cos(\phi_{\text{D}})}{\lambda_{\text{B}}(h_{\text{R}}-h_{\text{T}})}\left(\exp\left[\frac{-\lambda_{\text{B}}\ell_{\text{x}}(h_{\text{R}}-h_{\text{T}})}{\ell_{\text{2D}}\cos(\phi_{\text{D}})}\right] - \exp\left[\frac{-\lambda_{\text{B}}x_0(h_{\text{R}}-h_{\text{T}})}{\ell_{\text{2D}}\cos(\phi_{\text{D}})}\right]\right) + \frac{\lambda d_{\text{2D}}\exp(-\lambda_{\text{B}}h_{\text{T}})\sin(\phi_{\text{D}})}{\lambda_{\text{B}}(h_{\text{R}}-h_{\text{T}})}\left(\exp\left[\frac{-\lambda_{\text{B}}\ell_{\text{y}}(h_{\text{R}}-h_{\text{T}})}{\ell_{\text{2D}}\sin(\phi_{\text{D}})}\right] - \exp\left[\frac{-\lambda_{\text{B}}y_0(h_{\text{R}}-h_{\text{T}})}{\ell_{\text{2D}}\sin(\phi_{\text{D}})}\right]\right)\right). \quad (5)$$

$$\mathbb{P}_{\text{LoS}}(\ell_{\text{2D}},\phi_{\text{D}}) = \left(1-\exp\Big(-\frac{(h_{\text{m}}^0)^2}{2\sigma^2}\Big)\right)\times \exp\left(\frac{-\lambda\ell_{\text{2D}}\cos(\phi_{\text{D}})\sigma\sqrt{\pi}\Big(\exp\Big(\frac{h_{\text{T}}^2\sigma^2-h_{\text{T}}^2}{2\sigma^2}\Big)\Big)\Big(\text{erf}\Big(\frac{(h_{\text{R}}-h_{\text{T}})\ell_{\text{x}}+h_{\text{T}}\ell_{\text{2D}}\cos(\phi_{\text{D}})\sigma}{\sqrt{2}\ell_{\text{2D}}\cos(\phi_{\text{D}})\sigma}\Big) - \text{erf}\Big(\frac{(h_{\text{R}}-h_{\text{T}})x_0+h_{\text{T}}\ell_{\text{2D}}\cos(\phi_{\text{D}})\sigma}{\sqrt{2}\ell_{\text{2D}}\cos(\phi_{\text{D}})\sigma}\Big)\Big)}{\sqrt{2}(h_{\text{R}}-h_{\text{T}})} + \frac{-\lambda\ell_{\text{2D}}\sin(\phi_{\text{D}})\sigma\sqrt{\pi}\Big(\exp\Big(\frac{h_{\text{T}}^2\sigma^2-h_{\text{T}}^2}{2\sigma^2}\Big)\Big)\Big(\text{erf}\Big(\frac{(h_{\text{R}}-h_{\text{T}})\ell_{\text{y}}+h_{\text{T}}\ell_{\text{2D}}\sin(\phi_{\text{D}})\sigma}{\sqrt{2}\ell_{\text{2D}}\sin(\phi_{\text{D}})\sigma}\Big) - \text{erf}\Big(\frac{(h_{\text{R}}-h_{\text{T}})y_0+h_{\text{T}}\ell_{\text{2D}}\sin(\phi_{\text{D}})\sigma}{\sqrt{2}\ell_{\text{2D}}\sin(\phi_{\text{D}})\sigma}\Big)\Big)}{\sqrt{2}(h_{\text{R}}-h_{\text{T}})}\right). \quad (6)$$

*which leads to a closed-form solution in (5).*

**Corollary 3.** *For the Rayleigh distributed block heights $H_B \sim$ Rayleigh$(\sigma)$, the LoS probability is provided by*

$$\mathbb{P}_{LoS}(\ell_{2D},\phi_D) = \left[1-\exp\Big(-\frac{\big(h_m^0(\ell_{2D},\phi_D)\big)^2}{2\sigma^2}\Big)\right]\times \exp\left(-\lambda\int_{x_0}^{\ell_x}\left[\exp\Big(-\frac{\big(h_m^x(x,\ell_{2D},\phi_D)\big)^2}{2\sigma^2}\Big)\right]dx - \lambda\int_{y_0}^{\ell_y}\left[\exp\Big(-\frac{\big(h_m^y(y,\ell_{2D},\phi_D)\big)^2}{2\sigma^2}\Big)\right]dy\right), \quad (17)$$

*which leads to a closed-form solution in (6).*

We continue with a characterization of the area LoS probability for the UAV that is located randomly within the BS cell area as depicted in Fig. 2.

**Proposition 2.** *The area LoS probability, $\mathbb{P}_{LoS}^*$, for the UAV that is located randomly and uniformly within the BS coverage area having the radius of $R$ is given by*

$$\mathbb{P}_{LoS}^* = p_s + (1-p_s)\mathbb{P}_{LoS}, \quad (18)$$

*where $p_s$ is the probability that the UAV projection onto the ground plane is located along the typical street (with BS), while $\mathbb{P}_{LoS}$ is the LoS probability as the UAV is placed at any other point.*

*The derivation of $\mathbb{P}_{LoS}$ contains $f_\Phi(\phi_D) \sim \mathcal{U}(\phi_{D,1},\phi_{D,2})$, which is the pdf of the AoD. We define $f_L(\ell_{2D}) \sim \mathcal{U}(x_0/\cos(\phi_D), R)$ as the pdf of the 2D distance between the BS and the UAV located outside of the typical streets.*

$$\mathbb{P}_{LoS} = \int_{\phi_{D,1}}^{\phi_{D,2}} f_\Phi(\phi_D)d\phi_D \int_{\frac{x_0}{\cos(\phi_D)}}^{R} f_L(\ell_{2D})\left[F_{H_B}\big(h_m^0(\ell_{2D},\phi_D)\big)\times \exp\left(-\lambda\int_{x_0}^{\ell_x}\Big[1-F_{H_B}\big(h_m^x(x,\ell_{2D},\phi_D)\big)\Big]dx - \lambda\int_{y_0}^{\ell_y}\Big[1-F_{H_B}\big(h_m^y(y,\ell_{2D},\phi_D)\big)\Big]dy\right)\right]d\ell_{2D}. \quad (19)$$

*Proof.* According to the deployment geometry, the BS can be located either at the intersection of two perpendicular typical streets or on a typical street. In both cases, if the UAV projection onto the ground plane is placed on the typical street, the LoS path is not occluded. For all other UAV locations, there is a non-zero probability that the LoS path is blocked, $(1-\mathbb{P}_{\text{LoS}})$.

To determine $\mathbb{P}_{\text{LoS}}$, one needs to integrate (19) over all of the possible orientations and distances from the BS to the UAV located outside of the typical streets. Hence, to determine the area LoS probability, we have to provide $p_{\text{s}}$ together with the integration limits for the two considered BS locations. The integrands in (19) are given as

$$f_\Phi(\phi_{\text{D}}) = \frac{1}{\phi_{\text{D,2}}-\phi_{\text{D,1}}},$$
$$f_L(\ell_{\text{2D}}) = \frac{\cos(\phi_{\text{D}})}{R\cos(\phi_{\text{D}})-x_0}. \quad (20)$$

Let us first determine $p_{\text{s}}$ and the integration limits for the BS located at the intersection as depicted in Fig. 2(a). For the UAV that is distributed uniformly within the BS coverage area, the LoS AoD is also distributed uniformly in $(0,2\pi)$. We then calculate the minimum $\phi_{\text{D,1}}$ and the maximum $\phi_{\text{D,2}}$ AoD for

the UAV projection onto the ground plane located outside of the typical street to establish

$$\phi_{\mathrm{D},1} = \arcsin(K_{\mathrm{h}} w_{\mathrm{h}}/R),\ \phi_{\mathrm{D},2} = \arccos(K_{\mathrm{v}} w_{\mathrm{v}}/R). \quad (21)$$

The probability of the UAV being placed on the typical street with BS, $p_{\mathrm{s}}$, is then available as a ratio of the street area to the total cell area, $\pi R^2$. To establish the typical street area, we calculate the segment area associated with the angle $\theta_{\mathrm{v},1}$ and the typical vertical street, see Fig. 2(a). The opposite segment area is obtained by using the angle $\theta_{\mathrm{v},2}$. We then subtract these areas from the circle area and arrive at the typical vertical street area.

The same approach is employed to characterize the area of the typical horizontal street. Accordingly, we add two typical street areas together and then subtract the common intersection area as it appears two times. We thus have

$$p_{\mathrm{s}} = 2 - \frac{\theta_{\mathrm{v},1} - \sin(\theta_{\mathrm{v},1})}{2\pi} - \frac{\theta_{\mathrm{v},2} - \sin(\theta_{\mathrm{v},2})}{2\pi} - \frac{w_{\mathrm{h}} w_{\mathrm{v}}}{\pi R^2} - \\ - \frac{\theta_{\mathrm{h},1} - \sin(\theta_{\mathrm{h},1})}{2\pi} - \frac{\theta_{\mathrm{h},2} - \sin(\theta_{\mathrm{h},2})}{2\pi}, \quad (22)$$

where the angles $\theta_{\mathrm{v},1}$, $\theta_{\mathrm{v},2}$, $\theta_{\mathrm{h},1}$, and $\theta_{\mathrm{h},2}$ are as in Fig. 2(a):

$$\theta_{\mathrm{v},1} = 2\arccos\left(\frac{K_{\mathrm{v}} w_{\mathrm{v}}}{R}\right),\ \theta_{\mathrm{h},1} = 2\arccos\left(\frac{K_{\mathrm{h}} w_{\mathrm{h}}}{R}\right), \\ \theta_{\mathrm{v},2} = 2\arccos\left(\frac{(1-K_{\mathrm{v}}) w_{\mathrm{v}}}{R}\right), \\ \theta_{\mathrm{h},2} = 2\arccos\left(\frac{(1-K_{\mathrm{h}}) w_{\mathrm{h}}}{R}\right). \quad (23)$$

For the BS located on the typical street, the approach is similar but has minor changes due to the deployment geometry, see Fig. 2(b). Particularly, the distances from point $T$ to the first endpoint of the $TR$ projection on the $X$- and $Y$-axis are

$$x_0 = K_{\mathrm{v}} w_{\mathrm{v}},\ y_0 = K_{\mathrm{v}} w_{\mathrm{v}} \tan(\phi_{\mathrm{D}}). \quad (24)$$

The minimum and the maximum angles for the location of the UAV residing outside the area of the typical street are given by

$$\phi_{\mathrm{D},1} = 0,\ \phi_{\mathrm{D},2} = \arccos(K_{\mathrm{v}} w_{\mathrm{v}}/R). \quad (25)$$

Finally, the probability that the UAV projection is placed on the street where the BS is positioned can be delivered by a ratio of the respective areas. Simplifying, we establish

$$p_{\mathrm{s}} = 1 - \frac{\theta_{\mathrm{v},1} - \sin(\theta_{\mathrm{v},1})}{2\pi} - \frac{\theta_{\mathrm{v},2} - \sin(\theta_{\mathrm{v},2})}{2\pi}, \quad (26)$$

where the angles to calculate the area segments are available as

$$\theta_{\mathrm{v},1} = 2\arccos\left(\frac{K_{\mathrm{v}} w_{\mathrm{v}}}{R}\right), \\ \theta_{\mathrm{v},2} = 2\arccos\left(\frac{(1-K_{\mathrm{v}}) w_{\mathrm{v}}}{R}\right). \quad (27)$$

After identifying the integration limits, we arrive at the integral form (19). Substituting (19) into (18), we conclude the proof for both cases. □

TABLE II
BASELINE SYSTEM PARAMETERS

| Parameter | Value |
|---|---|
| Height of BS, $h_{\mathrm{T}}$ | 10 m |
| Width of typical vertical street, $w_{\mathrm{v}}$ | 20 m |
| Width of typical horizontal street, $w_{\mathrm{h}}$ | 20 m |
| Coefficient $K_{\mathrm{v}}$ | 0.5 |

TABLE III
URBAN GRID GEOMETRY

| Type | Mean building height, $\mu_{\mathbf{H}}$ | Mean side width, $\mu_{\mathbf{b}}$ | Mean street width, $\mu_{\mathbf{s}}$ |
|---|---|---|---|
| Suburban | 10 m | 37 m | 10 m |
| Urban | 19 m | 45 m | 13 m |
| Dense urban | 25 m | 60 m | 20 m |
| Highrise urban | 63 m | 60 m | 20 m |

## V. NUMERICAL RESULTS

In this section, we evaluate the developed model numerically and illustrate the UAV LoS probability for several practical deployments. We start with assessing the accuracy and the applicability of our model by comparing its results with those obtained based on computer simulations. Then, we proceed by studying the impact of the system parameters and the urban deployment types on the UAV LoS probability. Finally, we compare the results of the proposed modeling to those discussed in the standards.

The default system parameters are summarized in Table II. To parametrize the scenario[2], we rely upon settings for an urban district as made available in [12] and [30]. Particularly, we consider four different urban grid types: (i) suburban, (ii) urban, (iii) dense urban, and (iv) highrise urban. We derive the relevant parameters of the considered urban deployments from the density of buildings, the fraction of land covered by them to the total area, as well as the variable for the height distribution provided by ITU-R [12], [30] to collect these in Table III.

### A. Accuracy and Applicability Limits

We begin by verifying the accuracy of the developed model and assessing its applicability limits. For this purpose, we develop a simulator that relaxes the following key assumption on the urban deployment as adopted in Section III: the probability that the LoS projection intersects a building block is always one. Recall that this assumption stems from the typical urban deployments, where the street width is usually much smaller than the block width.

In Fig. 3, we offer a comparison between the UAV LoS probability obtained with the developed mathematical model vs. computer simulations for a dense urban deployment (see Table III), Rayleigh distribution of the building heights $H_{\mathrm{B}} \sim$ Rayleigh(20) as in [30], block and street mean widths ($\mu_{\mathrm{b}}$ and $\mu_{\mathrm{s}}$) of 60 m and 20 m, respectively. The simulations were conducted by employing the method of replications [34].

[2]The general form of the LoS probability in (7) can accept any building height distribution. Moreover, one can parametrize our model by using the statistical data of a particular city or district by extracting it from the database.

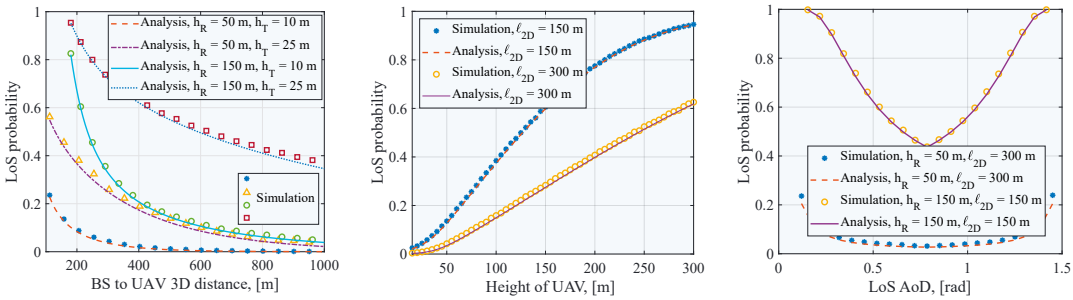


(a) As function of 3D distance (b) As function of UAV height (c) As function of LoS AoD

Fig. 3. LoS probability as function of UAV location in dense urban deployments. Building heights follow Rayleigh distribution $H_{\mathrm{B}} \sim \mathrm{Rayleigh}(20)$. BS is located in the center of intersection of two typical streets with the width of 20 m. LoS AoD $\phi_{\mathrm{D}}$ for subplots (a) and (b) is $30^o$.

First, in a single run, our modeler generates the considered deployment and then assesses the LoS path to the UAV located within the region at a certain distance, height, and angle with respect to the $X$-axis. A sequence of these runs forms statistically independent samples. Due to acceptable complexity of modeling the environment, we were able to carry out a sufficient number of experiments, such that the confidence intervals were always under $0.01$ of the respective absolute values for the level of significance set to $0.95$.

As a result, Fig. 3 demonstrates only point statistical estimates. As one may observe, the simulation output agrees tightly with the analytical results across a realistic range of the input parameters. The computational complexity of the simulations grows linearly as the density of building blocks increases. Specifically, the system-level modeling complexity is $O(N)$, whereas for the analytical derivations it remains constant at $O(1)$. Statistical LoS/nLoS probability models have proven themselves as computationally effective yet accurate tools [10]. Hence, we primarily resort to our developed analytical model for the purposes of this numerical analysis.

Observe that our assumption of LoS path always intersecting the block is actually close to reality where the block width is much larger than the street width as assumed in Fig. 3.

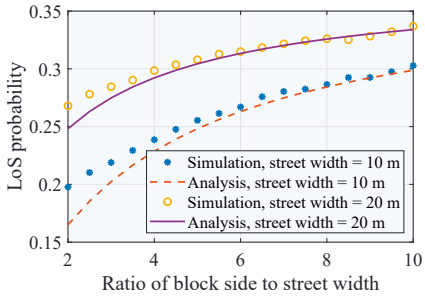


Fig. 4. Effects of the ratio of block side to street mean width on modeling accuracy. Building heights follow Rayleigh distribution $H_{\mathrm{B}} \sim \mathrm{Rayleigh}(20)$. BS is located in the center of intersection of two typical streets. UAV height is 150 m, 2D distance between BS and UAV is 300 m, LoS AoD $\phi_{\mathrm{D}}$ is $30^o$.

Let us now consider the response of our model to different ratios of block side to street mean widths as studied in Fig. 4 for a dense urban deployment, Rayleigh distribution ($H_{\mathrm{B}} \sim \mathrm{Rayleigh}(20)$) of the building heights, UAV altitude of 150 m, 300 m 2D distance to the UAV, and LoS AoD of $30^o$.

Analyzing the collected data, one may observe that the accuracy of the considered model heavily depends on the ratio between the block width and the street width. If the block width becomes larger than the street width, as in typical urban deployments, our formulation is more accurate in approximating the LoS probability. For the ratio of two and the street widths of 10 and 20 m, the difference between the simulation and the analysis is around 3% and 2%, respectively. After increasing the ratio further, this difference decreases. This behavior demonstrates the dominant effect of the block side width compared to the street width on the LoS probability analysis.

### *B. UAV LoS Blockage Analysis*

*1) Effects of UAV and BS Positions:* We continue by assessing the effects of the UAV and BS placement on the UAV LoS probability. We first address the impact of the UAV location with respect to the BS. Particularly, Fig. 3 illustrates the influence of the BS to UAV 3D distance, UAV height, BS height, and LoS AoD on the UAV LoS probability for the Rayleigh distribution ($H_{\mathrm{B}} \sim \mathrm{Rayleigh}(20)$) of the building heights. As our typical deployment, we choose dense urban layout characterized by the mean street width of 20 m and the side width of 60 m.

We consider the effect of 3D distance as displayed in Fig. 3(a) for the LoS AoD of $30^o$, BS height of 10 m, and two UAV flight heights, 50 and 150 m. As one may observe, the UAV LoS probability decreases exponentially with the growing distance from the BS. Further, the impact of the UAV height is of paramount importance. The difference in the absolute values of LoS probabilities between the two considered altitudes can reach $0.7$.

We then increase the BS height to 25 m as one of the typical heights for the Urban Macro scenarios specified by 3GPP [11]. We note that for the lower UAV height of 50 m, the BS height

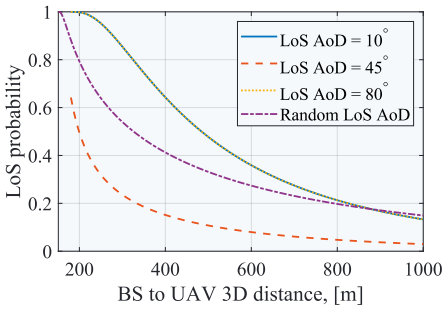


Fig. 5. Angle-dependent and -independent UAV LoS probability for dense urban deployment. Building heights follow Rayleigh distribution $H_{\mathrm{B}} \sim$ Rayleigh(20). BS is located in the center of intersection of two typical streets with width of 20 m. UAV height is 150 m.

increase from 10 to 25 m, and the 2D separation distance of 100 m the LoS probability grows by 2.3 times. For the same set of parameters and the greater UAV height of 150 m, the BS height of 25 m yields the growth of the LoS probability by 1.1 times.

Fig. 3(b) details this aspect by presenting the UAV LoS probability across a wide range of UAV altitudes for two 2D distances between the UAV and the BS. As one may note, by increasing the UAV height up to 300 m and for the 2D distance of 150 m, the LoS probability may reach 0.95.

The orientation of the UAV with respect to the BS is also essential for the LoS probability assessment as confirmed by Fig. 3(c). As one may learn, the LoS probability for the UAV height of 150 m and the 2D distance of 150 m is around 1 for the LoS AoD close to 0 and $\pi/2$. At these LoS AoDs, the UAV is located sufficiently close to the typical street where the BS is deployed. Such a proximity reduces the number of buildings potentially occluding the LoS between the UAV and the BS, thus leading to higher LoS probability. It then gradually decreases and reaches its minimum at $\pi/4$ orientation of the LoS AoD, see Fig. 3(c).

We note that this behavior is an important property of realistic non-isotropic deployments that is not captured by the standard Poisson-like models, which implies that the LoS probability heavily depends on the UAV location with respect to its BS. This effect is further emphasized in Fig. 5, which shows the UAV LoS probability for different LoS AoDs as well as the area LoS probability (BS is located at the intersection) as a function of 3D distance between the BS and the UAV for the UAV height of 150 m. As one may see, the LoS probabilities for the LoS AoDs of $10^o$ and $80^o$ coincide due to equal intensity of points along the $X$- and $Y$-axes.

Furthermore, the area LoS probability may drastically deviate from the LoS probability for a particular LoS AoD, which accentuates the importance of the LoS AoD when evaluating the LoS probability for the UAVs. Regarding position-dependent UAV LoS probability, we conclude that the relative position of the UAV with respect to its BS largely affects the LoS probability even when the UAV height is much greater than the mean building height, which calls for a careful planning of UAV flight trajectories.

*2) Effects of Building Height Distribution:* As one may expect, the building height distribution produces a substantial impact on the UAV LoS probability. Most of the models proposed to date capture only the first moment of the building height by completely disregarding its higher moments as well as the form of the distribution itself. However, the architecture of urban districts may yield a considerable variation in the building heights.

In Fig. 6, we explore the impact of the building height distribution on the UAV LoS probability. To this aim, we evaluate the UAV LoS probability for a set of candidate building height distributions (uniform, gamma, Rayleigh, and exponential) as a function of its mean value for a constant variance of 33, see Fig. 6(a). In Fig. 6(b), we plot the LoS probability as a function of the standard deviation for a constant mean related to a certain district type (see Table III) and a gamma distribution of the building heights. Here, the 2D separation distance is 300 m, the LoS AoD is $30^o$, and the UAV height is 150 m.

As one may infer by analyzing the data in Fig. 6(a), the form of the distribution has a major effect on the UAV LoS probability. Particularly, up to the mean building height of 20 m, the results for all three distributions deviate in-

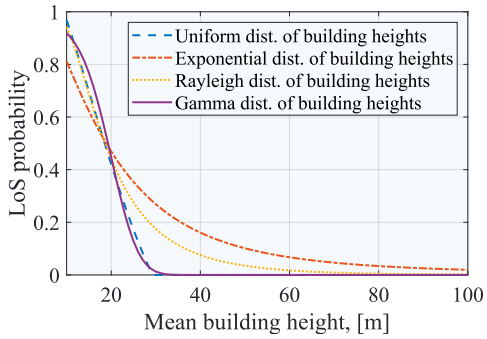


(a) Constant variance = 33

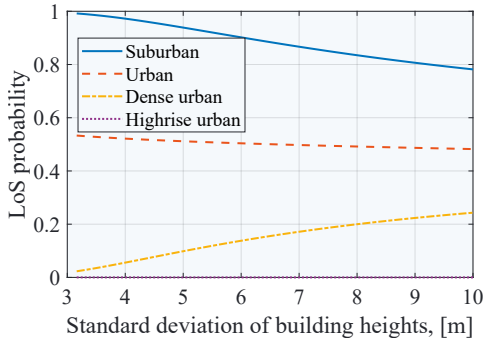


(b) Constant mean

Fig. 6. LoS probability as function of building height distribution for 2D separation distance of 300 m, LoS AoD of $30^o$, and UAV height of 150 m.

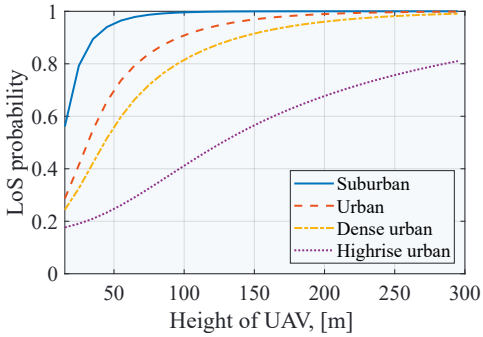


Fig. 7. Impact of urban deployment type on area LoS probability. BS coverage radius is 150 m and building height distribution is $H_{\mathrm{B}} \sim \text{Rayleigh}(\gamma)$.

significantly and remain within approximately 0.1 of each other. However, for greater average building heights of up to 60 m, which are typical for highrise urban deployments, the difference can become more substantial. A further increase in the mean building heights yields the LoS probability of close to 0, with almost no difference across various building height distributions.

Fig. 6(b) further illustrates the impact of the building height distribution as a function of the standard deviation, while keeping its mean related to a particular urban deployment as in Table III. Understanding the presented results, one may note that the difference is observable across the entire range of the standard deviations and for all the urban deployment types. Hence, we may conclude that for those layouts where the mean building height is under 20 m (e.g., suburban, urban, and dense urban), the models capturing the mean and the variance are sufficient for an accurate assessment of the UAV LoS probability.

For the deployments characterized by greater mean building heights (e.g., highrise urban), capturing the form of the height distribution is, however, essential. Regarding the effects of the building height distribution, we note that not only the first two moments but also the form of the distribution affect the UAV LoS probability, especially in the range [20 m,...,60 m] of the mean building heights. In what follows, we compare our proposed model with those standardized to date, which tend to disregard this crucial parameter.

*3) Effects of Urban Deployment Type:* We proceed with studying the effects of an urban deployment type on the UAV LoS probability by using the area LoS probability as specified in Proposition 2 for the scenario with the BS located at the intersection of two typical streets. Particularly, Fig. 7 demonstrates the considered parameter of interest as a function of the UAV height for the UAVs deployed uniformly within the BS coverage of 150 m. The building height distribution is assumed to be $H_{\mathrm{B}} \sim \text{Rayleigh}(\gamma)$, where $\gamma$ is equal to $\mu_H\sqrt{\frac{2}{\pi}}$. As one may observe, the area LoS probability is highly sensitive to the type of urban deployment since the absolute deviation may be up to 0.8.

As one may notice, for all of the deployments except for the highrise urban case the trend is exponential. In the case of a highrise urban deployment, the area LoS probability grows slower than exponential for the UAV heights under approximately 63 m. This effect is attributed to the relation between the mean UAV height and the mean building height. Particularly, whenever $\mu_{\mathrm{H}} \geq h_{\mathrm{R}}$, the rise is slower than exponential. Regarding the impact of urban deployments, we may deduce that in practice the minimum height of the UAV needs to be different for various layout options.

### C. Comparison with Standardized Models

We conclude with a comparison of our proposed LoS formulation against the presently standardized models to quantify the impact of more detailed parametrization. Fig. 8 demonstrates a comparison between the considered LoS probability model and the models specified in [11], [12] as functions of BS-to-UAV 2D distance in Fig. 8(a) and UAV height in Fig. 8(b). The standardized models were discussed earlier in subsection II-C, where (1) represents the ITU-R model while the 3GPP model is captured by (2).

We observe that the ITU-R LoS model completely disregards the features of spatial urban deployments by assuming

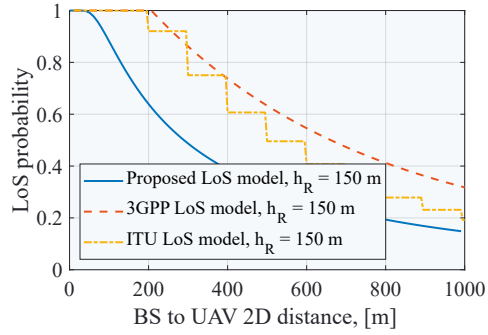


(a) As function of 2D distance

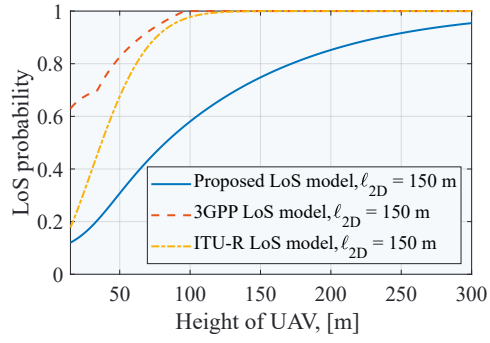


(b) As function of UAV height

Fig. 8. Area LoS probability as function of UAV location for three models: (i) proposed LoS model for dense urban deployment and BS located at the intersection of two streets, building height distribution is $H_{\mathrm{B}} \sim \text{Rayleigh}(20)$; (ii) 3GPP UMi street canyon LoS model (see 2); and (iii) ITU LoS model (see 1).

the building bases to be perpendicular to the LoS projection. Further, the 3GPP model does not specify the deployment parameters to characterize the LoS model. Hence, to provide a fair comparison between the formulations in question, Fig. 8 reports the area LoS probability for the dense urban deployment and the BS located at the intersection of two streets.

Analyzing the presented results, one may note that both ITU-R and 3GPP models capture the qualitative behavior of the UAV LoS probability since all three options lead to an exponential decrease for the parameter of interest in Fig. 8(a) under the growing 2D separation distance. However, both ITU-R and (especially) 3GPP formulations provide overly optimistic results for the practical separation distances. This is because the difference in terms of the absolute values can be up to $0.4$, which limits the use of these models for various urban grid deployments. One may also observe the stepwise behavior of the ITU-R formulation caused by a floor function in the model specification, which may complicate the use of this approach for analytical assessment.

Comparing the considered models with respect to the UAV height in Fig. 8(b), one may learn that both 3GPP and ITU-R options again drastically overestimate the actual UAV LoS probability. It is noted that both standardized formulations are much closer to each other than to our more exact model, where the difference may reach $0.4$. *We emphasize that a part of this discrepancy can be attributed to the fact that the 3GPP model does not capture the essential features of urban deployments, such as the distribution of building heights and does not specify the exact deployment parameters it employed.*

At the same time, the ITU-R model considers the deployment parameters as well as assumes a Rayleigh distribution of building heights but only accounts for a fixed number of buildings between the BS and its user. It also disregards the spatial distribution of buildings. All of these facts lead to a significant overestimation of the LoS probability by contrast to the proposed LoS probability model, which captures the essential features of urban deployments.

## VI. Conclusion and Future Work

In this work, we develop a model for the LoS probability evaluation on the BS-to-UAV link operating over mmWave frequency bands in 3D regular urban grid deployments as a function of building density as well as heights of the UAV, BS, and buildings. For a set of well-known building height distributions, closed-form expressions for the LoS probability are provided. In contrast to similar past formulations, our model allows to account for different building height distributions, spatial link orientations, as well as various deployment parameters, such as density of buildings. As a result, the flexibility of our formulation permits to study dissimilar urban deployment types, including suburban, urban, dense urban, and highrise urban layouts. We also note that the developed model can be suitable for systems other than mmWave, assuming an optical LoS for modeling purposes.

Our numerical results demonstrate that the UAV LoS probability heavily depends on the BS-to-UAV link orientation with respect to the non-isotropic deployment grid. For instance, the BS-to-UAV LoS AoD of $\pi/4$ makes the LoS probability drop by almost a half as compared to the LoS AoD equal to $\pi/2$. This implies that the choice of the UAV flight trajectory is crucial for maintaining high LoS probability and thus reliable connectivity between the UAV and the BS. Further, our study accentuates the importance of accounting for the building height distribution as it has a profound impact on the LoS probability. By comparing our model with the standard ITU and 3GPP alternatives, we argue that they both provide extremely coarse approximations for the UAV LoS probability as they do not capture the essential features of urban grid deployments, while our approach can be more accurate and applicable to various deployments.

To ensure reliable UAV support, it is imperative to conduct a thorough analysis of the underlying network deployment. The developed LoS probability formulation can thus become an integral part of comprehensive system-level modeling frameworks. The latter can merge the evaluated LoS probability values with the UAV-to-ground propagation model [35], [36] by additionally accounting for the transmit power, antenna gains at the BS and UAV sides, possible beam misalignment, as well as blockage-induced attenuation. Since conventional cellular deployments employ downtilted antennas, the existence of an unobstructed LoS path between the UAV and the BS does not however guarantee that communication is feasible [37]. To capture this situation, one needs to account for the antenna downtilt and evaluate the maximum user height to be supported by the BS main lobe at a given distance as well as the probability of having side lobes available. These results may project, e.g., the required BS density to minimize the link interruption times between the UAV and the terrestrial network infrastructure.

## Appendix A
## Consideration of Rooftop BSs

Reliable support of UAVs in early-stage 5G deployments may require provisional network nodes mounted on, e.g., rooftops of the buildings. The model developed in this work can capture this important case as demonstrated below.

When the height of a rooftop-mounted BS is known in advance, one may directly apply our formulation by setting the appropriate height in (7). Alternatively, one may assume random heights of rooftop-mounted BSs. To account for this case, we need to modify (7) as

$$\mathbb{P}_{\text{LoS}}(\ell_{\text{2D}},\phi_{\text{D}}) = \int_0^{\infty} \Bigg( F_{H_{\text{B}}}\big(h^0_{\text{m}}(\ell_{\text{2D}},\phi_{\text{D}},z)\big)\times \exp\Bigg(-\lambda\int_{x_0}^{\ell_{\text{x}}}\Big[1-F_{H_{\text{B}}}\big(h^x_{\text{m}}(x,z,\ell_{\text{2D}},\phi_{\text{D}})\big)\Big]\text{d}x- \lambda\int_{y_0}^{\ell_{\text{y}}}\Big[1-F_{H_{\text{B}}}\big(h^y_{\text{m}}(y,z,\ell_{\text{2D}},\phi_{\text{D}})\big)\Big]\text{d}y\Bigg) f_{H_{\text{B}}}(z)\text{d}z\Bigg), \quad (28)$$

where $f_{H_{\text{B}}}$ is the pdf of the building heights and $z$ is the height of the rooftop BS.

## REFERENCES


[1] Z. Xiao, P. Xia, and X. Xia, "Enabling UAV cellular with millimeter-wave communication: potentials and approaches," *IEEE Communications Magazine*, vol. 54, no. 5, pp. 66–73, May 2016.

[2] Y. Zeng, J. Lyu, and R. Zhang, "Cellular-connected UAV: Potential, challenges, and promising technologies," *IEEE Wireless Communications*, vol. 26, no. 1, pp. 120–127, February 2019.

[3] 3GPP, "3GPP SA6 accelerates work on new verticals!" 3GPP available at: https://www.3gpp.org/news-events/2045-sa6_verticals, June 2019.

[4] ——, "Enhancement for unmanned aerial vehicles; stage 1 (Release 17)," 3GPP TR 22.829 V17.0.0, September 2019.

[5] W. Xia, M. Polese, M. Mezzavilla, G. Loianno, S. Rangan, and M. Zorzi, "Millimeter wave remote UAV control and communications for public safety scenarios," in *2019 16th Annual IEEE International Conference on Sensing, Communication, and Networking (SECON)*, 2019, pp. 1–7.

[6] A. A. Khuwaja, Y. Chen, N. Zhao, M. Alouini, and P. Dobbins, "A survey of channel modeling for UAV communications," *IEEE Communications Surveys & Tutorials*, vol. 20, no. 4, pp. 2804–2821, Fourthquarter 2018.

[7] M. Mozaffari, W. Saad, M. Bennis, Y. Nam, and M. Debbah, "A tutorial on UAVs for wireless networks: Applications, challenges, and open problems," *IEEE Communications Surveys & Tutorials*, vol. 21, no. 3, pp. 2334–2360, Thirdquarter 2019.

[8] H. Shakhatreh, A. H. Sawalmeh, A. Al-Fuqaha, Z. Dou, E. Almaita, I. Khalil, N. S. Othman, A. Khreishah, and M. Guizani, "Unmanned aerial vehicles (UAVs): A survey on civil applications and key research challenges," *IEEE Access*, vol. 7, pp. 48 572–48 634, 2019.

[9] W. Khawaja, I. Guvenc, D. W. Matolak, U. Fiebig, and N. Schneckenburger, "A survey of air-to-ground propagation channel modeling for unmanned aerial vehicles," *IEEE Communications Surveys & Tutorials*, vol. 21, no. 3, pp. 2361–2391, thirdquarter 2019.

[10] T. S. Rappaport, Y. Xing, G. R. MacCartney, A. F. Molisch, E. Mellios, and J. Zhang, "Overview of millimeter wave communications for fifth-generation (5G) wireless networks-with a focus on propagation models," *IEEE Transactions on Antennas and Propagation*, vol. 65, no. 12, pp. 6213–6230, 2017.

[11] 3GPP, "Study on enhanced LTE support for aerial vehicles, (Release 15)," TR 36.777 V15.0.0, January 2018.

[12] ITU-R, "Propagation data and prediction methods required for the design of terrestrial broadband radio access systems operating in a frequency range from 3 to 60 GHz," Rec. ITU-R P.1410, February 2012.

[13] ——, "Technical feasibility of IMT in bands above 6 GHz," Report ITU-R M.2376-0, July 2015.

[14] T. Bai and R. W. Heath, "Analysis of self-body blocking effects in millimeter wave cellular networks," in *48th Asilomar Conference on Signals, Systems and Computers*, 2014, pp. 1921–1925.

[15] M. Gapeyenko, A. Samuylov, M. Gerasimenko, D. Moltchanov, S. Singh, E. Aryafar, S. Yeh, N. Himayat, S. Andreev, and Y. Koucheryavy, "Analysis of human-body blockage in urban millimeter-wave cellular communications," in *IEEE International Conference on Communications (ICC)*, 2016, pp. 1–7.

[16] R. Kovalchukov, D. Moltchanov, A. Samuylov, A. Ometov, S. Andreev, Y. Koucheryavy, and K. Samouylov, "Evaluating SIR in 3D millimeter-wave deployments: Direct modeling and feasible approximations," *IEEE Transactions on Wireless Communications*, vol. 18, no. 2, pp. 879–896, February 2019.

[17] M. Comisso and F. Babich, "Coverage analysis for 2D/3D millimeter wave peer-to-peer networks," *IEEE Transactions on Wireless Communications*, vol. 18, no. 7, pp. 3613–3627, 2019.

[18] J. G. Andrews, T. Bai, M. N. Kulkarni, A. Alkhateeb, A. K. Gupta, and R. W. Heath, "Modeling and analyzing millimeter wave cellular systems," *IEEE Transactions on Communications*, vol. 65, no. 1, pp. 403–430, January 2017.

[19] E. Ogawa and A. Satoh, "Propagation path visibility estimation for radio local distribution systems in built-up areas," *IEEE Transactions on Communications*, vol. 34, no. 7, pp. 721–724, July 1986.

[20] S. Saunders, C. Tzaras, and B. Evans, "Physical–statistical methods for determining state transition probabilities in mobile–satellite channel models," *International Journal of Satellite Communications*, vol. 19, no. 3, pp. 207–222, May 2001.

[21] Q. Feng, E. K. Tameh, A. R. Nix, and J. McGeehan, "WLCp2-06: Modelling the likelihood of line-of-sight for air-to-ground radio propagation in urban environments," in *IEEE Global Communications Conference*, November 2006, pp. 1–5.

[22] T. Bai, R. Vaze, and R. W. Heath Jr., "Analysis of blockage effects on urban cellular networks," *IEEE Transactions on Wireless Communications*, vol. 13, no. 9, pp. 5070–5083, September 2014.

[23] K. Han, K. Huang, and R. W. Heath, "Connectivity and blockage effects in millimeter-wave air-to-everything networks," *IEEE Wireless Communications Letters*, vol. 8, no. 2, pp. 388–391, April 2019.

[24] T. Bai and R. W. Heath, "Coverage and rate analysis for millimeter-wave cellular networks," *IEEE Transactions on Wireless Communications*, vol. 14, no. 2, pp. 1100–1114, February 2015.

[25] X. Liu, J. Xu, and H. Tang, "Analysis of frequency-dependent line-of-sight probability in 3-D environment," *IEEE Communications Letters*, vol. 22, no. 8, pp. 1732–1735, 2018.

[26] F. Baccelli and X. Zhang, "A correlated shadowing model for urban wireless networks," in *2015 IEEE Conference on Computer Communications (INFOCOM)*, April 2015, pp. 801–809.

[27] A. Colpaert, E. Vinogradov, and S. Pollin, "Aerial coverage analysis of cellular systems at LTE and mmWave frequencies using 3D city models," *Sensors*, vol. 18, no. 12, 2018.

[28] J. Järveläinen, S. L. H. Nguyen, K. Haneda, R. Naderpour, and U. T. Virk, "Evaluation of millimeter-wave line-of-sight probability with point cloud data," *IEEE Wireless Communications Letters*, vol. 5, no. 3, pp. 228–231, 2016.

[29] M. K. Samimi, T. S. Rappaport, and G. R. MacCartney, "Probabilistic omnidirectional path loss models for millimeter-wave outdoor communications," *IEEE Wireless Communications Letters*, vol. 4, no. 4, pp. 357–360, 2015.

[30] A. Al-Hourani, S. Kandeepan, and S. Lardner, "Optimal LAP altitude for maximum coverage," *IEEE Wireless Communications Letters*, vol. 3, no. 6, pp. 569–572, December 2014.

[31] D. E. Berraki, S. M. D. Armour, and A. R. Nix, "Benefits of the sparsity of mmwave outdoor spatial channels for beamforming and interference cancellation," *Physical Communication*, vol. 27, pp. 170–180, April 2018.

[32] D. R. Cox and V. Isham, *Point processes*. CRC Press, 1980, vol. 12.

[33] L. Chen, J. Hang, M. Sandberg, L. Claesson, S. Di Sabatino, and H. Wingo, "The impacts of building height variations and building packing densities on flow adjustment and city breathability in idealized urban models," *Building and Environment*, vol. 118, pp. 344–361, June 2017.

[34] R. Jain, *The art of computer systems performance analysis: techniques for experimental design, measurement, simulation, and modeling*. John Wiley & Sons, 1990.

[35] M. Polese, L. Bertizzolo, L. Bonati, A. Gosain, and T. Melodia, "An experimental mmwave channel model for UAV-to-UAV communications," in *4th ACM Workshop on Millimeter-Wave Networks and Sensing Systems (mmNets'20)*, 2020.

[36] M. T. Dabiri, H. Safi, S. Parsaeefard, and W. Saad, "Analytical channel models for millimeter wave UAV networks under hovering fluctuations," *IEEE Transactions on Wireless Communications*, vol. 19, no. 4, pp. 2868–2883, 2020.

[37] G. Geraci, A. Garcia-Rodriguez, L. Galati Giordano, D. López-Pérez, and E. Björnson, "Understanding UAV cellular communications: From existing networks to massive MIMO," *IEEE Access*, vol. 6, pp. 67 853–67 865, 2018.


**Margarita Gapeyenko** is a Ph.D. candidate at the Unit of Electrical Engineering at Tampere University, Finland. She earned M.Sc. degree in Telecommunication Engineering from University of Vaasa, Finland, in 2014, and B.Sc. degree in Radio Engineering, Electronics, and Telecommunications from KSTU, Kazakhstan, in 2012. Her research interests include mathematical analysis, performance evaluation, and optimization methods for mmWave networks, UAV communications, and (beyond-)5G heterogeneous systems.

**Dmitri Moltchanov** received the M.Sc. and Cand.Sc. degrees from St. Petersburg State University of Telecommunications, Russia, in 2000 and 2003, respectively, and the Ph.D. degree from Tampere University of Technology in 2006. Currently, he is a University Lecturer with the Faculty of Information Technology and Communication Sciences, Tampere University, Finland. He has (co-)authored over 150 publications. His current research interests include 5G/5G+ systems, ultra-reliable low-latency service, industrial IoT applications, mission-critical V2V/V2X systems, and blockchain technologies.

**Sergey Andreev** (SM'17) is an associate professor of communications engineering and Academy Research Fellow at Tampere University, Finland. He has been a Visiting Senior Research Fellow with King's College London, UK (2018-20) and a Visiting Postdoc with University of California, Los Angeles, US (2016-17). He received his Ph.D. (2012) from TUT as well as his Specialist (2006), Cand.Sc. (2009), and Dr.Habil. (2019) degrees from SUAI. He is lead series editor of the IoT Series (2018-) for IEEE Communications Magazine and served as editor for IEEE Wireless Communications Letters (2017-19). He (co-)authored more than 200 published research works on intelligent IoT, mobile communications, and heterogeneous networking.

**Robert W. Heath Jr.** (S'96 - M'01 - SM'06 - F'11) received the B.S. and M.S. degrees from the University of Virginia, Charlottesville, VA, in 1996 and 1997 respectively, and the Ph.D. from Stanford University, Stanford, CA, in 2002, all in electrical engineering. From 1998 to 2001, he was a Senior Member of the Technical Staff then a Senior Consultant at Iospan Wireless Inc, San Jose, CA where he worked on the design and implementation of the physical and link layers of the first commercial MIMO-OFDM communication system. From 2002-2020 he was with The University of Texas at Austin, most recently as Cockrell Family Regents Chair in Engineering and Director of UT SAVES. He is presently a Distinguished Professor at North Carolina State University. He is also President and CEO of MIMO Wireless Inc. He authored "Introduction to Wireless Digital Communication" (Prentice Hall, 2017) and "Digital Wireless Communication: Physical Layer Exploration Lab Using the NI USRP" (National Technology and Science Press, 2012), and co-authored "Millimeter Wave Wireless Communications" (Prentice Hall, 2014) and "Foundations of MIMO Communication" (Cambridge University Press, 2018).

Dr. Heath has been a co-author of a number award winning conference and journal papers including recently the 2016 IEEE Communications Society Fred W. Ellersick Prize, the 2016 IEEE Communications and Information Theory Societies Joint Paper Award, the 2017 Marconi Prize Paper Award, the 2019 IEEE Communications Society Stephen O. Rice Prize, and the 2020 IEEE Signal Processing Society Overview Paper Award. He received the 2017 EURASIP Technical Achievement award and the 2019 IEEE Kiyo Tomiyasu Award. In 2017, he was selected as a Fellow of the National Academy of Inventors. He is a member-at-large on the IEEE Communications Society Board-of-Governors (2020-2022) and is a past member-at-large on the IEEE Signal Processing Society Board-of-Governors (2016-2018). He was Editor-in-Chief of IEEE Signal Processing Magazine from 2018-2020. He is also a licensed Amateur Radio Operator, a Private Pilot, a registered Professional Engineer in Texas.

# PUBLICATION

# IV

**An Analytical Representation of the 3GPP 3D Channel Model Parameters for MmWave Bands**

M. Gapeyenko, V. Petrov, D. Moltchanov, S. Andreev, Y. Koucheryavy,
M. Valkama, M. R. Akdeniz and N. Himayat

*Proceedings of the 2nd ACM Workshop on Millimeter Wave Networks and Sensing Systems*2018, 33–38

# An Analytical Representation of the 3GPP 3D Channel Model Parameters for mmWave Bands

Margarita Gapeyenko, Vitaly Petrov, Dmitri Moltchanov, Sergey Andreev, Yevgeni Koucheryavy, Mikko Valkama
Tampere University of Technology, Finland

Mustafa Riza Akdeniz, Nageen Himayat
Intel Corporation, Santa Clara, CA, USA

## ABSTRACT

Accurate performance prediction for the emerging 3GPP New Radio (NR) technology over millimeter-wave (mmWave) bands is crucial for the upcoming deployments of 5G and beyond cellular networks, utilizing NR. 3GPP has recently presented a 3D multipath cluster-based mmWave channel model for 5G NR, which captures the salient propagation characteristics of the mmWave bands, allowing for better prediction of mmWave system performance. However, it is difficult to directly employ the 3GPP models for analytical system characterization, as most of the parameters are computed through iterative algorithms. In the paper, we address this problem by presenting a statistical approximation for the important parameters of the 3GPP 3D cluster-based channel model, particularly, zenith angle of arrival and power share of every cluster. We then show how the constructed approximation can be used to analytically derive the performance indicators for mmWave NR systems, including outage probability. We compare the results obtained with our proposed statistical approximation model with those given by state-of-the-art simplified single cluster analytical models as well as illustrate the improvements in the accuracy of results.

## KEYWORDS

3GPP New Radio, 5G wireless communications, mmWave multipath propagation, 3D channel model

## 1 INTRODUCTION AND MOTIVATION

While the first release of 3GPP New Radio (NR) technology specification has been completed [9], ongoing research continues to explore challenges related to advanced networking options for 5G [7, 11]. These efforts require detailed performance evaluation and optimization models that capture the specifics of inherently complex millimeter-wave (mmWave) band propagation.

This work was supported by Intel Corporation, the Academy of Finland (projects WiFiUS and PRISMA), and by the project TAKE-5: The 5th Evolution Take of Wireless Communication Networks, funded by Tekes. The work of M. Gapeyenko has been supported by Nokia Foundation. V. Petrov acknowledges the support of HPY Research Foundation funded by Elisa.

The propagation dynamics of mmWave wireless channels in realistic deployments were conventionally assessed with real measurements and/or ray-tracing simulations [2, 8]. These results were later mapped onto models for further performance assessment in realistic deployments. There are two large classes of models proposed for mmWave channels. The first one is presented in [1] and introduces the notion of clusters that describe the rays between the transmitter (Tx) and the receiver (Rx), which experience similar propagation impairments in terms of delay, power attenuation, and geometry of arrival and departure. This model explicitly captures multipath propagation and randomness associated with each of the arriving components. The second class of the models employs "averaging" considerations for simplicity, so-called single cluster, where the impairments of the propagation environment are averaged out to provide the mean propagation losses at a certain separation distance. Both model classes also feature extensions to human body blockage effects [4].

Performance assessment of 5G NR in various deployments and use-cases is currently conducted with both analytical tools and system-level simulations (SLS). However, so far, the assumptions regarding the channel model used in such performance assessment fundamentally differ. In SLS-based studies [12], the authors chiefly rely on 3GPP 3D cluster-based channel model specified in [1] as it provides a much more detailed description of the propagation phenomena that explicitly captures power, delay, and geometry of each cluster arriving at the Rx. However, it comes at the expense of more complex model structure, where the resulting parameters are calculated algorithmically for a given set of environmental and system conditions. As a result, the model is not analytically tractable; therefore, the authors working with analytical modeling of 5G NR [3, 10] mainly utilize simpler models that provide "average" propagation losses (single cluster case) in typical environments, such as 3GPP UMi-street canyon path loss model for line-of-sight (LoS) and non-LoS (nLoS) from [1]. The use of "averaged" models affects the accuracy of the results and complicates the process of calibration between the SLS and analytical tools.

In this paper, aiming to improve the accuracy of analytical performance evaluation frameworks for 3GPP NR, we follow

a statistical approach to develop analytical approximations for the output parameters of the 3GPP 3D cluster-based channel model in case of LoS. As an illustrative example, we focus on zenith angle of arrival as well as the associated cluster power shares, which become the parameters for our first-order performance analysis of 5G mmWave cellular in urban scenarios with human body blockage. We show that these parameters follow well-known distributions for a wide range of environmental and system conditions. We also apply the proposed approximations to analytically derive the outage probability in 5G mmWave systems. Finally, we compare the results obtained with the proposed approximations against those given by an algorithmic implementation of the 3GPP 3D cluster-based channel model as well as those derived by employing the UMi-street canyon model (single LoS cluster) with blockage enhancements [5]. We demonstrate that our approximation model offers more accurate results as compared to the "averaged" UMi-street canyon model.

The rest of this paper is organized as follows. First, in Section 2, we describe the 3GPP 3D cluster-based channel model parameters. In Section 3, we construct our proposed analytical approximations. Finally, in Section 4, we assess the accuracy of the developed approximation as well as consider an illustrative example of the use of the formulated model. Conclusions are drawn in the last section.

## 2 3GPP 3D CLUSTER-BASED MODEL

The standardized 3GPP 3D cluster-based channel model presented in [1] assumes that the received power at the user equipment (UE) comprises power coming from a number of clusters, including LoS path and several reflected components. It thus binds the specifics of mmWave propagation environment to (i) zenith angle of arrival/departure (ZOA/ZOD) and azimuth angle of arrival/departure (AOA/AOD) of a cluster, (ii) delay of every cluster, and (iii) fraction of power contributed by a cluster. However, this model involves complex functions of random variables, which complicates its usage in applied mathematical analysis.

According to 3GPP, 3D cluster-based channel modeling can be decomposed into three steps: (i) specifying the scenario and calculating its geometry, such as LoS ZOA/ZOD and LoS AOA/AOD, (ii) deriving correlated large-scale parameters, including delay spread (DS), angular spreads, Ricean K-factor ($K$), and shadow fading (SF), as well as (iii) generating small-scale parameters: delay, power, AOA/AOD, and ZOA/ZOD. The procedure describing the generation of large-scale parameters is given in sub-clause 3.3.1 of WINNER II Deliverable [6]. Note that the total number of clusters could be chosen within the range of 4 to 20 [1], and this will affect the values of some of the parameters of the model.

The $n$-th cluster's delay is obtained as in Section 7.5 of [1],

$$\tau_n' = -r_\tau \mathrm{DS} \ln(X_n), \tag{1}$$

where $\tau'$ is the delay before sorting procedure, $r_\tau$ is the delay distribution proportionality factor taken from Table 7.5-6 Part 1 of TR 38.901 [1], DS is the delay spread with mean and variance given in Table 7.5-6 Part 1 [1], while the generation procedure is described in [1], $X_n$ is drawn from the uniform distribution in $(0, 1)$, and $n$ is the cluster index $\{1, 2 \dots N\}$. Once all the delays are calculated, they are normalized by subtracting the minimum delay and then sorted in the increasing order, $\tau_n = \mathrm{sort}[\tau_n' - \min(\tau_n')]$.

The delays in case of LoS take the following form

$$\tau_n^{\mathrm{LoS}} = \tau_n / C_\tau, \tag{2}$$

where $C_\tau = 0.7705 - 0.0433K + 0.0002K^2 + 0.000017K^3$ and $K$ is the Ricean K-factor expressed in dB.

Once delays are calculated and sorted, one proceeds by specifying the received power of each cluster. The power of cluster $n$, $P_n$, is obtained at step 6 of Section 7.5 in [1] as

$$P_n' = \exp\left(-\tau_n \frac{r_{\tau_n} - 1}{r_{\tau_n} \mathrm{DS}}\right) 10^{\frac{-Z_n}{10}}, \tag{3}$$

where $Z_n$ captures the effect of per-cluster shadowing and follows a normal distribution with the zero mean and variance $\sigma^2$. The cluster powers in LoS conditions are given as

$$P_n = \frac{1}{K_R + 1} \frac{P_n'}{\sum_{n=1}^{N} P_n'} + \delta(n-1) P_{1,\mathrm{LOS}}, \tag{4}$$

where $\delta(\cdot)$ is the Dirac delta function, $K_R$ is the Ricean K-factor converted to linear scale, and $P_{1,\mathrm{LOS}} = K_R/(K_R + 1)$.

According to step 7 of Section 7.5 in [1], ZOA is

$$\theta_{n,\mathrm{ZOA}}' = -\frac{\mathrm{ZSA} \ln(P_n / \max(P_n))}{C_\theta}, \tag{5}$$

where $C_\theta = C_\theta^{\mathrm{NLoS}}(1.308 + 0.0339K - 0.0077K^2 + 0.0002K^3)$ for LoS and $C_\theta^{\mathrm{NLoS}}$ is given in Section 7.5 of [1].

Finally, the ZOA in LoS conditions is

$$\theta_{n,\mathrm{ZOA}} = [X_n \theta_{n,\mathrm{ZOA}}' + Y_n] - [X_1 \theta_{1,\mathrm{ZOA}}' + Y_1 - \theta_{\mathrm{LoS,ZOA}}], \tag{6}$$

where $X_n$ is a discrete random variable (RV) that is uniformly distributed over $\{-1, 1\}$, $Y_n$ follows a normal distribution with the zero mean and variance $(\mathrm{ZSA}/7)^2$, and $\theta_{\mathrm{LoS,ZOA}}$ is the ZOA of the LoS path calculated from the scenario geometry.

The generation procedure for the remaining parameters, such as ZOD and AOA/AOD, follows a similar approach and is presented in step 7 of Section 7.5 in [1].

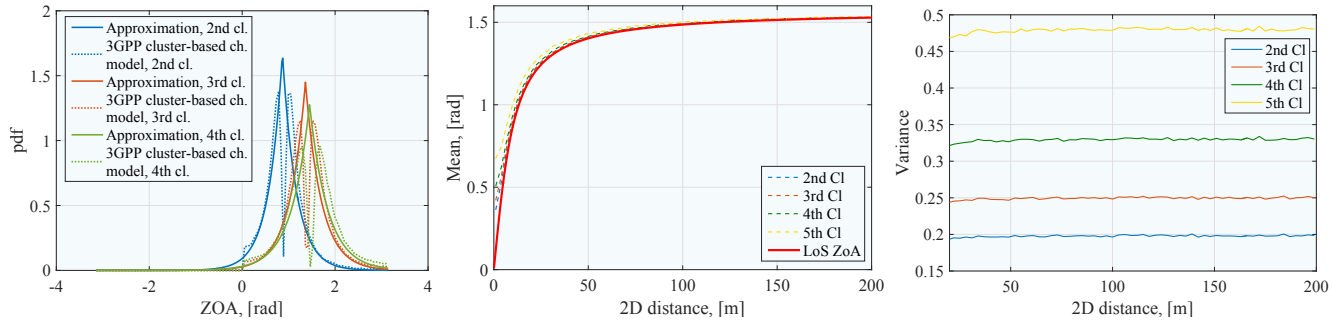


(a) ZOA marginal pdfs for clusters of 3GPP model (b) Mean of ZOA (c) Variance of ZOA

**Figure 1: 3GPP ZOA characteristics and proposed approximations for $N = 5$ clusters.**

## 3 OUR PROPOSED APPROXIMATION

In this section, we outline the proposed approximation for the important output parameters of the 3GPP 3D cluster-based model in case of LoS. For illustrative purposes, we concentrate on two parameters required in the performance evaluation of 5G mmWave cellular, accounting for random signal blockage: 1) ZOA and 2) received power share. We note that assuming the positions of blockers according to a Poisson point process (PPP), the AOA becomes irrelevant as the field of blockers is stochastically similar in any direction. The approach may also be used to approximate other parameters of the 3GPP cluster-based model. The settings used for the numerical examples are summarized in Table 1.

### 3.1 3GPP ZOA approximation

We begin with ZOA, whose characteristics are presented in Fig. 1(a) for the heights of the mmWave access point (AP) and the UE equal to $h_A = 10$ m and $h_U = 1.5$ m, respectively; we also focus on 5 strongest clusters for simplicity. The 2D distance, $x$, between the AP and the UE is set to 10 m, 40 m, and 70 m for the illustration of 2-nd cluster, 3-rd cluster, and 4-th cluster, respectively. One may observe that ZOA can be well approximated by a Laplace distribution with the marginal probability density function (pdf) given by

$$f_{\theta_n}(y) = \frac{1}{2b_n} \exp\left(-\frac{|y - a_n|}{b_n}\right), \; n = 2, 3, \ldots, \tag{7}$$

where $a_n$ and $b_n$, $n = 2, 3, \ldots, N$, are the distribution parameters, while $N$ is the number of clusters. While Fig. 1(a) shows some mismatch between the statistical pdf and the proposed approximation, the presented solution can be applied for the first-order analysis as further illustrated in Section 4.

We now proceed with calculating the parameters of the approximating Laplace distribution, since its mean and variance may depend on the scenario geometry (e.g., the distance between the nodes). To this end, Fig. 1(b) shows that the mean value for all the clusters, $a_n$, coincides with the 3GPP LoS ZOA. Hence, the value of $a_n$ can be estimated as

$$a_n = \frac{\pi}{2} - \arctan\left(\frac{h_A - h_U}{x}\right), \; n = 2, 3, \ldots, N. \tag{8}$$

The second key parameter of the Laplace distribution is $b_n$, which is related to the distribution variance as $b_n = \sqrt{\sigma^2_{\theta_n}/2}$.

Fig. 1(c) reports on the empirical variance of ZOA as a function of the 2D distance between the nodes. As can be observed, the variance for each of the clusters can be approximated by a constant value, from which we find $b_n$ as

$$b_1 = 0, b_2 = 0.3146, b_3 = 0.3529, b_4 = 0.4056, b_5 = 0.4897. \tag{9}$$

Since both the approximating distribution and its key parameters have been established, we conclude that the approximation of the ZOA parameter of the 3GPP cluster-based model is constructed by combining (7), (8), and (9).

### 3.2 3GPP power share approximation

The knowledge of ZOA allows to carefully model the process of clusters blockage by humans or other obstacles and thus estimate the probability for each of the clusters to be blocked. To evaluate the received power for certain clusters, we need to identify the share of power that they contribute at the Rx. This will further allow for estimating the key metrics of interest, such as outage probability and link capacity.

Recall that according to 3GPP channel model outlined in Section 2, the received power from each cluster is calculated as a product of the received power determined by the averaged path loss and a random power share for each of the clusters normalized over the range $(0, 1)$. Fig. 2(a) presents the pdfs of the power share values for first 5 clusters ($h_A = 10$ m and $h_U = 1.5$ m) as well as illustrates the fitting of empirical pdfs by a log-normal distribution for the 2-nd, 3-rd, 4-th, and 5-th clusters (the 1-st cluster is a special case discussed below), in the following form

$$f_{P_{s,n}}(z) = \frac{1}{z d_n \sqrt{2\pi}} \exp\left(-\frac{(\ln z - c_n)^2}{2d_n^2}\right), \; n = 2, 3, \ldots, N, \tag{10}$$

where $c_n$ and $d_n$ are the parameters of the distribution.

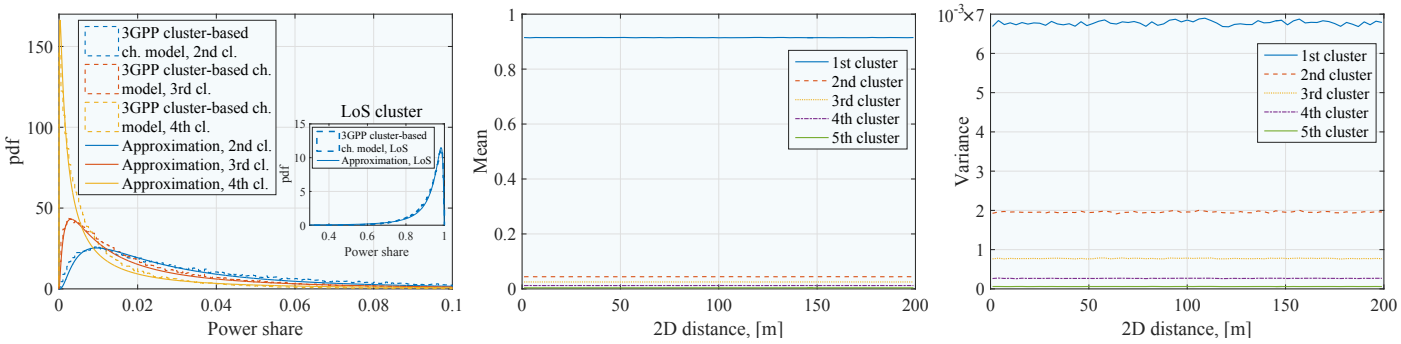


(a) Power share marginal pdfs for clusters (b) Mean of power share (c) Variance of power share

**Figure 2: 3GPP power share characteristics and proposed approximations for $N = 5$ clusters.**

The fraction of LoS power shown in Fig. 2(a) (1-st cluster) is always the cluster characterized by the strongest power. This value can be well approximated by a log-normal distribution with the argument $(1 - x)$ and the parameters $(c_1, d_1)$,

$$f_{P_{s,1}}(z) = \frac{1}{(1-z)d_1\sqrt{2\pi}} \exp\left(-\frac{(\ln(1-z)-c_1)^2}{2d_1^2}\right). \quad (11)$$

The discretized version of the $\chi^2$ goodness-of-fit test has been applied to the distributions in Fig. 2(a) with the level of significance set to 0.95, which shows that the hypothesis about the log-normal distribution does hold for the considered set of parameters. A similar conclusion applies to other system parameters as well. Therefore, the power shares can be approximated by the log-normal distribution and we continue by deriving its parameters.

We first notice that there is a direct relationship between the distribution parameters ($c_n$ and $d_n$) and the estimated mean and variance ($\mu_n$ and $\sigma_n^2$). Following the approach, we estimate the parameters of the power share distributions as

$$c_1 = -2.88,\ c_2 = -3.55,\ c_3 = -4.1,\ c_4 = -4.98,\ c_5 = -6.2,$$
$$d_1 = 1.2,\ d_2 = 1.1,\ d_3 = 1.3,\ d_4 = 1.8,\ d_5 = 2.51. \quad (12)$$

In summary, the power share values can be well approximated by a combination of (10), (11), and (12). Hence, two key parameters of the 3GPP 3D cluster-based model to account for random blockage in 5G NR systems have been approximated by tractable analytical functions. The outlined approximations as well as the derived parameters $a_n$, $b_n$, $c_n$, and $d_n$ also hold for other environmental conditions ($h_A$, $h_U$, etc.) as long as $N = 5$.

# 4 APPLICATION OF OUR MODEL

In this section, we illustrate the applicability of the developed approximation to the analysis of 5G mmWave cellular systems. We particularly calculate the UE outage probability. We assume that the power share and ZOA do not depend on each other; we demonstrate with simulations that this assumption does not affect the outage probability. We then proceed by comparing the obtained results with those based on the algorithmic implementation of the 3GPP cluster-based channel model and UMi-street canyon channel model.

## 4.1 Outage probability

We consider the UE located at a fixed 2D distance of $x$ from its serving mmWave AP. The heights of AP and UE are assumed to be constant and set to $h_A$ and $h_U$. Blockers are represented by cylinders with the base radius of $r_B$ and the constant height of $h_B$. The blockers form a PPP with the density of $\lambda_B$. Owing to the random propagation environment, the ZOA, $\theta_n(x)$, and the received power share from each cluster, $P_{s,n}(x)$, are all RVs, where index 1 corresponds to the LoS path, $n = 2, 3, \ldots, N$ are clusters sorted in the increasing order according to their delays. The UE is always associated with the link having the strongest power. The UE is in outage when all the clusters are blocked or when the received power of the "best" cluster is below the target level.

Let $p_n$ be the probability that the $n$-th cluster of the link between the AP and the UE is blocked and first consider the blockage of the LoS path, $p_1$. Employing the results of [5], the LoS blockage probability is given by

$$p_1(x) = 1 - e^{2r_B\left(x\frac{h_B-h_U}{h_A-h_U}+r_B\right)}. \quad (13)$$

In the 3GPP 3D cluster-based channel modeling algorithm, the exact location of the reflection point is not specified. However, by using ZOA, the blockage probability for the $n$-th cluster, $p_n(x)$, could be calculated as

$$p_n(x) = \int_{-\pi}^{\pi} f_{\theta_n}(y;x)q_n(y)dy, \quad (14)$$

where $f_{\theta_n}(y;x)$ is the distribution of the ZOA at the distance of $x$ approximated by the Laplace distribution with the parameters $a_n(x)$, $b_n(x)$, $n = 2, 3, \ldots, N$, all estimated from statistical data, $q_n(y)$ is the probability of blockage as a function of ZOA, which is given as

$$q_n(y) = 1 - e^{-2\lambda_B r_B(\tan y(h_B-h_U)+r_B)}. \quad (15)$$

**Table 1: Baseline system parameters**

| Parameter | Value |
|---|---|
| Height of UE, $h_U$ and AP, $h_A$ | 1.5 m and 10 m |
| Height and radius of blocker, $h_B$ and $r_B$ | 1.7 m and 0.25 m |
| Number of clusters, $N$ | 5 |
| Transmit power, $P_T$ | 35 dBm |
| SNR threshold | 3 dB |
| Carrier frequency, $f_c$ | 28 GHz |
| Bandwidth | 1 GHz |

Substituting (15) and Laplace pdf (7) into (14), we obtain

$$p_n(x) = \int_{-\pi}^{\pi} \frac{1 - e^{-2\lambda_B r_B(\tan y(h_B - h_U) + r_B)}}{2b_n e^{\frac{|y - a_n(x)|}{b_n}}} dy, \qquad (16)$$

which can be evaluated numerically.

The received power of every cluster can be written as

$$P_n = P_{s,n} 10^{(P_T - 30 - L)/10},\ n = 1, 2, \ldots, N, \qquad (17)$$

where $L$ is the path loss and $P_T$ is the transmit power. Using the 3GPP UMi LoS path loss model in (17), we arrive at

$$P_n = P_{s,n} 10^{(P_T - 30 - 32.4 - 20\log_{10} f_c - 21\log_{10}(D_3))/10}, \qquad (18)$$

where $D_3$ is the 3D distance between the AP and the UE.

Note that $P_n$ is a function of a RV. Therefore, by utilizing the RV transformation technique, the pdf of $P_n$ is given as

$$f_{P_n}(z; x) = \frac{1}{10^{(P_T - 30 - 32.4 - 20\log_{10} f_c - 21\log_{10}(D_3))/10}} f_{P_{s,n}}\left(\frac{P_n(x)}{10^{(P_T - 30 - 32.4 - 20\log_{10} f_c - 21\log_{10}(D_3))/10}}\right). \qquad (19)$$

To evaluate the received power of the strongest cluster, we employ a weighted sum of the received power pdfs

$$f_P(z; x) = \sum_{n=1}^{N} \left[ (1 - p_n(x)) \prod_{j=1}^{n-1} p_j(x) \right] f_{P_n}(z; x), \qquad (20)$$

where the weights are the probabilities of choosing cluster $n$.

We now proceed by obtaining the outage probability. Observe that outage occurs when the following mutually exclusive events happen: (i) all clusters are blocked or (ii) at least one cluster is non-blocked but the received signal falls below a certain threshold, $S_T$. The former probability is given as

$$p_{O,1}(x) = \prod_{n=1}^{N} p_n(x). \qquad (21)$$

The probability that the received signal falls below $S_T$ is

$$p_{O,2}(x) = \int_0^{S_T} f_P(z; x) dz, \qquad (22)$$

which leads to the outage probability in the following form

$$p_O(x) = \prod_{n=1}^{N} p_n(x) + \int_0^{S_T} f_P(z; x) dz. \qquad (23)$$

## 4.2 Numerical results

We continue with a numerical illustration of the outage probability under LoS conditions and human blockage environment as well as compare the results based on the proposed approximations against: (1) those given by an algorithmic implementation of the 3GPP cluster-based channel model [1] and (2) analytical model based on the 3GPP UMi-street canyon channel model [5]. In the second case, only the LoS path loss is considered for the analysis. In case of the LoS blockage, the received power is reduced by the human body loss (20 dB). The scenario parameters are given in Table 1.

Fig. 3 demonstrates the outage probability as a function of 2D distance between the AP and the UE and $\lambda_B = 0.1$ for three approaches. We may observe four major intervals in this figure. For our set of parameters these are: (i) up to 28 m; (ii) from 28 to 44 m; (iii) from 44 m to 170 m; (iv) over 170 m.

The first interval shows outage probability close to 0 for all three models due to the short distance between AP and UE leading to a small LoS blockage probability and sufficiently high received power at the UE side even in case of blockage. In the second interval, both the simulation and approximation curves start increasing, since the chances of having the paths blocked are not negligible anymore. Meanwhile, the 3GPP UMi model underestimates the outage probability, as the modeled human body loss is not high enough to result in SNR being lower than the threshold value.

The third interval shows a considerable gap between the 3GPP UMi model and the cluster-based model together with its approximation. This is explained by increased blockage probability and only a single cluster when considering the 3GPP UMi model. In case of blockage of a single LoS cluster, the UE is considered in outage, while in cluster-based channel model the UE may communicate on different reflected clusters if some of them are not blocked and the received power is higher than the target level. Finally, the fourth interval illustrates a close match between all three models as the received clusters in the cluster-based models are contributing low power, so UE mainly employs the LoS cluster.

Fig. 4 shows the outage probability as a function of the density of blockers for two AP–UE 2D distances of 70 m and 49 m. The approximation gives a tight match with the cluster-based model for a wide range of densities of blockers. Some deviation from the simulation plots at higher densities of blockers is due to imperfections of the approximated ZoA distribution. However, the 3GPP UMi model considerably overestimates the outage probability as compared to the cluster-based model, especially at higher distances. This is caused by increased blockage probability for higher densities of blockers. For the 3GPP UMi model, this growth leads to a significantly increased outage probability due to the absence of cluster diversity. Meanwhile, the outage probability for

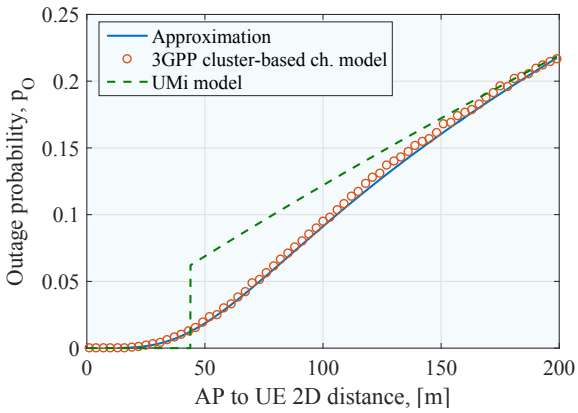


**Figure 3: Outage probability $p_O$ vs. distance.**

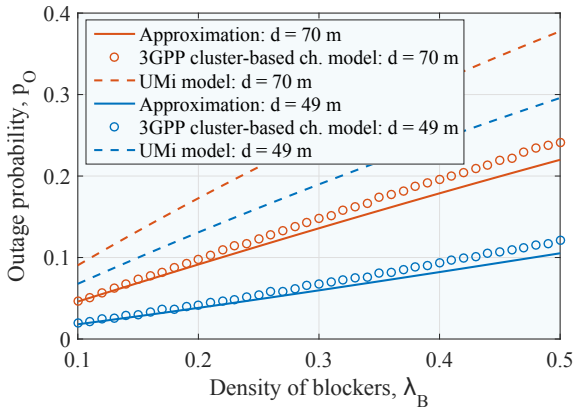


**Figure 4: Outage probability $p_O$ as a function of $\lambda_B$.**

the cluster-based model increases much slower than that for the 3GPP UMi model due to the presence of alternative clusters that can be used in case of LoS blockage.

## 5 CONCLUSIONS

In this work, we developed analytically tractable approximations for the important parameters of the algorithmic 3D cluster-based channel model by 3GPP, including the zenith angle of arrival and the received power share of the clusters in LoS conditions. We demonstrated that these parameters can be well approximated by analytical distributions over a wide range of the environmental and system conditions. We also applied the proposed approximations to analytically characterize the outage probability in 5G mmWave cellular. We showed that the results obtained with our approximations closely match those directly produced by the algorithmic 3GPP 3D cluster-based model, in contrast to a simplistic model not capturing the multipath mmWave propagation.

The use of our proposed approximations improves the accuracy of known analytical approaches for the performance evaluation of NR systems. In addition, the outlined methodology can be further applied to construct more accurate approximations for both outlined and other important parameters of the 3GPP 3D cluster-based channel model, thus enabling more precise yet analytically tractable constructions for 5G and beyond mmWave networks.

## REFERENCES


[1] 3GPP. 2018. *Study on channel model for frequencies from 0.5 to 100 GHz (Release 15).* 3GPP TR 38.901 V15.0.0.

[2] M. R. Akdeniz, Y. Liu, M. K. Samimi, S. Sun, S. Rangan, T. S. Rappaport, and E. Erkip. 2014. Millimeter wave channel modeling and cellular capacity evaluation. *IEEE Journal on Selected Areas in Communications* 32, 6 (June 2014), 1164–1179.

[3] J. G. Andrews, T. Bai, M. N. Kulkarni, A. Alkhateeb, A. K. Gupta, and R. W. Heath. 2017. Modeling and Analyzing Millimeter Wave Cellular Systems. *IEEE Transactions on Communications* 65, 1 (January 2017), 403–430.

[4] M. Gapeyenko, A. Samuylov, M. Gerasimenko, D. Moltchanov, S. Singh, M. R. Akdeniz, E. Aryafar, N. Himayat, S. Andreev, and Y. Koucheryavy. 2017. On the Temporal Effects of Mobile Blockers in Urban Millimeter-Wave Cellular Scenarios. *IEEE Transactions on Vehicular Technology* 66, 11 (November 2017), 10124–10138.

[5] M. Gapeyenko, A. Samuylov, M. Gerasimenko, D. Moltchanov, S. Singh, E. Aryafar, S. Yeh, N. Himayat, S. Andreev, and Y. Koucheryavy. 2016. Analysis of Human Body Blockage in Urban Millimeter-Wave Wireless Communications Systems. In *2016 IEEE International Conference on Communications.*

[6] IST-WINNER II. 2007. *WINNER II Channel Models.* Deliverable 1.1.2 v.1.2.

[7] C. De Looper. 2018. *AT&T names first three cities chosen to receive 5G networks by the end of 2018.* https://www.digitaltrends.com/mobile/att-5g-rollout/. Accessed on 14.08.18.

[8] G. R. MacCartney, T. S. Rappaport, and A. Ghosh. 2017. Base Station Diversity Propagation Measurements at 73 GHz Millimeter-Wave for 5G Coordinated Multipoint (CoMP) Analysis. In *IEEE Global Communications Workshops (GLOBECOM Wkshps).* 1–7.

[9] F. Mademann. 2017. *System architecture milestone of 5G Phase 1 is achieved.* http://www.3gpp.org/NEWS-EVENTS/3GPP-NEWS/1930-SYS_ARCHITECTURE. Accessed on 14.08.18.

[10] V. Petrov, M. A. Lema, M. Gapeyenko, K. Antonakoglou, D. Moltchanov, F. Sardis, A. Samuylov, S. Andreev, Y. Koucheryavy, and M. Dohler. 2018. Achieving End-to-End Reliability of Mission-Critical Traffic in Softwarized 5G Networks. *IEEE Journal on Selected Areas in Communications* 36, 3 (March 2018), 485–501.

[11] J. Smith. 2018. *Verizon to use Samsung for first commercial 5G network rollout.* https://www.zdnet.com/article/verizon-to-use-samsung-routers-for-initial-5g-rollout/. Accessed on 14.08.18.

[12] M. Zhang, M. Polese, M. Mezzavilla, S. Rangan, and M. Zorzi. 2017. Ns-3 Implementation of the 3GPP MIMO Channel Model for Frequency Spectrum above 6 GHz. In *Workshop on ns-3.*

# PUBLICATION V

**Spatially-Consistent Human Body Blockage Modeling: A State Generation Procedure**

M. Gapeyenko, A. Samuylov, M. Gerasimenko, D. Moltchanov, S. Singh, M. Akdeniz, E. Aryafar, S. Andreev, N. Himayat and Y. Koucheryavy

*IEEE Transactions on Mobile Computing* 19.9 (2020), 2221–2233

# Spatially-Consistent Human Body Blockage Modeling: A State Generation Procedure

Margarita Gapeyenko, Andrey Samuylov, Mikhail Gerasimenko, Dmitri Moltchanov, Sarabjot Singh, Mustafa Riza Akdeniz, Ehsan Aryafar, Sergey Andreev, Nageen Himayat, and Yevgeni Koucheryavy

**Abstract**—*Spatial correlation* has been recognized by 3GPP as one of the key elements in *millimeter-wave* (mmWave) channel modeling. Correlated channel behavior is induced by macro objects, such as buildings, as well as by micro objects, including humans around the mmWave receivers. The 3GPP's three-dimensional (3D) spatially consistent channel model designed to capture these phenomena assumes a-priori knowledge of the correlation distance between the receivers. In this paper, we propose a novel *spatially-consistent human body blockage state generation procedure*, which extends the standardized 3D channel model by 3GPP to capture the correlation between the line-of-sight (LoS) links and the reflected cluster states affected by human body blockage. The proposed model is based on analytical expressions for the *conditional link state probability*, thus permitting the parametrization of the spatial field of receivers. It also does not require any a-priori information on the correlation distance as the latter is identified explicitly based on the environmental parameters. We compare the results for the proposed model with those obtained with the uncorrelated blockage model and conclude that in many special cases correlation manifests itself in quantitatively different propagation conditions experienced at the nearby receivers.

**Index Terms**—5G, mmWave, 3GPP 3D channel model, human body blockage, spatial consistency, correlation.

## 1 Introduction

Millimeter-wave (mmWave) communication is considered to be the core part of the emerging 5G mobile networks, which are capable of supporting the stringent requirements of IMT-2020 [1]. Larger available bandwidths make the extremely high frequency bands an attractive candidate for serving advanced future applications [2]–[5].

Despite a number of benefits delivered by mmWave, there are also several challenges to be solved. For example, due to shorter wavelengths, smaller objects in the channel may produce a considerable impact on the mmWave propagation. According to the recent studies, human body blockage leads to a significant attenuation of the mmWave signal [6]–[8] and should be taken into account in mmWave channel modeling [9], [10].

An example of such models is the 3GPP three-dimensional (3D) stochastic channel model (SCM) proposed in [11] that has further been improved and ratified by 3GPP in Release 15 [9]. It is currently utilized by both academia and industry to capture the mmWave channel properties in system-level simulation (SLS) tools [12], [13].

If mmWave-based receivers are located next to one another, they often experience similar propagation conditions [14]–[16]. This effect, known as *spatial correlation*, has been recently recognized by 3GPP as an important consideration in the mmWave channel modeling [9]. The correlated state of the channel at the receiver (Rx) may affect the implementation and performance of beamsearching and beamtracking mechanisms, resource allocation strategies, as well as multiple-input multiple-output (MIMO) system design [9], [17]–[20].

### 1.1 Background and Related Studies

3GPP has recently extended its 3D SCM channel model to capture the correlation of large and small scale parameters (LSP and SCP) as well as (non)-line-of-sight (n)LoS states. In [9], [21], three such methods have been proposed. In the first one, named *method of spatially-consistent random variables*, the spatial correlation of channel clusters is accounted for by introducing the so-called spatial consistency to the channel cluster specific random variables taken from the 3GPP 3D SCM model [9].

The second method is known as *geometric stochastic approach*. In this case, the large scale parameters (LSP) are pre-computed for every grid, and each Rx inside it is associated with these LSP. The grid has a rectangular shape with the side length of correlation distance that is provided a-priori. In the third alternative, called *method of geometrical cluster locations* (grid-based GSCM, GGSCM), the cluster, path angles, and delays are defined by the geometrical positions $(x, y)$ of the appropriate scatterers. In all these models, the correlation distance is arbitrarily chosen as an

*M. Gapeyenko, A. Samuylov, M. Gerasimenko, D. Moltchanov, S. Andreev, and Y. Koucheryavy are with Tampere University, Tampere, Finland (e-mail: {firstname.lastname, evgeni.kucheryavy}@tuni.fi)*
*S. Singh is with Uhana (e-mail: sarabjotsingh.in@gmail.com)*
*M. R. Akdeniz and N. Himayat are with Intel Corporation, Santa Clara, CA, USA (e-mail: {mustafa.akdeniz, nageen.himayat}@intel.com)*
*E. Aryafar is with Portland State University, Portland, OR, USA (e-mail: earyafar@pdx.edu)*

input parameter, which leads to non-uniqueness of the resulting propagation environment.

With the help of a ray-based simulator, the authors in [22] demonstrated a profound impact of spatial consistency on the path loss modeling. The work in [23] described a spatially consistent path loss model for the street urban scenarios. In [24], the authors presented their simulator wherein the spatially consistent channel model is integrated.

In addition to macro objects affecting the LoS/nLoS state, smaller objects (e.g., humans, vehicles, etc.) induce blockage of the mmWave channel. When modeling highly crowded realistic urban environments, such as squares and stadiums, the use of ray-tracing approaches is often difficult due to the associated computational complexity. Recently, a number of analytical models for blockage phenomena were proposed [25]–[27]. However, these constructions either do not capture the effect of spatial correlation or do not offer a method to optimize the channel model. In [28], the authors measured the channel from different base station (BS) locations and demonstrated how the knowledge of correlation distance may help find another best BS in case of blockage. Further, in [29], the authors argued for the importance of correlated blockage consideration. They proposed a model to establish the probability that a certain target is blocked, while having more than one transceiver communicating with that target.

Recently, there have been multiple attempts within 3GPP to extend the SCM model by capturing the spatial correlation of blockage caused by micro objects, including the human crowd [9]. Particularly, in [9], a human body has been modeled and two blockage models, namely, $A$ and $B$, were introduced. The model $A$ stochastically generates $M$ $2D$ blockage regions uniformly distributed around each Rx. The parameter $M$ is a fixed number that may be changed in case the density of blockers varies. The latter model does not account for the height of blockers and assumes a fixed distance between Rx and blocker, which significantly reduces the applicability of this model. In order to account for the spatial correlation between blockers, a certain autocorrelation function is applied to the centers of blockers. The limitation of this model is in the correlation distance, which is a parameter that needs to be specified in advance.

In model $B$, a total of $M$ rectangular screens are physically placed on a map. This allows to account for any density, dimensions of blockers, as well as spatial consistency during the simulation time. However, the computational complexity of this method increases significantly with the growing numbers of blockers, thus making it infeasible to apply for modeling densely crowded environments.

### 1.2 Contributions of This Work

In this paper, we complement the existing 3GPP 3D channel model for the frequencies of 0.5 to 100 GHz [9] by accounting for the spatial correlation caused by micro objects (particularly, humans bodies) in crowded scenarios, e.g., squares, stadiums, etc. Particularly, we propose a novel spatially consistent blockage state generation procedure, which employs our analytical framework for the conditional link state probabilities. Compared to 3GPP blockage models, our approach features the following advantages: (i) correlation distance does not need to be specified in advance, (ii) spatial correlation is captured across all of the blockers, and (iii) computational complexity does not depend on the density of blockers, which makes it possible to model crowded environments.

Our main contributions are therefore as follows:

- We analyze the spatial correlation of human body blockage caused by a dense crowd around the receivers for the mmWave channel by proposing a novel mathematical framework. We derive the conditional channel state probabilities for every link generated within the scenario, such as Transmitter-Rx links or Reflector-Rx links.
- We integrate the proposed analytical model into the SLS software [30], with our new blockage state generation procedure taking into account the actual correlation across micro objects. This blockage generation procedure allows to optimize the channel model by introducing an additional channel state (blocked/non-blocked) for every link, which captures the spatially-consistent human body blockage.
- We characterize the absolute received power difference when disregarding the correlation due to micro objects in the mmWave channel by conducting extensive simulations. We thus demonstrate that the spatial correlation is a local effect, which leads to significant received power variations at nearby locations when it is not accounted for.

The rest of this paper is organized as follows. The system model and its assumptions are introduced in Section 2. Our mathematical framework is developed in Section 3. The spatially-consistent blockage state generation procedure for mmWave propagation modeling is outlined in Section 4. The key numerical results are reported in Section 5. Conclusions are drawn in the last section.

## 2 System Model and Assumptions

### 2.1 Propagation Environment

The considered scenario is illustrated in Fig. 1. The transmitter (Tx) is assumed to be located at the origin and has the height of $h_T$. The human body blockers (referred to as blockers further on) are uniformly

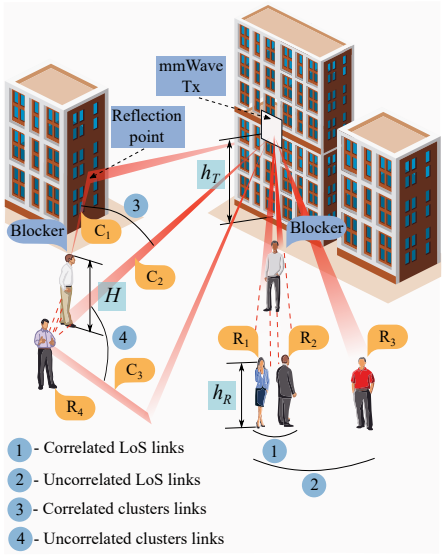


Fig. 1. The considered scenario of interest.

distributed in the area and modeled as cylinders [31] with the random height of $H$ as well as the constant base diameter of $d_m$. The blocker heights are assumed to be approximated by a Normal distribution $H \sim N(\mu_H, \sigma_H)$ [32]. The centers of the cylinder bases follow a 2D Poisson point process (PPP) with the density of $\lambda_B$. A total of $K$ Rx are uniformly distributed in the area $S$ with the coordinates $x_{R,k}, y_{R,k}$, $k = 1, \ldots, K$. The size of Rx is assumed to be infinitesimally small. The rest of the parameters are summarized in Table 1.

As one may observe in Fig. 1, there are multiple *clusters* arriving at Rx.

TABLE 1
Summary of notation and parameters

| Notation | Description |
|---|---|
| $h_T$, $h_R$ | Height of Tx, Rx |
| $x_{R,k}, y_{R,k}$ | x-, y- coordinates of Rx $k$, $k = 1, \ldots, K$ |
| $x_T$, $y_T$ | x-, y- coordinates of Tx |
| $x_{C,kn}, y_{C,kn}, z_{C,kn}$ | x-, y-, z- coordinates of reflecting point for cluster $n$ of Rx $k$ |
| $\phi_{D,kn}$, $\phi_{A,kn}$ | Angles of departure and arrival of cluster $n$ |
| $\theta_{D,kn}$, $\theta_{A,kn}$ | Zenith angles of departure and arrival of cluster $n$ |
| $\tau_{kn}$ | Delay of cluster $n$ |
| $H$, $d_m$ | Height and diameter of a blocker, $H \sim N(\mu_H, \sigma_H)$ |
| $F_H(x)$ | CDF of the blocker height |
| $\lambda_B$ | Density of blockers per unit area |
| $h_C$, $h_1$, $h_2$ | Heights of points $P$, $O$, and $M$ |
| $r_0$ | Two-dimensional distance from $O$ to $P$ |
| $d$ | Two-dimensional distance from $O$ to $M$ |
| $\alpha$ | Angle $\angle POM$ |
| $p_{00}$, $p_{01}$ | Conditional probabilities to reside in non-blocked/blocked states at point $M$ (0 and 1) given that there was non-blocked state at $O$ |
| $p_{10}$, $p_{11}$ | Conditional probabilities to reside in non-blocked/blocked states at point $M$ (0 and 1) given that there was blocked state at $O$ |

**Definition 1.** *A cluster is a set of rays that travel from Tx to Rx with a small variation in their angles of arrival and departure caused by diffuse reflections on the same surface.*

The correlation between the current channel states of the links is a consequence of the separation angle of clusters. Particularly, two Rx, $R_1$ and $R_2$, in Fig. 1 are located nearby, which leads to the correlation between their LoS links. In contrast, $R_1$ and $R_3$ are well-separated, which implies that the presence of blockage at $R_1$ does not affect the LoS link at $R_3$. The situation is similar with the clusters. Two clusters, $C_1$ and $C_2$, arriving at Rx $R_4$ are correlated with each other as they are not well-separated in space, and a single blocker occludes their paths. At the same time, clusters $C_2$ and $C_3$ are independent. A spatially-consistent model for mmWave channel needs to take the effects of spatially-consistent human body blockage into account.

### 2.2 3GPP 3D Channel Model

It is important to note that the proposed blockage state generation procedure is compatible with any channel model. Below, we briefly review the 3GPP models with and without spatial correlation as they are widely acceptable. 3GPP 3D channel model for bands higher than 6 GHz was introduced in [9]. The proposed considerations are based on a similar logic as those in the LTE specifications [33], with modifications specific to mmWave frequencies. The model thus allows to generate a set of correlated (with each other) parameters (angle-of-departure (AoD), angle-of-arrival (AoA), zenith-of-departure (ZoD), zenith-of-arrival (ZoA), powers, delays, etc.) for each cluster based on the measurements conducted in a specific radio environment.

In Section 7.6.3 of [9], a spatially-consistent extension to the 3GPP 3D channel model is proposed. The modeling procedure comprises two parts: 1) generation of spatially-consistent large scale and small scale parameters for a static Rx drop; and 2) correlated Rx mobility modeling. In step one, a regular horizontal grid is generated, whose inter-site distance equals the correlation distance specified in advance. The standard mmWave model is used to specify the propagation conditions for each node of the grid. The propagation parameters of Rx are then interpolated based on the nearest nodes, see [34] for details. When Rx mobility is added, the delay, departure/arrival angles, and cluster powers are updated according to user direction and speed.

### 2.3 3GPP Cluster Localization Process

According to the 3GPP 3D channel model, there are $N$ clusters arriving at every Rx in the scenario, where $N$ is a scenario-specific parameter [9]. The model provides the AoA, AoD, ZoD, ZoA, delay, etc. for

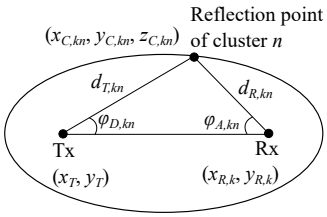


Fig. 2. Illustration of location of a cluster.

each cluster, which become the input parameters for our analytical framework outlined in Section 3. To introduce our spatially-consistent blockage state generation procedure described in Section 4 and based on a novel analytical framework introduced in Section 3, it is also required to obtain the coordinates of the cluster's reflection points for Rx $k$, $(x_{C,kn}, y_{C,kn}, z_{C,kn})$. In order to do that, we follow [21] by assuming that Tx and Rx are located at the foci of an ellipse, and that the reflection point of a single bounce is located at the arc of this ellipse as shown in Fig. 2. With this method, we can extract the $x$-, $y$-, and $z$-coordinates of the reflecting point of cluster $n$ for Rx $k$, which are required to parametrize our analytical framework, as follows:

- as the random generation of AoA and AoD according to 3GPP [9] does not guarantee that the arrival and departure clusters will intersect in 3D space, we randomly choose Tx-side or Rx-side;
- compute the coordinates $(x_{C,kn}, y_{C,kn})$ as:
  - choosing Tx-side, we have:

$$\begin{aligned} x_{C,kn} &= x_T + d_{T,kn}\cos\phi_{D,n}, \\ y_{C,kn} &= y_T + d_{T,kn}\sin\phi_{D,n}, \end{aligned} \tag{1}$$

  - alternatively, choosing Rx-side we have:

$$\begin{aligned} x_{C,kn} &= x_{R,k} + d_{R,kn}\cos\phi_{A,kn}, \\ y_{C,kn} &= y_{R,k} + d_{R,kn}\sin\phi_{A,kn}, \end{aligned} \tag{2}$$

    where $d_{T,kn}$ and $d_{R,kn}$ are the distances between the reflecting point of cluster $n$ and Tx or Rx $k$, respectively, $x_T$, $y_T$, $x_{R,k}$, and $y_{R,k}$ are the coordinates of Tx and Rx $k$, $\phi_{D,kn}$ and $\phi_{A,kn}$ are the angles of departure and arrival of cluster $n$, $d_{kn} = d_{T,kn} + d_{R,kn}$ is the total travel distance of cluster $n$ estimated as $c\tau_{kn}$, where $\tau_{kn}$ is the delay and $c$ is the speed of light;
- since $(x_{C,kn}, y_{C,kn})$ are the coordinates in case of a single reflection, the distance may be chosen uniformly between this point and Tx/Rx location. The new distance from the last or first reflection, depending on which side (Tx or Rx) is considered, is denoted as $d_{u,kn}$;
- compute the coordinate $z_{C,kn}$ as:
  - in case of Tx-side, we have:

$$z_{C,kn} = h_T + d_{u,kn}\tan\theta_{D,kn}, \tag{3}$$

  - alternatively, in case of Rx-side we have:

$$z_{C,kn} = h_R - d_{u,kn}\tan\theta_{A,kn}, \tag{4}$$

    where $h_T$ and $h_R$ are the heights of Tx and Rx $k$, while $\theta_{D,kn}$ and $\theta_{A,kn}$ are the zenith angles of departure and arrival of cluster $n$, respectively.

## 3 Mathematical Framework

In this section, we develop a novel mathematical framework for characterizing the conditional link state probabilities. The considerations below are a comprehensive extension of our previous model in [27] that allow to consider different heights of points $O$ and $M$. In what follows, we first introduce the preliminary details and then proceed by deriving the unconditional and conditional link state probabilities with respect to the channel with known blockage state. These metrics form the foundation of the proposed spatially-consistent human body blockage state generation procedure for the mmWave channel model introduced in Section 4.

### 3.1 Important Preliminaries

Consider Fig. 3 illustrating the top-view of the scenario where two clusters are arriving/departing at/from two location points $O$ and $M$. These clusters are departing/arriving from/at a common point $P$. In the first case, Tx acts as a common entity located at point $P$, which is associated with two Rx located at points $O$ and $M$. In the second case, Rx is considered as a common entity located at point $P$, which receives two clusters from the reflector points located at $O$ and $M$. Note that $O$ and $M$ may also be the coordinates of two Tx communicating with a single Rx located at $P$ or, in general, the coordinates of any other nodes.

To establish the conditional link state probability for the general case, we operate with the following terminology: point $P$ with height $h_C$, point $O$ with height $h_1$, and link state (i.e., blocked or non-blocked) derived with unconditional link state probability, as well as point $M$ with height $h_2$ and link state derived with conditional link state probability. To capture the spatial correlation with respect to the blockage between two links, we are interested in the *conditional link state probabilities* $p_{ij}$.

**Definition 2.** *$p_{ij}$, $i, j = 0, 1$, are the conditional link state probabilities (conditional probabilities) that the state of a node at point $M$ is non-blocked ($j = 0$) or blocked ($j = 1$) given that the state of this node at point $O$ is non-blocked ($i = 0$) or blocked ($i = 1$), $p_{ij} = \mathbb{P}[M \text{ is in state } j | O \text{ is in state } i]$.*

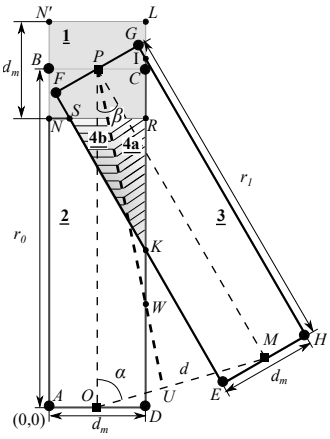


Fig. 3. A top-view illustration of correlation between links.

These probabilities can be organized into the following matrix

$$\mathbf{P} = \begin{pmatrix} p_{00} & p_{01} \\ p_{10} & p_{11} \end{pmatrix}, \tag{5}$$

where states $0$ and $1$ reflect the non-blocked and blocked states, respectively. The matrix $\mathbf{P}$ is a function of the following variables:

- $r_0$ is the two-dimensional distance from $O$ to $P$;
- $d$ is the two-dimensional distance from $O$ to $M$;
- $\alpha$ is the angle $\angle POM$, see Fig. 3;
- $\lambda_B$ is the density of blockers;
- $h_C$, $h_1$, and $h_2$ are the heights of points $P$, $O$, and $M$.

Since the following holds [27]

$$p_{00} = 1 - p_{01},\, p_{10} = 1 - p_{11}, \tag{6}$$

in order to parametrize (5), it is required to obtain $p_{00}$ and $p_{10}$.

The geometry of our proposed methodology is demonstrated in Fig. 3, where two rectangles $ABCD$ and $EFGH$ represent the areas affecting the link $PO$ and $PM$ blockage. The width and length of these rectangles are equal to $d_m$ (the diameter of a blocker) and $r_0/r_1$ (the 2D distances $PO$ and $PM$), respectively. One may notice that the intersection area of two rectangles is the area affecting both links $PO$ and $PM$. For further analysis, the rectangles are divided into multiple zones having a different impact on the conditional probabilities as illustrated in Fig. 3

- **Zone** $1$, $NN'LR$, is the square area around the point $P$. Further derivations are simplified significantly by omitting this zone, while the general impact of this zone is considered to be negligible due to its smaller size.
- **Zone** $2$, $ANSKD$, is related to the path $PO$ and influences the conditional probability in case $PO$ path is blocked.
- **Zone** $3$, $IKEH$, affects the $PM$ path and does not depend on the state at point $O$.
- **Zone** $4$, $SRK$, is the common zone affecting both links simultaneously and impacting the dependency between the states at points $O$ and $M$.

Zone $4$ can be split further into two smaller zones, $4a$ and $4b$, which represent the area on the right and left sides, respectively, along with $PU$, which is the line of intersection of two planes as shown in Fig. 3. These zones are used to determine whether a blocker that is blocking/not blocking the lower plane, is also blocking/not blocking the upper one. Depending on the heights of the involved entities, these zones will correspond to different planes, which is reflected in subsequent derivations.

### 3.2 Unconditional Link State Probability

We begin with characterizing the unconditional link state probability by deriving it for point $O$ located at the distance of $r$ from point $P$.

**Definition 3.** *Unconditional link state probability, $\mathbb{P}_{\mathrm{nB}}$, is the probability that a given link is not occluded by a human body, without taking into account the condition of blocked/non-blocked state of the neighboring links.*

We follow [26] to briefly sketch the derivation in question. Consider a rectangular blockage zone in Fig. 3 with the width corresponding to the diameter of a blocker, $d_m$, and the length of $r$. Recalling that the process associated with the centers of blockers is homogeneous Poisson, the coordinates of each particular blocker are distributed uniformly over $(0, d_m)$ and $(0, r)$, which corresponds to $OY$ and $OX$ coordinates of the rectangle sides, respectively. Hence, the blockage probability is the probability that at least one blocker resides in the area of interest and occludes the link at hand.

For different values of $h_C$, $h_1$, and the distribution of the blocker height $H$, a blocker falling into the considered area occludes the link when $P\{H > h_m(x)\}$, where $x \in (0, r)$ and $h_m(x)$ is

$$h_m(x) = \frac{h_C - h_1}{r} x + h_1, \;\; x \in (0, r). \tag{7}$$

The non-blocked state probability can now be obtained in terms of the void probability for the PPP as

$$\mathbb{P}_{\mathrm{nB}} = \exp\left[\lambda_B d_m \int_0^r \left(F_H(h_m(x)) - 1\right) dx\right], \tag{8}$$

where $F_H(x)$ is the CDF of the blocker height.

The result in (8) is then employed to derive the conditional link state probabilities. In subsections 3.3, 3.4, and 3.5 we establish the conditional probabilities for the general case, where all of the entities are located at different heights in relation to each other.

$$\mathbb{P}_{nbz} = f_P(0, \lambda_B\ S_z) + \sum_{i=1}^{\infty} f_P(i, \lambda_B\ S_z) \frac{\left[\sum_{j=1}^{N} \int_{x_j}^{x_{j+1}} \int_{y_j}^{y_{j+1}} F_H\left(\frac{gy-fx-e}{h}\right)\ dy\ dx\right]^i}{S_z^i}. \quad (9)$$

$$\mathbb{P}^*_{nbz} = \exp\left[\lambda_B \sum_{j=1}^{N} \int_{x_j}^{x_{j+1}} \int_{y_j}^{y_{j+1}} \left[F_H\left(\frac{gy-fx-e}{h}\right) - F_H\left(\frac{by-ax-d}{c}\right) - 1\right] dydx\right]. \quad (10)$$

### 3.3 Probabilities $p_{10}$ and $p_{11}$ for $h_C > h_2$

By observing Fig. 3, one may notice that the planes $(ABC)$ and $(EFG)$ intersect at $PU$. The zones $4a$ and $4b$ are located on the right and left sides of $PU$, respectively. By using the 3D view of the scenario in Fig. 6, where $h_C > h_2$, we may conclude that the zone $4a$ of Area 1, which corresponds to plane $(ABC)$ from Fig. 3, is *always higher* than the corresponding zone of Area 2 depicted as plane $(EFG)$. Alternatively, in Fig. 7, when $h_C < h_2$, the zone $4a$ of Area 1 is *always lower* than the zone $4a$ of Area 2. Therefore, the conditional probabilities are independent of the height $h_1$, and it is sufficient to consider two cases, $h_C > h_2$ and $h_C < h_2$.

Let $\widetilde{L}_z$ and $L_z$ be the events of having no blockers in zone $z$ that occlude the link paths at $O$ and $M$, respectively. The events complementary to $\widetilde{L}_z$ and $L_z$ are denoted by $\widetilde{N}_z$ and $N_z$. Note that $\widetilde{L}_z$ and $L_z$ occur when there are no blockers in zone $z$ or all the blockers are not high enough to occlude the link. When $h_C > h_2$, $p_{10}$ can be written as

$$p_{10} = \frac{\mathbb{P}\left[M \text{ is non-Blocked} \cap O \text{ is Blocked}\right]}{\mathbb{P}\left[O \text{ is Blocked}\right]}. \quad (11)$$

**Lemma 1.** *The probability $p_{10}$ for $h_C > h_2$ given in (11) is simplified to the following form*

$$p_{10} = \frac{\mathbb{P}_{nb3}\left(\widetilde{\mathbb{P}}_{b2}\widetilde{\mathbb{P}}_{nb4b}\mathbb{P}_{nb4a} + \mathbb{P}^*_{nb4b}\mathbb{P}_{nb4a}\right)}{1 - \widetilde{\mathbb{P}}_{nb2}\widetilde{\mathbb{P}}_{nb4a}\widetilde{\mathbb{P}}_{nb4b}}, \quad (12)$$

*where $\mathbb{P}_{nbz}$ and $\mathbb{P}_{bz}$ are the probabilities of the events $L_z$ and $N_z$, $\mathbb{P}^*_{nb4b}$ is the probability of $\widetilde{N}_{4b} \cap L_{4b}$, and $\widetilde{\mathbb{P}}_{nbz}$ is the probability of having no blockers affecting the link in the corresponding zone for point $O$.*

*Proof:* See proof in Appendix A, available in the online supplemental material. □

The probabilities $\mathbb{P}_{nbz}$ are derived similarly to the unconditional link state probability in subsection 3.2. They are given by (9), where the auxiliary parameters are provided in Appendix B, available in the online supplemental material, $f_P(i, \lambda_B S_z)$ is the probability of having $i$ blockers in the zone $z$ with the density of blockers $\lambda_B$, $S_z$ is the area of zone $z$, and $F_H([gy - fx - e]/h)$ is the probability that a blocker with the coordinates $x,\ y$ is lower than the link $PM$. Note that here each zone is actually a polygon formed by the intersection of the projections of planes. Since, in fact, (9) integrates over the area of the corresponding zone, it is easier to represent the entire zone as a set of trapezoids and/or triangles with their lower and upper bounds represented as variables $x_j, x_{j+1}$ and $y_j, y_{j+1}$. The integration limits are provided in our technical report [35].

Using the Maclaurin series expansion of an exponential function, (9) can be simplified as

$$\mathbb{P}_{nbz} = e^{\lambda_B(I - S_z)}. \quad (13)$$

Finally, the probability $\mathbb{P}_{nbz}$ is written as

$$\mathbb{P}_{nbz} = \prod_{j=1}^{N} e^{\lambda_B \int_{x_j}^{x_{j+1}} \int_{y_j}^{y_{j+1}} \left[F_H\left(\frac{gy-fx-e}{h}\right)-1\right] dydx}. \quad (14)$$

Consider now $\widetilde{\mathbb{P}}_{nbz}$, which corresponds to the case where all of the blockers are lower than the plane $(ABC)$. These probabilities are obtained similarly to $\mathbb{P}_{nbz}$ and read as

$$\widetilde{\mathbb{P}}_{nbz} = \prod_{j=1}^{N} e^{\lambda_B \int_{x_j}^{x_{j+1}} \int_{y_j}^{y_{j+1}} \left[F_H\left(\frac{by-ax-d}{c}\right)-1\right] dydx}. \quad (15)$$

To simplify (12), observe that the following holds

$$\begin{aligned} \widetilde{\mathbb{P}}_{nb2,4} &= \widetilde{\mathbb{P}}_{nb2}\widetilde{\mathbb{P}}_{nb4a}\widetilde{\mathbb{P}}_{nb4b}, \\ \widetilde{\mathbb{P}}_{b2} &= 1 - \frac{\widetilde{\mathbb{P}}_{nb2,4}}{\widetilde{\mathbb{P}}_{nb4}}, \\ \widetilde{\mathbb{P}}_{nb4} &= \widetilde{\mathbb{P}}_{nb4a}\widetilde{\mathbb{P}}_{nb4b}, \end{aligned} \quad (16)$$

where $\widetilde{\mathbb{P}}_{nb2,4}$ is the probability of having no blockers in the rectangle $ADRN$ for the link $PO$. It is calculated by utilizing the generic form (9), which leads to

$$\widetilde{\mathbb{P}}_{nb2,4} = p_0 + \sum_{i=1}^{\infty} p_i \left[\int_0^{x_R} \int_0^{y_R} \frac{F_H\left[\frac{by-ax-d}{c}\right] dydx}{||AD||||DR||}\right]^i, \quad (17)$$

where the integration starts at $0$, since the point $A$ is located in the center of coordinates.

Finally, using the Maclaurin series expansion of the exponential function, the probabilities $\mathbb{P}^*_{nbz}$ are given by (10), while the integration limits are provided in our technical report [35]. The complementary probability $p_{11}$ is $1 - p_{10}$.

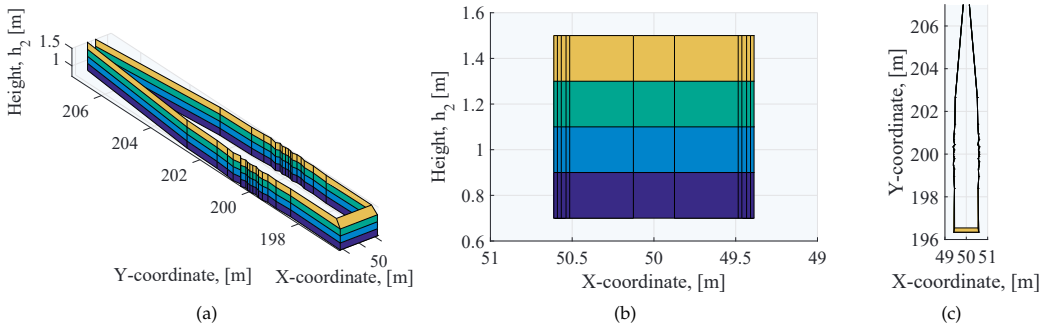


Fig. 4. Illustration of spatially-consistent zone for $h_C = 4$ m, $h_1 = 1.5$ m, and $h_2 \in (0.5 \text{ m} - 1.5 \text{ m})$.

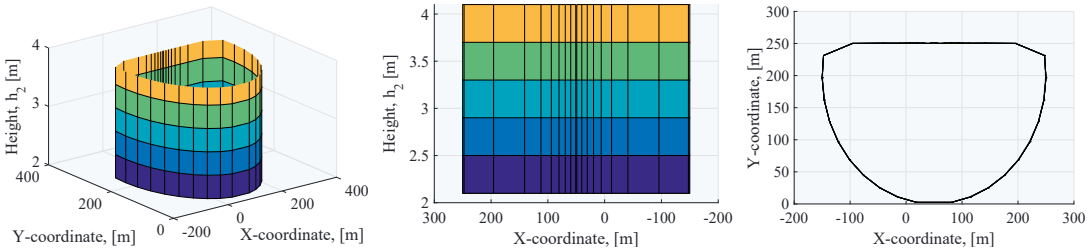


Fig. 5. Illustration of spatially-consistent zone for $h_C = 1.5$ m, $h_1 = 4$ m, and $h_2 \in (2.1 \text{ m} - 4.1 \text{ m})$.

### 3.4 Probabilities $p_{00}$ and $p_{01}$ for $h_C > h_2$

First, the conditional probability $p_{00}$ can be written as

$$\mathbb{P}\left[M \text{ is non-blocked} | O \text{ is non-blocked}\right] = \frac{\mathbb{P}\left[M \text{ is non-blocked} \cap O \text{ is non-blocked}\right]}{\mathbb{P}\left[O \text{ is non-blocked}\right]}. \quad (18)$$

Note that the event $(M \text{ is non-blocked})$ corresponds to the event $L_3 \cap L_{4a} \cap L_{4b}$, while the event $(O \text{ is non-blocked})$ corresponds to the event $\widetilde{L}_2 \cap \widetilde{L}_{4a} \cap \widetilde{L}_{4b}$. Observe that zone $4a$ exists in both planes, while $4a$ of one plane is always higher than that of another plane. If a blocker in zone $4a$ is lower for the plane $(FGH)$, it is lower for the upper plane as well; therefore, the following holds: $\widetilde{L}_{4a} \cap L_{4a} = L_{4a}$. The same applies to $\widetilde{L}_{4b} \cap L_{4b} = \widetilde{L}_{4b}$. Hence, (18) can be written as

$$p_{00} = \frac{\mathbb{P}\left[L_3 \cap L_{4a} \cap L_{4b} \cap \widetilde{L}_2 \cap \widetilde{L}_{4a} \cap \widetilde{L}_{4b}\right]}{\mathbb{P}\left[\widetilde{L}_2 \cap \widetilde{L}_{4a} \cap \widetilde{L}_{4b}\right]} = \frac{\mathbb{P}\left[L_3 \cap L_{4a}\right]}{\mathbb{P}\left[\widetilde{L}_{4a}\right]}. \quad (19)$$

Finally, the conditional probability $p_{00}$ can be established as

$$p_{00} = \frac{\mathbb{P}_{nb3}\mathbb{P}_{nb4a}}{\widetilde{\mathbb{P}}_{nb4a}}, \quad (20)$$

where $\mathbb{P}_{nbz}$ is the probability of having no blockers in zone $z$, which is produced by (14), while $\widetilde{\mathbb{P}}_{nbz}$ is derived in (15). The complementary probability $p_{01}$ is $1 - p_{00}$.

### 3.5 Conditional Probabilities $p_{ij}$ for $h_C < h_2$

Consider now the case where a common entity height, $h_C$, is lower than the second entity height, $h_C < h_2$. The analysis in this case is similar to the case of $h_C > h_2$, which has been completed previously, but with one important exception. Here, zones $4a$ and $4b$ are located differently with respect to the plane having the non-blocked link path. Hence, we modify (19) for $p_{00}$ as

$$p_{00} = \frac{\mathbb{P}\left[L_3 \cap L_{4b}\right]}{\mathbb{P}\left[\widetilde{L}_{4b}\right]}, \quad (21)$$

and the conditional probability $p_{00}$ thus becomes

$$p_{00} = \frac{\mathbb{P}_{nb3}\mathbb{P}_{nb4b}}{\widetilde{\mathbb{P}}_{nb4b}}. \quad (22)$$

The complementary probability $p_{01}$ can now be established as $p_{01} = 1 - p_{00}$. Modifying (11) similarly, we arrive at

$$p_{10} = \frac{\mathbb{P}_{nb3}\left(\widetilde{\mathbb{P}}_{b2}\widetilde{\mathbb{P}}_{nb4a}\mathbb{P}_{nb4b} + \mathbb{P}^{*}_{nb4a}\mathbb{P}_{nb4b}\right)}{1 - \widetilde{\mathbb{P}}_{nb2}\widetilde{\mathbb{P}}_{nb4a}\widetilde{\mathbb{P}}_{nb4b}}. \quad (23)$$

The complementary probability $p_{11}$ can now be established as $p_{01} = 1 - p_{10}$.

### 3.6 Shape of Spatially-Consistent Zone

To assess the effect of correlation caused by human bodies, consider the shape of the *spatially-consistent (SpCon) zone*.

**Definition 4.** *A spatially consistent zone is the 2D zone around the target node where for every node located inside the SpCon zone the fraction of two conditional link state probabilities, $p_{10}/p_{00}$, is lower than the value $\Delta x$ ($\Delta x = 0.99$). Every point at the edge of the SpCon zone coincides with the distance where two conditional probabilities, $p_{00}$ and $p_{10}$, converge to unconditional probability, $\mathbb{P}_{\mathrm{nB}}$ [27]. Any node in the SpCon zone has a spatially consistent blockage state with the target node link state.*

The spatially-consistent zone for the case of $h_C = 4$ m and $h_1 = 1.5$ m as well as the distance between points $P$ and $O$ of 50 m, is exemplified in Fig. 4, where the height of point $M$, $h_2$, varies within the range $(0.5, 1.5)$ m. The SpCon zone for the case of $h_C = 1.5$ m and $h_1 = 4$ m is illustrated in Fig. 5.

As one may observe, the dimensions of the SpCon zone for the second case, $h_C < h_2$, are considerably larger that those for the first case where $h_C > h_2$. To explain this behavior, consider two 3D illustrations for the two considered cases, $h_C > h_2$ and $h_C < h_2$, as displayed in Fig. 6 and Fig. 7, respectively. Here, point $P$ represents the common entity with the height of $h_C$. Points $O$ and $M$ are the entities with known and unknown states, respectively. All the blockers are smaller than the plane $\Omega$, which is the maximum considered height of a blocker.

Analyzing Fig. 6, which reflects the case of $h_C > h_2$, we note that the area of the zone inducing the correlation between the states is rather small. Indeed, the zone $F_cG_cH_cI_c$ (2D plane in Fig. 6) is the common zone that affects both $O$ and $M$, while only zone $J_cK_cH_cI_c$ is responsible for the dependence between the states. Most of the common zone is located high enough, where the blockers do not affect the link in question. Hence, the dimension of the SpCon zone in its minor axis is very small, since an increase in the distance between points $O$ and $M$ decreases the intersection area.

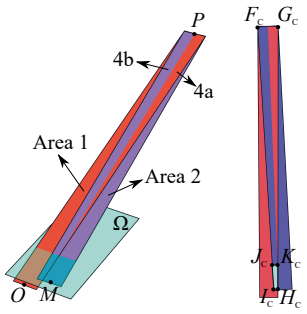


Fig. 6. Illustration of the case $h_C > h_2$.

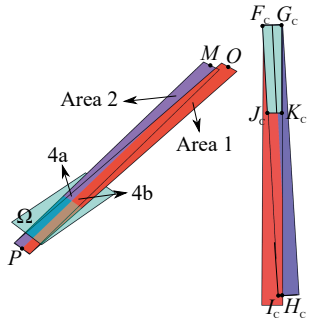


Fig. 7. Illustration of the case $h_C < h_2$.

In Fig. 7, the zone $F_cG_cH_cI_c$ (2D plane in Fig. 7) is the common zone that affects both $O$ and $M$. Here, only zone $F_cG_cJ_cK_c$ is responsible for the dependence between the states. Hence, an increase in the distance between the two entities maintains the correlation farther than in the first case.

## 4 Spatially-Consistent Blockage State Generation Procedure

After obtaining the unconditional and conditional link state probabilities, we proceed with specifying a spatially-consistent blockage state generation procedure for micro objects (human bodies). Our proposed procedure can be overlaid on top of the standard 3GPP channel model or on top of any 3GPP-like channel model.

The main goal of the proposed procedure is to assign the spatially consistent blocked/non-blocked state to every link in a given scenario. Algorithm 1 is responsible for generating blocked/non-blocked states among all the Tx-Rx links, whereas Algorithm 2 is responsible for generating blocked/non-blocked states among all the Reflector-Rx links. Both algorithms employ our analytical framework to derive the conditional link state probabilities given in Section 3. The computation complexity of the algorithms grows linearly with the number of Rx nodes i.e., the overall modeling complexity is $O(K)$, where $K$ is the number of Rx generated in the scenario. Note that the algorithms do not depend on the blocker density, since this density is a parameter of the analytical framework.

The proposed state generation procedure comprises three phases. At the first phase, we associate every Rx with the state (blocked/non-blocked) of the LoS path. Initially, we generate $K$ Rx with uniformly distributed $x$- and $y$-coordinates. Further, we introduce two sets, $N_{\mathrm{U1}}$ and $N_{\mathrm{U2}}$, containing the coordinates of Rx without and with generated blockage states. The set $N_{\mathrm{U,s}}$ contains blockage states of LoS links for all Rx. Further, we choose the first Rx from the set $N_{\mathrm{U1}}$ and find the unconditional state of that Rx by using the unconditional link state probability, $\mathbb{P}_{\mathrm{nB}}$, from (8). We

**Algorithm 1:** Blocked/non-blocked LoS state generation

**Result:** Blocked/non-blocked LoS states for all Rx

Generate uniformly distributed coordinates $(x_{R,1}, y_{R,1}), \ldots, (x_{R,K}, y_{R,K})$ of $K$ Rx
Define the sets $N_{\text{U1}} = \varnothing$ and $N_{\text{U2}} = \varnothing$ for the coordinates of Rx w/o and w/ blocked/non-blocked state, respectively
Define the set $N_{\text{U,s}} = \varnothing$ for blocked/non-blocked states of every Rx
Save the coordinates of every Rx to the set $N_{\text{U1}} = \{(x_{R,1}, y_{R,1}), \ldots, (x_{R,K}, y_{R,K})\}$
**while** $N_{U1} \neq \varnothing$ **do**
  Choose the coordinates of Rx $k$ from the set $N_{\text{U1}}$
  Find the unconditional state $q^R_{u,k} = \{0 \text{ or } 1\}$ of Rx $k$ based on the unconditional probability, $\mathbb{P}_{\text{nB}}$, from (8)
  Save the state of Rx $k$ to the set $N_{\text{U,s}} = N_{\text{U,s}} \cup q^R_{u,k}$
  Remove the coordinates of Rx $k$ from the set $N_{\text{U1}}$
  Add the coordinates of Rx $k$ to the set $N_{\text{U2}} = N_{\text{U2}} \cup (x_{R,k}, y_{R,k})$
  **while** $N_{U2} \neq \varnothing$ **do**
    Choose the coordinates of Rx $l$ from the set $N_{\text{U2}}$
    Calculate the SpCon zone (see Definition 4) for Rx $l$ using the conditional probabilities, $p_{10}$ from (12), $p_{00}$ from (20), and the unconditional probability, $\mathbb{P}_{\text{nB}}$ from (8)
    Remove the coordinates of Rx $l$ from $N_{\text{U2}}$
    Find any Rx from the set $N_{\text{U1}}$ in the SpCon zone of Rx $l$
    **if** *Rx $m$ from the set $N_{U1}$ is in the SpCon zone* **then**
      Find the conditional state $q^R_{c,m} = \{0 \text{ or } 1\}$ of Rx $m$ using (12) or (20)
      Add the coordinates of Rx $m$ to the set $N_{\text{U2}} = N_{\text{U2}} \cup (x_{R,m}, y_{R,m})$
      Save the state of Rx $m$ to the set $N_{\text{U,s}} = N_{\text{U,s}} \cup q^R_{c,m}$
      Remove the coordinates of Rx $m$ from the set $N_{\text{U1}}$

**Algorithm 2:** Blocked/non-blocked link state generation for every cluster of each Rx

**Result:** Blocked/non-blocked states for all clusters

Generate the cluster channel parameters $(\phi_{A,kn}, \phi_{D,kn}, \theta_{A,kn}, \theta_{D,kn}, \tau_{kn})$ for all $K$ Rx [9]
Define the set $N_{\text{C}} = \varnothing$ for the parameters of clusters for every Rx w/o state
Define the set $N_{\text{Ck,s}} = \varnothing$ for the blocked/non-blocked states of every cluster for each Rx
Add all the parameters of clusters for each Rx to the set $N_{\text{C}} = (\phi_{A,kn}, \phi_{D,kn}, \theta_{A,kn}, \theta_{D,kn}, \tau_{kn})$
**while** $N_{\text{C}} \neq \varnothing$ **do**
  Choose the parameters of clusters for Rx $k$ from the set $N_{\text{C}}$
  Find $x_{C,kn}$, $y_{C,kn}$, and $z_{C,kn}$ coordinates of clusters $n = 1, \ldots, N$, see subsection 2.3
  Remove the parameters of clusters for Rx $k$ from the set $N_{\text{C}}$
  Define the sets $N_{\text{Ck1}} = \varnothing$ and $N_{\text{Ck2}} = \varnothing$ for the coordinates of clusters for Rx $k$, w/o and w/ state respectively
  Add the coordinates of clusters for Rx $k$ to the set $N_{\text{Ck1}} = \{(x_{C,k1}, y_{C,k1}, z_{C,k1}), \ldots, (x_{C,kN}, y_{C,kN}, z_{C,kN})\}$
  **while** $N_{Ck1} \neq \varnothing$ **do**
    Choose the coordinates of cluster $l$ from the set $N_{\text{Ck1}}$
    Find the unconditional state $q^C_{u,l} = \{0 \text{ or } 1\}$ of cluster $l$ based on the unconditional probability, $\mathbb{P}_{\text{nB}}$, from (8)
    Save the state of cluster $l$ to the set $N_{\text{Ck,s}} = N_{\text{Ck,s}} \cup q^C_{u,l}$
    Add the coordinates of cluster $l$ to the set $N_{\text{Ck2}} = N_{\text{Ck2}} \cup (x_{C,kl}, y_{C,kl}, z_{C,kl})$
    Remove the coordinates of cluster $l$ from the set $N_{\text{Ck1}}$
    **while** $N_{Ck2} \neq \varnothing$ **do**
      Choose the coordinates of cluster $e$ from the set $N_{\text{Ck2}}$
      Find the conditional probabilities $p_{10}$ and $p_{00}$ for the link state of cluster $m$ from the set $N_{\text{Ck1}}$
      Remove the coordinates of cluster $e$ from the set $N_{\text{Ck2}}$
      **if** $p_{10}/p_{00} < \Delta x$ **then**
        Find the conditional state $q^C_{c,m} = \{0 \text{ or } 1\}$ of the cluster $m$ based on the conditional probabilities $p_{10}$ or $p_{00}$
        Save the state of cluster $m$ to the set $N_{\text{Ck,s}} = N_{\text{Ck,s}} \cup q^C_{c,m}$
        Add the coordinates of cluster $m$ to the set $N_{\text{Ck2}}$
        Remove the coordinates of cluster $m$ from the set $N_{\text{Ck1}}$

continue by calculating the SpCon zone for the first selected Rx by following the Definition 4. All of the Rx that fall into the SpCon zone have their link states correlated with the link state of a chosen Rx. In case where no Rx are in the SpCon zone, the next Rx from the set $N_{\text{U1}}$ is selected and the procedure repeats. The generation procedure continues up until all the Rx are assigned with blocked/non-blocked LoS states.

At the second phase, we generate the cluster channel parameters (AoA, AoD, ZoA, ZoD, and delay) for every Rx by following the 3GPP channel model generation procedure [21]. Finally, at the last phase, the state of each cluster for every Rx is generated. The set $N_{\text{C}}$ contains the aforementioned cluster channel parameters of all clusters for all the Rx. The sets $N_{\text{Ck1}}$ and $N_{\text{Ck2}}$ contain cluster coordinates without and with blocked/non-blocked states. The set $N_{\text{Ck,s}}$ contains the states of every cluster for each Rx in the scenario. We choose the first cluster of Rx $k = (1, \ldots, K)$ and find the state by using the unconditional probability, $\mathbb{P}_{\text{nB}}$, (8). Due to different heights of the arrived clusters, there is no common 2D SpCon zone for a given cluster reflection point. Therefore, the rest of the clusters without the link states are compared individually with the chosen cluster to identify any correlated links among the clusters. Any chosen cluster is considered

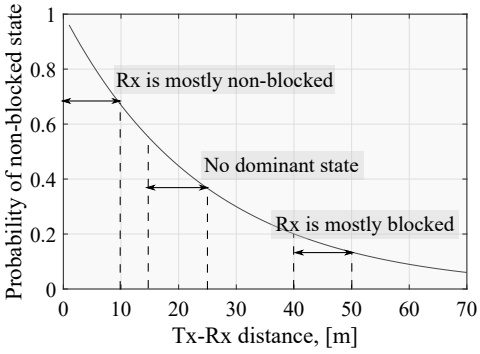


Fig. 8. Unconditional probability, $\mathbb{P}_{\mathrm{nB}}$, of non-blocked state, $\lambda_B$ = 1.

to have its link state correlated with the link state of cluster 1 if the fraction of two conditional link state probabilities, $p_{10}/p_{00}$, is lower than a certain value $\Delta x$ ($\Delta x = 0.99$). The conditional state probabilities $p_{10}$ and $p_{00}$ are calculated based on (12)/(23) and (20)/(21) by taking into account the heights of the considered clusters and the Rx. The generation procedure continues up until all the clusters of all the Rx are assigned with blocked/non-blocked states.

The pseudo code for the above phases is provided in Algorithms 1 and 2, where Algorithm 1 covers the first phase, while Algorithm 2 implements the second and third phases.

## 5 Key Numerical Results

In this section, we illustrate the performance of our generation procedure as well as study the effects of correlation caused by micro objects (human bodies) in the mmWave channel, which we compare with the case of no correlation among the links. We consider a crowded environment, where the density of blockers in the modeled area is $\lambda_B = 1$ blockers per square meter. The height of Tx is 4 m and the height of each Rx is 1.5 m. The Tx is located at the origin $(0, 0)$, while $K$ Rx are distributed uniformly within the area of interest. The received power of every Rx is established by using the 3GPP urban micro (UMi) street canyon path loss model and the cluster based channel model [9]. In case the link is blocked, we assume 20 dB loss [36]. The link blockage state is derived by employing our spatially-consistent human body blockage state generation algorithm as well as independent generation of the link blockage states. The remaining parameters are collected in Table 2.

Let the coordinates of $K$ Rx be uniformly distributed in three different areas of 10 by 10 square meters. The left bottom edges of these areas are located at $(x_{L,B}, y_{L,B})$ coordinates of $(1, 1)$, $(15, 15)$, and $(40, 40)$ referring to the different 2D separation distances between the Tx and the closest Rx. These coordinates where chosen to study the impact of the most probable link state in three different cases: (i) Rx are mostly in non-blocked state (probability of non-blocked state is about 0.8 in Fig. 8); (ii) there is no dominant state (probability of non-blocked state is about 0.5 in Fig. 8), and (iii) Rx are mostly in blocked state (probability of non-blocked state is about 0.2 in Fig. 8). Below, we formulate our key findings in terms of several important statements.

We first compare the output of our algorithms with the data from our simulator [30], where blockers were captured explicitly. We model them as cylinders with the density of $\lambda_B = 1$ blockers per square meter for the scenario described above. In Fig. 9(b), it may be observed that the simulation results match closely the ones derived with the proposed algorithm. A slight mismatch between the data sets is explained by the assumption of the analytical model, where a blocker occludes a link if its height is lower than the LoS link at the point, where the blocker's center is located. In the simulator, the blocker might still occlude the path with its edge in some cases.

**Observation 1: Spatial consistency across the blockage states of the links does not impact the mean received power averaged over a large area of interest but affects the received power of the neighboring links.** Fig. 9 demonstrates the CDFs of the received power, $P_R$, for three different assumptions regarding the blockage state generation: (i) no blockers (all the Rx are in LoS); (ii) uncorrelated blockage states; (iii) correlated blockage states for three different positions of the left bottom edge of the Rx distribution area of 10 m×10 m: $(1, 1)$, $(15, 15)$, and $(40, 40)$. Here, the number of Rx, $K$, was set to 100. As one may observe in Fig. 9, the CDFs of the received power coincide for the scenarios with correlated and uncorrelated blockage states. The reason is that the received power averaged across all of the Rx distributed in the area larger than the SpCon zone of one Rx remains the same on average. However, if we consider the area that is much smaller than the SpCon zone of one Rx, e.g., 1 m×1 m, the difference in the CDFs of the received power for correlated and uncorrelated blockage states becomes noticeable as confirmed in

TABLE 2
Baseline system parameters

| Parameter | Value |
|---|---|
| Height of Tx, $h_T$ | 4 m |
| Height of Rx, $h_R$ | 1.5 m |
| Height of a blocker, $N(\mu_H, \sigma_H)$ | $N(1.7\text{ m}, 0.1\text{ m})$ |
| Diameter of a blocker, $d_m$ | 0.5 m |
| Coordinates of the left bottom edge of the area with distributed $K$ Rx, $(x_{L,B}, y_{L,B})$ | $(1, 1)$, $(15, 15)$, and $(40, 40)$ |
| Density of blockers, $\lambda_B$ | 1 bl/m$^2$ |
| Carrier frequency | 28 GHz |
| Transmit power | 35 dBm |
| Blockage penalty | 20 dB |
| Number of clusters, $N$ | 5 |

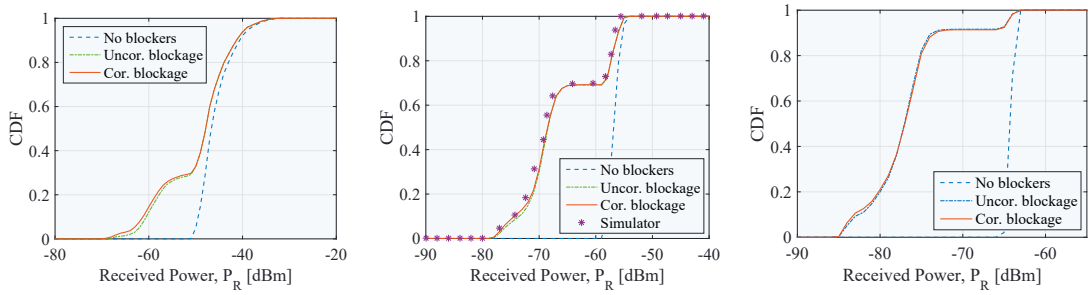


(a) $(x_{L,B}, y_{L,B}) = (1, 1)$ (b) $(x_{L,B}, y_{L,B}) = (15, 15)$ (c) $(x_{L,B}, y_{L,B}) = (40, 40)$

Fig. 9. Received power CDF: 100 Rx distributed in 10 m×10 m area.

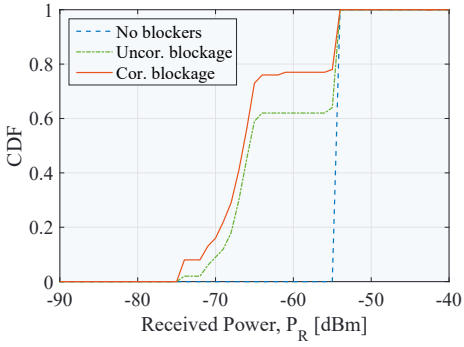


Fig. 10. Received power CDF: 100 Rx, 1 m×1 m area, $(x_{L,B}, y_{L,B}) = (15, 15)$.

Fig. 10. It is explained by the fact that most of the Rx are falling into the SpCon zone of one Rx, so that all the links are correlated with each other. Therefore, the correlation across the blockage states highly affects the performance of the neighboring links.

*However, note that these results do not imply that the knowledge of correlated states of receivers cannot improve the system performance. Even though there is no difference in the CDFs, one can schedule for service those Rx, which currently reside in non-blocked conditions by benefiting from knowing the correlated states of Rx.*

**Observation 2: Increased density of Rx leads to a higher number of correlated links.** The effect of Rx density on the proportion of correlated links is demonstrated in Fig. 11 and Fig. 12, where the total numbers of Rx per 10 m×10 m area are 20 and 100, respectively. The plots illustrate the difference in the received power calculated for the same set of Rx but with different blockage state generation procedure: (i) correlated blockage states and (ii) uncorrelated blockage states. The figures reflect only those Rx, which see a difference in the received power. The positions of the small squares in the plots represent the aforementioned Rx locations and the color of the squares demonstrates the absolute power difference. It is observed that for one particular realization of the field of Rx displayed in the plots the percentage of receivers with correlated link states increases from 45% among 20 Rx to 97% Rx among 100 Rx in 10 m×10 m area.

However, the number of Rx with different received power is significantly smaller referring to the 10% among 20 Rx and 16% among 100 Rx. The reason

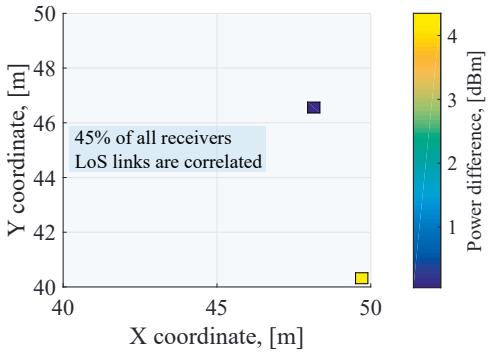


Fig. 11. Number of correlated receivers among 20 Rx in 10 m×10 m area, $(x_{L,B}, y_{L,B}) = (40, 40)$.

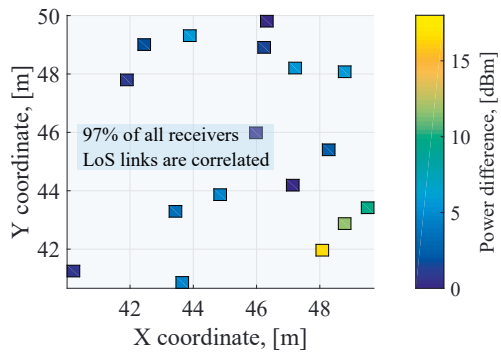


Fig. 12. Number of correlated receivers among 100 Rx in 10 m×10 m area, $(x_{L,B}, y_{L,B}) = (40, 40)$.

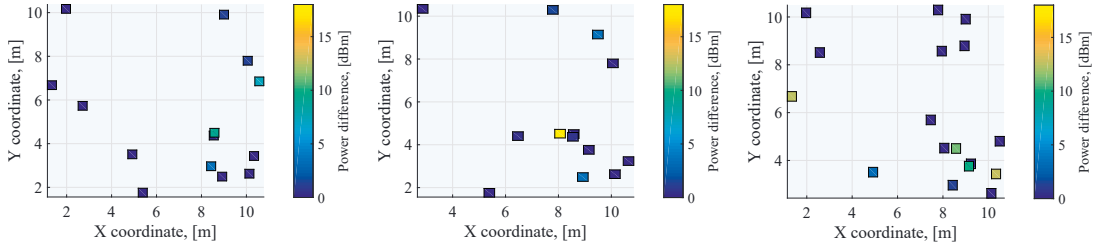


(a) Random state generator for first Rx (b) Forcing first Rx to be in non-blocked state (c) Forcing first Rx to be in blocked state

Fig. 13. Absolute received power difference between correlated and uncorrelated blockage state generation for 50 Rx, $(x_{L,B}, y_{L,B}) = (1, 1)$.

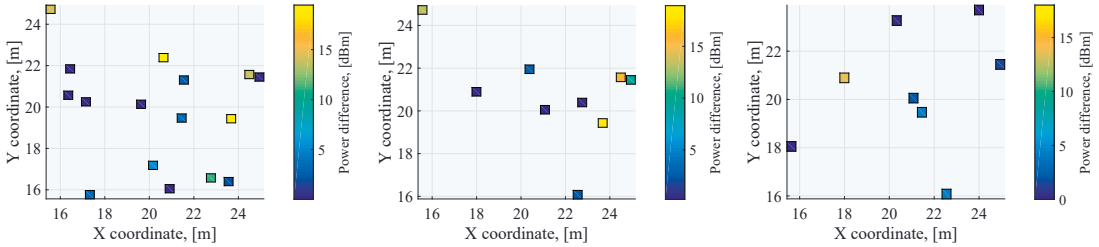


(a) Random state generator for first Rx (b) Forcing first Rx to be in non-blocked state (c) Forcing first Rx to be in blocked state

Fig. 14. Absolute received power difference between correlated and uncorrelated blockage state generation for 50 Rx, $(x_{L,B}, y_{L,B}) = (15, 15)$.

is that there is a number of Rx, which are assigned a blocked/non-blocked state based on the unconditional probability in the spatially consistent blockage state generation procedure. For high unconditional blockage probability, these states will most probably be blocked states. The receivers that are located in the SpCon zone of the Rx with unconditional blockage states having a high probability will follow the link state of the latter Rx. Therefore, the number of Rx with different received power is low, since most of the Rx will be assigned the most probable link state.

**Observation 3: The difference between received power calculated with the help of the correlated and uncorrelated state generation procedures in a single realization increases when the first chosen Rx is assigned a less probable state (e.g., the unconditional non-blockage probability is 0.8, but with the probability 0.2 the Rx could be assigned the blocked state, which is a less probable state).** It was noted in the previous plots that the number of Rx with different received power for two different blockage state generation cases (conditional and unconditional) is rather small, since the Rx is assigned the most probable link states. With Fig. 13 and Fig. 14, we study the effect of the link state that deviates from the most probable case. For the three subplots in Fig. 13, a set of 50 Rx was generated once in the 10 m×10 m area with the left bottom coordinates $(x_{L,B}, y_{L,B}) = (1, 1)$. The small squares refer to the positions of Rx with different received power for the correlated and uncorrelated blockage state generation cases. Also, the position of every Rx is the same for each subplot of Fig. 13. The first Rx chosen by the spatially consistent blockage state generation procedure is assigned a blockage state following three different strategies: (i) the first chosen Rx is assigned a blockage state based on the unconditional probability; (ii) the first chosen Rx is assigned a non-blocked state; (iii) the first chosen Rx is assigned a blocked state. The latter strategies were chosen to study the effects related to a single link state.

It was observed that the number of Rx with different received power for the two scenarios (unconditional and conditional blockage state generation cases) increases when the first chosen Rx is assigned a less probable state. For Fig. 13, this state is the blocked state, since the unconditional non-blockage probability is about 0.8. To further demonstrate the impact of the most probable state of the Rx, we generate 50 Rx in the area of 10 m×10 m area with $(x_{L,B}, y_{L,B}) = (15, 15)$; the results are depicted in Fig. 14. These coordinates were chosen, since there is no most probable state of the Rx (unconditional blockage probability is around 0.5). The results indicate no major difference between the number of Rx with different received power when assigning the first Rx with a blocked or non-blocked state.

## 6 Conclusions

In this paper, we proposed a new 3GPP-compatible spatially-consistent human body blockage state generation procedure for dense urban mmWave deployments. The contributed model is built on top of a globally accepted 3GPP methodology and extends it to the case of correlated signal behavior caused by a human crowd around the mmWave receivers. We also investigated in detail the effects of correlation created by human bodies to demonstrate that it manifests itself in a local fluctuation of the received signal strength as well as heavily depends on the density of the receivers. The main application area for the proposed state generation procedure is in system-level simulations of the emerging cellular mmWave technology. In this setting, our model can be used as an extension to the 3GPP model with correlated macro objects, thus inducing additional dependency in the received signal strength field caused by the human crowd. The computational complexity of our model does not depend on the blocker density, which makes it suitable for characterizing densely crowded environments.

## Acknowledgment

This work was supported by the Academy of Finland (projects PRISMA and WiFiUS). The work of S. Andreev was supported by a Research Fellow project RADIANT from the Academy of Finland.

## References

[1] ITU-R, "IMT vision framework and overall objectives of the future development of IMT for 2020 and beyond," Recommendation ITU-R M.2083-0, September 2015.

[2] J. G. Andrews, S. Buzzi, C. Wan, S. V. Hanly, A. Lozano, A. C. K. Soong, and J. C. Zhang, "What will 5G be?" *IEEE Journal on Selected Areas in Communications*, vol. 32, no. 6, pp. 1065–1082, June 2014.

[3] A. Ghosh, T. A. Thomas, M. C. Cudak, R. Ratasuk, P. Moorut, F. W. Vook, T. S. Rappaport, G. R. MacCartney, S. Sun, and S. Nie, "Millimeter-wave enhanced local area systems: A high-data-rate approach for future wireless networks," *IEEE Journal on Selected Areas in Communications*, vol. 32, no. 6, pp. 1152–1163, June 2014.

[4] J. G. Andrews, T. Bai, M. N. Kulkarni, A. Alkhateeb, A. K. Gupta, and R. W. Heath, "Modeling and analyzing millimeter wave cellular systems," *IEEE Transactions on Communications*, vol. 65, no. 1, pp. 403–430, January 2017.

[5] M. Gapeyenko, V. Petrov, D. Moltchanov, S. Andreev, N. Himayat, and Y. Koucheryavy, "Flexible and reliable UAV-assisted backhaul operation in 5G mmWave cellular networks," *IEEE Journal on Selected Areas in Communications*, vol. 36, no. 11, pp. 2486–2496, November 2018.

[6] M. Abouelseoud and G. Charlton, "The effect of human blockage on the performance of millimeter-wave access link for outdoor coverage," in *IEEE Vehicular Technology Conference (VTC Spring)*, June 2013, pp. 1–5.

[7] M. N. Kulkarni, A. O. Kaya, D. Calin, and J. G. Andrews, "Impact of humans on the design and performance of millimeter wave cellular networks in stadiums," in *IEEE Wireless Communications and Networking Conference (WCNC)*, March 2017, pp. 1–6.

[8] T. Wu, T. S. Rappaport, and C. M. Collins, "The human body and millimeter-wave wireless communication systems: Interactions and implications," in *IEEE International Conference on Communications (ICC)*, June 2015, pp. 2423–2429.

[9] 3GPP, "Study on channel model for frequencies from 0.5 to 100 GHz (Release 15)," 3GPP TR 38.901 V15.0.0, June 2018.

[10] METIS, "Initial channel models based on measurements," METIS deliverable D1.2, April 2014.

[11] T. A. Thomas, H. C. Nguyen, and G. R. MacCartney, "3D mmWave channel model proposal," in *IEEE Vehicular Technology Conference (VTC Fall)*, September 2014, pp. 1–6.

[12] M. Zhang, M. Mezzavilla, R. Ford, S. Rangan, S. Panwar, E. Mellios, D. Kong, A. Nix, and M. Zorzi, "Transport layer performance in 5G mmWave cellular," in *2016 IEEE Conference on Computer Communications Workshops (INFOCOM WKSHPS)*, April 2016, pp. 730–735.

[13] M. Gapeyenko, V. Petrov, D. Moltchanov, S. Andreev, Y. Koucheryavy, M. Valkama, M. R. Akdeniz, and N. Himayat, "An analytical representation of the 3GPP 3D channel model parameters for mmWave bands," in *2nd ACM Workshop on Millimeter-Wave Networks and Sensing Systems*, October 2018, pp. 1–6.

[14] F. Baccelli and X. Zhang, "A correlated shadowing model for urban wireless networks," in *IEEE Conference on Computer Communications (INFOCOM)*, August 2015, pp. 801–809.

[15] S. Sun, H. Yan, G. R. MacCartney, and T. S. Rappaport, "Millimeter wave small-scale spatial statistics in an urban microcell scenario," in *IEEE International Conference on Communications (ICC)*, May 2017, pp. 1–7.

[16] C. S. Choi, J. O. Woo, and J. G. Andrews, "On the coverage probability of a spatially correlated network," in *IEEE International Symposium on Information Theory (ISIT)*, June 2017, pp. 466–470.

[17] G. R. MacCartney, M. K. Samimi, and T. S. Rappaport, "Exploiting directionality for millimeter-wave wireless system improvement," in *IEEE International Conference on Communications (ICC)*, June 2015, pp. 2416–2422.

[18] M. N. Kulkarni, A. Ghosh, and J. G. Andrews, "A comparison of MIMO techniques in downlink millimeter wave cellular networks with hybrid beamforming," *IEEE Transactions on Communications*, vol. 64, no. 5, pp. 1952–1967, May 2016.

[19] A. K. Gupta, J. G. Andrews, and R. W. Heath, "Macrodiversity in cellular networks with random blockages," *IEEE Transactions on Wireless Communications*, vol. 17, no. 2, pp. 996–1010, February 2018.

[20] V. Va, J. Choi, and R. W. Heath, "The impact of beamwidth on temporal channel variation in vehicular channels and its implications," *IEEE Transactions on Vehicular Technology*, vol. 66, no. 6, pp. 5014–5029, June 2017.

[21] Nokia *et al.*, "5G channel model for bands up to 100 GHz," 5GCM white paper available at: http://www.5gworkshops.com, October 2016.

[22] A. Molisch, A. Karttunen, S. Hur, J. Park, and J. Zhang, "Spatially consistent pathloss modeling for millimeter-wave channels in urban environments," in *Proc. Eur. Conf. Antennas Propag.(EuCAP)*, pp. 1–5.

[23] A. Karttunen, A. F. Molisch, S. Hur, J. Park, and C. J. Zhang, "Spatially consistent street-by-street path loss model for 28-GHz channels in micro cell urban environments," *IEEE Transactions on Wireless Communications*, vol. 16, no. 11, pp. 7538–7550, November 2017.

[24] S. Ju and T. S. Rappaport, "Simulating motion - incorporating spatial consistency into the NYUSIM channel model," in *IEEE 88th Vehicular Technology Conference (VTC Fall)*, August 2018, pp. 1–6.

[25] T. Bai, R. Vaze, and R. W. Heath, "Analysis of blockage effects on urban cellular networks," *IEEE Transactions on Wireless Communications*, vol. 13, no. 9, pp. 5070–5083, September 2014.

[26] M. Gapeyenko, A. Samuylov, M. Gerasimenko, D. Moltchanov, S. Singh, E. Aryafar, S.-p. Yeh, N. Himayat, S. Andreev, and Y. Koucheryavy, "Analysis of human-body blockage in urban millimeter-wave cellular communications," in *2016 IEEE International Conference on Communications (ICC)*. IEEE, May 2016, pp. 1–7.

[27] A. Samuylov, M. Gapeyenko, D. Moltchanov, M. Gerasimenko, S. Singh, N. Himayat, S. Andreev, and Y. Koucheryavy, "Characterizing spatial correlation of blockage statistics in urban

mmWave systems," in *IEEE Global Communications Workshops (GLOBECOM Wkshps)*, December 2016, pp. 1–7.
[28] G. R. MacCartney, T. S. Rappaport, and A. Ghosh, "Base station diversity propagation measurements at 73 GHz millimeter-wave for 5G coordinated multipoint (CoMP) analysis," in *IEEE Global Communications Workshops (GLOBECOM Wkshps)*, December 2017, pp. 1–7.
[29] S. Aditya, A. F. Molisch, N. Rabeah, and H. M. Behairy, "Localization of multiple targets with identical radar signatures in multipath environments with correlated blocking," *IEEE Transactions on Wireless Communications*, vol. 17, no. 1, pp. 606–618, January 2018.
[30] "WINTERsim system-level simulator, 2015," *http://winter-group.net/downloads/*.
[31] M. Jacob, S. Priebe, T. Kurner, M. Peter, M. Wisotzki, R. Felbecker, and W. Keusgen, "Fundamental analyses of 60 GHz human blockage," in *Proc. of European Conference on Antennas and Propagation (EuCAP)*, April 2013, pp. 117–121.
[32] C. L. Ogden, C. D. Fryar, M. D. Carroll, and K. M. Flegal, "Mean body weight, height, and body mass index, United States 1960–2002," *Centers for Disease control and prevention*, no. 347, October 2004.
[33] 3GPP, "Study on 3D channel model for LTE (release 12)," *TR 36.873 V12.7.0*, January 2018.
[34] ——, "Winner II channel models," *IST-4-027756 WINNER II, D1.1.2 V1.2*, 2008.
[35] A. Samuylov *et al.*, "Characterizing spatial correlation of blockage statistics," Tampere University, Technical report available at: https://drive.google.com/drive/folders/1ZTaab10ChUuIt5UNdUTWLwYlvFdouTnu, 2016.
[36] K. Haneda *et al.*, "5G 3GPP-like channel models for outdoor urban microcellular and macrocellular environments," in *IEEE 83rd Vehicular Technology Conference (VTC Spring)*, May 2016, pp. 1–7.

**Margarita Gapeyenko** is a Ph.D. candidate at the Unit of Electrical Engineering at Tampere University, Finland. She earned her M.Sc. degree in Telecommunication Engineering from University of Vaasa, Finland, in 2014, and B.Sc. degree in Radio-Engineering, Electronics, and Telecommunications from Karaganda State Technical University, Kazakhstan, in 2012. Her research interests include mathematical analysis, performance evaluation, and optimization methods of future wireless networks, device-to-device communication, and 5G-grade heterogeneous networks.

**Andrey Samuylov** received the M.Sc. in Applied Mathematics and Cand.Sc. in Physics and Mathematics from the RUDN University, Russia, in 2012 and 2015, respectively. Since 2015 he is working at Tampere University as a researcher, focusing on mathematical performance analysis of various 5G wireless networks technologies. His research interests include P2P networks performance analysis, performance evaluation of wireless networks with enabled D2D communications, and mmWave band communications.

**Mikhail Gerasimenko** is a Researcher at Tampere University in the Unit of Electrical Engineering. Mikhail received Specialist degree from Saint-Petersburg University of Telecommunications in 2011. In 2013, he obtained Master of Science degree from TUT. In 2018 he also obtained Doctor of Science degree from Tampere University of Technology. Mikhail started his academic career in 2011 and since then he appeared as (co-)author of multiple scientific journal and conference publications, as well as several patents. He also acted as reviewer and participated in educational activities. His main subjects of interest are wireless communications, machine-type communications, and heterogeneous networks.

**Dmitri Moltchanov** is a Senior Research Scientist in the Unit of Electrical Engineering, Tampere University, Finland. He received his M.Sc. and Cand.Sc. degrees from Saint-Petersburg State University of Telecommunications, Russia, in 2000 and 2002, respectively, and Ph.D. degree from Tampere University of Technology in 2006. His research interests include performance evaluation and optimization issues of wired and wireless IP networks, Internet traffic dynamics, quality of user experience of real-time applications, and traffic localization P2P networks. Dmitri Moltchanov serves as TPC member in a number of international conferences. He authored more than 80 publications.

**Sarabjot Singh** ('SM 09, M' 15) is a Principal Engineer at Uhana Inc. CA. He received the B. Tech. from IIT, India, and the M.S.E and Ph.D. in EE from UT Austin. His past affiliations include Intel, Nokia Technologies, Bell Labs, and Qualcomm Inc, where he worked on protocol and algorithm design for next generation of cellular and WiFi networks. Dr. Singh is interested in the system and architecture design of wireless networks leveraging theoretical and applied tools. He is a co-author of more than 40 patent applications, and multiple conference and journal papers. He was the recipient of the President of India Gold Medal in 2010, the ICC Best Paper Award in 2013, and recognized for being a prolific inventor at Intel Corp.

**Mustafa Riza Akdeniz** (S'09) received the B.S. degree in electrical and electronics engineering from Bogazici University, Istanbul, Turkey, in 2010 and the Ph.D. degree in electrical and computer engineering at New York University Tandon School of Engineering, Brooklyn, NY in 2016. He is working as a research scientist for Intel Labs in Santa Clara, CA. His research interests include wireless communications, wireless channel modeling, and information theory.

**Ehsan Aryafar** is an Assistant Professor of Computer Science at Portland State University. Prior to that and from 2013 to 2017, he was a Research Scientist at Intel Labs in Santa Clara, CA. He received the B.S. degree in Electrical Engineering from Sharif University of Technology, Iran, in 2005, and the M.S. and Ph.D. degrees in Electrical and Computer Engineering from Rice University, Houston, Texas, in 2007 and 2011, respectively. From 2011 to 2013, he was a Post-Doctoral Research Associate in the Department of Electrical Engineering at Princeton University. His research interests are in the areas of wireless networks and networked systems, and span both algorithm design as well as system prototyping. He has more than 30 issued and pending patents in the areas of mobile and wireless systems.

**Sergey Andreev** is an assistant professor of communications engineering and Academy Research Fellow at Tampere University, Finland. Since 2018, he has also been a Visiting Senior Research Fellow with the Centre for Telecommunications Research, King's College London, UK. He received his Ph.D. (2012) from TUT as well as his Specialist (2006) and Cand.Sc. (2009) degrees from SUAI. He serves as editor for IEEE Wireless Communications Letters (2016-) and as series editor of the IoT Series (2018-) for IEEE Communications Magazine. He (co-)authored more than 200 published research works on intelligent IoT, mobile communications, and heterogeneous networking.

**Nageen Himayat** is a Principal Engineer with Intel Labs, where she leads a team conducting research on several aspects of next generation (5G/5G+) of mobile broadband systems. Her research contributions span areas such as multi-radio heterogeneous networks, mm-wave communication, energy-efficient designs, cross layer radio resource management, multi-antenna, and non-linear signal processing techniques. She has authored over 250 technical publications, contributing to several IEEE peer-reviewed publications, 3GPP/IEEE standards, as well as holds numerous patents. Prior to Intel, Dr. Himayat was with Lucent Technologies and General Instrument Corp, where she developed standards and systems for both wireless and wire-line broadband access networks. Dr. Himayat obtained her B.S.E.E degree from Rice University, and her Ph.D. degree from the University of Pennsylvania. She also holds an MBA degree from the Haas School of Business at University of California, Berkeley.

**Yevgeni Koucheryavy** is a Full Professor in the Unit of Electrical Engineering of Tampere University, Finland. He received his Ph.D. degree (2004) from Tampere University of Technology. He is the author of numerous publications in the field of advanced wired and wireless networking and communications. His current research interests include various aspects in heterogeneous wireless communication networks and systems, the Internet of Things and its standardization, as well as nanocommunications. He is Associate Technical Editor of IEEE Communications Magazine and Editor of IEEE Communications Surveys and Tutorials.

# PUBLICATION VI

**On the Degree of Multi-Connectivity in 5G Millimeter-Wave Cellular Urban Deployments**

M. Gapeyenko, V. Petrov, D. Moltchanov, M. R. Akdeniz, S. Andreev, N. Himayat and Y. Koucheryavy

*IEEE Transactions on Vehicular Technology* 68.2 (2019), 1973–1978

# On the Degree of Multi-Connectivity in 5G Millimeter-Wave Cellular Urban Deployments

Margarita Gapeyenko, Vitaly Petrov, Dmitri Moltchanov, Mustafa Riza Akdeniz,
Sergey Andreev, Nageen Himayat, and Yevgeni Koucheryavy

***Abstract*—Outage event caused by dynamic link blockage at millimeter-wave (mmWave) frequencies is a challenging problem for cell-edge users. To address it, 3GPP is currently working on *multi-connectivity* mechanisms that allow a user to remain connected to several mmWave access points simultaneously as well as switch between them in case its active connection drops. However, the actual number of such simultaneous links – named the *degree of multi-connectivity* – to reach the desired trade-off between the system design simplicity and the outage probability levels remains an open research question. In this work, we characterize the *outage probability* and *spectral efficiency* associated with different degrees of multi-connectivity in a typical 5G urban scenario, where the line-of-sight propagation path can be *blocked* by *buildings* as well as *humans*. These results demonstrate that the degrees of multi-connectivity of up to 4 offer higher relative gains. Our analytical framework can be further employed for the performance analysis of multi-connectivity-capable mmWave systems across their different deployment configurations.**

***Index Terms*—mmWave systems, multi-connectivity, macro diversity, dynamic human body blockage, outage probability.**

## I. Introduction

The millimeter-wave (mmWave) radio links are known to be susceptible to abrupt quality degradation due to the line-of-sight (LoS) blockage by various objects in the channel including the human crowd [1], [2]. To make mmWave systems suitable for the applications that demand high reliability, 3GPP has proposed the concept of *multi-connectivity* (MC) [3].

Currently, there is a number of multi-connectivity solutions, such as dual connectivity (DC) or coordinated multi-point (CoMP) transmission/reception [4], [5]. Originally proposed in LTE Release 12, DC provides a user equipment (UE) with the radio resources of two cells residing on the same band but having different types or on multiple bands with the same cell type (multi-RAT). The multi-RAT DC for 5G is a generalization of the earlier where the UE may leverage the resources of two cells, one of which provides E-UTRA access and another one offers NR access [3]. Further, DC can be extended to multi-connectivity where the resources of two or more cells are made available to a UE. One of the MC solutions named CoMP allows to receive/transmit a signal from/to multiple cells on the same frequency [6]. It should be noted that an exact architecture for each MC option may vary and there are alternative realizations proposed [7]–[9].



This work was supported by Intel Corporation and the Academy of Finland (Projects WiFiUS and PRISMA). The work of V. Petrov was supported by the HPY Research Foundation funded by Elisa.

M. Gapeyenko, V. Petrov, D. Moltchanov, S. Andreev, and Y. Koucheryavy are with Tampere University of Technology, Tampere, Finland (e-mail: {firstname.lastname, evgeni.kucheryavy}@tut.fi).

M. R. Akdeniz and N. Himayat are with Intel Corporation, Santa Clara, CA, USA (e-mail: {mustafa.akdeniz, nageen.himayat}@intel.com).

The advantages of MC techniques in mmWave and microwave bands have been demonstrated in [10]–[12]. Particularly, in [11], the authors proposed a scheduling framework to distribute mmWave and microwave resources while satisfying the quality-of-service (QoS) constraints. Further, in [13], caching was employed to mitigate handover failures and reduce energy consumption at the UE side. In [14], an analysis of signal-to-interference-plus-noise ratio with MC has been contributed.

However, to satisfy high-rate constraints of the emerging applications, reliance only on microwave resources may not be sufficient. Therefore, another wave of studies related to MC was dedicated to considering multiple mmWave APs. For example, in [4], the authors employed their simulation framework to demonstrate that MC increases per-user throughput in CoMP-based scenarios, while a comparison of various AP switching strategies for MC-aided mmWave networks was targeted by [15]. In [16], an active set management scheme was proposed to avoid service interruptions.

One of the key practical aspects that has not been addressed comprehensively so far is selecting the *degree of MC*, that is, the number of simultaneously supported links. While higher degrees of MC can potentially lead to improved performance indicators and more reliable service, this also increases complexity of the networking protocols and may yield significant signaling overheads [17]. Targeting the said system design aspect, this paper analytically characterizes the outage probability and spectral efficiency in a typical outdoor urban 3GPP scenario as a function of the degree of MC with both *static* (caused by buildings) and *dynamic* (caused by humans) LoS *blockage*. We particularly focus on cell-edge users that on average experience poor channel conditions even with their closest AP.

The main contributions of this work are:

- To study the outage and spectral efficiency metrics for multi-connectivity mmWave environments in the presence of LoS blockage caused by stationary and dynamic objects, a unified mathematical framework based on stochastic geometry and probability theory is proposed.
- To evaluate relative performance benefits of higher degrees of MC, a mathematical methodology is employed. We demonstrate that the use of $4$ simultaneous mmWave links allows to achieve up to $95\%$ gain in the outage probability and up to $74\%$ gain in the spectral efficiency, while improvements brought by higher degrees are marginal.

The remainder is organized as follows. Our system model is introduced in Section II. The outage probability and spectral efficiency for the cell-edge users in MC-aided mmWave networks are derived in Sections III and IV. Numerical results illustrating the effect of the degree of MC are offered in Section V. Conclusions are drawn in the last section.

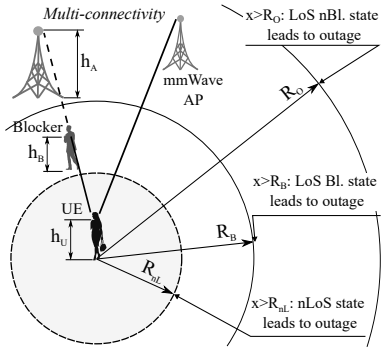


Fig. 1. Scenario considered for our analytical modeling.

## II. System Model

### A. Deployment Model

The system model is illustrated in Fig. 1. Assume that the locations of mmWave APs follow a Poisson point process (PPP) in $\Re^2$ with the density of $\lambda_A$. The AP height is fixed and set to $h_A$. We consider a single *cell-edge UE* dropped randomly in $\Re^2$, such that the distance between this UE and its nearest AP is sufficient to result in an outage; hence, the signal-to-noise ratio (SNR) is below its threshold value if the LoS link between the UE and the closest AP is blocked. The target user is assumed to remain stationary throughout its operation. The UE height, $h_U$, is constant as well.

The humans in the pedestrian area around the UE act as potential blockers. Their spatial density in $\Re^2$ is $\lambda_B$. These blockers are modeled as cylinders and have the radius, $r_B$ [2]. The height of the humans is assumed constant and set to $h_B$, $h_B > h_U$. To capture the mmWave LoS signal dynamics, we assume that humans move according to a random direction mobility (RDM, [18]) model.

### B. Propagation Model

The LoS path between a mmWave AP and a UE in dense urban environments can be blocked by: (i) large static objects, such as buildings (nLoS state), and (ii) smaller dynamic objects, such as humans (blocked state). There are four possible states for the link of interest: LoS non-blocked (nBl.) – no large or small objects are occluding the LoS link, LoS blocked (Bl.) – only small object is occluding the LoS link, nLoS non-blocked – large object is blocking the LoS, and nLoS blocked – LoS is blocked by a large object and all nLoS paths are blocked by small objects. Following the current 3GPP considerations [19], we distinguish only three of them by disregarding the worst case (nLoS blocked). The reason is that the probability that all the available independent nLoS paths are blocked simultaneously is negligible.

The LoS probability for the 2D distance $x$ between the mmWave AP and the UE, $p_L(x)$, is obtained by using the 3GPP urban micro (UMi) street canyon model [19] as

$$p_L(x) = \begin{cases} 1, & x \leq 18 \text{ m} \\ \left(18 + xe^{-\frac{x}{36}} - 18e^{-\frac{x}{36}}\right)/x, & x > 18 \text{ m}. \end{cases} \quad (1)$$

The associated UMi path loss measured in dB for three different states (LoS nBl., LoS Bl., nLoS) is given by

$$L = \begin{cases} 32.4 + 21.0\log_{10}(d) + 20\log_{10} f_c, \text{ LoS nBl.}, \\ 52.4 + 21.0\log_{10}(d) + 20\log_{10} f_c, \text{ LoS Bl.}, \\ 32.4 + 31.9\log_{10}(d) + 20\log_{10} f_c, \text{ nLoS}, \end{cases} \quad (2)$$

where $d$ is the three-dimensional (3D) distance between the mmWave AP and the UE, while $f_c$ is the carrier frequency in GHz. Targeting the mean SNR value at the cell-edge, we omit the consideration of small-scale fading for simplicity.

Following the recent measurements of human body blockage effects at mmWave frequencies [1], the LoS path occlusion by humans is assumed to (on average) result in 20 dB of additional degradation in the received signal strength. Note that human body loss is a parameter and various values may be applied [20] by modifying the LoS Bl. expression in (2).

As mmWave communications employ directionality, we model directional antenna systems at both the AP and the UE sides. They are characterized by the antenna gains $G_A$ and $G_U$ (equal for LoS and nLoS), respectively. For simplicity, we assume cone-shaped antenna radiation patterns at both the AP and the UE, thus disregarding possible negative effects of the side lobes [21]. We also assume perfect beam alignment between the AP and UE beams in both LoS and nLoS.

### C. Connectivity Model

The UE initially selects $N$ APs with the highest received signal strength, where $N$ is the degree of MC. We assume that the channels of a UE have been measured for sufficiently long to determine the *set* of the closest APs regardless of their instantaneous blockage situation; therefore, the static UE maintains this set of APs (e.g., a steady-state set) and does not connect to any AP beyond the $N$ initially selected ones. The state of each selected link changes from Bl. to nBl. by following the dynamic blockage process[1] as detailed in subsection II-A. At any instant of time, the UE always chooses the best link out of $N$ (e.g., by monitoring the received signal strength or SNR) for its data transmission, while connections over other backup links are maintained constantly via MC [9].

In our analysis, the UE first selects its closest AP in nBl. state as the one with the best SNR; in case all of the APs are blocked, it selects the closest AP in Bl. state having the SNR higher than the SNR threshold (no connection re-establishment is required when the UE selects another AP). In case all APs are blocked and/or their SNR values are below the threshold, the UE suffers from outage. Since 3GPP standardization of the MC operation is still in progress, the delay and overhead values introduced by switching between the mmWave APs are not known yet, even though they are envisioned to remain small in most scenarios [3]. In this paper, we assume idealistic switching process where the UE can instantaneously transition to its best AP out of $N$ selected initially.

## III. Multi-Connectivity Analysis

### A. Outage Distance

First, let SNR at the UE be

$$S = P_A + G_A + G_U - L(f_c, d) - N_0(B), \quad (3)$$

[1]This work assumes independent blockage state changes for simplicity.

where $P_A$ is the transmit power, $G_A$ and $G_U$ are the antenna gains, $L(f_c, d)$ is the path loss, while $N_0(B)$ is the total noise power at the receiver and $B$ is the bandwidth.

We define outage as a situation, when SNR at the receiver becomes lower than a certain threshold ($S < S_T$). Hence, the minimal 2D distances between the mmWave AP and the UE resulting in outage w.r.t. the link conditions (nLoS, blocked LoS, non-blocked LoS) are given by

$$R_O = \sqrt{10^{\frac{P_A+G_A+G_U-N_0-S_T-32.4-20\log_{10} f_c}{21}} - [h_A - h_U]^2},$$
$$R_B = \sqrt{10^{\frac{P_A+G_A+G_U-N_0-S_T-52.4-20\log_{10} f_c}{21}} - [h_A - h_U]^2},$$
$$R_{nL} = \sqrt{10^{\frac{P_A+G_A+G_U-N_0-S_T-32.4-20\log_{10} f_c}{31.9}} - [h_A - h_U]^2}, \quad (4)$$

where $R_O$ is the distance at which the link enters outage in non-blocked LoS state, $R_B$ is the distance at which the link enters outage in blocked LoS state, $R_{nL}$ is the distance at which the link enters outage in nLoS state, while $S_T$ is the SNR threshold in dB. Analysis of (4) readily yields that $R_O$ is the highest, while the relation between $R_{nL}$ and $R_B$ depends on the input parameters. For the sake of exposition, we further assume that $R_{nl} < R_B$ as the effect of nLoS is on average more severe than the effect of human body blockage. However, our proposed approach is generally applicable for $R_{nl} > R_B$.

### *B. Outage Probability*

Recall that for the cell-edge users we assume no APs closer than $R_{nL}$ to the target UE. Let $A$ and $B$ denote the events that there are no APs in non-outage conditions in the rings $(R_{nL}, R_B)$ and $(R_B, R_O)$. Denoting the outage probability for the degree of MC $N$ by $q_{O,N}$ and using the independence property of PPP, we have $q_{O,N} = Pr(A)Pr(B)$. Consider now event $A$ and observe that it may occur when the following two mutually exclusive events happen: (i) event $A_1$ of having no APs in the ring $(R_{nL}, R_B)$ and (ii) event $A_2^1$ of having at least one AP in the ring $(R_{nL}, R_B)$ jointly with the event $A_2^2$ of having all these APs in nLoS conditions. Let us denote the probabilities of these events by $Pr(A_1)$ and $Pr(A_2^1, A_2^2)$.

Further, event $B$ occurs when the following mutually exclusive events happen: (i) event $B_1$ of having no APs in the ring $(R_B, R_O)$, (ii) event $B_2^1$ of having at least one AP in the ring $(R_B, R_O)$ jointly with event $B_2^2$ of having all these APs in nLoS conditions, and (iii) event $B_3^1$ of having the nearest $\min(N, m)$ APs in LoS blocked state jointly with the event $B_3^2$ of having exactly $m$ APs in LoS conditions in the ring $(R_B, R_O)$, and event $B_3^3$ of having at least one AP in that ring. We denote these probabilities by $Pr(B_1)$, $Pr(B_2^1, B_2^2)$, and $Pr(B_3^1, B_3^2, B_3^3)$. The outage probability, $q_{O,N}$, is then

$$q_{O,N} = \Big(Pr(A_1) + \big(1 - Pr(A_1)\big)Pr(A_2^2|A_2^1)\Big)\Big(Pr(B_1) + \big(1 - Pr(B_1)\big)\big(Pr(B_2^2|B_2^1) + Pr(B_3^1, B_3^2|B_3^3)\big)\Big). \quad (5)$$

Consider events $A_1$ and $B_1$. Recall that the mmWave APs follow a PPP with the density of $\lambda_A$. Hence, the probability of having no APs in the ring $(R_{nL}, R_B)$ is offered by

$$Pr(A_1) = p_0^{R_{nL,B}} = e^{-\lambda_A \pi [R_B^2 - R_{nL}^2]}, \quad (6)$$

and, similarly, $Pr(B_1) = p_0^{R_{B,O}} = e^{-\lambda_A \pi [R_O^2 - R_B^2]}$.

To determine the probability that all of the APs in the ring $(R_{nL}, R_B)$ are in nLoS, given that there is at least one AP in this ring, $Pr(A_2^2|A_2^1)$, we define a new process of APs that includes only those APs, which are currently in LoS. We obtain this new process as a probabilistic thinning of the original one with the probability of $p_L(x)$, thus arriving at a non-homogeneous Poisson process of APs with the density of $\lambda_A p_L(x)$, $x > R_{nL}$, which decreases along the radial lines.

The density of APs residing in LoS in $(R_{nL}, R_B)$ is

$$\Lambda_L^{R_{nL,B}} = \frac{1}{R_B^2 - R_{nL}^2} \int_{R_{nL}}^{R_B} 2x\lambda_A p_L(x) \mathrm{d}x, \quad (7)$$

which implies that the sought probability is given by

$$Pr(A_2^2|A_2^1) = e^{-\Lambda_L^{R_{nL,B}} \pi [R_B^2 - R_{nL}^2]}. \quad (8)$$

Similarly to (8), we can obtain

$$Pr(B_2^2|B_2^1) = e^{-\Lambda_L^{R_{B,O}} \pi [R_O^2 - R_B^2]}, \quad (9)$$

where $\Lambda_L^{R_{B,O}} = \frac{1}{R_O^2 - R_B^2} \int_{R_B}^{R_O} 2x\lambda_A p_L(x) \mathrm{d}x$.

Finally, consider the probability that there are $m$ APs residing in LoS in $(R_B, R_O)$ and the nearest $\min(N, m)$ APs are blocked, given that there is at least one AP in this ring, $Pr(B_3^1, B_3^2|B_3^3)$. Since the UE always connects to its nearest AP, we need to have the nearest $\min(N, m)$ APs in LoS.

When there is at least one AP in LoS conditions in $(R_B, R_O)$, we first need to obtain the distance distribution to $i$-th nearest AP in the ring $(R_B, R_O)$. Let $X^{R_{B,O}}$ be the random variable (RV) denoting the distance to a randomly chosen AP in LoS conditions in $(R_B, R_O)$ and let $f_{X^{R_{B,O}}}(x)$ be its probability density function (pdf). We thus have [22]

$$f_{X^{R_{B,O}}}(x) = \frac{x p_L(x)}{\int_{R_B}^{R_O} x p_L(x) \mathrm{d}x}. \quad (10)$$

Conditioning on $m$ APs in the ring $(R_B, R_O)$, the pdf of distance to the $i$-th nearest AP, between $m$ independent and identically distributed (i.i.d) RVs, $Y_i^{R_{B,O}}$, becomes

$$f_{Y_i^{R_{B,O}}}(x; m) = m f_{X^{R_{B,O}}}(x) \binom{m-1}{i-1} \times F_{X^{R_{B,O}}}(x)^{i-1} \Big(1 - F_{X^{R_{B,O}}}(x)\Big)^{m-i}, \quad (11)$$

where $F_{X^{R_{B,O}}}(x)$ is the CDF of $X^{R_{B,O}}$ obtained from (10).

Consider the process of LoS blockage by dynamically moving blockers around a stationary user of interest and a mmWave AP located at the distance of $x$ from the UE to concentrate on non-blockage probability. Recall that a blocker that moves according to the RDM model in a certain area is distributed uniformly in this area [18]. The probability that there is a non-blocked LoS path is then given by

$$p_{nB}(x) = e^{-2r_B \lambda_B \left[x \frac{h_B - h_U}{h_A - h_U} + r_B\right]}. \quad (13)$$

Denote by $p_{O,i}(m)$ the outage probability with $i$-th nearest AP in $(R_B, R_O)$ that is currently in LoS conditions, given that there are $m$ APs in LoS conditions in this ring. We arrive at

$$p_{O,i}(m) = \int_{R_B}^{R_O} f_{Y_i^{R_{B,O}}}(x; m)\big[1 - p_{nB}(x)\big] \mathrm{d}x, \; i \le m. \quad (14)$$

$$q_{O,N} = \left( e^{-\lambda_A \pi [R_B^2 - R_{nL}^2]} + \left(1 - e^{-\lambda_A \pi [R_B^2 - R_{nL}^2]}\right) e^{-\Lambda_L^{R_{nL,B}} \pi [R_B^2 - R_{nL}^2]} \right) \times \left( e^{-\lambda_A \pi [R_O^2 - R_B^2]} + \left(1 - e^{-\lambda_A \pi [R_O^2 - R_B^2]}\right) \left( e^{-\Lambda_L^{R_{B,O}} \pi [R_O^2 - R_B^2]} + \sum_{m=1}^{\infty} p_m^{R_{B,O}} \prod_{i=1}^{\min(N,m)} p_{O,i}(m) \right) \right). \quad (12)$$

The probability of having $m$ LoS APs in $(R_B, R_O)$ is

$$p_m^{R_{B,O}} = \frac{\left(\Lambda_L^{R_{B,O}} \pi [R_O^2 - R_B^2]\right)^m}{m!} e^{-\Lambda_L^{R_{B,O}} \pi [R_O^2 - R_B^2]}. \quad (15)$$

Combining (14) and (15), the sought probability is

$$Pr(B_3^1, B_3^2 | B_3^3) = \left[1 - p_0^{R_{B,O}}\right] \sum_{m=1}^{\infty} p_m^{R_{B,O}} \prod_{i=1}^{\min(N,m)} p_{O,i}(m). \quad (16)$$

The outage probability, $q_{O,N}$, is then derived by substituting (6), (8), (9), and (16) into (5). The final result is given in (12).

## IV. Spectral Efficiency

According to SNR analysis in subsection III-A, the UE is associated with $j$-th AP in LoS non-blocked conditions out of the nearest $\min(N, k)$ APs in the ring $(R_{nL}, R_O)$, if $k > 0$. If there are no such APs, the UE is associated with $j$-th nearest AP in the ring $(R_{nL}, R_B)$, which currently resides in LoS blocked conditions, if any. Otherwise, the spectral efficiency remains 0 until any of the APs becomes non-blocked again. Hence, spectral efficiency is a mixed RV with the probability mass at 0, the weight of $q_{O,N}$, and several "branches".

The first branch corresponds to the event of having the nearest non-blocked LoS AP with index $j$ out of $\min(N, k)$ APs jointly with the event of having $k$ APs residing in LoS in the ring $(R_{nL}, R_O)$ and at least one AP in that ring. The associated probability, $q_{n,nB}$, is given by

$$q_{n,nB} = \left(1 - p_0^{R_{nL,O}}\right) \sum_{k=1}^{\infty} p_k \sum_{j=1}^{\min(N,k)} v_{j,k}, \quad (17)$$

where $p_0^{R_{nL,O}} = e^{-\lambda_A \pi [R_O^2 - R_{nL}^2]}$ is the probability of having zero APs in the ring $(R_{nL}, R_O)$ and $p_k$ is the probability of having $k$ APs in LoS in the ring $(R_{nL}, R_O)$.

The probability $v_{j,k}$ that the nearest AP in $(R_{nL}, R_O)$ residing in nBl. LoS conditions has index $j = 1, 2, \ldots, \min(N, k)$, given that there are $k$ APs in $(R_{nL}, R_O)$, is

$$v_{j,k} = \left(1 - p_{B,j,k}\right) \prod_{s=1}^{j-1} p_{B,s,k}, \quad (18)$$

where $p_{B,j,k}$ is the probability of blockage at $j$-th nearest AP

$$p_{B,j,k} = \int_{R_{nL}}^{R_O} f_{Z_j}(x; k) \left[1 - p_{nB}(x)\right] \mathrm{d}x, \quad (19)$$

where $Z_j$ is the RV characterizing the distance to $j$-th nearest AP given that there are $k$ APs, $k \geq j$, in the ring $(R_{nL}, R_O)$. Note that $f_{Z_j}(x; k)$ can be established similarly to $f_{Y_i}(x; m)$.

The second branch of the spectral efficiency is associated with the event of having the closest LoS AP reside in the ring $(R_{nL}, R_B)$ jointly with the event of seeing $\min(N, k)$ LoS APs in blocked state having non-zero APs in LoS in the ring $(R_{nL}, R_O)$. The corresponding probability, $q_{n,B}$, is given by

$$q_{n,B} = \left(1 - p_0^{R_{nL,O}}\right) \sum_{k=1}^{\infty} p_k w^{R_{nL,B}} p_{B,k} \prod_{j=2}^{\min(N,k)} p_{B,j,k}, \quad (20)$$

where $p_{B,k}$ is the probability of blockage for the closest AP in the ring $(R_{nL}, R_B)$,

$$p_{B,k} = \int_{R_{nL}}^{R_B} f_{Z_1}(x; k) \left[1 - p_{nB}(x)\right] \mathrm{d}x, \quad (21)$$

while $f_{Z_1}(x) = k f_{X^{R_{nL,O}}}(x)(1 - F_{X^{R_{nL,O}}}(x))^{k-1}$, where $f_{X^{R_{nL,O}}}(x)$ and $F_{X^{R_{nL,O}}}(x)$ are the pdf and CDF of distance to a randomly chosen LoS AP in the ring $(R_{nL}, R_O)$ obtained similarly to (10).

The final term in (20), $w^{R_{nL,B}}$, is the probability that the closest LoS AP resides in the ring $(R_{nL}, R_B)$, given by

$$w^{R_{nL,B}} = \int_{R_{nL}}^{R_B} k f_{X^{R_{nL,O}}}(x) \left(1 - F_{X^{R_{nL,O}}}(x)\right)^{k-1} \mathrm{d}x. \quad (22)$$

After obtaining the probabilities for the branches of interest, the mean spectral efficiency takes the following form

$$E[C_N] = \left(1 - p_0^{R_{nL,O}}\right) \sum_{k=1}^{\infty} p_k \sum_{j=1}^{\min(N,k)} v_{j,k} \times \int_{R_{nL}}^{R_O} f_{Z_j}(x; k) \log_2\left(1 + S_{nB,j}(x)\right) \mathrm{d}x + \left(1 - p_0^{R_{nL,O}}\right) \sum_{k=1}^{\infty} p_k w^{R_{nL,B}} p_{B,k} \prod_{j=2}^{\min(N,k)} p_{B,j,k} \times \int_{R_{nL}}^{R_B} f_{Z_1}(x; k) \log_2\left(1 + S_{B,1}(x)\right) \mathrm{d}x, \quad (23)$$

where $S_{nB,j}(x)$ is the SNR with $j$-th nearest nBl. LoS AP and $S_{B,1}(x)$ is the SNR for the first Bl. LoS AP in $(R_{nL}, R_B)$.

## V. Numerical Assessment

In this section, we numerically investigate the impact of the MC degree together with the density of blockers and APs on the outage probability and spectral efficiency. The utilized system parameters follow 3GPP and are provided in Table I. The outage thresholds, $R_{nL} = 92\,\mathrm{m}$, $R_B = 107\,\mathrm{m}$, and $R_O = 963\,\mathrm{m}$ for the SNR threshold of $S_T = 3\,\mathrm{dB}$ are computed with (2). The choice of the SNR threshold was made with a reference to services that might require high SNR levels [23]. The percentage illustrated in the plots demonstrates the difference between the metrics for the MC degree of 1 and the degree in question.

In order to verify our assumptions and analysis, we cross-check the selected analytical results against those obtained with the simulations conducted in Matlab. The geometrical deployment closely follows the procedures detailed in subsection II-A, while the channels between all of the nodes are modeled according to the 3GPP considerations [19].

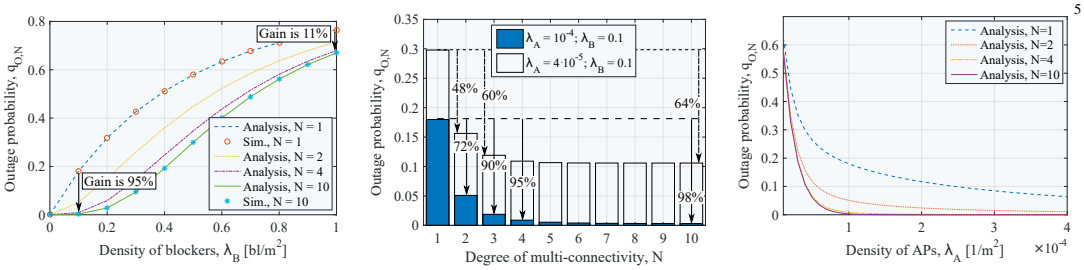


(a) Outage probability for $\lambda_A = 10^{-4}$ (b) Outage probability as function of $N$ (c) Outage probability for $\lambda_B = 0.1$

Fig. 2. Outage probability depending on density of blockers and APs, $\lambda_B$ and $\lambda_A$, and degree of multi-connectivity, $N$.

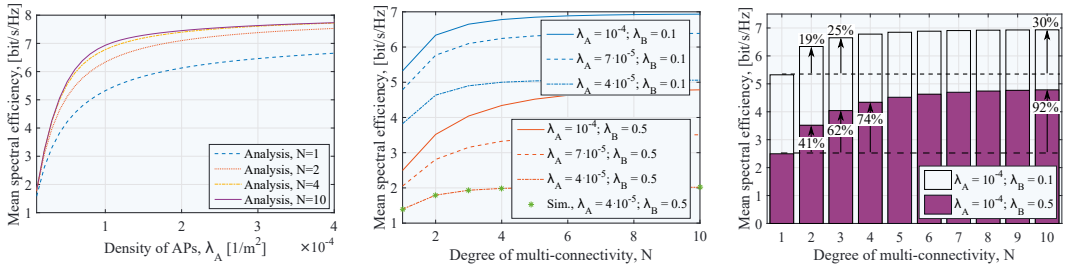


(a) Mean spectral efficiency for $\lambda_B = 0.1$ (b) Mean spectral efficiency as function of $N$ (c) Mean spectral efficiency $\lambda_B = 10^{-4}$.

Fig. 3. Mean spectral efficiency depending on density of blockers and APs, $\lambda_B$ and $\lambda_A$, and degree of multi-connectivity, $N$.

This framework operates in a time-driven regime with a step of 0.05 s (resulting in human movement of not more than 5 cm with the speed of 1 m/s). Each simulation round begins with a re-deployment of all the nodes of interest and then runs for 60 s of real time by reporting time-averaged performance indicators. All the intermediate simulation results have been further averaged across $1,000$ independent replications. The scenario was modeled for all the considered sets of input parameters, which demonstrated a close match between the analytical and the simulation output.

In Fig. 2(a), the outage probability is illustrated as a function of blocker density. We observe that for low densities of blockers, $\lambda_B = 0.1$, the MC degree $N = 4$ reduces the outage probability by $95\%$ as compared to $N = 1$. However, higher densities of blockers, $\lambda_B = 1$, decrease the difference in the outage probability between the MC degrees $N = 4$ and $N = 1$ by only $11\%$. For the chosen system design parameters and the degree of MC, the multi-connectivity gains diminish as the density of blockers increases. The underlying reason roots in approximately geometric behavior of the probability that all the available links reside in outage conditions.

Fig. 2(b) demonstrates the impact of the MC degree on the outage probability for different AP and blocker densities $\lambda_B = 0.1$. For $\lambda_A = 10^{-4}$, adding only one additional link reduces the outage probability by $72\%$. Increasing the MC degree further leads to much smaller gains that vanish after $N = 4$. This is explained by the behavior of blockage probability, which tends to 1 with an increased distance between the AP and the UE. Also, decreasing the density of APs down to $\lambda_A = 4 \cdot 10^{-5}$ shrinks the difference between the two neighboring bars as compared to the same bars with $\lambda_A = 10^{-4}$. It could be explained by the fact that the APs in sparse deployments are located (on average) farther away, which leads to lower non-blockage probabilities. Moreover, the benefit of having $N = 4$ links comprises $97\%$ of all the available gains when increasing the degree MC to $\infty$. Also note that increased SNR thresholds lead to a decreased number of APs, which a UE may communicate with at increased AP-UE distances. Therefore, the UE cannot exploit higher degrees of MC when the SNR threshold is high.

TABLE I
BASELINE SYSTEM PARAMETERS

| Parameter | Value |
|---|---|
| Heights of AP, UE, and blockers, $h_A, h_U, h_B$ | 10 m, 1.5 m, 1.7 m, [19] |
| Radius of a blocker, $r_B$ | 0.25 m, [2] |
| Frequency and bandwidth | 28 GHz and 1 GHz, [19] |
| Transmit power, $P_A$ | 35 dBm, [19] |
| Gain, Rx- and Tx-side, $G_U$ and $G_A$ | 5 dB and 10 dB, [24], [25] |
| SNR threshold, $S_T$ | 3 dB, [23] |

Fig. 2(c) and 3(a) highlight the effects of AP density on the outage probability and the mean spectral efficiency. As can be seen in the plot, for a lower density of APs (e.g., $\lambda_A = 10^{-5}$) the outage probability is rather low as well; moreover, the gains at higher degrees of MC are negligible. It can be explained by the fact that the distance between the closest AP and the UE is large, which makes the received signal weak (due to blockage and path loss). Farther located APs cannot deliver better signal quality, as they experience even worse channel conditions. The benefit in the increased degrees of MC is noticed for the density of APs equal to $\lambda_A = 3 \cdot 10^{-5}$ to $\lambda_A = 2 \cdot 10^{-4}$. By growing the density of APs further, the main AP offers channel conditions that are sufficient for the UE to reside on the same AP without switching to other ones.

In Fig. 3(b), the mean spectral efficiency as a function of the MC degree is shown for different values of $\lambda_B$ and $\lambda_A$. As one may observe, high densities of blockers (e.g., $\lambda_B = 0.5$) can be partially compensated by denser AP deployments and higher MC degrees. With the latter parameters, the same spectral efficiency is observed at much lower blocker densities,

$\lambda_B = 0.1$, and for a sparse AP deployment $\lambda_A = 4 \cdot 10^{-5}$. Therefore, the mean spectral efficiency in highly crowded scenarios may be improved by densifying the AP deployment and enabling the MC capability. However, one should note that densification may lead to increased interference, which can require coordination. In our study, for the given AP density we assume noise-limited operation [26].

The relative MC gains for the mean spectral efficiency are further depicted in Fig. 3(c). As one may notice, the relation between the increased MC degree and the corresponding benefits follows the same trend as the outage probability assessed in Fig. 2(b). The main contributions are observed with $N = 2$ and then with $N = 3$. A further increase of the MC degree provides negligible impact. Note that $N = 2$ offers the highest relative gain of over $40\%$ in crowded environments with higher densities of APs as compared to under $20\%$ in low blockage scenarios with $\lambda_B = 0.1$. The latter effect is explained by already high spectral efficiency at lower densities, which is sufficiently close to its upper limit.

## VI. Conclusion

*Multi-connectivity* is a recently introduced 3GPP consideration to improve the performance in the emerging mmWave networks. However, it is also expected to increase the complexity and signaling overheads of its enabling protocols. Hence, a careful selection of the *degree of MC* for a given deployment is of particular importance. In this work, we develop an analytical model to study the *outage probability* and the *spectral efficiency* in mmWave networks with the MC capability by capturing the key mmWave deployment, accounting for *nLoS*, *blocked*, and *non-blocked LoS* link conditions, as well as dynamic transitions between these states. Future work on this topic may include a performance study of upper-layer protocols and beamforming overheads, as well as the consideration of spatial and temporal consistency and the effect of blocker density on the attenuation, among others.

Our numerical results support the following observations:

• For a moderately dense human crowd, $\lambda_B \in [0.05; 0.7]$, the use of the MC degrees of 2–4 notably improves both outage and spectral efficiency metrics for the cell-edge users over a given range of deployment parameters. In contrast, any higher MC degree does not significantly benefit the performance, which is important to note, since a higher degree of MC may impose additional overheads on connectivity management.

• The MC technique is most beneficial at moderate densities of human blockers around the UE, $\lambda_B \in [0.05; 0.7]$. With lower values of $\lambda_B$, the environment does not benefit from reliance on the MC operation, whereas even the MC degree of 10 cannot mitigate the outage probability for ultra-dense crowds, since all of the possible paths around the UE become blocked.

## References


[1] K. Haneda *et al.*, "5G 3GPP-like channel models for outdoor urban microcellular and macrocellular environments," in *IEEE 83rd Vehicular Technology Conference (VTC Spring)*, pp. 1–7, May 2016.

[2] M. Gapeyenko *et al.*, "On the temporal effects of mobile blockers in urban millimeter-wave cellular scenarios," *IEEE Transactions on Vehicular Technology*, vol. 66, pp. 10124–10138, November 2017.

[3] 3GPP, "NR; Multi-connectivity; Overall description (Release 15)," 3GPP TS 37.340 V15.2.0, June 2018.

[4] F. B. Tesema, A. Awada, I. Viering, M. Simsek, and G. P. Fettweis, "Mobility modeling and performance evaluation of multi-connectivity in 5G intra-frequency networks," in *IEEE Globecom Workshops (GC Wkshps)*, pp. 1–6, December 2015.

[5] D. Ohmann, A. Awada, I. Viering, M. Simsek, and G. P. Fettweis, "Impact of mobility on the reliability performance of 5G multi-connectivity architectures," in *IEEE Wireless Communications and Networking Conference (WCNC)*, pp. 1–6, March 2017.

[6] L. Cheng *et al.*, "Coordinated multipoint transmissions in millimeter-wave radio-over-fiber systems," *Journal of Lightwave Technology*, vol. 34, pp. 653–660, January 2016.

[7] A. Ravanshid *et al.*, "Multi-connectivity functional architectures in 5G," in *Proc. of IEEE International Conference on Communications Workshops (ICC)*, pp. 187–192, May 2016.

[8] D. S. Michalopoulos, I. Viering, and L. Du, "User-plane multi-connectivity aspects in 5G," in *Proc. of 23rd International Conference on Telecommunications (ICT)*, pp. 1–5, May 2016.

[9] M. Giordani, M. Mezzavilla, S. Rangan, and M. Zorzi, "An efficient uplink multi-connectivity scheme for 5G millimeter-wave control plane applications," *IEEE Transactions on Wireless Communications*, vol. 17, pp. 6806–6821, October 2018.

[10] M. Polese, M. Giordani, M. Mezzavilla, S. Rangan, and M. Zorzi, "Improved handover through dual connectivity in 5G mmWave mobile networks," *IEEE Journal on Selected Areas in Communications*, vol. 35, pp. 2069–2084, September 2017.

[11] O. Semiari, W. Saad, and M. Bennis, "Joint millimeter wave and microwave resources allocation in cellular networks with dual-mode base stations," *IEEE Transactions on Wireless Communications*, vol. 16, pp. 4802–4816, July 2017.

[12] V. Petrov *et al.*, "Achieving end-to-end reliability of mission-critical traffic in softwarized 5G networks," *IEEE Journal on Selected Areas in Communications*, vol. 36, pp. 485–501, March 2018.

[13] O. Semiari, W. Saad, M. Bennis, and B. Maham, "Caching meets millimeter wave communications for enhanced mobility management in 5G networks," *IEEE Transactions on Wireless Communications*, vol. 17, pp. 779–793, February 2018.

[14] D. Öhmann, A. Awada, I. Viering, M. Simsek, and G. P. Fettweis, "Achieving high availability in wireless networks by inter-frequency multi-connectivity," in *Proc. of IEEE International Conference on Communications (ICC)*, pp. 1–7, May 2016.

[15] V. Petrov *et al.*, "Dynamic multi-connectivity performance in ultra-dense urban mmwave deployments," *IEEE Journal on Selected Areas in Communications*, vol. 35, pp. 2038–2055, September 2017.

[16] F. B. Tesema, A. Awada, I. Viering, M. Simsek, and G. Fettweis, "Multiconnectivity for mobility robustness in standalone 5G ultra dense networks with intrafrequency cloud radio access," *Wireless Communications and Mobile Computing*, pp. 1–17, January 2017.

[17] F. B. Tesema, A. Awada, I. Viering, M. Simsek, and G. Fettweis, "Evaluation of context-aware mobility robustness optimization and multi-connectivity in intra-frequency 5G ultra dense networks," *IEEE Wireless Communications Letters*, vol. 5, pp. 608–611, December 2016.

[18] P. Nain, D. Towsley, B. Liu, and Z. Liu, "Properties of random direction models," in *IEEE 24th Annual Joint Conference of the IEEE Computer and Communications Societies*, vol. 3, pp. 1897–1907, March 2005.

[19] 3GPP, "Study on channel model for frequencies from 0.5 to 100 GHz (Release 15)," 3GPP TR 38.901 V15.0.0, June 2018.

[20] J. S. Lu, D. Steinbach, P. Cabrol, and P. Pietraski, "Modeling human blockers in millimeter wave radio links," *ZTE communications*, vol. 10, pp. 23–28, December 2012.

[21] V. Petrov *et al.*, "Interference and SINR in millimeter wave and terahertz communication systems with blocking and directional antennas," *IEEE Transactions on Wireless Communications*, vol. 16, pp. 1791–1808, March 2017.

[22] D. Moltchanov, "Distance distributions in random networks," *Elsevier Ad Hoc Networks*, vol. 10, pp. 1146–1166, August 2012.

[23] K. Belbase, Z. Zhang, H. Jiang, and C. Tellambura, "Coverage analysis of millimeter wave decode-and-forward networks with best relay selection," *IEEE Access*, vol. 6, pp. 22670–22683, 2018.

[24] K. Sahota, "5G mmwave radio design for mobile products," tech. rep., 5G Summit, June 2017.

[25] M. Matalatala *et al.*, "Performance evaluation of 5G millimeter-wave cellular access networks using a capacity-based network deployment tool," *Mobile Information Systems*, pp. 1–9, 2017.

[26] M. Rebato, M. Mezzavilla, S. Rangan, F. Boccardi, and M. Zorzi, "Understanding noise and interference regimes in 5G millimeter-wave cellular networks," in *22th European Wireless Conference*, May 2016.

# PUBLICATION VII

**Effects of Blockage in Deploying mmWave Drone Base Stations for 5G Networks and Beyond**

M. Gapeyenko, I. Bor-Yaliniz, S. Andreev, H. Yanikomeroglu and Y. Koucheryavy

*2018 IEEE International Conference on Communications Workshops (ICC Workshops)*2018, 1–6

# Effects of Blockage in Deploying mmWave Drone Base Stations for 5G Networks and Beyond

Margarita Gapeyenko†, Irem Bor-Yaliniz⋆, Sergey Andreev†, Halim Yanikomeroglu⋆, and Yevgeni Koucheryavy†
†Tampere University of Technology, Tampere, Finland
⋆Carleton University, Ottawa, Canada

*Invited Paper*

***Abstract*—Due to their unconstrained mobility and capability to carry goods or equipment, *unmanned aerial vehicles* (UAVs) or *drones* are considered as a part of the fifth-generation (5G) wireless networks and become attractive candidates to carry a base station (BS). As 5G requirements apply to a broad range of uses cases, it is of particular importance to satisfy those during *spontaneous and temporary events*, such as a marathon or a rural fair. To be able to support these scenarios, mobile operators need to deploy significant radio access resources quickly and on demand. Accordingly, by focusing on 5G cellular networks, we investigate the use of drone-assisted communication, where a drone is equipped with a millimeter-wave (mmWave) BS. Being a key technology for 5G, mmWave is able to facilitate the provisioning of the desired per-user data rates as drones arrive at the service area whenever needed. Therefore, in order to maximize the benefits of *mmWave-drone-BS* utilization, this paper proposes a methodology for its optimized deployment, which delivers the optimal height, coordinates, and coverage radius of the drone-BS by taking into account the *human body blockage* effects over a mmWave-specific channel model. Moreover, our methodology is able to maximize the number of offloaded users by satisfying the target signal quality at the cell edge and considering the maximum service capacity of the drone-BS. It was observed that the mmWave-specific features are extremely important to consider when targeting efficient drone-BS utilization and thus should be carefully incorporated into analysis.**

***Index Terms*—5G networks and beyond; mmWave; human body blockage; network slicing; drone-cell communications.**

## I. Introduction and Motivation

The recent developments in *unmanned aerial vehicles* (UAVs) attracted an increased attention from the wireless communications community. It is envisioned that UAVs are about to become a part of the fifth generation (5G) of wireless networks [1]. One of the emerging applications is the use of the UAVs equipped with wireless transceivers, or *drone base stations* (BSs), which have been proposed to improve the connectivity levels in 5G systems and beyond [2]. In particular, latest research illustrates that autonomous flying robots become an attractive solution to boost network capacity on demand, which is particularly desirable for spontaneous and temporary events, such as rural fair [3] or marathon use cases [4]. This paper specifically argues for the use of drones enhanced with high-rate millimeter-wave (mmWave) radio technology to support these scenarios.

While an autonomous fleet of drones flying around the city [5] may still be a futuristic concept, the utilization of several specialized drones operating under human control is possible from an engineering perspective already today [6], [7]. At the same time, the use of drone-BSs introduces new challenges, such as extra operating costs, endurance, and backhauling [2], [8]. In order to seamlessly integrate drone-BSs into the 5G system architecture, a new concept named network slicing might become an appropriate candidate [2]. Slicing can facilitate the integration of aerial BSs with the terrestrial network by providing a slice with the necessary fronthaul, backhaul, and network functions by also considering mobility of the drone-BS. Smart integration of drones into the 5G infrastructure additionally requires efficient drone placement mechanisms to improve the overall system performance.

Despite a number of research works on drone deployment [9]–[11], the specifics of mmWave-based drone-assisted communication has remained insufficiently studied so far. Operating in extremely high frequency (EHF) bands and having larger bandwidths at its disposal, mmWave radio technology is being shaped as the 5G New Radio [12]. Along with their benefits, mmWave systems are facing many challenges. One of these is shorter wavelengths for which smaller objects, such as humans, become obstacles for the line-of-sight (LoS) radio propagation [13], [14]. Hence, it is crucial to account for the *human body blockage* when evaluating the performance or planning the deployment of mmWave-BSs. In contrast to lower frequencies, another challenge at mmWave bands is that the path loss (PL) increases significantly with the growing distance from a transmitter (Tx) to a receiver (Rx) [15]. Hence, there is a trade-off between placing a drone at a higher altitude (which would provide better LoS links) and keeping the PL minimal (which increases with the growing distance).

There are several important benefits that motivate the utilization of mmWave-based drone-BSs, particularly for the temporary and spontaneous events, as described below:

- Able to arrive at the crowded location quickly, drones equipped with wireless access capabilities help operators serve events, where traffic demand becomes higher than expected for a certain period of time, but where it is not feasible to deploy a static network infrastructure to serve such amounts of data on a regular basis.
- Even though higher altitudes lead to larger probabilities to maintain the LoS link, they also increase the three-dimensional (3D) distance, thus making the PL higher. Therefore, the optimal altitude may exist. While the terrestrial infrastructure cannot alter the height of the BSs quickly in order to improve the signal quality, the flexibility of the drone-BSs offers an opportunity to place them over the crowd and adjust their height when needed.

- To achieve 100 Mbit/s per user expected of the 5G systems, mmWave communication is an appropriate solution whereas the conventional infrastructure will need a significant number of cellular BSs to support the required data rate, which leads to severe interference. The latter could be shown using simple analysis where the link capacity for the cell edge-user over mmWave with the carrier of 28 GHz and the conventional microwave cellular link with the carrier of 2.1 GHz is calculated as $r(x) = B_u \log[1 + S(x)]$. Here, $B_u$ is the bandwidth available to the user of interest and $S(x)$ is the average signal-to-noise ratio (SNR) for this user at the cell edge of radius $x$. For the same number of active users, the cellular link with the maximum available bandwidth (B) of 20 MHz delivers about 10 times lower data rates than what mmWave (B = 1 GHz) does, even in ideal conditions where no interference is assumed. In an optimistic case, to provide the average data rate of 100 Mbit/s per user, for a cell having 50 m radius and 70 users, one mmWave-BS is sufficient, whereas the required number of the conventional BSs is 10 times higher. Therefore, the larger bandwidth of mmWave-BSs accentuates the utilization of those to support the mass events and mitigate the growth of interference to deliver the 5G date rates [16].

All of the above motivates the need for efficient placement of mmWave-drone-BSs to provide with a better link quality and benefit from the maximum number of users offloaded from the cellular infrastructure, where the main features of mmWave communication would be considered. In this paper, we investigate efficient deployment of a mmWave-drone-BS by taking into account the properties of mmWave communication, where the LoS link may be blocked by a human body. Having in mind that the height of the mmWave-drone-BS is comparable with the height of the BSs mounted on the walls of the buildings and assuming quasi-stationary drones hovering at a certain altitude [17], we approximate the air-to-ground channel model with the terrestrial channel model [18] for the sake of our first-order analysis.

The main contributions of this paper are as follows.

- By adopting a terrestrial mmWave channel model for the air-to-ground mmWave communication as well as by accounting for the human body blockage, we derive the optimal height of the drone-BS.
- By assuming a Poisson distribution of user locations for the adopted mmWave PL model, we formulate and solve a 3D placement problem. The latter produces the optimal height and horizontal location for the drone-BS as well as the cell radius. Our theoretical results for the optimal height demonstrate a tight match with those obtained by solving the 3D placement problem.

The rest of this text is organized as follows. In Section II, we introduce our system model with its main assumptions. Then, the proposed optimization methodology is described in Section III. The numerical results are offered in Section IV. Conclusions are drawn in the last section.

## II. System model

Our example rural-fair scenario considers a set of identical users, $\mathbb{M}$, which are distributed randomly in the area of interest as illustrated in Fig. 1. We assume that the existing operator's infrastructure is not planned for such a spontaneous and temporary mass event. Therefore, the operator is incapable of serving all the users at the fair. Hence, we consider the assistance of a mmWave-drone-BS to inject capacity across space and time. The mmWave-drone-BS is integrated into the current infrastructure via a dedicated long range backhaul channel over a different frequency [19].

Inspired by the adoption of terrestrial channel models for air-to-ground channels of quasi-stationary drone-BSs [9], [10], [17], we employ the model in [20] for the first-order analysis of mmWave-drone-BSs. There are two motivations for choosing a terrestrial channel model. First, contemporary drone-BSs with a rotary wing [21] can be made as stationary as cell towers, especially under mild weather conditions. Second, the short range of mmWave links prevents from using high-altitude drones due to the inherently high PL with increasing distance between the Tx and Rx. Therefore, the altitude of a mmWave-drone-BS must be comparable with the altitude of the static mmWave-BSs deployed on the walls, lamp posts, etc. For the sake of our analysis, the small scale fluctuations in the environment are neglected as proposed in [17].

The considered scenario consists of the mmWave-drone-BS located at height $h_D$ and human blockers modeled as cylinders with the average height of $h_B$ and the average diameter of $g_B$. For a snapshot analysis, assume a Poisson field of static human blockers with the density of $\lambda$, where $|\mathbb{M}|$ humans are distributed across the area $S$ with the parameter $\lambda S$, and $|\cdot|$ indicates the cardinality of a set. Note that all users are considered as blockers for each other. The user terminal is assumed to be located at the height $h_R$, where $h_R < h_B$, since the terminal carried by a human is usually lower than the height of the human itself. Hence, if the user $i$ is communicating with the mmWave-drone-BS, then all other users/humans in the coverage area $\mathcal{A}$ with radius $R$ are

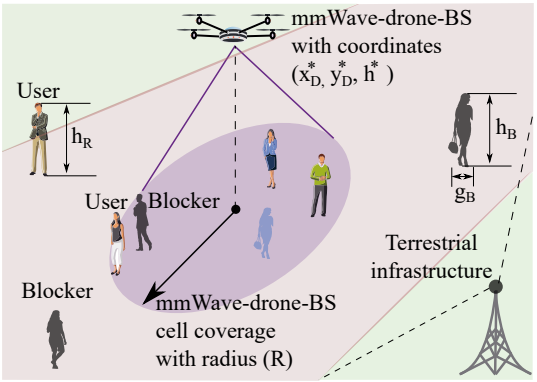


Fig. 1. Target scenario with mmWave-drone-BS, users, and blockers.

TABLE I
NOTATION AND PARAMETERS

| Parameter | Description |
|---|---|
| $S$ | Area of interest |
| $h_D$, $h_R$, $h_B$ | Height of drone-BS, Rx, and human blockers |
| $R$ | Cell radius of the drone-BS |
| $d_i$, $r_i$ | 3D, 2D distance between drone-BS and $i^{\text{th}}$ Rx |
| $g_B$ | Diameter of human blockers |
| $\lambda$ | Density of human blockers |
| $\mathbb{P}_L$ | Probability of LoS |
| $L_{L,i}$, $L_{N,i}$ | Path loss for LoS/nLoS $i^{\text{th}}$ Rx |
| $L_{a,i}$ | Average path loss for $i^{\text{th}}$ Rx |
| $\lvert\mathbb{M}\rvert$ | Total number of humans in the area of interest |
| $h^*$ | Optimal height of the drone-BS |
| $({x_D}^*, {y_D}^*)$ | Optimal 2D position of the drone-BS |
| $N$ | Maximum number of users served by one drone-BS |
| $Q$, $\sigma_i$ | Target SNR, SNR for $i^{\text{th}}$ Rx |
| $\gamma$ | Maximum tolerable path loss |

blockers, if their heights are large enough to block the LoS between Rx and Tx. Note that the coverage radius $R$ depends on the ability of drone-BS to support on average the minimum quality-of-service (QoS) experienced by the cell edge user; therefore, it is highly affected by the height of the drone-BS and the probability of LoS as will be shown later.

Following [22], we assume that radio interference does not have a major effect, which is a common assumption for most mmWave-based systems with highly directional antennas, and that the system under study is *noise-limited*.

Recall that the PL models for LoS and nLoS links at mmWave frequencies follow [18] and are given as

$$\begin{aligned} L_{L,i} &= \alpha_L + 10\beta_L \log_{10}(d_i), \\ L_{N,i} &= \alpha_N + 10\beta_N \log_{10}(d_i), \end{aligned} \tag{1}$$

where $\alpha_L$, $\beta_L$, $\alpha_N$, and $\beta_N$ are the parameters of the LoS and nLoS PL models, and $d_i = \sqrt{(x_i - x_D)^2 + (y_i - y_D)^2 + (h_D - h_R)^2}$ is the 3D distance between the drone-BS and Rx.

In order to account for the human body blockage, we adopt the probability of LoS, $\mathbb{P}_L$, for a user $i$ from [20] by modifying it in the case of the constant height and diameter of blockers for further analytic tractability as

$$\mathbb{P}_L(r_i, h_D) = \exp\left( -\lambda g_B \frac{r_i(h_B - h_R)}{(h_D - h_R)} \right), \tag{2}$$

where $r_i$ is 2D distance between drone-BS and Rx.

Then, the average PL for the cell edge user $i$, located at distance $R$ from Tx, becomes

$$L_{a,i} = \mathbb{P}_L(R, h_D) L_{L,i} + [1 - \mathbb{P}_L(R, h_D)]\, L_{N,i}. \tag{3}$$

As one may find in [17] and similar works, the average value of PL is sufficient to perform the first-order analysis. Since the random behavior with the corresponding distribution is not the focus of this study, the distributions of fading and shadowing are disregarded. As it was observed in [20], there exists the optimal height of the Tx, where the average PL assumes its minimum value.

## III. mmWAVE-DRONE-BS DEPLOYMENT

In order to support the current cellular infrastructure and provide higher data rates for every user in the area, the aim is to offload as many users as possible to the mmWave-drone-BS. Because the users are randomly distributed in the region, the area to be covered by a mmWave-drone-BS (drone-cell coverage) and the altitude of the drone-BS are not known a priori.

On the one hand, deploying a mmWave-drone-BSs at a higher altitude leads to the greater LoS probability as can be observed from (2). On the other hand, mmWave-drone-BSs are energy critical devices and higher altitudes may require more transmission power due to increased distance between the users and the drone-BSs to compensate for larger PL. Therefore, the objective of covering the maximum number of users with minimum energy means the smallest area enclosing the highest number of users, while the minimum height that can provide coverage over that area must be derived.

As observed in (2) and (3), the average PL depends on the altitude of the Tx, as well as the horizontal distance between the Tx and Rx. Therefore, the optimal placement of a mmWave-drone-BS involves all dimensions, namely, the optimal position is $({x_D}^*, {y_D}^*, h^*)$. Fixing the horizontal location of the drone-BS and searching for $h^*$ to provide the maximum number of users to be covered (*1D search*), or fixing the altitude and searching for $({x_D}^*, {y_D}^*)$ (*2D search*) may not result in the most effective deployment. The search for the optimal position of a mmWave-drone-BS must thus be performed in 3D. Not only the expansion of the search space to 3D makes it very hard to conduct an exhaustive search, but also (3) is analytically difficult. Therefore, in this section, we propose an efficient 3D placement method for mmWave-drone-BSs.

The problem to find $(x_D^*, y_D^*, h^*)$ can be formulated as

$$\underset{x_D, y_D, h, \{m_i\}}{\text{maximize}} \quad \sum_{i \in \mathbb{M}} m_i \tag{4a}$$

subject to

$$m_i \sigma_i \geq m_i Q, \qquad \forall i = 1, ..., |\mathbb{M}|, \tag{4b}$$

$$\sum_{i \in \mathbb{M}} m_i \leq N, \qquad \forall i = 1, ..., |\mathbb{M}|, \tag{4c}$$

$$x_l \leq x_D \leq x_u, \tag{4d}$$

$$y_l \leq y_D \leq y_u, \tag{4e}$$

$$h_l \leq h \leq h_u, \tag{4f}$$

$$m_i \in \{0, 1\}, \qquad \forall i = 1, ..., |\mathbb{M}|, \tag{4g}$$

where $m_i$ is a binary variable indicating whether the $i^{th}$ user of the set $\mathbb{M}$ is covered (1) or not (0), $x_D, y_D$ are the possible coordinates of the drone-BS, $h = h_D - h_R$, and $\sigma_i$ is the SNR for the user $i$. Then, $Q$ and $N$ represent the target SNR level for the served user $i$ and the capacity of the drone-BS in terms of the maximum number of users that it can serve, respectively. The upper and the lower limits of the available positions across all three dimensions are indicated by the subscripts $u$ and $l$,

correspondingly. While (4b) determines which users can be served, (4c) captures the maximum number of the served users.

Apart from the antenna gains, transmit power, etc., the maximum tolerable PL for the $i^{th}$ user, $\gamma$, corresponds to the target SNR of the $i^{th}$ user, $Q$. Hence, using (3), (4b) becomes $m_i L_{a,i} \leq \gamma$. Note that our approach is not limited to the model in [18], and other channel models may be considered as well. After further derivations, the QoS depicted in (4b) can be represented in terms of distance between user $i$ and the drone-BS as

$$r_i^2 + h^2 \leq 10^{[2\tilde{\gamma}+\mathbb{P}_L(R,h)k_2]/[\mathbb{P}_L(R,h)k_3+k_4]}, \tag{5}$$

where $r_i = \sqrt{(x_i - x_D)^2 + (y_i - y_D)^2}$ is 2D distance between user $i$ and the drone-BS, $\tilde{\gamma} = \gamma - \alpha_N$, $k_2 = \alpha_N - \alpha_L$, $k_3 = 10(\beta_L - \beta_N)$, $k_4 = 10\beta_N$, whereas $R$ is the coverage radius of the drone-BS. Note that any user with the horizontal distance of less than $R$ will be served, since its minimum SNR requirements at the cell edge are satisfied on average. Furthermore, introducing the variable $\omega = R/h$ and expressing $\mathbb{P}_L(R,h)$ in terms of $\omega$, (4b) becomes

$$r_i^2 \leq \Gamma(\omega), \tag{6}$$

where $\Gamma(\omega)$ is the following

$$\Gamma(\omega) = \frac{10^{(2\tilde{\gamma}+k_2 e^{\omega k_1})/(k_3 e^{\omega k_1}+k_4)}}{1+\frac{1}{\omega^2}}, \tag{7}$$

where $k_1 = -\lambda g_B(h_B - h_R)$, $h_B > h_R$.

**Proposition 1.** *The function $\Gamma(\omega)$ has the maximum point $\omega^*$, which is considered to be optimal.*

*Proof.* To find the maximum point, we first need to establish an extremum point of $\Gamma(\omega)$, by taking a derivative, equating it to zero, and solving the following

$$\begin{aligned} &k_1 e^{\omega k_1}(\omega^3 + \omega)(k_2 k_4 - k_3\tilde{\gamma})\ln(10) \\ &+ (e^{\omega k_1}k_3 + k_4)^2 = 0. \end{aligned} \tag{8}$$

Note that the above always has a solution for $\beta_L < \beta_N$ and $h_B > h_R$. It could be solved numerically and offers the extremum point, $\omega^*$. By taking the second derivative of (8) and obtaining the negative value at the extremum point $\omega^*$, we establish that $\omega^*$ is also the maximum of $\Gamma(\omega)$.

As there is no closed form solution to find $\omega^*$, it is important to show the uniqueness of this point, which is formally proven in Appendix. □

The optimal value, $\Gamma(\omega^*)$, can be inserted into (6). The resulting optimization problem is then

$$\underset{x_D, y_D, \{m_i\}}{\text{maximize}} \quad \sum_{i\in\mathbb{M}} m_i \tag{9a}$$

subject to

$$r_i \leq \sqrt{\Gamma(\omega^*)} + K(1 - m_i), \ \forall i = 1, ..., |\mathbb{M}|, \tag{9b}$$

$$x_l \leq x_D \leq x_u, \tag{9c}$$

$$y_l \leq y_D \leq y_u, \tag{9d}$$

$$m_i \in \{0, 1\}, \qquad \forall i = 1, ..., |\mathbb{M}|, \tag{9e}$$

where $K$ is a large enough value [9]. Once $x_D^*$ and $y_D^*$ are obtained, $R$ can be calculated by identifying the user at the drone-cell edge, i.e., $\max_{m_i\in\mathbb{M}}(r_i | m_i = 1)$. Then, $h^*$ can be derived by using $\omega^*$.

Moreover, the optimal height can also be produced directly from (3) by taking a derivative of the average PL. Note that in this case, the cell coverage $R$ should be known beforehand. In this paper, we propose an approach to numerically establish the optimal height of Tx, $h^*$, by solving the following

$$\begin{aligned} &- C\big[\alpha_L - \alpha_N\big]\big[(h^* - h_R)^2 + R^2\big]e^{\frac{C}{h^* - h_R}} \\ &+ 10C\big[\beta_N - \beta_L\big]\log_{10}\left(\sqrt{(h^* - h_R)^2 + R^2}\right) \\ &+ \frac{10\big[\beta_L - \beta_N\big]\big[h^* - h_R\big]^3}{\ln(10)}e^{\frac{C}{h^* - h_R}} + 10\beta_N = 0, \end{aligned} \tag{10}$$

where the auxiliary variable $C = -\lambda g_B R(h_D - h_R)$.

The above 3D placement problem can be solved by using e.g., interior-point optimization method via MOSEK [23], both efficiently and accurately. Indeed, the efficient 3D placement algorithm in (9a) offers the same result as in (10) for the same value of $R$ derived with our 3D placement algorithm.

## IV. Numerical results and discussion

In this section, we illustrate representative numerical results produced for different human densities $\lambda$, where the humans are uniformly distributed within a 100x100 m$^2$ area. The parameters for the considered scenario are collected in Table II. Our target is to serve the maximum number of users from the set of total number of humans $|\mathbb{M}|$ with a mmWave-drone-BS. It should be noted that for every realization of the scenario the coordinates of the users as well as the total number $|\mathbb{M}|$ are known for the problem to solve. We set the maximum tolerable path loss, $\gamma$, equal to 110 dB based on the following assumed parameters: bandwidth is 1 GHz, Rx and Tx antenna gains are 5 dB and 10 dB, respectively, Tx power is 20 dBm, noise figure is 6 dB, and target SNR is 3 dB. Also, 95% confidence interval is calculated for the entire set of runs to demonstrate the consistency of the proposed method. The following formula is used for confidence interval calculations: $\bar{x} \pm \mathrm{Z}_{a/2} \times \frac{\sigma}{\sqrt{(n)}}$, where $\bar{x}$ is the mean, Z is the confidence coefficient, $a$ denotes the confidence interval, while $\sigma$ and $n$ represent the standard deviation and the sample size, respectively.

First, Fig. 2 demonstrates the behavior of the altitude of the mmWave-drone-BS as the density of blockers increases.

TABLE II
Baseline system parameters

| Parameter | Value |
|---|---|
| Height of Rx, $h_R$ | 1.3 m |
| Height of a human blocker, $h_B$ | 1.7 m |
| Diameter of a human blocker, $g_m$ | 0.5 m |
| Frequency band | 28 GHz |
| LoS path loss model parameters | $\alpha_L = 61.4$, $\beta_L = 2$ |
| nLoS path loss model parameters | $\alpha_N = 72$, $\beta_N = 2.92$ |
| Maximum number of users served by drone-BS, $N$ | 100 |
| Area of interest, $S$ | 100x100 m$^2$ |

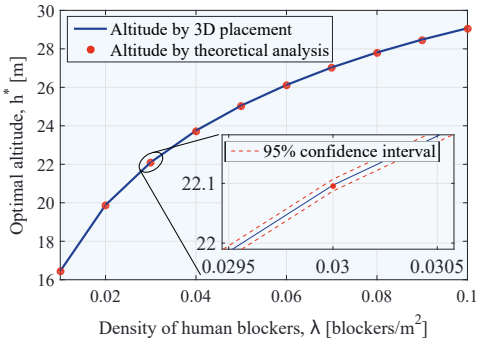


Fig. 2. Comparison of the optimal altitude results from 3D placement with theoretical analysis vs. density of blockers, $\lambda$.

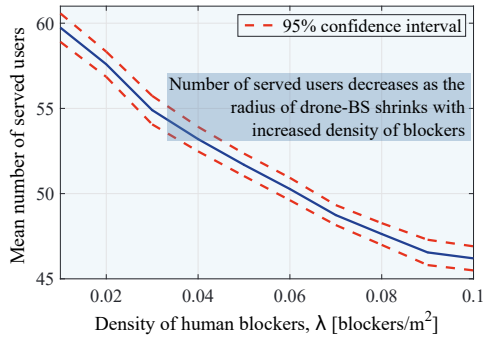


Fig. 4. Number of users served by mmWave-drone-BS vs. density of blockers, $\lambda$.

We observe that the altitude becomes higher as the density grows. The reason is that higher altitude makes the probability of blockage lower but sacrifices the radius of the drone-BS coverage in order to reduce the 3D distance, in order to satisfy the minimum SNR. This confirms the importance of appropriate height selection. In addition, the plot shows a comparison of the altitude by the 3D placement with that derived from the theoretical result in (10). The analysis requires the cell coverage obtained with the 3D placement in order to produce the height of the BS. The results indicate a reasonable match between the two. It should be noted that the proposed 3D placement provides the coordinates of the drone-BS, not only altitude but also the location in the horizontal plane, which allows for efficient drone-cell deployment in order to serve the maximum number of users.

In Fig. 3, the aforementioned relation between the mean value of the mmWave-drone-BS cell coverage and the density of blockers is displayed. It is observed that the cell radius, $R$, decreases as the density grows. This could be explained by the fact that the probability of blockage becomes larger, thus yielding a higher altitude of the drone-BS and smaller cell radius to reduce 3D distance in order to facilitate the satisfaction of the minimum SNR requirements.

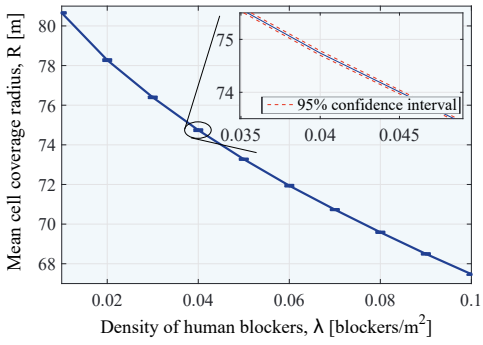


Fig. 3. Radius, R, (m) vs. density of blockers, $\lambda$, with error bar.

Further, we consider the number of served users as illustrated in Fig. 4. We learn that the average number of users served by one drone-BS decreases as the density of blockers grows. This could be explained by the fact that the effective cell radius degrades as it was shown earlier. Therefore, the density of blockers highly affects the optimal height of the drone-BS, which then impacts the shrinking of the cell coverage, and finally the reduced number of served users. This implies the importance of considering all of the variables as they have a major effect on the load of the BS as well as its ability to satisfy the minimum QoS requirements.

## V. Conclusion and Future Work

Drone-assisted cellular communication is currently attracting significant research attention from both academia and industry by becoming a new frontier in 5G wireless networks and beyond. While mmWave radio systems are expected to deliver the required 100 Mbit/s of user experienced data rate, there still remains a question of how to boost cell capacity quickly and on-demand, which is highly relevant for spontaneous and temporary events, such as open-air festivals in rural areas or marathons [4]. To ensure efficient support of these emerging scenarios, we advocate for the use of mmWave-drone-BSs.

Despite a number of past papers on drone-BS placement, the specifics of mmWave communication, including LoS blockage by human bodies, has not been taken into consideration before. In this paper, we study the effective deployment of a mmWave-drone-BS as well as derive the corresponding height and cell radius. Further, we produce an analytical result for the optimal height of Tx. We thus observe that the density of blockers has a dramatic effect on the desired height, the coverage radius, and the number of served users. Furthermore, an increase in the density of blockers leads to a sharp drop in the total number of users that could be served satisfactorily. Therefore, our future work is to consider the effects related to multiple drone-BSs and their needed densities in order to serve all of the users.

## APPENDIX

In order to demonstrate the uniqueness of the maximum point $\omega^*$, we prove that the $\Gamma(\omega)$ function is quasiconcave by following the definition [24]

$$\Gamma\big(\lambda_C x + [1-\lambda_C]y\big) \geq \min\{\Gamma(x), \Gamma(y)\}, \tag{11}$$

where $\lambda_C \in [0,1]$, $x, y \in S_C$, and $S_C \to \mathbb{R}$.

Assume that $x < y$, then (11) could be written as

$$\frac{10^{\frac{2\tilde{\gamma}+k_2\exp\left(k_1(\lambda_C x+[1-\lambda_C]y)\right)}{k_3\exp\left(k_1(\lambda_C x+[1-\lambda_C]y)\right)+k_4}}}{1+\frac{1}{(\lambda_C x+(1-\lambda_C)y)^2}} \geq \frac{10^{\frac{2\tilde{\gamma}+k_2\exp(zk_1)}{k_3\exp(zk_1)+k_4}}}{1+\frac{1}{z^2}}, \tag{12}$$

where $z$ is equal to $x$ or $y$ depending on the minimum value of $\Gamma$.

It is easy to see that by transferring the right part to the left side of (12) and reducing to a common denominator, the last one is always greater than 0. Therefore, to make the overall expression be greater than 0, one should prove the positive sign of the numerator.

Let $A = \frac{2\tilde{\gamma}+k_2\exp\left(k_1(\lambda_C x+[1-\lambda_C]y)\right)}{k_3\exp\left(k_1(\lambda_C x+[1-\lambda_C]y)\right)+k_4}$ and $B = \frac{2\tilde{\gamma}+k_2\exp(zk_1)}{k_3\exp(zk_1)+k_4}$, then the numerator of (12) becomes

$$10^A\left(1+\frac{1}{z^2}\right) - 10^B\left(1+\frac{1}{\big(\lambda_C x+[1-\lambda_C]y\big)^2}\right) \geq 0. \tag{13}$$

Note that $\Gamma(\omega)$ for $\omega \in (0, \omega^*)$ is increasing; therefore, (12) is always true.

After further derivations, it could be shown that $A \geq B$ for $z = y$. The calculations are omitted here due to a large number of simple algebraic transformations. When $\min\{\Gamma(x), \Gamma(y)\} = \Gamma(y)$, $z = y$, (13) takes the form of

$$10^A + \frac{10^A}{y^2} - 10^B - \frac{10^B}{\big(\lambda_C x+[1-\lambda_C]y\big)^2} \geq 0. \tag{14}$$

Finally, it is easy to see that $(10^A - 10^B) \geq 0$ and $\big(\frac{10^A}{y^2} - \frac{10^B}{(\lambda_C x+[1-\lambda_C]y)^2}\big) \leq (10^A - 10^B)$ in (14). Therefore, (12) holds for $z = y$ as well.

Therefore, $\omega^*$ is a maximum point of $\Gamma$, [24].

## ACKNOWLEDGMENTS

This work was funded in part by the Academy of Finland (project PRISMA) and supported in part by Huawei Canada Co., Ltd. The work of M. Gapeyenko was supported by the Nokia Foundation.

## REFERENCES

[1] 3GPP, "Study on scenarios and requirements for next generation access technologies (Release 14)," 3GPP TR 38.913 V14.3.0, August 2017.

[2] I. Bor-Yaliniz and H. Yanikomeroglu, "The new frontier in RAN heterogeneity: Multi-tier drone-cells," *IEEE Communications Magazine Special Issue on 5G Radio Access Network Architecture and Technologies*, vol. 54, no. 11, pp. 48–55, November 2016.

[3] Z. Xiao, P. Xia, and X. Xia, "Enabling UAV cellular with millimeter-wave communication: potentials and approaches," *IEEE Communications Magazine*, vol. 54, no. 5, pp. 66 – 73, May 2016.

[4] METIS, "Updated scenarios, requirements and KPIs for 5G mobile and wireless system with recommendations for future investigations," Deliverable D1.5, April 2015.

[5] I. Bekmezci, O. K. Sahingoz, and S. Temel, "Flying ad hoc networks (FANETs): A survey," *Ad Hoc Networks*, vol. 11, no. 3, pp. 1254–1270, May 2013.

[6] S. Chandrasekharan, K. Gomez, A. Al-Hourani, S. Kandeepan, T. Rasheed, L. Goratti, L. Reynaud, D. Grace, I. Bucaille, T. Wirth, and S. Allsopp, "Designing and implementing future aerial communication networks," *IEEE Communications Magazine*, vol. 54, no. 5, pp. 26–34, May 2016.

[7] D. Solomitckii, M. Gapeyenko, V. Semkin, S. Andreev, and Y. Koucheryavy, "Technologies for efficient amateur drone detection in 5G millimeter-wave cellular infrastructure," *IEEE Communications Magazine*, vol. 56, no. 1, pp. 43–50, January 2018.

[8] E. Kalantari, M. Z. Shakir, H. Yanikomeroglu, and A. Yongacoglu, "Backhaul-aware robust 3D drone placement in 5G+ wireless networks," in *IEEE International Conference on Communications Workshops (ICC Wkshps)*, May 2017.

[9] I. Bor-Yaliniz, A. El-Keyi, and H. Yanikomeroglu, "Efficient 3-D placement of an aerial base station in next generation cellular networks," in *2016 IEEE International Conference on Communications*, May 2016.

[10] M. Mozaffari, W. Saad, M. Bennis, and M. Debbah, "Drone small cells in the clouds: Design, deployment and performance analysis," in *IEEE Global Communications Conference (GLOBECOM)*, December 2015.

[11] ——, "Efficient deployment of multiple unmanned aerial vehicles for optimal wireless coverage," *IEEE Communications Letters*, vol. 20, no. 8, pp. 1647–1650, August 2016.

[12] J. G. Andrews, S. Buzzi, C. Wan, S. V. Hanly, A. Lozano, A. C. K. Soong, and J. C. Zhang, "What will 5G be?" *IEEE Journal on Selected Areas in Communications*, vol. 32, no. 6, pp. 1065–1082, June 2014.

[13] M. Abouelseoud and G. Charlton, "The effect of human blockage on the performance of millimeter-wave access link for outdoor coverage," in *IEEE 77th Vehicular Technology Conference*, June 2013.

[14] M. Gapeyenko, A. Samuylov, M. Gerasimenko, D. Moltchanov, S. Singh, M. R. Akdeniz, E. Aryafar, N. Himayat, S. Andreev, and Y. Koucheryavy, "On the temporal effects of mobile blockers in urban millimeter-wave cellular scenarios," *IEEE Transactions on Vehicular Technology*, vol. 66, no. 11, pp. 10 124–10 138, November 2017.

[15] S. Sun, T. Rappaport, T. A. Thomas, A. Ghosh, H. C. Nguyen, I. Z. Kovacs, I. Rodriguez, O. Koymen, and A. Partyka, "Investigation of prediction accuracy, sensitivity, and parameter stability of large-scale propagation path loss models for 5G wireless communications," *IEEE Transactions on Vehicular Technology*, vol. 65, no. 5, pp. 2843–2860, May 2016.

[16] 3GPP, "Study on channel model for frequencies from 0.5 to 100 GHz (Release 14)," 3GPP TR 38.901 V14.3.0, January 2018.

[17] A. Al-Hourani, S. Kandeepan, and S. Lardner, "Optimal LAP altitude for maximum coverage," *IEEE Wireless Communications Letters*, vol. 3, no. 6, pp. 569–572, December 2014.

[18] M. R. Akdeniz, Y. Liu, M. K. Samimi, S. Sun, S. Rangan, T. S. Rappaport, and E. Erkip, "Millimeter wave channel modeling and cellular capacity evaluation," *IEEE Journal on Selected Areas in Communications*, vol. 32, no. 6, pp. 1164–1179, June 2014.

[19] S. Hur, T. Kim, D. J. Love, J. V. Krogmeier, T. A. Thomas, and A. Ghosh, "Millimeter wave beamforming for wireless backhaul and access in small cell networks," *IEEE Transactions on Communications*, vol. 61, no. 10, pp. 4391–4403, October 2013.

[20] M. Gapeyenko, A. Samuylov, M. Gerasimenko, D. Moltchanov, S. Singh, E. Aryafar, S. Yeh, N. Himayat, S. Andreev, and Y. Koucheryavy, "Analysis of human body blockage in urban millimeter-wave wireless communications systems," in *2016 IEEE International Conference on Communications*, May 2016.

[21] Y. Zeng, R. Zhang, and T. J. Lim, "Wireless communications with unmanned aerial vehicles: opportunities and challenges," *IEEE Communications Magazine*, vol. 54, no. 5, pp. 36–42, May 2016.

[22] J. G. Andrews, T. Bai, M. Kulkarni, A. Alkhateeb, A. Gupta, and R. W. Heath Jr., "Modeling and analyzing millimeter wave cellular systems," *IEEE Transactions on Communications*, vol. 65, no. 1, pp. 403–430, January 2016.

[23] "MOSEK ApS optimization software," *https://www.mosek.com/*.

[24] R. Webster, *Convexity*. Oxford University Press, 1994.

# PUBLICATION VIII

**Flexible and Reliable UAV-Assisted Backhaul Operation in 5G mmWave Cellular Networks**

M. Gapeyenko, V. Petrov, D. Moltchanov, S. Andreev, N. Himayat and Y. Koucheryavy

*IEEE Journal on Selected Areas in Communications* 36.11 (2018), 2486–2496

# Flexible and Reliable UAV-Assisted Backhaul Operation in 5G mmWave Cellular Networks

Margarita Gapeyenko, Vitaly Petrov, Dmitri Moltchanov,
Sergey Andreev, Nageen Himayat, and Yevgeni Koucheryavy

***Abstract*—To satisfy the stringent capacity and scalability requirements in the fifth generation (5G) mobile networks, both *wireless access and backhaul links* are envisioned to exploit millimeter wave (mmWave) spectrum. Here, similar to the design of access links, mmWave backhaul connections must also address many challenges such as multipath propagation and dynamic link blockage, which calls for advanced solutions to improve their reliability. To address these challenges, 3GPP New Radio (NR) technology is considering a *flexible* and *reconfigurable* backhaul architecture, which includes dynamic link rerouting to alternative paths. In this paper, we investigate the use of aerial relay nodes carried by e.g., *unmanned aerial vehicles* (UAVs) to allow for such dynamic routing, while mitigating the impact of occlusions on the terrestrial links. This novel concept requires an understanding of mmWave backhaul dynamics that accounts for: (i) realistic 3D multipath mmWave propagation; (ii) dynamic blockage of mmWave backhaul links; and (iii) heterogeneous mobility of blockers and UAV-based assisting relays. We contribute the required mathematical framework that captures these phenomena to analyze the mmWave backhaul operation in characteristic urban environments. We also utilize this framework for a new assessment of mmWave backhaul performance by studying its spatial and temporal characteristics. We finally quantify the benefits of utilizing UAV assistance for more reliable mmWave backhaul. The numerical results are confirmed with 3GPP-calibrated simulations, while the framework itself can aid in the design of robust UAV-assisted backhaul infrastructures in future 5G mmWave cellular.**

***Index Terms*—5G New Radio; millimeter wave; multipath 3D channel model; UAV communications; integrated access and backhaul; dynamic human body blockage; moving cells.**

## I. Introduction

Over the past years, the work on fifth-generation (5G) networks has achieved impressive results [1], [2]. 3GPP has recently ratified non-standalone 5G New Radio (NR) technology to augment further LTE evolution. Currently, the standardization has completed the standalone 5G NR specifications to allow for independent NR-based deployments [3]. Catering for high-rate and reliable wireless connectivity, the 5G cellular paradigm aims to densify the network with terrestrial base stations [4] by additionally employing moving (e.g., car-mounted) small cells for on-demand capacity boost as well as harnessing more abundant millimeter-wave (mmWave) spectrum for both access and backhaul radio links [5], [6].

Manuscript received April 16, 2018; revised September 15, 2018; accepted September 28, 2018. This work was supported by Intel Corporation, and the Academy of Finland (projects WiFiUS and PRISMA). The work of M. Gapeyenko was supported by Nokia Foundation. V. Petrov acknowledges the support of HPY Research Foundation funded by Elisa. *(Corresponding author: Margarita Gapeyenko.)*

M. Gapeyenko, V. Petrov, D. Moltchanov, S. Andreev, and Y. Koucheryavy are with Tampere University of Technology, Tampere, Finland (e-mail: {firstname.lastname, evgeni.kucheryavy}@tut.fi).

N. Himayat is with Intel Corporation, Santa Clara, CA, USA (e-mail: nageen.himayat@intel.com).

Despite the notable benefits of the mmWave band, it also poses new challenges due to highly directional mmWave links subject to complex multipath propagation, which is susceptible to link blockage phenomena because of a wide range of obstacles [7]–[9]. There has been a surge in research work on reliability analysis of mmWave access to outline techniques for mitigating the inherent limitations of mmWave-based communication [10]–[14].

As that work matures, provisioning of high-rate backhaul capabilities for 5G has attracted recent attention, as mmWave backhaul links remain vulnerable to similar blockage issues [15]. Aiming to assess and improve reliability of mmWave backhaul operation in 5G NR systems, 3GPP has initiated a new study on integrated access and backhaul, which specifies the respective challenges and requirements. The panned specifications target to construct a flexible and reconfigurable system architecture with dynamic backhaul connections. In this context, the capability to reroute backhaul links in case of their blockage by moving humans and car bodies becomes essential [16]. Extending the 3GPP studies on the matter, the utilization of unmanned aerial vehicles (UAVs) equipped with radio capabilities and acting as mobile relay nodes may be considered to further improve flexibility and reliability of backhaul operation.

The recent acceleration in user traffic fluctuations calls for more flexible and reliable backhaul solutions in 5G mmWave cellular, which may require dynamic rerouting. Therefore, the integration of both terrestrial and aerial network components to achieve this goal is essential. The corresponding performance assessment requires an appropriate evaluation methodology that may capture the dynamics of backhaul links, mmWave radio propagation properties, and blockage phenomena caused by moving objects. Different from mmWave access, the research literature on 5G mmWave backhaul is scarce. In [17], the authors propose an analytical model for coexistence of access and backhaul links, while in [18] the capacity evaluation of cellular networks with in-band wireless backhaul was proposed. In [19], a performance evaluation of mmWave backhaul links is conducted.

To the best of our knowledge, an integrated methodology for flexible mmWave backhaul operation with dynamic links that reroute subject to the channel conditions has not been available as of yet. Addressing that gap, this work offers a new methodology that can assess complex scenarios with multiple terrestrial and aerial base stations. These are equipped with mmWave backhaul capabilities and can reroute their links to maintain uninterrupted connectivity over unreliable blockage-prone channels, while leveraging UAV-based relay assistance as illustrated in Fig. 1.

Our considered scenario captures three important compo-

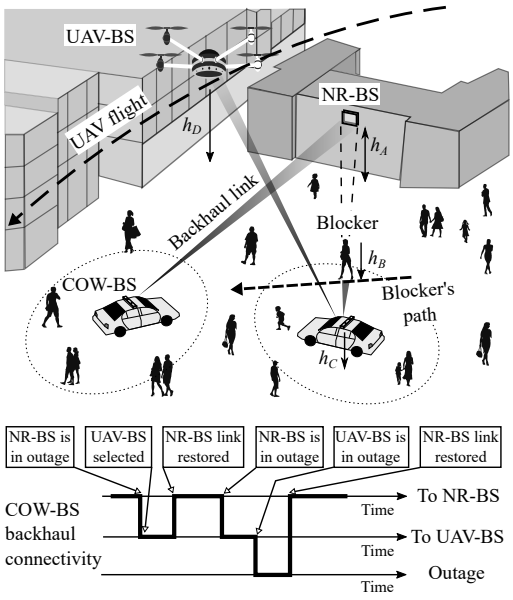


Fig. 1. Scenario of interest with UAV-BS assistance.

nents of future 5G mmWave backhaul solutions: (i) dynamic blockage of mmWave links; (ii) complex multipath propagation in urban environments; and (iii) flexible mobility of assisting UAV relays. A range of simpler scenarios can also be assessed by applying the relevant components of our developed framework with opportunistic UAV mobility model (e.g., those with static deployment of UAV-based relays [20]–[22]). The contributions of this work are therefore as follows.

- A novel mathematical framework that captures the essential features of mmWave backhaul operation under dynamic blockage by moving humans as well as possible link rerouting to UAV-based relay nodes in realistic scenarios under 3D multipath propagation. This analytical framework is further verified with detailed system-level simulations (SLS) that explicitly model the 3GPP 3D multipath propagation channel.
- A performance assessment of flexible mmWave backhaul operation in crowded urban deployments that includes both time-averaged and time-dependent metrics of interest, such as outage probability and spectral efficiency together with outage and non-outage duration distributions. A highlight of our methodology is characterization of uninterrupted connectivity duration, which accounts for tolerable outage time subject to application-specific requirements.
- An understanding of benefits made available with UAV relay assistance to mmWave backhaul reliability in realistic city scenarios. We demonstrate that under certain speed, intensity, and service capacity, the use of UAV-based relays enables significant gains for the system performance. In particular, outage probability and outage duration in the considered scenario become notably reduced, while spectral efficiency increases substantially.

The rest of this text is organized as follows. In Section II, our system model of the target urban scenario is introduced. The analytical framework for time-averaged performance evaluation of mmWave backhaul operation is outlined in Section III. Further, an analytical model to assess temporal metrics of interest in mmWave backhaul is contributed by Section IV. The corresponding numerical results that explore the spatial and temporal characteristics of flexible mmWave backhaul by leveraging assistance of UAV relay nodes are offered in Section V. Conclusions are drawn in the last section.

## II. System Model

### A. Network deployment and COW-BSs

We consider a circular area with the radius of $R$, where several *"Cell on Wheels"* base stations (COW-BSs) are distributed uniformly according to a Poisson Point Process (PPP) with the density of $\lambda_C$. These COW-BSs provide connectivity to the human users in their vicinity and are equipped with mmWave backhaul links to the terrestrial New Radio base stations (NR-BSs) as well as aerial UAV-carried base stations (UAV-BSs) as illustrated in Fig. 2. In the scenarios where over-provisioning leads to increased operator expenses (e.g., temporary and unexpected events), on-demand network densification with COW-BSs might become a viable option. The height of a COW-BS is $h_C$. A terrestrial NR-BS is located at the circumference of the circle area at the height of $h_A$. Since the height of a consumer vehicle is generally lower than that of a pedestrian, the latter may act as a potential blocker to the mmWave signal [23]. We assume that walking pedestrians form a PPP with the density of $\lambda_B$ and the height of $h_B$, where $h_A > h_B > h_C$.

The human blockers in our scenario are *dynamic* and their travel patterns are assumed to follow the Random Direction Mobility (RDM) model. The angle of movement in this formulation is chosen uniformly within $[0, 2\pi)$, while the time of travel until the subsequent turn is distributed exponentially. The UAV-BSs may fly through the center of the circle by entering and leaving it at random points that are distributed uniformly across its circumference [24]. This work considers

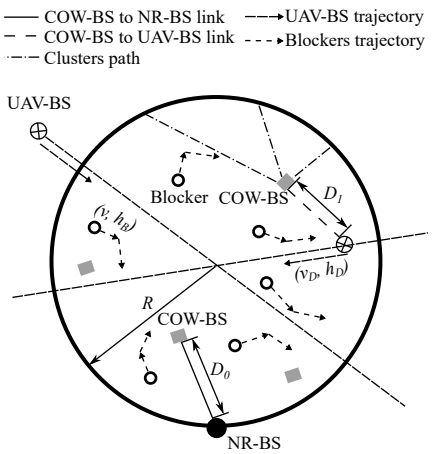


Fig. 2. Geometrical 2D illustration of target setup.

mobility of the UAV-BS as it becomes a distinguishing feature for this new type of BSs. In [25], the authors demonstrate the benefits of dynamic over static UAV deployments. Therefore, mobility modeling is important to assess system-level performance in the scenarios where several types of BSs may coexist. The speed of the UAV-BSs is $v_D$ and their altitude is $h_D$. The process of entering the circle by the UAV-BSs is assumed to be Poisson in time with the intensity of $\lambda_D$. The remaining important notation is summarized in Table I.

### B. 3D channel model and dynamic blockage of backhaul links

In order to model the mmWave backhaul links, we employ the current 3GPP 3D multipath channel model [11] by taking into account all of the key features of mmWave communication. The model assumes that there are multiple alternative paths (named *clusters*) between the Tx and the Rx (see Fig. 3), each featured by its own delay, pathloss, and zenith of arrival/departure angles. Each of these paths can be blocked or non-blocked by the moving human blockers using the analytical model from [8].

The COW-BSs utilize beamsteering mechanisms to always use the *best* path, which is currently non-blocked and has the strongest signal. Beamsteering employed at all the communicating nodes also minimizes the level of interference between the backhaul links, thus making the considered mmWave regime noise-limited [26]. Signal blockage by buildings is not modeled, as none occlude the backhaul links between the COW-BSs and the NR-BSs/UAV-BSs in the target scenario.

While the employed 3GPP model is sufficiently detailed and accurate [27], the complexity of the used algorithms [11] challenges its analytical tractability. Therefore, in our mathematical study, we utilize a statistical approximation of the key modeling parameters [28], such as power of every cluster transmitted by the NR-BS and the UAV-BS, $P_{A,i}$ and $P_{D,i}$, and zenith angle of arrival (ZOA) for every cluster, $\theta_{A,i}$ and $\theta_{D,i}$, where $i = 1, 2, \ldots, N$ is the cluster number.

### C. mmWave backhaul connectivity model

The radio channel conditions of the backhaul links are dynamic in nature due to temporal variations of the propagation environment. These are captured by the utilized propagation model [28], while the mobility of human blockers surrounding the COW-BSs is modeled explicitly in our work. The NR-BS is assumed as the primary option for the backhaul links of COW-BSs (see Fig. 1). When COW-BS is currently in outage

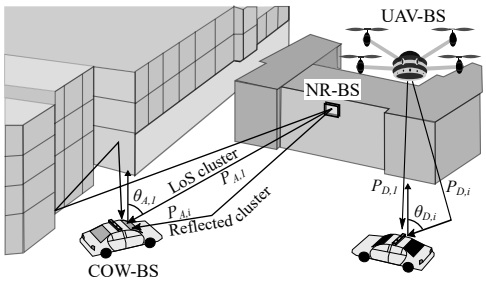


Fig. 3. 3GPP-driven 3D multipath channel model.

TABLE I
SUMMARY OF NOTATION AND PARAMETERS

| Notation | Description |
|---|---|
| *Deployment* | |
| $h_A$, $h_C$, $h_D$ | Heights of NR-BS, COW-BS, UAV-BS |
| $\lambda_C$, $\lambda_B$ | Density of COW-BSs and blockers per unit area |
| $r_B$, $v$, $h_B$ | Radius, speed, and height of a blocker |
| $R$ | Radius of the service area |
| $\lambda_D$ | Temporal intensity of UAV-BSs entering the service area |
| $T_D$, $v_D$ | Time and speed of UAV-BSs traversing the service area |
| $K_D$ | UAV-BS service capacity |
| *Technology* | |
| $N$ | Number of 3D multipath propagation clusters |
| $\theta_{A,i}$ and $\theta_{D,i}$ | ZOA of $i$-th cluster from NR-BS and UAV-BS |
| $f_{\theta_{A,i}}$ and $f_{\theta_{D,i}}$ | Pdf of ZOA of $i$-th cluster from NR-BS and UAV-BS |
| $C$ and $E[C]$ | Spectral efficiency and its mean value |
| $p_O$ | Outage probability |
| $\Delta_O$ | Tolerable outage duration |
| $T_U$ and $E[T_U]$ | Uninterrupted connectivity time and its mean value |
| *Mathematical framework* | |
| $p_{D,av}$ | Probability of UAV-BS availability |
| $P_A$ and $P_D$ | Received power at NR-BS to COW-BS and UAV-BS to COW-BS links |
| $f_{P_A}$ and $f_{P_D}$ | Pdf of received power at NR-BS to COW-BS and UAV-BS to COW-BS links |
| $f_{P_{A,i}}$ and $f_{P_{D,i}}$ | Pdf of power of $i$-th cluster arriving from NR-BS and UAV-BS |
| $u_n$ | Pmf of number of UAV-BSs available for COW-BS |
| $p_{A,i}$ and $p_{D,i}$ | Blockage probability of $i$-th cluster arriving from NR-BS and UAV-BS |
| $\lambda_{B,T}$ | Temporal intensity of blockers crossing the blockage zone |
| $T_B$ and $L_B$ | Time and distance walked inside the blockage zone by a single blocker |
| $f_\eta$, $f_\omega$ | Pdf of blocked and unblocked intervals |
| $f_O$ and $f_G$ | Pdf of outage and non-outage duration |

with respect to NR-BS (i.e., the signal received from NR-BS is too weak), COW-BS may temporarily reroute its backhaul traffic to UAV-BS traversing the area. Once the radio link to NR-BS recovers, COW-BS reconnects to the terrestrial NR-BS and reroutes its backhaul traffic back to it. Hence, the UAV-BSs are employed in unfavorable conditions to improve the continuity of backhaul links.

We measure the capacity of UAV-BS in terms of the maximum number of simultaneously supported backhaul links, which we denote as $K_D$. This consideration reflects the potential limitations of the mmWave radio equipment carried by the UAV-BS as well as the specifics of the employed network architecture and connectivity protocols. In its turn, the connection between the UAV-BS and the core network is inherently characterized by unobstructed line-of-sight propagation without obstacles [29]. Therefore, this link is modeled as always reliable.

### D. Illustrative metrics of interest

To assess the performance quality of the mmWave backhaul links in the described scenario, we concentrate on two types of metrics, namely, time-averaged and time-dependent. In the former case, we address (i) outage probability, $p_O$, and (ii) spectral efficiency, $C$. In the latter, we assume that the system may tolerate a certain fixed outage duration $\Delta_O$ and thus derive (iii) the mean uninterrupted connectivity time, $E[T_U]$. As intermediate parameters, we also obtain (iv) the outage and non-outage duration distributions, $f_O$ and $f_G$, respectively.

## III. Time Averaged Analysis

In this section, we address the time-averaged system metrics, including outage probability and spectral efficiency.

### A. Outage Probability

The outage probability $p_O$ for a randomly chosen COW-BS in the area of interest is obtained as follows. Observe that the COW-BS is always associated with the NR-BS when the latter is in non-outage conditions. Otherwise, the COW-BS is connected to a randomly chosen UAV-BS that is available, provided that there is at least one UAV-BS in non-outage conditions having fewer than $K_D$ COW-BSs connected to it. Hence, the outage probability is produced as

$$p_O = p_{A,O}(u_0 + (1-u_0)(u_{0,n} + (1-u_{0,n})p_{D,nav})), \quad (1)$$

where $u_0$ is the probability of having no UAV-BS traversing the area at the moment, $u_{0,n}$ is the probability of having no UAV-BS in non-outage conditions, $p_{A,O}$ and $p_{D,nav}$ are the outage probability on the COW-BS to NR-BS link and the probability that the UAV-BS is currently unavailable, respectively. In what follows, we derive these unknown terms.

*1) Outage probability on COW-BS to NR-BS and COW-BS to UAV-BS links:* Consider a randomly chosen COW-BS. Let $p_{A,i}$ be the probability that $i$-th cluster between the NR-BS and the COW-BS is blocked and first consider blockage of the LoS path, $p_{A,1}$. Fixing the distance $x$ between NR-BS and COW-BS, we observe that there is always a so-called *blockage zone* as shown in Fig. 4. At any given instant of time $t$, the number of blockers moving according to the RDM model within the service zone follows a Poisson distribution [30]. Hence, the probability that the LoS path is blocked is given by

$$p_{A,1}(x) = 1 - e^{\left(-2\lambda_B r_B \left[x\frac{h_B - h_C}{h_A - h_C} + r_B\right]\right)}. \quad (2)$$

Let $D_0$ be a random variable (RV) denoting the 2D distance between the NR-BS and a randomly chosen COW-BS, and let $f_{D_0}(x)$ be its probability density function (pdf). Noticing that the COW-BSs are uniformly distributed within a service area circle, the sought distance is [31]

$$f_{D_0}(x) = \frac{2x}{\pi R^2}\cos^{-1}\left(\frac{x}{2R}\right), 0 < x < 2R. \quad (3)$$

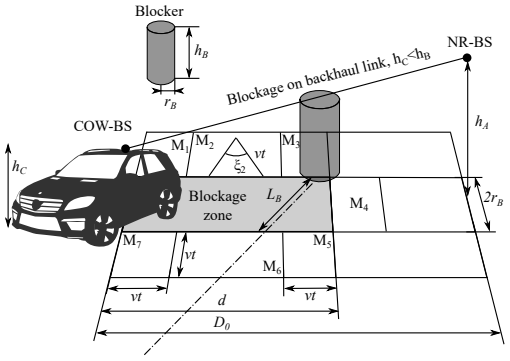


Fig. 4. Illustration of dynamic blockage process.

The LoS path blockage probability is then

$$p_{A,1} = \int_0^{2R} f_{D_0}(x)p_{A,1}(x)dx. \quad (4)$$

Consider now the blockage probability for $i$-th cluster, $i = 2, 3, \ldots, N$. As opposed to the LoS path, the 3GPP model does not explicitly specify where the reflected cluster comes from. Instead, it provides the ZOA, $\theta_{A,i}$ and $\theta_{D,i}$, $i = 2, 3, \ldots, N$. In [28], it was shown that the ZOA for all clusters follows a Laplace distribution and we denote it as the pdf $f_{\theta_{A,i}}(y; x)$.

The blockage probability $p_{A,i}(x)$ of every cluster is then

$$p_{A,i} = \int_{-\pi}^{\pi}\int_0^{2R} f_{\theta_{A,i}}(y; x)p_{A,i}(y)dxdy, \quad (5)$$

where $p_{A,i}(y)$ is the blockage probability as a function of the ZOA, derived as

$$p_{A,i}(y) = 1 - e^{[-2\lambda_B r_B(\tan y(h_B - h_C) + r_B)]}. \quad (6)$$

Substituting (6) and pdf of ZOA from [28], we obtain

$$p_{A,i} = \int_{-\pi}^{\pi}\int_0^{2R} \frac{1 - e^{-2\lambda_B r_B(\tan y(h_B - h_C) + r_B)}}{2b_z e^{\frac{y - a_z(x)}{b_z}}}dxdy, \quad (7)$$

where $a_z(x) = \frac{\pi}{2} - \arctan\left(\frac{h_A - h_C}{x}\right)$ and $b_z$, $z = 2, 3, \ldots, N$, are the parameters estimated from the statistical data (see [28] for details) and $b_z$ is given as

$$b_1 = 0, b_2 = 0.3146, b_3 = 0.3529, b_4 = 0.4056, b_5 = 0.4897. \quad (8)$$

After characterizing the blockage probabilities of individual clusters on the COW-BS to NR-BS link, we derive an expression for the received power. As shown in [28], the fraction of power of $i$-th cluster between the NR-BS and the COW-BS separated by the distance of $x$ follows a Log-normal distribution with the pdf $f_{P_{A,i}}(y; x)$.

Once the fraction of power distributions is obtained, the received power from every cluster is calculated as

$$P_{A,z} = P_{s,z}10^{(P_T - 30 - L)/10}, z = 1, 2, \ldots, \quad (9)$$

where $P_T$ is the transmit power in $dBm$ and $L$ is the path loss in $dB$. Then, $P_{A,z}$ is given as

$$P_{A,z} = P_{s,z}10^{(A_p - 21.0\log_{10}(D_{3,0}))/10}, \quad (10)$$

where $A_p = P_T - 30 - 32.4 - 20\log_{10} f_c$.

As one may observe, $P_{A,z}$ is a function of two RVs, $P_{s,z}$ and $D_{3,0}$, and $f_{D_{3,0}}(x)$ is the pdf of the 3D distance between the NR-BS and the COW-BS in the form

$$f_{D_{3,0}} = \frac{2x}{\pi R^2}\cos^{-1}\left(\frac{\sqrt{x^2 - (h_A - h_C)^2}}{2R}\right), \quad (11)$$

where $x \in (h_A - h_C, \sqrt{4R^2 + (h_A - h_C)^2})$.

Since $D_{3,0}$ and $P_{s,z}$ are independent, their joint pdf is

$$f_{P_{s,z},D_{3,0}}(x_1, x_2) = \frac{1}{x_1 d_z\sqrt{2\pi}}e^{\left(-\frac{(\ln x_1 - c_z)^2}{2d_z^2}\right)} \times \frac{2x_2}{\pi R^2}\cos^{-1}\left(\frac{\sqrt{x_2^2 - (h_A - h_C)^2}}{2R}\right), \quad (12)$$

where $c_z$ and $d_z$, $z = 2, 3, \ldots$, are the parameters derived from the statistical data (see [28] for details) and given as

$$c_1 = -2.88,\ c_2 = -3.55,\ c_3 = -4.1,\ c_4 = -4.98,\ c_5 = -6.2,$$
$$d_1 = 1.2,\ d_2 = 1.1,\ d_3 = 1.3,\ d_4 = 1.8,\ d_5 = 2.51. \quad (13)$$

Finally, the pdf of $P_{A,z}$ is

$$f_{P_{A,z}}(y) = \int_{x_{2,\min}}^{x_{2,\max}} f_{P_{s,z},D_{3,0}}\left(\frac{y}{10^{(A_p - 21.0\log_{10}(x_2))/10}}, x_2\right) \times \frac{1}{10^{(A_p - 21.0\log_{10}(x_2))/10}} dx_2, \quad (14)$$

where $x_{2,\min} = h_A - h_C$ and $x_{2,\max} = \sqrt{4R^2 + (h_A - h_C)^2}$.

Assuming mutual independence in the cluster blockage, the pdf of the received power is produced as

$$f_{P_A}(y) = \sum_{k=1}^{N} \left[ (1 - p_{A,k}) \prod_{j=1}^{k-1} p_{A,j} \right] f_{P_{A,k}}(y), \quad (15)$$

where the weights are the probabilities of choosing cluster $i$.

Finally, the outage probability with the NR-BS is

$$p_{A,O} = Pr\{P_A(y) \le N_0 T_S\} = \int_0^{N_0 T_S} f_{P_A}(y) dy, \quad (16)$$

where $N_0$ is the Johnson-Nyquist noise at the receiver and $T_S$ is the SNR threshold. Note that due to the complex structure of the conditional received power $f_{P_A}(y)$, the outage probability $p_{A,O}$ can only be produced with numerical integration.

The LoS path and $i$-th cluster blockage probability on a link between the UAV-BS and the COW-BS are obtained similarly except for the 2D distance between UAV-BS and COW-BS, $D_1$, with the pdf given as

$$f_{D_1}(x) = \frac{4x}{\pi R^2} \left[ \cos^{-1}\left(\frac{x}{2R}\right) - \frac{x}{2R}\sqrt{1 - \frac{x^2}{4R^2}} \right], \quad (17)$$

where $x \in (0, 2R)$. Using this result, the corresponding 3D distance between the UAV-BS and the COW-BS constitutes

$$f_{D_{3,1}} = \frac{4x}{\pi R^2} \left[ \cos^{-1}\left( \frac{\sqrt{x^2 - (h_D - h_C)^2}}{2R} \right) - \right.$$
$$\left. - \frac{\sqrt{x^2 - (h_D - h_C)^2}}{2R} \sqrt{1 - \frac{x^2 - (h_D - h_C)^2}{4R^2}} \right], \quad (18)$$

where $x \in (h_D - h_C < x < \sqrt{4R^2 + (h_D - h_C)^2})$.

*2) Availability probability of UAV-BS:* To complete the derivation of $p_O$, we find the probability that at least one UAV-BS in non-outage conditions is available for service, $p_{D,av}$.

The time spent by each UAV-BS within the service area is constant and equals $T_D = 2Rv_D$, where $v_D$ is the speed of UAV-BS. Hence, the number of UAV-BSs that are available in the service zone is captured by the $M/G/\infty$ queuing system with a constant service time. It is known that the number of customers in $M/G/\infty$ queue coincides with the number of customers in $M/M/\infty$ queue and follows a Poisson distribution with the parameter $\lambda_D T_D$ [32][1].

[1]To ensure a certain number of UAV-BSs above the area one may directly use a mean number of UAV-BSs.

Note that the availability of UAV-BSs is not sufficient for the COW-BS to be able to associate with them. In addition, there should be at least one UAV-BS in non-outage conditions. The intensity of such UAV-BSs is $\lambda_D T_D(1 - p_{D,O})$, where $p_{D,O}$ is the probability that a randomly selected UAV-BS resides in the outage conditions. Therefore, the number of UAV-BSs that are available for the COW-BS $U$ follows a Poisson distribution with the probability mass function (pmf) of

$$u_n = \frac{[\lambda_D T_D(1 - p_{D,O})]^n}{n!} e^{-\lambda_D T_D(1 - p_{D,O})}, \quad (19)$$

where $n = 0, 1, \ldots$.

Let $W$ denote the number of COW-BSs in the outage conditions. The number of COW-BSs in the service area follows a Poisson distribution with the density of $\lambda_C$. Hence, the number of COW-BSs in the outage conditions also follows a Poisson distribution with the parameter of $\lambda_C p_{A,O} \pi R^2$. The probability that the UAV-BS remains available for service is

$$p_{D,av} = Pr\{K_D U - W > 0\} = \sum_{i=1}^{\infty} Pr\{Z = i\}, \quad (20)$$

where $Z = K_D U - W$.

Observe that $K_D U$ is a scaled Poisson RV in (21), which implies that $p_{D,av}$ can be evaluated numerically for any value of $K_D$. The pmf of $Z$ is then established as

$$Pr\{Z = z\} = \sum_{x=0}^{\infty} \frac{|K_D x - 1|}{K_D} \frac{[\lambda_C p_{A,O} \pi R^2]^{(K_D x - z)}}{(K_D x - z)!} \times$$
$$e^{\left(-\lambda_C p_{A,O} \pi R^2 - \lambda_D T_D(1 - p_{D,O})\right)} \frac{[\lambda_D T_D(1 - p_{D,O})]^{x/K_D}}{(x/K_D)!}. \quad (21)$$

### *B. Spectral efficiency*

Consider now spectral efficiency of an arbitrarily chosen COW-BS. Observe that this COW-BS spends a fraction of time, $p_A$, connected to the NR-BS and a fraction of time, $p_D$, connected to the UAV-BS. The rest of the time, $p_O$, this COW-BS resides in outage. Hence, the spectral efficiency is

$$C = p_A \log_2\left[1 + \frac{P_A}{N_0}\right] + p_D \log_2\left[1 + \frac{P_D}{N_0}\right], \quad (22)$$

where $P_A$ and $P_D$ are the received powers whenever associated with NR-BS and UAV-BS.

Observe that $p_{A,O} = 1 - p_A$ is the outage probability when only NR-BS is available. Recalling that UAV-BS are only employed when the NR-BS to COW-BS link experiences outage conditions, the fraction of time that the COW-BS is associated with the UAV-BS is $p_D = p_{A,O} p_{D,av}$. Therefore, the mean spectral efficiency is provided by

$$E[C] = (1 - p_{A,O}) \int_0^{\infty} f_{P_A}(x) \log_2\left[1 + \frac{P_A}{N_0}\right] dx +$$
$$+ p_{A,O} p_{D,av} \int_0^{\infty} f_{P_D}(x) \log_2\left[1 + \frac{P_D}{N_0}\right] dx, \quad (23)$$

which can be evaluated numerically.

In addition to the mean value, the form of (22) enables us to determine the distribution of the spectral efficiency. Observe that the spectral efficiencies associated with the UAV-BS to

COW-BS and the NR-BS to COW-BS links are independent RVs. The resulting pdf takes the following form

$$f_C(x) = \begin{cases} \int_0^\infty \frac{(2^{f_{P_A}(y)}-1)(2^{f_{P_A}(x-y)}-1)}{(N_0^4 2^x \log^2 2)^{-1}} dy, \, x > 0, \\ p_O, \, x = 0, \end{cases} \quad (24)$$

where the convolution integral can be evaluated numerically.

## IV. Time Dependent Analysis

In this section, we continue by quantifying uninterrupted connectivity performance, including the outage and non-outage duration distributions as well as the uninterrupted connectivity duration.

### A. Dynamics of cluster blockage process

To capture the temporal dynamics of the blockage process for a single cluster, we need to track the blockers that are crossing the blockage zone, see Fig. 4. We begin by considering the dynamics of the LoS blockage process and concentrate on the temporal properties of the process when the blockers are entering the blockage zone and occluding the LoS.

We specify the area around the blockage zone as shown in Fig. 4, where the moving blockers may cross the blockage zone by occluding the LoS between the COW-BS and the NR-BS. To specify these conditions, the area around the blockage zone is further divided into $i$, $i = 1, 2, ...7$, zones. The intensity of blockers crossing the blockage zone of the COW-BS located at the distance of $x$ from the NR-BS is approximated as

$$\lambda_{B,T}(z) = \sum_{i=1}^{7} \iint_{M_i} \frac{g_i(x,y) Pr\{A_B\} Pr\{T_B > t\}}{(\lambda_B M_i)^{-1}} dx dy, \quad (25)$$

where the event $A_B$ is when a blocker moves towards the blockage zone (see Fig. 4), $M_i$ is the area of zone $i$, $g_i(x, y)$ is the pdf of the blocker locations in zone $i$. Here, $g_i(x, y) = 1/M_i$ as the blockers move according to the RDM model and at every instant of time their coordinates are distributed uniformly within the area [30], while $Pr\{T_B > t\} = e^{-1/E[\tau]}$ is the probability that such movement is longer than $t$ seconds.

Observe that the probability for a blocker to move towards CDEF is $Pr\{A_B\} = \xi_i(x, y)/2\pi$, where $\xi_i(x, y)$ is a range of movement angles within zone $i$ that lead to crossing the blockage zone. We thus simplify (25) as

$$\lambda_{B,T}(z) = \frac{\lambda_B e^{-1/E[\tau]}}{2\pi} \sum_{i=1}^{7} \iint_{M_i} \xi_i(x, y) \, dx \, dy, \quad (26)$$

where $\xi_i(x, y)$ are calculated as

$$\xi_1(x,y) = \xi_3(x,y) = \xi_5(x,y) = \xi_7(x,y) = \cos^{-1}\Big(\frac{x}{vt}\Big) + \tan^{-1}\Big(\frac{y}{x}\Big),$$
$$\xi_2(x,y) = \xi_6(x,y) = 2\cos^{-1}(x/vt),$$
$$\xi_4(x,y) = 2\tan^{-1}(x/y), \quad (27)$$

and $M_1 = M_3 = M_5 = M_7$ with $x$-coordinate within the range of $(0, vt)$ and $y$-coordinate within the range of $(0, vt/2)$, $M_2 = M_6$ with $x$-coordinate within the range of $(0, vt)$ and $y$-coordinate within the range of $(0, d - 2vt)$, $M_4$ with $x$-coordinate within the range of $(0, 2r_B)$ and $y$-coordinate within the range of $(0, vt)$, where $2r_B < vt$.

It has been shown in [33] that the process of meetings between a stationary node and a node moving inside a bounded area according to the RDM is approximately Poisson. We build on this result to approximate the nature of the process of blockers meeting the blockage zone. Due to the properties of the RDM model, the entry point is distributed uniformly over the three sides of the blockage zone [30].

Let $\eta$ and $\omega$ be the RVs denoting the blocked and non-blocked periods, respectively. Since blockers enter the zone in question according to a Poisson process with the intensity of $\lambda_{B,T}(x)$, the time spent in the unblocked part, $\omega$, follows an exponential distribution with the parameter of $\lambda_{B,T}(x)$, $F_\omega(t; x) = 1 - e^{-\lambda_{B,T}(x)t}$, as demonstrated in [8]. The pdf of $\eta$, $f_\eta(t; x)$, is the same as the distribution of the busy period in the $M/GI/\infty$ queuing system [34] given by (28), where $F_{T_B}$ is the CDF of time that one blocker spends in the blockage zone, which is provided in [8].

The pdfs of the blocked and non-blocked intervals, $f_\eta(t; x)$ and $f_\omega(t; x)$, are conditioned on the distance between COW-BS and NR-BS. Deconditioning with (3), we obtain the pdfs of the blocked and non-blocked intervals when associated with the NR-BS as

$$f_\eta(t) = \int_0^{2R} f_\eta(t; x) f_{D_0}(x; R) dx,$$
$$f_\omega(t) = \int_0^{2R} f_\omega(t; x) f_{D_0}(x; R) dx, \quad (29)$$

which can be calculated numerically.

To capture the dynamics of the cluster blockage process, we can represent it by using a continuous-time Markov chain (CTMC) process with two states, which is defined by the infinitesimal generator in the following form

$$\Lambda_{1,A} = \begin{bmatrix} -\alpha_{1,A} & \alpha_{1,A} \\ \beta_{1,A} & -\beta_{1,A} \end{bmatrix}, \quad (30)$$

where the subscript $(1, A)$ shows that the model is built for the LoS cluster of the NR-BS to COW-BS link, while $\alpha_{1,A} = 1/E[\eta]$ and $\beta_{1,A} = 1/E[\omega]$ are the means of blocked and non-blocked intervals of the LoS cluster given in (29).

The process of blockage for other clusters on the NR-BS to COW-BS link is analyzed similarly. The key difference is that the blockage zone is specified by the ZOA instead of the heights of NR-BS and COW-BS as well as the distance between them. Let us denote the generators of all clusters associated with the NR-BS to COW-BS link by $\Lambda_{i,A}$, $i = 1, 2, \ldots, N$. Assuming independence between the cluster blockage processes, the associated CTMC model, $\{S_A(t), t > 0\}$, $S_A(t) \in \{1, 2, \ldots, 2^N\}$, is a superposition of the individual blockage processes. The infinitesimal generator of $\{S_A(t), t > 0\}$ is then given by the Kronecker product of $\Lambda_{i,A}$, $i = 1, 2, \ldots, N$.

The blockage dynamics of the UAV-BS to COW-BS link is represented similarly by leading to the Markov process approximation $\{S_D(t), t > 0\}$, $S_D(t) \in \{1, 2, \ldots, 2^N\}$. Finally, the aggregate blockage model of both links is represented by a superposition of the blockage processes that characterize the NR-BS to COW-BS and the UAV-BS to COW-BS links. The resulting infinitesimal generator is $\Lambda = \Lambda_A \otimes \Lambda_D$.

$$F_\eta(x) = 1 - \left[ [1 - F_{T_B}(x)] \left[ 1 - \int_0^x (1 - F_\eta(x-z)) \exp(-\lambda_{B,T} F_{T_B}(z)) \lambda_{B,T} dz \right] + \int_0^x (1 - F_\eta(x-z)) |d e^{-\lambda_{B,T} F_{T_B}(z)}| \right]. \quad (28)$$

### B. Performance measures of interest

*1) Outage and non-outage duration distribution:* Having the CTMC representation of the outage process, we can now calculate time-dependent performance metrics of interest, including the distributions of consecutive intervals spent in outage and non-outage conditions, the corresponding distributions of residual time, as well as the distribution and the mean duration of uninterrupted connectivity.

Let RVs $G$ and $O$ denote the non-outage and outage time durations, respectively. The distribution of time spent in outage, $f_O(x)$, $x > 0$, is directly given by the sojourn time in the state where all clusters are blocked. For our model, it is always state 1. The distribution of time spent in the non-outage state can be found by modifying the CTMC to have an absorption state in outage. Then, the sought distribution is the first-passage time (FPT) to the outage state that can be established by using [35]. Particularly, let $f_G(t)$ be the pdf of the FPT from the set of non-blockage states, $\{2, 3, \ldots, 2 \times 2^N\}$, to the blockage state.

It is easy to see that the sought distribution is of the phase-type nature [36] with the representation $(\vec{\alpha}, S)$, where $\vec{\alpha}$ is the initial state distribution defined over $\{2, 3, \ldots, 2 \times 2^N\}$ and $S$ is obtained from the infinitesimal generator $\Lambda$ by excluding the first row and column. The pdf is then given by [37] as

$$f_G(t) = \vec{\alpha} e^{St} \vec{s}_0, \; t > 0, \quad (31)$$

where $\vec{s}_0 = -S\vec{1}$, $\vec{1}$ is the vector of ones with size $2^N - 1$, while $e^{St}$ is the matrix exponential defined as $e^{St} = \sum_{k=0}^{\infty} \frac{1}{k!} (St)^k$.

The initial state distribution, $\vec{\alpha}$, is determined by the normalized rates out of the outage state e.g.,

$$\alpha_i = \begin{cases} 0, & i = 1, \\ \pi_i / \sum_{j=2}^{2^N} \pi_j, & i = 2, 3, \ldots, 2^N. \end{cases} \quad (32)$$

*2) Uninterrupted connectivity time:* Consider now an application that may tolerate at most $\Delta_O$ in the outage conditions, which implies that all of the outages whose durations are less than $\Delta_O$ do not cause connectivity interruptions. The probability that a session is interrupted is

$$p_I = \int_0^{\Delta_O} x f_O(x) dx. \quad (33)$$

As one may observe, the duration of uninterrupted connectivity is produced by a geometrical distribution with the parameter $p_I$, which is scaled with the aggregate durations of non-outage and outage intervals conditioned on the event that it is smaller than $\Delta_O$. Hence, we have

$$E[T_U] = \frac{1}{p_I} (E[G] + E[O | O \le \Delta_O]), \quad (34)$$

where the means are readily given by

$$E[G] = \int_0^{\infty} x f_G(x) dx, \; E[O | O \le \Delta_O] = \int_0^{\Delta_O} x \frac{f_O(x)}{1 - p_I} dx. \quad (35)$$

## V. Numerical Results

In this section, the obtained analytical findings are illustrated, explained, and compared with the results produced with our SLS framework. Below is an illustrative example to demonstrate the capabilities of our proposed framework, which is applicable for a range of comprehensive and realistic deployment models currently under investigation.

We address a typical crowded urban deployment, where a pedestrian plaza (e.g., St. Peter's Square, Vatican City) is modeled. The area of interest is assumed to be of circular shape with the radius of 50 m. The terrestrial NR-BS is located at a side of the square on the wall of one of the buildings at the height of 10 m. Pedestrians move around the square by following their travel patterns as described in Section II with the fixed speed of 3 km/h. UAV-BSs are assumed to traverse the pedestrian plaza at the height of 20 m with the fixed speed that varies from 5 km/h to 40 km/h. The remaining modeling parameters are summarized in Table II. Our simulation parameters partially follow the guidelines in [24] with respect to the height and the speed of the UAV-BS, as well as refer to [11] for modeling the radio part.

To validate the assumptions of our developed analytical framework, we utilize an in-house SLS tool that incorporates all of the relevant procedures considered by our study. The mmWave-specific physical layer was designed by following the corresponding 3GPP guidelines; particularly, the 3GPP's 3D multipath channel model outlined in [11] was employed. This simulation tool captures the following key procedures: session arrival process, UAV-BS arrival and departure processes, UAV-BS and pedestrian mobility, and dynamic backhaul link rerouting between the UAV-BS and the NR-BS enhanced with multi-connectivity operation [38].

The tool operates in a time-driven manner with the step of 0.01 s. To match the capabilities of our analytical framework, idealistic and reliable signaling at all the connections has been assumed: if the current connection is interrupted, the COW-BS immediately attempts to reconnect via a UAV-BS and does not spend any additional resources for this migration. For the sake of better accuracy in the output results, all of the

TABLE II
Deployment and technology parameters

| Parameter | Value |
|---|---|
| *Deployment* | |
| Area radius, $R$ | 50 m |
| Height of NR-BS, $h_A$ | 10 m |
| Height of UAV-BS, $h_D$ | 20 m |
| Height of COW-BS, $h_C$ | 1.5 m |
| Height of blocker, $h_B$ | 1.7 m |
| Radius of blocker, $r_B$ | 0.2 m |
| Speed of blocker, $v$ | 1 m/s |
| *Technology* | |
| NR-BS transmit power | 35 dBm |
| UAV-BS transmit power | 23 dBm |
| Target SNR for non-outage conditions | 3 dB |
| COW-BS antenna gain | 5 dB |
| UAV-BS antenna gain | 7 dB |
| NR-BS antenna gain | 10 dB |
| Carrier frequency | 28 GHz |

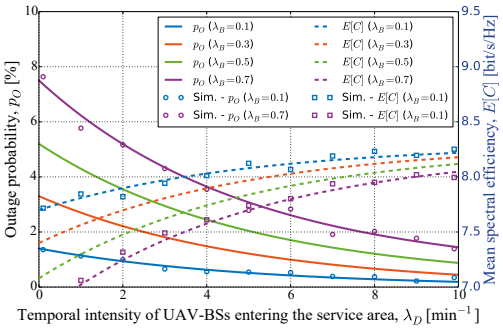


Fig. 5. Outage probability and mean spectral efficiency. Effect of crowd density and intensity of UAV-BS flights.

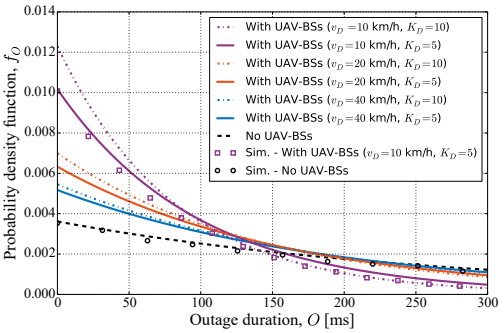


Fig. 7. Distribution of outage duration. Effect of UAV-BS speed and its capabilities.

collected intermediate data are averaged over 100 replications, each starting with a re-deployment of the layout. Each of such replications corresponds to 10 min of real-time operation. Hence, approximately 17 hours of real-time system operation have been modeled.

*1) Effect of UAV-BS flight intensity:* The UAV-BSs are assumed to move at a moderate speed of 10 km/h. The point 0 on the OX axis represents the baseline scenario with no UAV-BS assistance. Analyzing Fig. 5, we notice that both the outage probability and the spectral efficiency are improved with the growth in the intensity of UAV-BS traversals. Specifically, for $\lambda_B = 0.7$ the outage probability decreases from 7.5% for the baseline scenario to 1.5% for 10 UAV-BSs per minute. Meanwhile, the corresponding increase in the spectral efficiency is from 6.5 bit/s/Hz to 8 bit/s/Hz, which is around 25%.

Going further, we observe that the benefits of UAV-BS assistance for performance are more visible in challenging conditions (high density of humans, such as 0.7) rather than at low blocker densities (such as 0.1 or 0.3). Moreover, Fig. 5 clearly indicates that two UAV-BSs traversing the area of interest per minute with $\lambda_B = 0.7$ reduce the outage probability down to 5.3%, which is close to 5.2% observed with $\lambda_B = 0.5$ in the baseline scenario (no UAV-BSs, $\lambda_D = 0$).

We finally note that the results of our mathematical analysis match well with those obtained via the simulation tool, which confirms the accuracy of the analytical findings. A slight difference between them is due to several simplifying assumptions introduced by the mathematical framework for the sake of analytical tractability: e.g., an approximation of the 3GPP's multipath propagation model as detailed in Section III and [28].

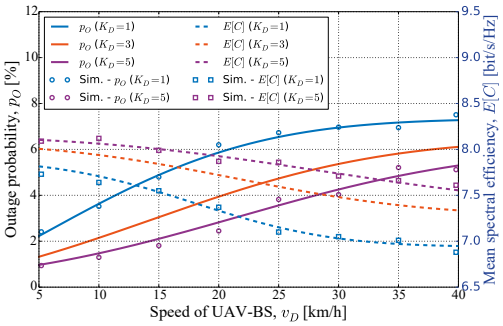


Fig. 6. Outage probability and mean spectral efficiency. Effect of UAV-BS speed and its capabilities.

*2) Effect of UAV-BS flight speed:* The intensity of UAV-BSs traversing the area, $\lambda_D$, is fixed and set to 10 UAV-BSs per min. We model a crowded scenario with $\lambda_B = 0.7$, while the maximum number of simultaneous backhaul connections per UAV-BS, $K_D$, varies from 1 to 5. We observe that a decrease in the UAV-BS speeds has a notable positive effect on performance. As an example, lowering UAV-BS speeds from 40 km/h down to 10 km/h for $K_D = 1$ results in reduced outage probability from 7.1% to 3.5%, which is over 2 times. The corresponding gain in the mean spectral efficiency, $E[C]$, is smaller but still visible: from 6.9 bit/s/Hz to 7.7 bit/s/Hz.

We continue by evaluating the effect of the UAV-BS speeds in Fig. 7, which presents the pdf of the outage duration for certain values of $v_D$ and $K_D$. The UAV-BS intensity, $\lambda_D$, is set to 10 per min, while the density of humans in the area, $\lambda_B$, equals 0.7. There is a notable decrease in the mean outage duration, $E[O]$, when UAV-BSs are utilized. Particularly, the said parameter decreases from 276 ms for the baseline deployment down to as low as 88 ms for ($v_D = 10$ km/h, $K_D = 10$) case. Finally, we notice that increasing the UAV-BS capacity, $K_D$, by two times (from 5 to 10 simultaneous connections) brings a notable decrease in the mean outage duration.

*3) Effect of service capacity of UAV-BSs, $K_D$:* To this aim, we analyze the primary backhaul session continuity related parameter – the average duration of the uninterrupted connectivity subject to a certain tolerable outage duration. In other words, a connection is assumed to be interrupted if and only if the outage duration is longer than a certain value, $\Delta_O$. We illustrate these results in Fig. 8 for two UAV-BS intensities ($\lambda_D = 1$ and 10 UAV-BSs per min).

Studying Fig. 8, we notice that for 100 ms of tolerable outage, the average duration of uninterrupted connectivity grows from 7 s for the baseline scenario to 46 s for 10 UAV-BSs per min, $K_D = 10$. We then observe that the impact of an increased UAV-BS capacity, $K_D$, is notable but weaker than that of the intensity of UAV-BS traversals: the curve for (10 UAV-BSs per min, $K_D = 1$) is much higher than the one for (1 UAV-BS per min, $K_D = 10$). This is mainly due to the fact that at least one out of 10 UAV-BSs is much more likely to reside in non-outage conditions with respect to the COW-BS than a single UAV-BS, regardless of the capacity.

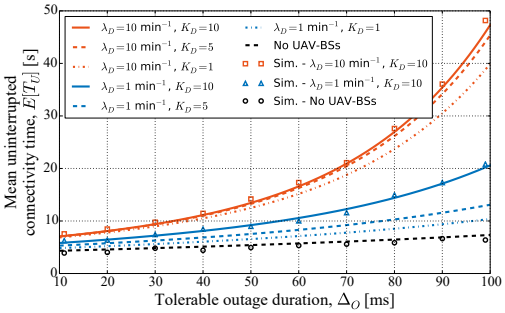


Fig. 8. Mean uninterrupted connectivity time. Effect of UAV-BS traversal intensity and its capabilities.

Finally, we observe that the relative impact of $K_D$ on the said parameter depends on the intensity of UAV-BS flights across the area. Particularly, the improvement brought by $K_D = 5$ and $K_D = 10$ vs. $K_D = 1$ is significant for 1 UAV-BS per min and marginal for 10 UAV-BSs per min. In summary, for high intensity of UAV-BS traversals, there is no need for higher capacity of the UAV-BSs. Meanwhile, if the intensity of UAV-BS flights is lower than required from the connectivity perspective, there is a driver to invest resources into advanced radio units on the UAV-BSs.

## VI. Conclusion

Dynamic and reconfigurable system architectures aiming to support backhaul operation in mmWave bands are one of the recent focus items in the ongoing 3GPP standardization. They can be further augmented by an emerging element in the 5G landscape – UAVs with flexible mobility and capability to carry radio equipment. These may become efficient backhaul connectivity providers in 5G and beyond networks, especially in case of highly dynamic traffic fluctuations to avoid excessive over-provisioning of network resources.

To this aim, we contribute a new analytical framework that incorporates 3GPP's multipath channel model, heterogeneous mobility of UAVs and humans, as well as human body blockage effects, which are identified by 3GPP as one of the main sources of performance degradation for the prospective NR operation. Our methodology allows to produce both time-averaged and continuous-time metrics in dependence on UAV-BS speed and traversal intensity, heights of the communicating entities within the scenario (NR-BS, UAV-BS, COW-BS, and human blockers), as well as blocker dimensions and speeds.

We demonstrate that UAV-BS assistance can offer significant benefits to mmWave backhaul under certain system parameters. For instance, the intensity of UAV-BS flights equal to 10 reduces the outage probability on a COW-BS backhaul link by 6 times. Moreover, by lowering the UAV-BS speed above the service area from 40 km/h down to 10 km/h, the said outage probability drops by 2 times. Further, one may derive the target intensity of UAV-BS traversals that is required to support the key performance indicators as a function of the blocker density. The contributed framework can be applied to a wide range of practical scenarios, such as conventional layouts with the near-static deployment of UAV-BSs by e.g., adjusting the speed parameter.

## References


[1] M. Shafi, A. F. Molisch, P. J. Smith, T. Haustein, P. Zhu, P. D. Silva, F. Tufvesson, A. Benjebbour, and G. Wunder, "5G: A Tutorial Overview of Standards, Trials, Challenges, Deployment, and Practice," *IEEE Journal on Selected Areas in Communications*, vol. 35, no. 6, pp. 1201–1221, June 2017.

[2] 5GPPP, "View on 5G Architecture," White paper v2.0, December 2017.

[3] 3GPP, "Report of 3GPP TSG RAN meeting #78," 3GPP RP-180516, December 2017.

[4] J. Sachs, G. Wikstrom, T. Dudda, R. Baldemair, and K. Kittichokechai, "5G Radio Network Design for Ultra-Reliable Low-Latency Communication," *IEEE Network*, vol. 32, no. 2, pp. 24–31, March 2018.

[5] U. Siddique, H. Tabassum, E. Hossain, and D. I. Kim, "Wireless backhauling of 5G small cells: Challenges and solution approaches," *IEEE Wireless Communications*, vol. 22, no. 5, pp. 22–31, October 2015.

[6] C. Dehos, J. L. Gonzalez, A. D. Domenico, D. Ktenas, and L. Dussopt, "Millimeter-wave access and backhauling: The solution to the exponential data traffic increase in 5G mobile communications systems?" *IEEE Communications Magazine*, vol. 52, no. 9, pp. 88–95, September 2014.

[7] T. Bai, R. Vaze, and R. W. Heath, "Analysis of blockage effects on urban cellular networks," *IEEE Transactions on Wireless Communications*, vol. 13, no. 9, pp. 5070–5083, September 2014.

[8] M. Gapeyenko *et al.*, "On the temporal effects of mobile blockers in urban millimeter-wave cellular scenarios," *IEEE Transactions on Vehicular Technology*, vol. 66, no. 11, pp. 10 124–10 138, November 2017.

[9] V. Petrov, M. Komarov, D. Moltchanov, J. M. Jornet, and Y. Koucheryavy, "Interference and SINR in Millimeter Wave and Terahertz Communication Systems With Blocking and Directional Antennas," *IEEE Transactions on Wireless Communications*, vol. 16, no. 3, pp. 1791–1808, March 2017.

[10] V. Petrov, M. A. Lema, M. Gapeyenko, K. Antonakoglou, D. Moltchanov, F. Sardis, A. Samuylov, S. Andreev, Y. Koucheryavy, and M. Dohler, "Achieving End-to-End Reliability of Mission-Critical Traffic in Softwarized 5G Networks," *IEEE Journal on Selected Areas in Communications*, vol. 36, no. 3, pp. 485–501, March 2018.

[11] 3GPP, "Study on channel model for frequencies from 0.5 to 100 GHz (Release 15)," 3GPP TR 38.901 V15.0.0, June 2018.

[12] F. B. Tesema, A. Awada, I. Viering, M. Simsek, and G. Fettweis, "Evaluation of context-aware mobility robustness optimization and multi-connectivity in intra-frequency 5G ultra dense networks," *IEEE Wireless Communications Letters*, vol. 5, no. 6, pp. 608–611, December 2016.

[13] O. E. Ayach, S. Subramanian, J. E. Smee, A. Sampath, and J. Li, "Method and apparatus for connection point discovery and association in a directional wireless network," October 2016, US9474013B2. [Online]. Available: https://patents.google.com/patent/US9474013B2/en

[14] M. Mousaei and B. Smida, "Optimizing pilot overhead for ultra-reliable short-packet transmission," in *IEEE International Conference on Communications*, May 2017.

[15] NGMN, "Small cell backhaul requirements," White paper, June 2012.

[16] 3GPP, "Study on integrated access and backhaul (Release 15)," 3GPP TR 38.874 V0.4.0, August 2018.

[17] C. Saha, M. Afshang, and H. S. Dhillon, "Integrated mmWave Access and Backhaul in 5G: Bandwidth partitioning and downlink analysis," *Available: https://arxiv.org/pdf/1710.06255.pdf*, 2018.

[18] K. Balachandran, J. Kang, K. Karakayali, and J. Singh, "Capacity benefits of relays with in-band backhauling in cellular networks," in *IEEE International Conference on Communications*, May 2008.

[19] M. Jaber, F. J. Lopez-Martinez, M. A. Imran, A. Sutton, A. Tukmanov, and R. Tafazolli, "Wireless backhaul: Performance modelling and impact on user association for 5G," *IEEE Transactions on Wireless Communications*, pp. 1–1, 2018.

[20] I. Bor-Yaliniz, A. El-Keyi, and H. Yanikomeroglu, "Efficient 3-D placement of an aerial base station in next generation cellular networks," in *IEEE International Conference on Communications*, May 2016.

[21] E. Kalantari, M. Z. Shakir, H. Yanikomeroglu, and A. Yongacoglu, "Backhaul-aware robust 3D drone placement in 5G+ wireless networks," in *IEEE International Conference on Communications Workshops (ICC Wkshps)*, May 2017, pp. 1–6.

[22] M. Mozaffari, W. Saad, M. Bennis, and M. Debbah, "Efficient deployment of multiple unmanned aerial vehicles for optimal wireless coverage," *IEEE Communications Letters*, vol. 20, no. 8, pp. 1647–1650, August 2016.

[23] K. Haneda *et al.*, "5G 3GPP-like channel models for outdoor urban microcellular and macrocellular environments," in *IEEE 83rd Vehicular Technology Conference (VTC Spring)*, May 2016.

[24] 3GPP, "Study on enhanced LTE support for aerial vehicles, (Release 15)," TR 36.777 V15.0.0, January 2018.

[25] A. Fotouhi, M. Ding, and M. Hassan, "Dynamic base station repositioning to improve performance of drone small cells," in *2016 IEEE Globecom Workshops (GC Wkshps)*, December 2016, pp. 1–6.

[26] J. G. Andrews, T. Bai, M. Kulkarni, A. Alkhateeb, A. Gupta, and R. W. Heath, "Modeling and analyzing millimeter wave cellular systems," *IEEE Transactions on Communications*, vol. 65, no. 1, pp. 403–430, January 2016.

[27] M. Zhang, M. Polese, M. Mezzavilla, S. Rangan, and M. Zorzi, "Ns-3 Implementation of the 3GPP MIMO Channel Model for Frequency Spectrum above 6 GHz," in *Workshop on ns-3*, June 2017.

[28] M. Gapeyenko, V. Petrov, D. Moltchanov, S. Andreev, Y. Koucheryavy, M. Valkama, M. R. Akdeniz, and N. Himayat, "An Analytical Representation of the 3GPP 3D Channel Model Parameters for mmWave Bands," in *2nd ACM Workshop on Millimeter-Wave Networks and Sensing Systems*, October 2018, pp. 1–6.

[29] Y. Zeng, R. Zhang, and T. J. Lim, "Wireless communications with unmanned aerial vehicles: Opportunities and challenges," *IEEE Communications Magazine*, vol. 54, no. 5, pp. 36–42, May 2016.

[30] P. Nain, D. Towsley, B. Liu, and Z. Liu, "Properties of random direction models," in *IEEE INFOCOM*, vol. 3, March 2005.

[31] A. M. Mathai, *An introduction to geometrical probability: Distributional aspects with applications*. CRC Press, 1999, vol. 1.

[32] G. Newell, "The M/G/$\infty$ queue," *SIAM Journal on Applied Mathematics*, vol. 14, no. 1, pp. 86–88, 1966.

[33] R. Groenevelt, "Stochastic models for mobile ad hoc networks," INRIA Sophia-Antipolis, PhD thesis, 2005.

[34] D. J. Daley, "The busy period of the M/GI/$\infty$ queue," *Queueing Systems: Theory and Applications*, vol. 38, no. 2, pp. 195–204, 2001.

[35] J. G. Kemeny, J. L. Snell *et al.*, *Finite Markov chains*. van Nostrand Princeton, NJ, 1960, vol. 356.

[36] T. Altiok, "On the phase-type approximations of general distributions," *IIE Transactions*, vol. 17, no. 2, pp. 110–116, 1985.

[37] M. F. Neuts, *Matrix-geometric solutions in stochastic models: an algorithmic approach*. Courier Corporation, 1981.

[38] V. Petrov *et al.*, "Dynamic multi-connectivity performance in ultra-dense urban mmWave deployments," *IEEE Journal on Selected Areas in Communications*, vol. 35, no. 9, pp. 2038–2055, September 2017.


**Margarita Gapeyenko** (margarita.gapeyenko@tut.fi) is a Ph.D. candidate at the Laboratory of Electronics and Communications Engineering at Tampere University of Technology, Finland. She earned her M.Sc. degree in Telecommunication Engineering from University of Vaasa, Finland, in 2014, and B.Sc. degree in Radio-Engineering, Electronics, and Telecommunications from Karaganda State Technical University, Kazakhstan, in 2012. Her research interests include mathematical analysis, performance evaluation, and optimization methods for mmWave networks, UAV communications, and (beyond-)5G heterogeneous systems.

**Vitaly Petrov** (vitaly.petrov@tut.fi) received the M.Sc. degree in information systems security from the Saint Petersburg State University of Aerospace Instrumentation, St Petersburg, Russia, in 2011, and the M.Sc. degree in communications engineering from the Tampere University of Technology, Tampere, Finland, in 2014, where he is currently pursuing the Ph.D. degree. He was a Visiting Scholar with the Georgia Institute of Technology, Atlanta, USA, in 2014 and a Strategic Intern with the Nokia Research Center, Helsinki, Finland, in 2012. He is the recipient of Best Student Paper Award at IEEE VTC-Fall'15 and Best Student Poster Award at IEEE WCNC'17. His current research interests are in Internet-of-Things, mmWave/THz band communications, nanonetworks, cryptology, and network security.

**Dmitri Moltchanov** (dmitri.moltchanov@tut.fi) is a Senior Research Scientist in the Laboratory of Electronics and Communications Engineering, Tampere University of Technology, Finland. He received his M.Sc. and Cand.Sc. degrees from Saint-Petersburg State University of Telecommunications, Russia, in 2000 and 2002, respectively, and Ph.D. degree from Tampere University of Technology in 2006. His research interests include performance evaluation and optimization issues of wired and wireless IP networks, Internet traffic dynamics, quality of user experience of real-time applications, and traffic localization P2P networks. Dmitri Moltchanov serves as TPC member in a number of international conferences. He authored more than 50 publications.

**Sergey Andreev** (sergey.andreev@tut.fi) received the Specialist and Cand.Sc. degrees from St. Petersburg State University of Aerospace Instrumentation, St. Petersburg, Russia, in 2006 and 2009, respectively, and the Ph.D. degree from Tampere University of Technology, Finland, in 2012. Since 2018, he has been a Visiting Senior Research Fellow with the Centre for Telecommunications Research, Kings College London, U.K. He is currently a Senior Research Scientist with the Laboratory of Electronics and Communications Engineering, Tampere University of Technology. He has authored or co-authored over 150 published research works on wireless communications, energy efficiency, heterogeneous networking, cooperative communications, and machine-to-machine applications.

**Nageen Himayat** is a Principal Engineer with Intel Labs, where she leads a team conducting research on several aspects of next generation (5G/5G+) of mobile broadband systems. Her research contributions span areas such as multi-radio heterogeneous networks, mm-wave communication, energy-efficient designs, cross layer radio resource management, multi-antenna, and non-linear signal processing techniques. She has authored over 250 technical publications, contributing to several IEEE peer-reviewed publications, 3GPP/IEEE standards, as well as holds numerous patents. Prior to Intel, Dr. Himayat was with Lucent Technologies and General Instrument Corp, where she developed standards and systems for both wireless and wire-line broadband access networks. Dr. Himayat obtained her B.S.E.E degree from Rice University, and her Ph.D. degree from the University of Pennsylvania. She also holds an MBA degree from the Haas School of Business at University of California, Berkeley.

**Yevgeni Koucheryavy** (evgeni.kucheryavy@tut.fi) received the Ph.D. degree from the Tampere University of Technology, in 2004. He is a Professor with the Laboratory of Electronics and Communications Engineering, Tampere University of Technology, Finland. He is the author of numerous publications in the field of advanced wired and wireless networking and communications. His current research interests include various aspects in heterogeneous wireless communication networks and systems, the Internet of Things and its standardization, and nanocommunications. He is an Associate Technical Editor of the IEEE Communications Magazine and Editor of the IEEE Communications Surveys and Tutorials.